

University of Bremen
Faculty of Geosciences

Nankai Trough fault slip behavior analyzed in-situ and in shear experiments

Dissertation in
Geosciences

by

Alexander Rösner

Submitted in Partial Fulfillment
of the Requirements
for the Degree of
– **Doctor rer. nat.** –

Reviewers / Gutachter

Prof. Dr. Achim J. Kopf

University of Bremen

MARUM - Centre for Marine Environmental Sciences

Leobener Str. 8

28359 Bremen, Germany

Prof. Dr. Michael Stipp

Martin-Luther-Universität Halle-Wittenberg

Dekanat der Naturwissenschaftlichen Fakultät III

Agrar- und Ernährungswissenschaften, Geowissenschaften und Informatik

06099 Halle Germany

Abstract

The Nankai Trough subduction zone hosts various modes of fault slip from slow to megathrust earthquakes. Slow earthquakes release energy slowly over days to years and can only be recorded geodetically or by borehole observatories. It is not well understood how they connect to regular earthquakes. In contrast, megathrust earthquakes are rapid events that often generate destructive tsunamis, documented for several centuries in the Nankai Trough. Successful earthquake mitigation strategies can only be developed with a better understanding of fault slip behavior and deformation processes within the seismogenic zone and the overlying accretionary prism.

The Nankai Trough Seismogenic Zone Experiment (NanTroSEIZE) is a multi-disciplinary and multi-expedition research project designed to investigate seismogenesis and fault mechanics in the Nankai Trough subduction zone. NanTroSEIZE employs in-situ geophysical measurements, direct sampling and (real-time) long-term monitoring combined with laboratory and numerical studies. Scientific results in this thesis are closely connected to those NanTroSEIZE scientific objectives related to laboratory and borehole observatory studies. Laboratory friction experiments are a powerful tool to investigate earthquake mechanical processes in simulated fault zones under controlled boundary conditions. A comprehensive set of laboratory friction experiments on Nankai Trough fault zone sediment analyzes strengthening and weakening mechanisms both are requirements for repeating earthquakes. Therefore, the sediment healing behavior, velocity and slip dependence of friction is tested in shear experiments. Deep sea borehole long-term observatories can detect fluid flow and strain perturbations by in-situ pressure and temperature measurements. The observatories are hydraulically disconnected from the open ocean and thus pressure and temperature perturbations represent fluid movement induced by strain changes within the accretionary prism.

In the scope of the NanTroSEIZE project several offshore boreholes were drilled along a transect covering the whole accretionary prism starting at the subducting plate and ending further landwards in the Kumano Basin. In this thesis a special focus is given on sediments from the major fault systems the megasplay fault (C0004, C0010) and frontal thrust zone (C0007, C0006) that were tested in a direct shear configuration at effective normal stresses ranging from $\sim 3 - 17$ MPa. The sediments were sheared as intact and powdered samples in a velocity stepping sequence from $0.01 - 30$ $\mu\text{m/s}$. Both, the coefficient of sliding friction and the velocity-dependent friction parameter $a - b$, a measure for how the coefficient of friction changes with velocity are found to be independent of the applied effective normal stress. All

samples showed mixtures of velocity weakening and velocity strengthening behavior but intact samples, where the in-situ fabric is conserved, tested at in-situ stress conditions showed systematically lower $a - b$ values; at shearing velocities $< 1 \mu\text{m/s}$ strong velocity weakening is observed. The velocity-weakening behavior of intact samples is explained by a larger b -value or evolutionary effect, due to a smaller area of real contact in the intact samples. The laboratory results suggest that former scientific studies mainly done on powdered sediments tested at high effective normal stresses overestimate $a - b$ values of Nankai Trough fault zone material. Thus, the Nankai Trough might be velocity weakening from seismogenic depth up to the seafloor.

This initial set of experiments on Nankai Trough natural fault zone material showed evidence for a systematic control of effective normal stress on slip dependence of friction. Therefore, the second laboratory study investigates the slip dependence of powdered C0004 fault zone sediment in constant and velocity step experiments under effective normal stresses from 2 to 18 MPa. Two different weakening mechanisms act in megasplay fault sediment: (i) velocity weakening, and (ii) slip weakening. Slip-dependent weakening is the dominant mechanism over millimeter-scale displacement. At low effective normal stresses, slip weakening is more pronounced and the sediment shows a higher peak friction coefficient. The higher peak friction suggests that more energy can be stored in the sediment before failure. Moreover, an increasing efficiency of slip weakening at shallow depth is energetically favorable for coseismic slip propagating updip along the megasplay fault. Thus, increasing slip weakening with decreasing depth favors coseismic slip along the megasplay fault up to the seafloor, causing large seafloor deformation and potentially accompanied tsunamis.

Another part of the NanTroSEIZE project was the installation of permanent borehole observatories, this is a sensitive tool to analyze spatial and temporal long-term changes in physical and hydrological properties in a subduction zone. In contrast to laboratory experiments on discrete samples, borehole observatories measure formation-scale wide properties derived from e.g. in-situ pressure and temperature. Pressure monitoring allows for calculation of the tidal loading efficiency that describes the damping of tidally induced pore water pressure signals into the sediment formation. The tidal loading efficiency is necessary to determine poroelastic formation properties e.g. permeability. The megasplay fault at Site C0010 has a formation permeability of $> 6.4 \cdot 10^{-13} \text{ m}^2$ determined from a 5.3 year-long pressure time series. Over this period, earthquakes caused mainly contraction in the accretionary prism indicated by an increase in formation pressure and a decrease in tidal loading efficiency. These earthquake induced perturbations follow a magnitude-distance relationship similar to earthquake driven transients in terrestrial water wells. The observed perturbations and later

recoveries are best explained by dynamic strains that exsolve dissolved gas from the pore water.

Furthermore, long-term borehole pressure records act as proxies for strain accumulation and release, where pressure increases account for sediment contraction and pressure decreases for sediment dilatancy. In combination with seafloor pressure gauges and ocean bottom seismometers, this allows a more precise detection of earthquake hypocenters than would be possible with conventional land-based stations. For example, land-based networks classified the Mie-ken Nanto-oki Mw 6 earthquake as an intraslab earthquake, whereas inversion results of close by acquired offshore data classified it as a plate boundary earthquake. Strains derived from two borehole formation pressure records were essential to narrow down possible fault plane solutions. Additionally, long-term pressure monitoring revealed repetitive shallow slow slip events (SSEs) in the Nankai Trough. The SSE recurrence interval is 4 – 15 months and can be explained by 1 – 4 cm of fault slip on the plate boundary thrust. This frequent release of accumulated strain accounts for 30 – 55 % of the plate motion. The SSEs are accompanied by swarms of low frequency tremor.

To bridge the gap between in-situ monitoring and small scale laboratory experiments the SSE stress drops were compared to laboratory derived stress drops from extrapolated healing experiments in a rotary shear system. SSE stress drop estimates from laboratory healing experiments on megasplay fault and frontal thrust zone sediment show higher stress drops for megasplay fault sediment because of a higher healing rate. Stress drops for both sediments are one to two orders of magnitude larger than the derived stress drops from seismic moments for the documented SSEs. The reasons for this large discrepancy between in-situ strength recovery and laboratory healing rates need further investigation.

My multi-disciplinary thesis reveals that the fault zone sediment is dominantly velocity and slip weakening and thus coseismic slip induced by a megathrust earthquakes is likely to propagate updip to the seafloor along the megasplay fault or the plate boundary thrust. Therefore, the risk for destructive tsunamis is much larger than previously thought. Additionally, borehole observatories improved the monitoring in time and space of different modes of fault slip in the shallow accretionary prism. The results focus on the shallow depth, for the continuation of earthquakes to the seafloor with associated tsunamigenic potential. In order to be able to extrapolate these results to seismogenic depths, samples from and observatories at seismogenic depths are necessary. This should be the focus of upcoming ocean drilling expeditions.

Zusammenfassung

In der Nankai Trough Subduktionszone entstehen verschiedene Arten von Erdbeben darunter langsame wie auch schnelle "megathrust"-Erdbeben. Langsame Erdbeben entladen ihre Energie über einen Zeitraum von Tagen bis zu Jahren und emittieren keine seismischen Wellen. Aus diesem Grund können sie nur mit geodätischen GPS-Messungen oder Bohrlochobservatorien beobachtet werden. Im Gegensatz zu langsamen Erdbeben entlädt sich die angestaute Energie in "megathrust"-Erdbeben in relativ kurzer Zeit. Aufgrund dieser Erdbeben entstehen häufig zerstörerische Tsunamis, welche über mehrere Jahrhunderte entlang des Nankai Trough dokumentiert sind. Die Zusammenhänge zwischen langsamen und "regulären" Erdbeben sind bisher nur unzureichend verstanden oder nachvollziehbar. Erfolgreiche Risikominimierungsstrategien für Erdbeben erfordern ein besseres und umfassenderes Verständnis des zu Grunde liegenden physikalischen Entstehungs- und Ausbreitungsprozesses in Tiefen in denen Erdbeben entstehen aber auch in flachen Tiefen nahe dem Meeresboden.

Das Nankai Trough Seismogenic Zone Experiment (NanTroSEIZE) ist ein multidisziplinäres, mehrjähriges und expeditionsübergreifendes Forschungsprojekt zur Untersuchung der Seismogenese und der Erdbebenmechanik im Nankai Trough. Im NanTroSEIZE Projekt kommen geophysikalische Messungen, Bohrungen und Langzeit- Bohrlochmessungen in Kombination mit Labor- und Numerischen- Studien zur Anwendung. Die wissenschaftlichen Studien, die im Rahmen meiner Dissertation durchgeführt wurden, verfolgen u.a. die ausgerufenen wissenschaftlichen Ziele für Labor- und Langzeit- Bohrlochstudien des NanTroSEIZE Projekts. Erdbebenmechanische Sedimenteigenschaften lassen sich besonders gut mit Reibungsexperimenten im Labor unter kontrollierten Bedingungen analysieren. Eine umfassende Reihe von Reibungsexperimenten analysiert das Schwächungs- und Heilungsverhalten von Nankai Trough Störungzonsensediment. Beide Mechanismen sind eine Grundvoraussetzung für sich wiederholende Erdbeben. Die Spannungsentladung erzeugt das Erdbeben, wohingegen das Wiedererstarken (Heilen) des Sediments erst die wiederholte Spannungsentladung ermöglicht. Im Gegensatz zu Laborexperimenten können Langzeitobservatorien in-situ Druck und Temperatur messen um u.a. Fluidbewegungen oder Sedimentdeformationen zu beobachten. Die Bohrlochobservatorien sind hydraulisch vom Ozean isoliert, sodass Druck- und Temperaturschwankungen auf Fluidbewegungen im Untergrund zurückzuführen sind, die vermutlich durch Spannungsänderungen im Akkretionskeil entstehen.

Im Rahmen des NanTroSEIZE Projekts wurden zahlreiche offshore Bohrlöcher entlang eines Transsektivs (Kumano Transsektiv) gebohrt, der sich über den gesamten Akkretionskeil beginnend bei den Inputsedimenten bis zum Kumano Becken erstreckt. In meiner Dissertation werden ausschließlich Sedimente aus den Hauptstörungszonen "megasplay fault" (C0004, C0010) und der "frontal thrust zone" (C0006, C0007) getestet. In Rahmenschergeräten bei effektiven normal Spannungen von $\sim 3 - 17$ MPa wurden die Sedimente als intakte und pulverisierte Proben bei unterschiedlichen Schergeschwindigkeiten von $0,01$ bis $30 \mu\text{m/s}$ geschert. Der dynamische Reibungskoeffizient als auch der geschwindigkeitsabhängige Reibungsparameter $a - b$, ein Maß dafür, wie sich der Reibungskoeffizient mit der Geschwindigkeit ändert, sind unabhängig von der effektiven Normalspannung. Materialien die bei zunehmender Geschwindigkeit steigende Reibungskoeffizienten verzeichnen, bezeichnet man als velocity-strengthening ($a - b > 0$) das Gegenteil von velocity-weakening ($a - b < 0$). Alle untersuchten Proben verhalten sich velocity-weakening aber auch velocity-strengthening. Intakte Proben bei denen das Sedimentgefüge im Urzustand ist und die unter in-situ Spannungen getestet wurden, weisen systematisch niedrigere $a - b$ Werte auf; insbesondere bei Schergeschwindigkeiten $< 1 \mu\text{m/s}$ ist starkes velocity-weakening zu beobachten. Die niedrigeren $a - b$ Werte kommen zu Stande, da die b Werte bei intakten Proben größer sind. Größere b Werte entstehen aufgrund der kleineren realen Kontaktfläche der Scherzone verglichen zur pulverisierten Proben. Die Laborergebnisse deuten darauf hin, dass frühere wissenschaftliche Studien, die überwiegend an pulverisierten Sedimenten und häufig unter sehr hohen effektiven Normalspannungen durchgeführt wurden, die $a - b$ Werte der Störungzonensedimente überschätzen. Es ist möglich, dass die Nankai Trough Störungzonensedimente von der seismogenen Zone bis zum Meeresboden durch velocity-weakening Verhalten charakterisiert sind.

Die zuvor beschriebene experimentelle Studie an Störungzonensediment des Nankai Troughs wies Indizien auf, dass die effektive Normalspannung das wegabhängige Schwächungsverhalten kontrolliert. Dieses Phänomen wurde in weiteren Reibungsexperimenten an pulverisierten C0004 Proben in konstanten und Geschwindigkeitsstufenexperimenten unter effektiven Normalspannungen von 2 bis 18 MPa untersucht. Das untersuchte "megasplay fault" Sediment ist durch zwei verschiedene Schwächungsmechanismen charakterisiert: (i) velocity-weakening und (ii) slip-weakening. Slip weakening beschreibt die Abnahme des Reibungskoeffizienten mit zunehmendem Scherweg. Slip weakening ist der dominierende Mechanismus in C0004 Proben über mehrere Millimeter Scherweg. Bei geringen effektiven Normalspannungen ist slip weakening stärker ausgeprägt und das Sediment zeigt zusätzlich einen höheren Spitzenreibungskoeffizienten. Die höhere Spitzenreibung lässt darauf schließen, dass vor dem Versagen des Sedimentes mehr Energie

gespeichert werden kann. Slip weakening wird effizienter bei geringeren Auflasten und somit geringeren Tiefen, was sich energetisch günstig auf die Erdbebenausbreitung entlang der "megasplay fault" auswirkt. Dieses Verhalten begünstigt Erdbebenausbreitungen von seismogener Tiefe bis hinauf zum Meeresboden, was möglicherweise zur Tsunamientstehung führen kann.

Im Rahmen des NanTroSEIZE Projektes wurden permanente Bohrlochobservatorien entlang des Kumano Transsekts installiert. Bohrlochobservatorien sind hoch empfindliche Messgeräte zur räumlichen und zeitlichen Analyse von physikalischen und hydrologischen Sedimenteigenschaften. Durch Druck- und Temperaturmessungen können Formationseigenschaften erfasst werden, wohingegen Laborexperimente die selbigen Eigenschaften nur an kleinen Probenmengen bestimmen können, was häufig zu einem Skalierungsproblem führt. Druckzeitreihen aus isolierten Bohrlöchern ermöglichen die Bestimmung des Formationsdämpfungsfaktors für das tidal erzeugte Porendrucksignal im Sediment. Der Dämpfungsfaktor ermöglicht es poroelastische Eigenschaften wie z.B. die Permeabilität näherungsweise zu bestimmen. Für die "megasplay fault" im Bohrloch C0010 konnte eine Permeabilität von $>6.4 \cdot 10^{-13} \text{ m}^2$ bestimmt werden. Eine 5,3 Jahre lange Druckzeitreihe ermöglicht es, die Veränderung des Drucksignals und damit auch des Dämpfungsfaktors während verschiedener Erdbeben zu erfassen. Während der Messperiode erzeugten Erdbeben überwiegend Kontraktionen im Akkretionskeil, welche sich in Druckanstiegen widerspiegelte. Diese erdbebenverursachten Druckschwankungen folgen einer Magnituden-Distanz Gesetzmäßigkeit, die vergleichbar mit Beobachtungen an Land ist. Die Druckanstiege und der darauffolgende längerfristige Druckabfall lassen sich am besten durch Erbeben verursachte dynamische Spannungen erklären, welche im Porenwasser gelöste Gase entmischen und die sich danach wieder über längere Zeit im Wasser lösen.

Spannungen im Sediment lassen sich aus Bohrlochdruckzeitreihen ableiten, wobei Sedimente, die gestaucht werden, Porendruckanstiege und Sedimente, die sich dehnen, Porendruckabfälle erzeugen. Im Zusammenspiel mit Meeresbodendruckzeitreihen und Ozeanbodenseismometern lassen sich Erdbebenherde wesentlich präziser lokalisieren als mit konventionellen Landseismometernetzwerken. Das Hypozentrum des Magnitude 6 Mie-ken Nanto Erdbebens offshore der Kii Halbinsel wurde von Landseismometernetzwerken als Erdbeben innerhalb der subduzierten Platte klassifiziert, wohingegen die zur Verfügung stehenden Offshoredaten das Erdbeben als Störungszonen- Erdbeben klassifiziert haben. Zur Bestimmung der Herdflächenlösung waren die Bohrlochdaten von entscheidender Bedeutung im Inversionsverfahren. Darüber hinaus konnten mit den Bohrlochdruckzeitreihen sich wiederholende flache, langsame Verschiebungseignisse (slow slip event - SSE) beobachtet werden. Diese SSEs wiederholen sich alle 4 – 15 Monate und erzeugen 1 – 4 cm Versatz an

der Hauptüberschiebung zwischen den beiden Erdplatten. Diese regelmäßigen Entlastungsereignisse setzen ca. 30 – 55 % der Spannung, die durch die Plattenbewegung erzeugt wird, frei. Die SSEs werden häufig von niederfrequentem Tremor begleitet.

Um mögliche Diskrepanzen zwischen in-situ Beobachtungen und Laborexperimenten zu untersuchen, wurden die Spannungsabfälle während des SSEs mit Spannungsabfällen, abgeleitet von extrapolierten Heilungsexperimenten, verglichen. Diese Heilungsexperimente wurden in einem Ringschergerät an "megasplay fault" und "frontal thrust zone" Sedimenten durchgeführt. Scherflächen in "megasplay fault" Sediment verheilen schneller als in "frontal thrust zone" Sediment und folglich sind größere Spannungsabfälle in "megasplay fault" zu erwarten. Beide im Labor getesteten Sedimente weisen 1 bis 2 Größenordnungen höhere Spannungsabfälle auf, als die Spannungsabfälle abgeleitet vom seismischen Moment der dokumentierten SSEs. Weitere Forschung ist nötig, um diese große Diskrepanz zwischen Labor und in-situ Spannungsabfall zu erklären.

Meine multidisziplinäre Dissertation hat gezeigt, dass Nankai Trough Störungzonensedimente mit steigender Geschwindigkeit und zunehmender Verschiebung niedrigere Reibungskoeffizienten aufweisen. Dieses sedimentmechanische Verhalten begünstigt die Entstehung und Ausbreitung von Erdbeben entlang einer Störungszone wie der "megasplay fault" und der "plate boundary thrust". Bei Erdbeben, die sich bis in den flachen Akkretionskeil ausbreiten, kommt es zur Verformung des Meeresbodens, was die Entstehung von Tsunamis wahrscheinlich macht. Der Einsatz von offshore Bohrlochobservatorien in Subduktionszonen ermöglicht eine verbesserte räumliche und zeitliche Beobachtung von Plattenverschiebungen jeglicher Art (langsam bis schnell) im flachen Akkretionskeil. Meine Ergebnisse basieren auf Experimenten und Zeitreihen die flache Tiefen simulieren oder in flachen Tiefen gemessen wurden, um die Störungzonenverschiebung bei starken Erdbeben und die mögliche Tsunamibildung zu evaluieren. Um diese Ergebnisse in die Tiefe projizieren zu können, benötigen wir Gesteinsproben und Daten aus Bohrlochobservatorien in der seismogenen Zone. In zukünftigen Ozeanbohrungsexpeditionen sollten diese Ziele hohe Priorität genießen.

Table of contents

Reviewers / Gutachter	i
Abstract	i
Zusammenfassung	iv
Table of contents	viii
1 Introduction	1
1.1 State of the art	1
1.2 From slow to fast earthquakes	2
1.2.1 Earthquakes	2
1.2.2 Slow earthquakes	4
1.3 The Nankai Trough subduction zone	6
1.4 NanTroSEIZE	9
1.5 Motivation and research hypotheses	12
1.6 Organization of this thesis	15
2 Friction studies	17
2.1 Introduction	17
2.1.1 Rate and state friction laws	18
2.1.2 Frictional properties of the Nankai Trough sediments	21
2.2 Manuscript 1 (EPSL submitted): Friction experiments under in-situ stress reveals unexpected velocity-weakening in Nankai accretionary prism samples	24
2.3 Manuscript 2 (in preparation): Slip dependent weakening revealed for a shallow megasplay fault in the Nankai subduction zone	48
2.4 Manuscript 3 (in preparation): Frictional healing of the Nankai frontal thrust and megasplay fault- Bridging the gap between laboratory and in-situ data	63
3 Long-term borehole monitoring studies	78
3.1 Introduction	78
3.1.1 History of borehole observatories in ocean drilling	78
3.1.2 Borehole observatories along the Nankai Trough	81
3.2 Manuscript 4 (JGR published): Near-field observations of an offshore Mw 6.0 earthquake from an integrated seafloor and subseafloor monitoring network at the Nankai Trough, southwest Japan [co-authorship]	83

3.3	Manuscript 5 (Science published): Recurring and triggered slow-slip events near the trench at the Nankai Trough subduction megathrust [co-authorship].....	107
3.4	Manuscript 6 (JGR published): Changes in Physical Properties of the Nankai Trough Megaseismic Fault Induced by Earthquakes, Detected by Continuous Pressure Monitoring [co-authorship].....	127
4	Conclusions and Outlook.....	158
Appendix A: Conference contributions.....i		
A.1	AGU Fall Meeting 2016 Abstracts	i
A.2	IODP-ICDP Kolloquium 2017 Abstract	vi
A.3	JPGU-AGU Joint Meeting 2017 Abstracts	viii
A.4	AGU Fall Meeting 2017 Abstract	xiii
A.5	AGU Fall Meeting 2018 Abstract	xiv
A.6	AOGS 2018 Abstract.....	xvi
A.7	JPGU 2018 Abstract.....	xvii
A.8	EGU General Assembly 2019 Abstract	xix
Appendix B: Cruises..... xxi		
B.1	Proceedings of the IODP Volume 365 Abstract.....	xxi
B.2	Proceedings of the IODP Volume 380 Abstract.....	xxiv
B.3	Report and preliminary results of R/V Sonne cruise SO251 Summary	xxvi
Acknowledgments		
		xxxii
References.....		
		xxxii
Declaration		
		li

1 Introduction

1.1 State of the art

Convergent margins host the most destructive natural hazard on our planet earth. The collision of two tectonic plates causes great earthquakes, volcanic activity, tsunamis and landslides. Convergent margins concentrate around the Pacific Ocean (the Pacific ring of fire) and Indian Ocean but can be also found in the Mediterranean and along the Lesser Antilles. Along the 55,000 km of convergent margin the 22 out of 23 most energetic earthquake on earth occurred (Stern, 2002). Convergent margins hosted the 11 out of 12 most explosive volcanic eruptions and the 19 deadliest tsunamis (Stern et al., 2016). Convergent plate margins are the seismically most active regions on earth and nucleate 90 % of the world earthquakes in terms of numbers and seismic moment (Byrne et al., 1988; Pacheco and Sykes, 1992). Coastal populations and economies are especially vulnerable to natural hazards, because many megacities center along convergent margins. Natural hazards associated with convergent plate margins are likely to have even more devastating effects in the near future because coastal populations are growing especially around Asia.

One type of convergent plate margin is the ensialic island arc type, where the thinner and denser oceanic lithosphere is subducted beneath continental lithosphere. An island arc forms on top of continental lithosphere but is separated from the continent by a marine basin consisting of oceanic lithosphere (e.g. Japan, Kuril, Aleutian). The plate margin can be structured in distinct morphological domains (from trench to the upper plate) i) deep sea trench, ii) forearc region comprising the outer ridge and forearc basin, iii) the volcanic arc and iv) the back arc basin (Frisch et al., 2011). A forearc prism may form when a thick sediment column on top of the incoming oceanic basement is subducted. The sediments are either subducted to great depths or are scraped off at the frontal tip and form an extensive accretionary prism at the upper plate (e.g. Nankai Trough). In contrast to accretion, other convergent margins are characterized by subduction erosion, where the upper plate is eroded by the subducting plate (e.g. Japan Trench).

The term convergent plate margin and subduction zone are often used interchangeably, but they describe different aspects. A subduction zone is the three dimensional manifestation of the recycling of sediments, oceanic crust and mantle lithosphere in the earth mantle, whereas the convergent plate margin describes the surficial manifestation (Stern, 2002). Subduction zones are defined by the occurrence of earthquakes down to 700 km depth on an inclined

plane towards the lower mantle (Stern, 2002). In the seismogenic zone strong plate interface coupling of the overriding and the underthrust plate cause thrust faulting that generates the most destructive earthquakes on earth. These earthquakes can nucleate typically at depths of 30 – 40 km, or shallower, and in some cases can rupture the entire downdip extent of the seismogenic zone; the size of the earthquake typically depends on the dimension of the rupture area (along-strike and along-dip) (Stern, 2002). The depth range of the seismogenic zone is thought to span from 5 – 10 km (updip end) to 40 – 50 km (downdip end), where the shallow part of the subduction zone (updip of the seismogenic zone) is often described as aseismic (Dixon and Moore, 2007). Shallow subduction zone megathrust earthquakes threaten coastal economies by physical ground shaking and by earthquake-triggered tsunamis. Recent devastating examples are the 26th December 2004 Sumatra and the 11th March 2011 Tohoku earthquake.

1.2 From slow to fast earthquakes

Traditionally earthquakes were described as sudden energy release, as two pieces of the Earth's crust slip past each other in a matter of seconds. The abrupt crustal motion radiates seismic energy, which are recorded by seismometers. I will refer to these earthquakes as regular earthquakes or simply as "earthquakes". In contrast, slow earthquakes occur slowly, over days to years, and emit energy too slowly to be recorded seismically. The first slow earthquakes were discovered ~40 years ago (Sacks et al., 1978), but the availability in the last two decades of densely spaced and sensitive geodetic and seismic monitoring networks have greatly enhanced the understanding of slow earthquake processes (Beroza and Ide, 2011; Schwartz and Rokosky, 2007).

1.2.1 Earthquakes

Earthquakes are the result of sudden slip on faults, which radiate energy and induce ground shaking. They release stored elastic strain energy resulting from long-term relative tectonic plate motion. Most of the energy is stored near or along plate boundaries as shear stress between adjacent tectonic plates (Kramer, 1996). When the shear stress at a point in the rock mass exceeds the shear strength, the rock fails and the stored elastic energy is released by fault slip. Generally, fault slip occurs along pre-existing fault planes, which are planes of weakness in the rock mass. The failure process releases energy in three different ways 1) radiated energy as seismic waves, 2) mechanically energy consumed by fracture growth and 3) thermal energy by frictional heating (Kanamori and Brodsky, 2004). Shallow marine

earthquake fault slip that displaces the seafloor often trigger tsunamis that can affect the shore line even hundreds of kilometers away.

The main driver for earthquakes is the movement of rigid tectonic plates, which can move relative to each other at mm to multi-cm/a rates. Most of the deformation occurs along the plate boundaries either aseismically (slowly and continuously) or seismically (fast and aperiodic). Plate boundaries host the majority of earthquakes. In the long-term, relative plate motion and resulting interseismic stress build up are in equilibrium with coseismic stress release over geological time scales, resulting in periodic instability (Figure 1 A). Considering an average stress accumulation rate and average coseismic stress drop a recurrence interval of 100 – 1000 years for major earthquakes along plate boundaries is derived, which is in good agreement with documented earthquake recurrence intervals (Kanamori and Brodsky, 2004). Nevertheless, stress accumulation rates could change over time and the shear strength of fault rocks might not be uniform over time. Transient changes in shear strength could be affected by fluid migration, mineral solution, alteration or pore fluid pressure build-up. Earthquake recurrence and stress drop characteristics may also change because the stress field is affected by nearby or far field earthquakes. Consequently, the simple sketch shown in Figure 1 A becomes much more complicated and interseismic periods between repeating earthquakes are less predictable (Figure 1 B).

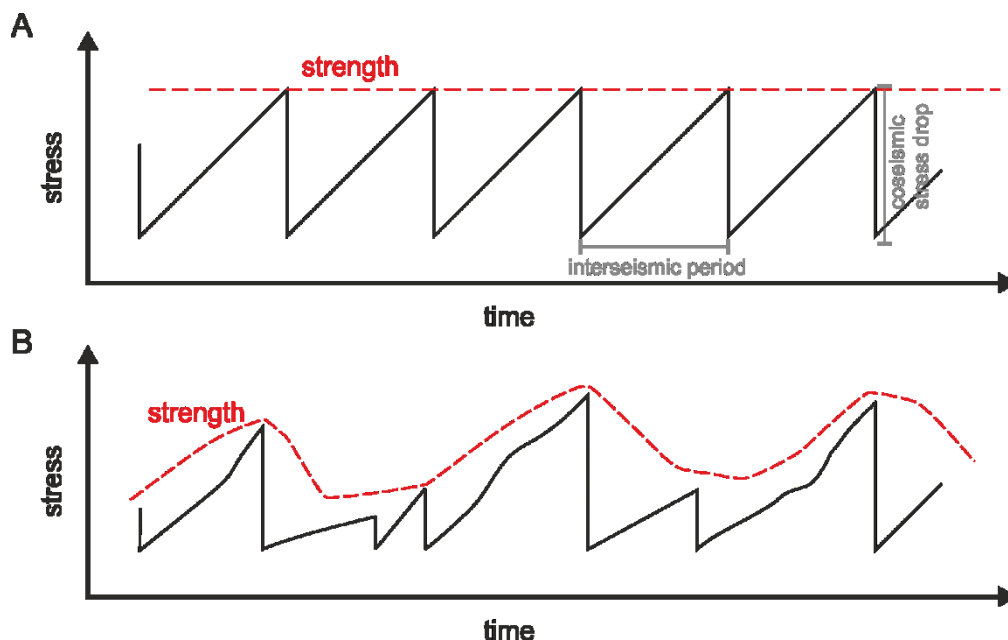


Figure 1: Temporal variations of stress drop, loading rate and shear strength of a fault during multiple earthquake cycles. (A) constant process (B) variable process (modified from Kanamori and Brodsky, 2001).

Figure 1 B illustrates different interseismic periods and stress drops for repeating earthquakes. The stress drop is a measure of the energy release, thus earthquakes of different sizes are produced over geological time scales on a fault. Earthquake size is often expressed by an

earthquake magnitude. One common scientifically used earthquake magnitude scale is the moment magnitude scale, which is based on the seismic moment of an event. The seismic moment is the product of average fault slip, fault area and rigidity. It is a measure of the work done by the earthquake and thus correlates well with the released elastic energy (Kramer, 1996).

For a long time earthquakes were thought to be a brittle fracture phenomena forming new cracks in a rock mass, but the observations of earthquake slip along pre-existing faults changed the understanding of earthquake mechanics towards a frictional phenomena (Scholz, 1998). Laboratory evidence for frictional stick slip behavior was presented by Brace and Byerlee (1966), where *stick* represents the interseismic period and *slip* the coseismic period. Frictional sliding velocities of regular earthquakes are in the order of 1 m/s.

Different scientific disciplines (e.g. seismology, paleoseismology, rock mechanics, among others) investigate the nature of earthquakes. Seismology derives information about the rupture process and earthquake location by studying the propagation of emitted elastic waves from an earthquake. In contrast, paleoseismology derives information about ancient earthquakes from field studies of rocks and sediments that have been deformed in the earthquake cycle. In contrast, rock mechanics investigates the mechanics of earthquake rupture and coseismic slip in analog laboratory experiments with rock and sediment samples tested under changing stress, temperature and sliding velocity conditions. These studies are able to simulate the full spectrum of fault slip behaviors from aseismic plate motion to fast earthquake rupture (Marone, 2019).

1.2.2 Slow earthquakes

Recently, expanding geophysical and geodetic networks along subduction zones including seismometers, strain meters, and GPS measurements revealed a transitional sliding mode between stable sliding and fast rupture along megathrust faults summarized as slow earthquakes (Obara and Kato, 2016; Schwartz and Rokosky, 2007). Slow earthquakes designate a group of earthquakes such as low frequency earthquakes (LFE), very low frequency earthquakes (VLF), tremor and geodetically detected short term and long term slow slip events (SSE) that all have longer durations than regular earthquakes. These different kinds of slow earthquakes arise from frictional fault slip similar to regular earthquakes on preexisting faults (often the megathrust fault), either down dip of the fully locked seismogenic zone or updip of the seismogenic zone beneath the accretionary prism at shallow depth (Ide et al., 2007; Marone, 2019). The different slip (LFE, VLFE, Tremor and SSE) phenomena occur often at the same location and time in a subduction zone (Araki et al., 2017; Ito et al., 2007; Rogers

and Dragert, 2003). The seismic moment of slow earthquakes is thought to scale with the event duration that differs from the scaling relationship of regular earthquakes (Ide et al., 2007). Megathrust earthquakes have interseismic periods of decades to centuries whereas slow earthquakes often show astonishing regularity and recurrence intervals of month to years (Beroza and Ide, 2011; Obara and Kato, 2016).

LFE and VLFE can be detected with seismometers whereas geodetic measurements or borehole tilt/strain meters can only detect SSE, because intermediate sliding rates of SSEs between long-term plate motion and rupture velocities of regular earthquakes do not radiate seismic waves (Saffer and Wallace, 2015). LFE and VLFE differ in terms of the radiated frequency spectrum and duration from regular earthquakes. Slow earthquakes mark a transition in terms of fault zone stability from steady aseismic creeping fault zone segments to fault zone segments failing in stick slip behavior (Obara and Kato, 2016).

Rock friction, low fault rigidity, fault heterogeneity and/or low effective normal stress due to elevated pore water pressure might be responsible for the transitional state of slow earthquakes (Saffer and Wallace, 2015). Slow earthquakes show stress drops 2 – 3 orders of magnitude smaller than regular earthquakes (Beroza and Ide, 2011; Gao et al., 2012; Saffer and Wallace, 2015), which would be consistent with low effective stresses on the fault.

Faults systems hosting a significant amount of slow earthquakes may reduce their seismic hazard, because the faults slip budget is partially covered by non-destructive slow earthquakes. On the other hand slow earthquakes might be responsible for stress transfer along the megathrust and could stress critically fully locked patches until failure (Obara and Kato, 2016). Changing recurrence intervals of slow earthquakes before large earthquakes have been observed in numerical models of slow slip cycles and thus could be potentially interpreted as precursory signals for larger earthquakes (Obara and Kato, 2016). Slow earthquakes play a significant role in the earthquake cycle along subduction megathrusts.

1.3 The Nankai Trough subduction zone

The archipelago of Japan is located at the northeastern margin of the Pacific Ocean and consists of the islands Kyushu, Shikoku, Honshu and Hokkaido (from southwest to northeast). It is close to the triple junction between the continental Eurasian Plate and the oceanic Pacific and Philippine Sea Plates (Figure 2). The islands of Japan are the result of the subduction of the Pacific and the Philippine Sea Plate beneath the Eurasian Plate, which forms an extensive island arc. In the south-east of Japan, between the Kyushu-Palau Ridge to the west and the Izu-Bonin Arc to the east, is located the Nankai Trough subduction zone.

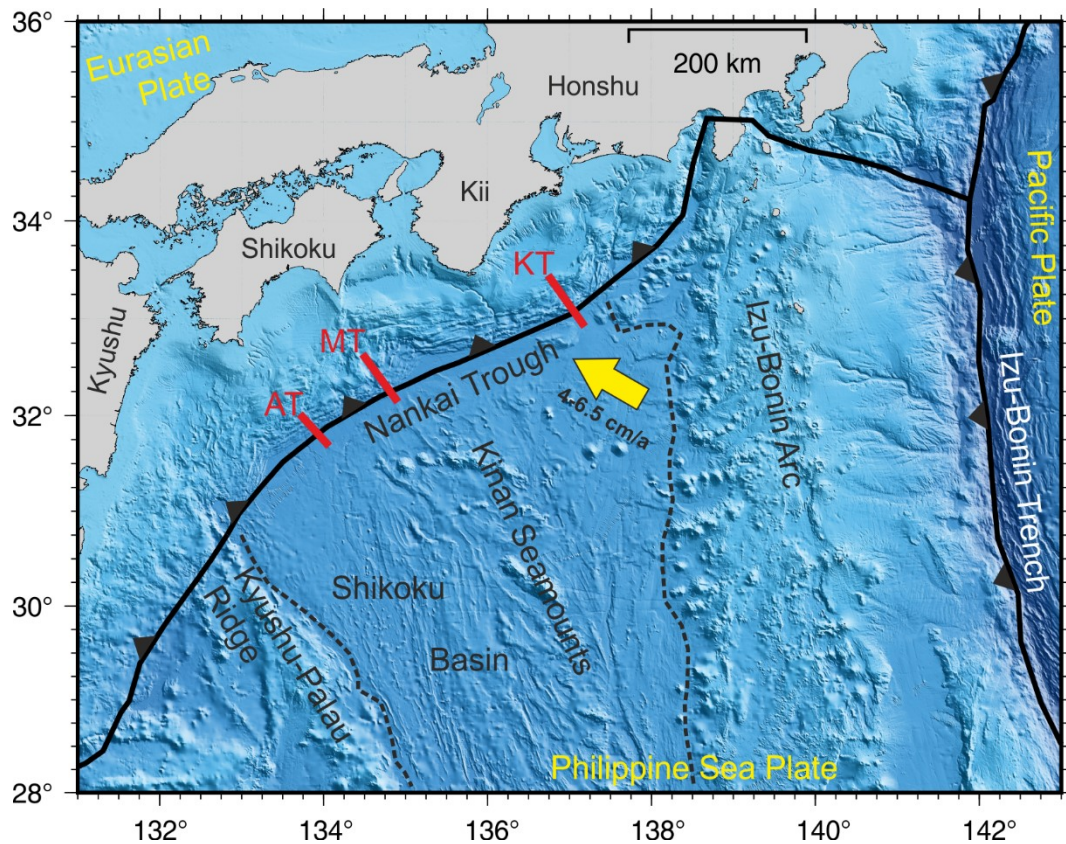


Figure 2: Regional geological setting of the Nankai Trough subduction zone (adapted from Taylor (1992)). Dashed lines indicate western and eastern boundaries of the Shikoku Basin. AT = Ashizuri, MT = Muroto and KT = Kumano drilling transect.

Currently, the Shikoku Basin provides the sedimentary input for the formation of an accretionary complex off the Kii peninsula (Underwood, 2018). The Shikoku Basin formed as a result of the Izu-Bonin back-arc rifting and seafloor spreading about 30 Ma ago (Chamot-Rooke et al., 1987; Okino et al., 1999). Seafloor spreading ceased 15 Ma ago but sporadic eruptions along the Kinan seamount chain, located on top of the extinct spreading axis, continued up to 7 Ma ago (Ishii et al., 2000). Plate tectonic reconstructions suggest the Pacific Plate was actively subducting along the proto Nankai Trough before 15 Ma (Hall, 2012; Wu et al., 2016). Sinistral slip along a transcurrent fault system in southeastern Japan shifted the

triple junction to the northeast (Kimura et al., 2014). This northeastward movement created the collision of the Izu-Bonin Arc with the Honshu Island Arc at 8 – 6 Ma. At about 6 Ma, a variation in the subduction direction of the Philippine Sea Plate re-initiated nearly trench-normal subduction, with the Philippine Sea Plate being now subducted at the proto Nankai Trough (Underwood, 2018; Wu et al., 2016). Consequently, over the last 30 Ma, the origin of the subducted sediments along the Nankai Trough changed from Pacific Plate to Philippine Sea Plate (Shikoku Basin sediment). The complex tectonic history created significant along strike variations in lithostratigraphy and diachronous facies boundaries throughout the Shikoku Basin (Pickering et al., 2013; Underwood, 2018). The total sediment thickness also increases from south to north (Higuchi et al., 2007), where a large amount of sediment along the trench axis is originating from the Izu-Honshu collision zone (Ike et al., 2008).

Various Expeditions of the Deep Sea Drilling Program (DSDP), the Ocean drilling Program (ODP), the Integrated Ocean Drilling Program (IODP) and the International Ocean drilling Program (IODP) targeted the 700 km long Nankai Trough subduction zone and its incoming sediment sequence. Three drilling transects: Ashizuri, Muroto and Kumano were drilled over the last 30 years (Figure 2). The Kumano transect, the most recent one, was drilled during a multistage project called Nankai Trough Seismogenic Zone Experiment (NanTroSEIZE).

At present time, the subduction direction along the Nankai Trough is slightly oblique to the trench and plate convergence varies along strike between $\sim 4 - 6.5$ cm/a (Miyazaki and Heki, 2001; Yokota et al., 2016) with an azimuth of $300 - 315^\circ$ (Seno et al., 1993; Zang et al., 2002). The deformation front is situated between 80 – 160 km offshore southeast Japan. Devastating tsunamigenic earthquakes have been documented in the Nankai Trough dating back 1300 years, with recurrence intervals of 90 – 150 years (Ando, 1975a; Hirose and Maeda, 2013; Rikitake, 1999). The last two megathrust earthquakes: i) the 1944 Tonankai (Mw 8.1), and ii) the 1946 Nankaido (Mw. 8.3) occurred in the vicinity of the Kumano drilling transect.

The Nankai Trough subduction zone can be divided in six major morphotectonic domains (Figure 3); landward from the trench: protothrust zone, frontal thrust zone, imbricate thrust zone, megasplay fault zone, Kumano Basin edge and Kumano forearc basin (Kopf et al., 2017; Moore et al., 2009). The incoming sediment column is 2.4 km thick at the deformation front and consists of 1.1 km Shikoku Basin sediment overlaid by ~ 1.3 km trench wedge sediment (Moore et al., 2009). A well-developed protothrust zone formed in the trench wedge sediment due to incipient (frontal-) thrust formation. The trench wedge sediment and half of the underlying sedimentary section is actively accreted at the deformation front (Moore et al., 2015). The ~ 100 km wide accretionary prism can be subdivided into an inner and outer part, that is separated by a major out-of-sequence thrust fault, often named megasplay fault. The

outer accretionary prism is formed of accreted trench turbidites and Shikoku Basin hemipelagic sediment (Moore et al., 2009); in contrast, the inner accretionary prism consists mainly of mudstone, which has been connected to a triple junction paleoenvironment (Underwood, 2018). Overlying the inner prism is the Kumano forearc basin, with a sediment thickness of up to 3 km. The basin fill is tilted landward, most likely because of fault slip on the megasplay fault (Park et al., 2002), which began at 1.95 Ma and created the accommodation space for the basin fill close the outer ridge (Underwood and Moore, 2012). The Quaternary sediments constituting the basin fill originate from the Kii Peninsula and from east Honshu (Moore et al., 2015). The Kumano Basin is characterized by different venting systems such as seeps and mud volcanoes, that dewater subducted sediments at depth. A total of 13 mud volcanoes exist in the Kumano Basin (Menapace et al., 2017) whereas most of the seep sites are located on the frontal part of the accretionary prism (Toki et al., 2014).

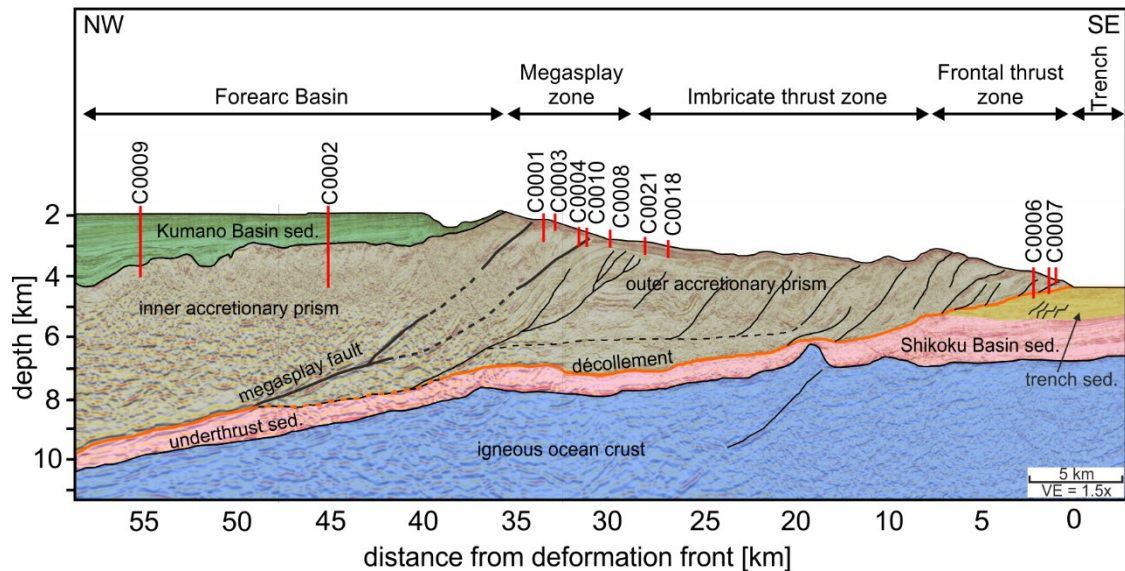


Figure 3: Interpreted seismic cross section of the Kumano drilling transect (modified from Moore et al. (2009)). Morphotectonic domains of the Nankai Trough subduction zone are indicated as well as all NanTroSEIZE drilling Sites. VE = vertical exaggeration, sed. = sediments.

1.4 NanTroSEIZE

In 2004, the Sumatra-Andaman earthquake and the thereafter resulting destructive Indian Ocean tsunami is one of many examples of how vulnerable coastal societies are to subduction zone earthquakes and related phenomena such as tsunamis and/or landslides (Lay et al., 2005; Vigny et al., 2005). Subduction zone megathrust earthquakes are one of the greatest natural hazards on our planet. To develop successful mitigation strategies a better understanding of earthquake mechanics and the dynamic of faulting processes is critical. Up to now, earthquake nucleation and slip propagation are not fully understood and a unifying theory, explaining these phenomena in the context of rock deformation rates, from seconds to years, is still missing. Accordingly, the existence of earthquake precursory signals, and therefore the chance to predict earthquakes, is still under debate. In-situ long term monitoring and sampling along the subduction zone conveyor belt from sedimentary inputs to sediments at seismogenic depth could provide valuable information on ambient conditions and mechanical properties of active submarine fault systems (Tobin and Kinoshita, 2006a).

In 2006, the Nankai Trough subduction zone was chosen as primary target for attempting to drill for the first time into a plate boundary thrust at seismogenic depth (Figure 2). The wealth of available geological and geophysical data as well as the regular occurrence of large megathrust earthquakes has favored the Nankai Trough as unique study area for earthquake mechanics at seismogenic depth (Tobin and Kinoshita, 2006b). Tsunamigenic earthquakes are documented by historical records of more than 1300 years (Ando, 1975b). Studies on the two recent megathrust earthquakes (Tonankai Mw 8.1 and Nankaido Mw 8.3) that occurred in 1944 and 1946, mapped the up-dip end of coseismic slip at depths accessible by drilling (Kikuchi et al., 2003; Tanioka and Satake, 2001). Based on the available 2D and 3D seismic reflection data specific drilling targets were defined, which are located in the operational limits of the riser-drilling vessel D/V Chikyu (riser drilling: maximum 2500 mbsl and 7000 mbsf). Furthermore, the development of the Dense Oceanfloor Network System for Earthquakes and Tsunamis (DONET) by the Japan Agency for Marine-Earth Science and Technology (JAMSTEC) made it possible to connect planned borehole observatories to a real-time ocean network (Kawaguchi et al., 2015).

Drilling into the seismogenic zone was advocated by an international group of proponents who submitted a complex IODP Drilling Proposal. The proposed “Kumano” drilling transect is located seaward of the Kii Peninsula, Honshu, Japan. The funded Nankai Trough Seismogenic Zone Experiment (NanTroSEIZE) is a multi-expedition, multi-stage and multi-disciplinary scientific project aiming to investigate dynamics and mechanics of deformational processes that integrate geodesy, seismology, rock mechanics, fluid fault interaction and tribology. **The**

NanTroSEIZE scientific operations include drilling, sampling and long-term monitoring of input sediments, of major fault systems that splay from the plate boundary thrust up to the seafloor and of the plate boundary thrust at seismogenic depth. The following scientific objectives and hypothesis were formulated over the duration of the project (e.g. Tobin and Kinoshita, 2007; Tobin and Kinoshita, 2006a; Tobin and Kinoshita, 2006b):

- a. Characterization of physical properties, state of stress and composition of accretionary prism sediment from aseismic to seismogenic depth
- b. Investigation of strain partitioning between plate boundary thrust and megasplay fault
- c. Investigation of the strength of the plate boundary fault
- d. Analysis of the evolution of fault rock properties and composition in time and space
- e. Investigation of the tsunamigenic potential of the megasplay fault
- f. Investigation of basement relief, fluid content and composition on plate boundary thrust formation
- g. Long-term monitoring of fluid pressure, thermal signals, geochemical tracers, tilt, micro-seismicity and volumetric strain at different depth levels over the seismic cycle
- h. Deciphering potential precursory signals before earthquakes
- i. Measurement of strain rate accumulation and release
- j. Localization of (slow) earthquakes at shallow depth

Objectives (a – f) involve sampling of discrete core samples that are tested under controlled boundary conditions in laboratory experiments, whereas the objectives (g – j) can be achieved with long-term data recorded with distributed observatories from the deformation front onwards towards seismogenic depth. The ultimate goal of NanTroSEIZE was to sample the seismogenic zone at 5500 – 6000 mbsf and set-up a long-term borehole monitoring system at the up-dip limit of the seismogenic zone (Tobin and Kinoshita, 2007; Tobin and Kinoshita, 2006b). Unfortunately, this could not be achieved within the 12 years of the NanTroSEIZE project.

The NanTroSEIZE project was organized in three operational stages (e.g. Tobin and Kinoshita, 2006b). During Stage 1 the frontal thrust system, mid-wedge mega-splay fault and the Kumano Basin sediment were drilled (Figure 3). The physical properties, composition, and state were analyzed. During Stage 2 the subduction zone inputs were drilled and the ultra-deep riser hole in the Kumano basin was deepened. In addition, the first temporary borehole observatories were installed. During Stage 3 the ultra-deep riser hole was deepened and three Long Term

Borehole monitoring systems (LTBMS) were set up. After 12 years and 13 IODP expeditions with the Japanese scientific drilling vessel D/V Chikyu the NanTroSEIZE project was completed in spring 2019 with IODP expedition 358 (Table 1). Nevertheless, the research based on the scientific and engineering achievements of the 13 expeditions will probably go on for the next few decades.

Table 1: All NanTroSEIZE expeditions in chronological order.

Exp.#	Stage	Name	Year
314	NanTroSEIZE Stage 1	LWD Transect	2007
315	NanTroSEIZE Stage 1	Megasplay Riser Pilot	2007
316	NanTroSEIZE Stage 1	Shallow Megasplay and Frontal Thrusts	2007- 2008
319	NanTroSEIZE Stage 2	Riser/Riserless Observatory	2009
322	NanTroSEIZE Stage 2	Subduction Inputs	2009
326	NanTroSEIZE Stage 3	Plate Boundary Deep Riser: Top Hole Engineering	2010
332	NanTroSEIZE Stage 2	Riserless Observatory	2010
333	NanTroSEIZE Stage 2	Subduction Inputs 2 and Heat Flow	2010- 2011
338	NanTroSEIZE Stage 3	NanTroSEIZE Plate Boundary Deep Riser 2	2012- 2013
348	NanTroSEIZE Stage 3	NanTroSEIZE Plate Boundary Deep Riser 3	2013- 2014
365	NanTroSEIZE Stage 3	Shallow Megasplay Long-Term Borehole Monitoring System	2016
380	NanTroSEIZE Stage 3	Frontal Thrust Long-Term Borehole Monitoring System (LTBMS)	2018
358	NanTroSEIZE Stage 3	NanTroSEIZE Plate Boundary Deep Riser 4	2018- 2019

1.5 Motivation and research hypotheses

Analyzing the deformation processes in time and space along subduction zones from close to the deformation front towards seismogenic depth is necessary to understand the entire spectrum of fault slip behavior from slow to regular earthquakes. The technological achievements of the NanTroSEIZE project in terms of offshore fault zone sampling as well as real-time in-situ monitoring expedited earthquake mechanics research.

My Ph.D. thesis is strongly related to the NanTroSEIZE project and the accompanied scientific goals. As an observatory specialist I sailed on IODP expeditions, 365 and 380 (Table 1) to recover a temporary borehole observatory and to set up advanced permanent LTBMS. Operations on IODP expedition 365 were extremely time efficient, which offered the opportunity for additional coring of the megasplay fault at Site C0010. The unexpected coring operations on board D/V Chikyu put me in charge of the physical properties measurements, which in the end turned out to shift the scope of my Ph.D. project from an originally planned time series analysis work to an interdisciplinary work on time series analysis and laboratory friction experiments.

Initially the Ph.D. project was planned to focus predominantly on the two cruises I sailed, and thus on long-term LTBMS data analysis in sealed boreholes with a special focus on pressure, temperature, tilt and volumetric strain. Pressure, tilt and volumetric strain are parameters to monitor strain accumulation and strain release in subduction zone settings. Contraction and dilation can be monitored in space and time with distributed LTBMS along the Kumano Transect. This information are valuable inputs to dislocation models to narrow down potential focal mechanisms and to determine earthquake hypocenters (e.g. Wallace et al., 2016a). Pore pressure directly affects fault stability and strength. Fault zone overpressure reduces the effective normal stress leading to mechanically weak and predominantly aseismic faults (Kitajima and Saffer, 2012). Pressure and temperature measurements in fault settings act as proxies for fluid flow. Faults acting as conduits could drain ambient overpressured sediments resulting in increasing effective normal stress and consolidation (e.g. Hammerschmidt et al., 2013b). In addition, tidal signals in pore pressure records are a valuable tool to analyze on a formation scale elastic and hydrological properties within the accretionary prism (e.g. Davis et al., 2009). In general, formation scale properties can be only inferred from short term borehole packer tests or slug tests (e.g. Fisher and Zwart, 1997; Screaton et al., 1997). The long-term LTBMS systems provide the opportunity to investigate long term and short-term changes associated with fault zone processes e.g. aseismic creep, earthquake rupture, seismic wave passing or coseismic slip on different time scales.

Initially the following research questions were defined for my Ph.D. project, all closely related to observatory studies:

- 1) Do offshore LTBMS greatly advance the detection of earthquake phenomena in the Nankai Trough accretionary prism?
- 2) Is slow earthquake detection possible only with pore pressure data (proxy for volumetric strain) and without geodetic GPS stations along the Nankai Trough subduction zone?
- 3) Do Nankai Trough elastic formation properties change in time and space?

As a consequence of the unexpected availability of core material from Site C0010 and excited by the lessons learned during the sampling party of IODP expedition 365 I chose to change the focus of my thesis from time series analysis to scientific questions related to earthquake mechanics and frictional behavior of Nankai Trough fault zone sediment. For more than 50 years, scientists analyzed the frictional behavior of various rock and sediment types under changing pressure, temperature and sliding velocity conditions. These kind of laboratory friction experiments could reproduce repetitive stick slip events (e.g. Brace and Byerlee, 1966). Moreover, friction experiments characterize the potential for instability of the tested samples (e.g. Ikari and Saffer, 2011). Recent advances in frictional physics could reproduce laboratory scale slow earthquakes and were able to predict laboratory stick slip behavior (e.g. Ikari, 2019; Rouet-Leduc et al., 2017). One of the major NanTroSEIZE goals was to analyze the potential of the megasplay fault for tsunamigenesis and to characterize the evolution of physical properties along the major fault zones. Frictional properties are of major importance to constrain the occurrence of regular and slow earthquakes and therefore to characterize the different deformation processes acting in the Nankai Trough. This analyzes can be done with direct and rotary shear apparatuses in the rock mechanical laboratory at *MARUM – Center for Marine Environmental Sciences, University of Bremen*.

The availability of new core data from IODP expedition 365 expanded the research questions of my Ph.D. thesis, because all of a sudden “ground-truthing” of some long-term data represented a vital and crucial goal:

- 4) How does sample state and simulated depth influence the stability of shallow fault zone sediment in the Nankai Trough accretionary prism?
- 5) How does frictional behavior along the shallow megasplay fault influence the potential for tsunamigenesis?

- 6) Is in-situ fault zone re-strengthening between repetitive SSEs comparable with laboratory derived re-strengthening on discrete fault zone samples?

In summary, the initially planned NanTroSEIZE time series analysis Ph.D. thesis changed to a combined thesis based on discrete core samples and long-term pore pressure records from the drilled boreholes along the Kumano drilling transect.

1.6 Organization of this thesis

This doctoral thesis was written at the *MARUM – Center for Marine Environmental Sciences, University of Bremen (MARUM)* in the working group of *Marine Geotechnics* run by Prof. A.J. Kopf in close collaboration with the junior working group *Experimental Geomechanics* run by Dr. M.J. Ikari in the research field “Seafloor Dynamics”. For more than a decade scientist from both working groups have been participating in IODP expeditions related to the NanTroSEIZE project. Most of the data shown in the manuscripts, e.g. core samples or pressure time series, were acquired in the scope of the NanTroSEIZE project. The manuscripts presented in the following aim to enhance the understanding of deformation mechanism and earthquake mechanics in subduction zones with a special focus on the Nankai Trough.

This chapter outlines the thesis structure and briefly summarizes the highlights of each manuscript that was written during my three years of Ph.D. funding. In total six scientific manuscripts are presented in this Ph.D. thesis. The first three are first author manuscript focusing on laboratory friction experiments done in the rock mechanics lab at the MARUM. One of them is submitted to the scientific peer-reviewed journal *Earth and Planetary Science Letters*, whereas the other two are still under preparation. The second manuscript will be submitted to the peer-reviewed journal *Geophysical Research Letters* and the third one to *Tectonophysics*. The other manuscripts, where I contributed as co-author, are based on long-term LTBMS data and are already published in peer-reviewed journals. In addition, the appendices summarize all my contributions to national and international conferences and scientific cruises related to the Nankai Trough and in particular to the NanTroSEIZE project. All published manuscripts are reprinted as full text. My contributions to each manuscript are described in detail at the end of each sub-chapter.

Chapter 1 provides an overview of earthquake processes along convergent plate margins with a special focus on the Nankai Trough subduction zone offshore south west Japan. It also introduces the multi expedition NanTroSEIZE project and the research objectives of this Ph.D. thesis.

Chapter 2 encompasses three manuscripts that present the experimental studies of my Ph.D. thesis and summarizes the results of frictional experiments carried out on Nankai Trough samples.

The first manuscripts presents a study of the difference between powdered and intact fault zone samples on the frictional stability tested under simulated shallow depth conditions at four different IODP sites along the Kumano drilling transect. The article is submitted to journal *Earth and Planetary Science Letters*.

The second manuscript is a study of the contribution of slip weakening behavior to the tsunamigenic potential of the shallow megasplay fault at IODP Site C0004. The manuscript is ready for submission to the journal *Earth, Planets and Space*.

The third manuscript bridges the gap between laboratory friction experiments and in-situ long-term monitoring by LTBMS. Frictional re-strengthening rates measured in a rotary shear configuration are compared to in-situ healing rates between repetitive SSEs. Laboratory work and data analysis are completed, but the discussion and conclusion is still in progress.

Chapter 3 encompasses three more manuscripts presenting long-term borehole monitoring studies and a brief summary on the history of borehole observatories in ocean drilling.

The fourth manuscript presents offshore seismic network and borehole observatory data that helped to narrow down the possible range of fault plane solutions for an Mw 6.0 offshore subduction zone earthquake. The article is published in the journal *Journal of Geophysical Research: Solid Earth*.

The fifth manuscript presents recurring and triggered slow slip events accompanied with low frequency tremor identified in borehole observatories in order to give in-sights on the slip behavior and conditions of slow earthquakes along tectonic faults. The article is published in the journal *Science*.

The sixth manuscript presents a 5.3 year time series of formation pore fluid pressure which is used to characterize the elastic properties of the formation and its changes due to earthquakes. The article is published in the journal *Journal of Geophysical Research: Solid Earth*.

Chapter 4 summarizes the main conclusions of the manuscripts presented earlier and it presents an outlook on subduction zone research.

Appendix A lists the abstracts of conference contributions.

Appendix B lists the abstracts of scientific cruises/expeditions I have contributed to.

2 Friction studies

2.1 Introduction

Since the 1960s, the mechanics of earthquakes and faulting have been studied in laboratory experiments under controlled boundary conditions. Stick-slip motion observed on preexisting artificial faults in rocks were interpreted by Brace and Byerlee (1966) as the laboratory equivalent of earthquakes. The stick period represents the interseismic period whereas the slip with the accompanying stress drop represents the earthquake (event) in the seismic cycle. Laboratory stick slip behavior on preexisting faults provides an explanation for the relatively small stress drops observed in shallow megathrust earthquakes, compared to large stress drops from rock fracturing. Nevertheless, laboratory stress drops are an order of magnitude larger than stress drops for real earthquakes (Byerlee and Brace, 1968; Dieterich, 1972). Considering movement along a preexisting fault makes the stick-slip motion a frictional rather than a fracture phenomenon. Frictional behavior of rocks or materials in general (e.g. wood, metal, glass) is controlled by many factors including rock composition, confining pressure, temperature, machine stiffness, surface roughness, cumulative slip and strain rate. Early studies by Byerlee and Brace (1968) investigated strain rate and machine stiffness effects, whereas Brace and Byerlee (1970) focused on the temperature dependence on frictional characteristics and in particular on stick slip. At that time, many of the previously mentioned factors influencing friction were well known from frictional studies conducted on metals in material sciences. Dieterich (1972) was inspired by the work done on metals by Rabinowicz (1951) who has investigated the evolution of measured peak friction upon re-shearing after the shear surfaces were held stationary. The time dependence of friction in different rock types with a thin layer of fault gouge (product of frictional wear) between the sliding surfaces was analyzed by Dieterich (1972). The coefficient of static friction (peak friction after a hold period) increases with the logarithm of time and thus is highly time dependent (Figure 4 A). The time dependence can be explained in the context of the adhesion theory of friction introduced by Bowden and Tabor (1964). In the concept of adhesion theory, the two surfaces in contact have a distinct topography and thus are in contact only at a few points called asperities, resulting in a much smaller real contact area. These contact asperities yield plastically until the normal stress can be supported causing adhesion due to welding of the contact points. The sum of the shear strength of welded contacts defines the frictional behavior.

Time-dependence is explained either by the contact area growth of individual asperities or the increase of the number of asperities with time and applied normal stress caused by indentation creep processes (Dieterich and Kilgore, 1994). This same concept was postulated to cause the observed velocity dependence of friction (Dieterich, 1978; Scholz and Engelder, 1976) (Figure 4 B). The observed change in friction after velocity changes occurs over a characteristic distance which is assumed to represent the distance to eliminate the population of asperity contacts characteristic for the old velocity (Dieterich, 1978). Consequently, the lifetime of asperity contacts is inversely proportional to the sliding velocity because higher velocities reduce the time for creep induced asperity contact area growth. In summary, two competing processes are responsible for sliding friction. On the one hand, aging sliding surfaces increase the resistance to slip whereas on the other hand slip destroys the old contacts and replaces them with new (weaker) contacts (Dieterich, 1979, 1978). The experimental observations of frictional velocity and time dependence between bare rock sliding surfaces and within fault gouge resulted in the development of a set of constitutive equations describing frictional behavior (later termed rate and state dependent friction or *RSF* laws) (Dieterich, 1981, 1979; Ruina, 1983).

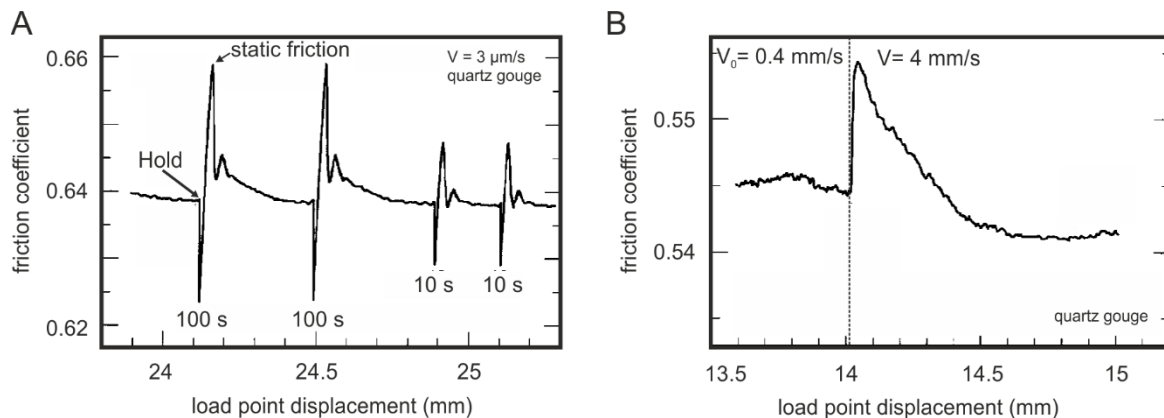


Figure 4: Laboratory friction data showing time and velocity dependence of friction. **A)** Friction coefficient versus load point displacement showing 100 and 10 s hold times. Static friction at 100 s is larger than at 10 s indicating strengthening with time. **B)** Ten-fold velocity increase shows direct and evolutionary effect in friction coefficient. Quartz gouge weakens with increasing loadpoint velocity (modified after Marone (1998a)).

2.1.1 Rate and state friction laws

The rate and state dependent friction laws are a powerful tool to investigate earthquake mechanics, because a wide range of laboratory friction data is well described by RSF. The RSF laws are able to reproduce all modes of fault slip e.g. stable sliding, preseismic slip, earthquake nucleation, dynamic rupture, postseismic slip and slow earthquakes (Dieterich, 1992, 1986; Dieterich and Kilgore, 1996b; Liu and Rice, 2009; Marone et al., 1990; Rice, 1980; Shibazaki and Iio, 2003; Tse and Rice, 1986). Despite the very good fitting of laboratory data

by RSF modelling, the largest drawback is its empirical nature. Moreover, RSF modelling of small scale laboratory experimental results can not be extrapolated easily to natural seismogenic faults because of scaling problems (Marone, 1998a). The first unifying constitutive law that explains velocity dependence of sliding friction and time dependence of static friction was formulated by Dieterich (1979), shown in its modern form (Dieterich, 1979; Marone, 1998a; Ruina, 1983):

$$\mu = \mu_o + a \ln\left(\frac{V}{V_o}\right) + b \ln\left(\frac{V_o \theta}{Dc}\right) \quad (1)$$

where a and b are empirical dimensionless constants, θ is a state variable having units of time, V_o is the initial sliding velocity and V is the new fault slip velocity. Dc is the critical slip distance that represents the slip necessary to renew all asperity contacts after a change in velocity. The state variable θ represents the state of the contacts, often interpreted as the surface memory of previous slip (Ruina, 1983). The evolution of state expresses how the memory will be overwritten corresponding to velocity. μ_o is the steady state friction coefficient at the initial sliding velocity. The second term in Equation (1) describes the immediate change in friction often expressed as direct effect following a velocity change whereas the third term describes the evolutionary effect (Figure 4 B). The variables V and θ are described by first-order differential equations (Scholz, 2018). The evolution of the state variable θ can be described by various formulations. I will introduce the most widely used laws the Dieterich (aging) and the Ruina (slip) law.

Dieterich state evolution law

$$\frac{d\theta}{dt} = 1 - \frac{V \theta}{Dc} \quad (2)$$

Ruina state evolution law

$$\frac{d\theta}{dt} = -\frac{V \theta}{Dc} \ln\left(\frac{V \theta}{Dc}\right) \quad (3)$$

The difference between the two laws arises when considering the evolution of state and thus friction at stationary contact ($V=0$). State increases without movement under truly stationary contact in the Dieterich law whereas the Ruina law requires slip for a change in state. When modelling velocity step experiments the Dieterich law results in an asymmetry for up and down steps in velocity, because the necessary slip for steady state scales with velocity (Marone, 1998a). In contrast, Ruina's law models velocity up and down step symmetrically because steady state is independent of time (Marone, 1998a). Nevertheless, the two evolutionary laws are similar when the time derivative of the state variable does not change, defining steady state sliding conditions. At steady state sliding, the two laws reduce to the same equation:

$$a - b = \frac{\Delta\mu_{ss}}{\Delta \ln V} \quad (4)$$

where, μ_{ss} is the friction coefficient at steady state sliding. When $a > b$ (positive $a - b$) steady state friction increases with sliding velocity termed velocity strengthening, while the opposite $a < b$ (negative $a - b$) is termed velocity weakening. Materials that exhibit velocity strengthening behavior do not allow the nucleation of sliding instabilities, whereas velocity weakening behavior is a prerequisite for unstable slip that may result in earthquake nucleation.

Modelling of experimental data is only possible when the RSF equations are coupled with a differential equation accounting for the stiffness of the shearing apparatus. The time it takes to transmit a change in machine velocity from the initial velocity to the new sliding velocity to the sample takes time and depends on the shear apparatus stiffness (Gu et al., 1984; Marone, 1998a). This can be described by a single degree of freedom elastic coupling:

$$\frac{d\mu}{dt} = k(V_{lp} - V) \quad (5)$$

where V_{lp} is the velocity at the load point and k the spring constant.

Modelling of frictional changes induced by velocity perturbations is only possible when Equations (1), (5) and (2) or (3) are solved with an inverse modelling technique at the same time (Reinen and Weeks, 1993). I used for RSF modelling the program Xlook, which is based on the former text based program Look. It was developed by the student Lokman Alwi at the Massachusetts Institute of Technology in 1995 (Alwi, 1995).

2.1.2 Frictional properties of the Nankai Trough sediments

For many years, the Nankai Trough subduction zone with its three ocean drilling transects has been a high priority site to study fault zone frictional properties on discrete rock and sediment samples. Various scientific studies investigated the frictional strength and stability of fault zone, wall rock and input sediments from different sites to better understand fault zone deformation processes. The following sub-chapter summarizes briefly scientific results based on Nankai Trough frictional studies conducted over the last two decades. First, results based on core samples from the southern Nankai Trough, especially the Muroto drilling transect, are presented followed by results based on the more recently drilled Kumano drilling transect. The Kumano drilling transect results are presented in spatial order starting with results based on the input sediments towards ancient exhumed fault zones on land.

One long lasting hypothesis for the updip limit of seismogenesis is the transformation from smectite to illite at temperatures between 100 – 150 °C. This was tested by Saffer et al. (2012b), who tested intact sediment wafers of the accretionary prism toe Site 1174 from the Muroto drilling transect (Figure 2). Samples with decreasing smectite content from 80 to 20 % were analyzed, spanning a depth window from 700 – 1100 mbsf. The water saturated samples were tested under effective normal stresses of 20 – 150 MPa over a range of sliding velocities from 0.005 to 5 $\mu\text{m/s}$. Coefficient of sliding friction varies between 0.28 – 0.40. The samples exhibit only velocity-strengthening behavior, unable to host instability suggesting that illitization does not trigger unstable frictional behavior (Saffer et al., 2012b). This interpretation is supported by experimental results on natural Shikoku Basin input samples, mineral standards and mineral mixtures tested in direct and ring shear configurations under effective normal stresses between 1 and 40 MPa (Brown et al., 2003; Kopf and Brown, 2003). Brown et al. (2003) do not observe a velocity weakening response in smectite, illite and chlorite clay. Additionally, the input sediments that form probably the future plate boundary fault offshore the Shikoku peninsula show minor abundance of smectite, unlikely to be responsible for the onset of seismogenesis (Brown et al., 2003).

The entire sedimentary sequence entering the subduction zone in the future was sampled at the Kumano transect input reference Sites C0011 and C0012 (Figure 3). Analyses of the mechanical properties of the major lithological units provide insights into plate boundary fault formation and fault zone properties that control megathrust earthquake nucleation, coseismic slip propagation and the architecture of the accretionary prism. Shear strength analysis of incoming sediment combined with critical taper analysis revealed that the plate boundary fault coincides with the major frontal thrust fault in the nowadays accretionary prism (Ikari et al.,

2013a). Ongoing subduction causes the plate boundary fault progressively step downwards because of decreasing friction coefficient with increasing depth (Ikari et al., 2013a).

Multiple studies investigate the velocity dependence and frictional strength of the megasplay fault and frontal thrust zone region of the Kumano transect (Ikari et al., 2009; Ikari and Kopf, 2017; Ikari and Saffer, 2011; Stipp et al., 2013; Tsutsumi et al., 2011; Ujiie and Tsutsumi, 2010) (Figure 3). These experiments were performed under a variety of simulated overburden stresses ranging from 0.6 – 25 MPa and shearing velocities ranging from plate rate motion to coseismic slip. Ikari and Saffer (2011) analyzes fault zone sediment frictional properties of the megasplay fault, plate boundary fault (Muroto transect) and the frontal thrust region to better understand the modes of expected fault slip at shallow depth. Fault zone and wall rock samples tested under 25 MPa effective normal stress and shear rates of 0.03 – 100 $\mu\text{m/s}$ exhibit low coefficients of sliding friction, with the weakest samples from the plate boundary fault. All tested samples exhibit primarily velocity-strengthening behavior, which makes unstable slip unlikely. Nevertheless, a pronounced minimum in velocity dependence is observed in all samples at shear rates comparable to SSE sliding velocities (Ikari et al., 2009; Ikari and Saffer, 2011). Additional, shear experiments performed at plate rate shear velocities reveal the potential for unstable slip and SSE nucleation in weak clay rich megasplay fault sediment, which has been not observed at higher shearing velocities (Ikari and Kopf, 2017). In contrast to the low velocity experiments done by Ikari et al, Japanese scientists performed rotary shear experiments at high and intermediate slip velocities at low effective normal stresses up to 5 MPa on megasplay fault samples (Tsutsumi et al., 2011; Ujiie and Tsutsumi, 2010). These experiments revealed a mix of velocity weakening and strengthening for intermediate slip velocities but dramatic weakening at high velocities (Tsutsumi et al., 2011). Thus, coseismic slip may propagate through the clay rich fault gouge of the megasplay fault up to the seafloor (Ujiie and Tsutsumi, 2010).

The previously described studies on fault zone sediments tested exclusively hemipelagic (clay rich) sediment which are together with terrigenous turbidites the main lithologies of accretionary prisms (Underwood, 2007). The Nankai Trough accretionary prism minor lithological units are sandstone, siltstone and tuff that were tested together with the dominant clayey and silty mudstones at in-situ conditions in a triaxial apparatus (Takahashi et al., 2014; Takahashi et al., 2013). These inner accretionary prism lithologies were sampled at the deep riser Site C0002 underlying the Kumano basin sediment (Figure 3). Results show that with decreasing clay content, the frictional strength increases and the slip dependent frictional behavior changes from slip weakening to slip hardening (Takahashi et al., 2014). All samples reveal velocity strengthening behavior in velocity step tests (Takahashi et al., 2014). A detailed analysis of the clayey and silty mudstone samples revealed an eight times longer failure

process in the clayey mudstone samples and a lower shear strength than the silty mudstone (Takahashi et al., 2013). Therefore, it was suggested that the weak clayey mudstone samples preferential host faulting and show a tendency for slow slip failure mechanisms (Takahashi et al., 2014; Takahashi et al., 2013).

Another hypothesis suggests that lithification processes at depth (e.g. diagenesis and low-grade metamorphism) affect the mechanical behavior of subduction zone wall rock and fault zone sediment. These processes might be responsible for the onset of megathrust earthquake nucleation at a depth of 5 – 10 km. Friction experiments on fossil subduction zone sediments from the Shimanto Belt complex onshore Japan are representative for samples at seismogenic depth in the nowadays active Nankai subduction zone (Trütner et al., 2015). Direct shear experiments simulating seismogenic temperature and depth conditions reveal velocity weakening behavior in intact sediment samples whereas powdered versions show velocity strengthening behavior. The potential for unstable slip is removed by destroying the sample lithification (Trütner et al., 2015).

In summary, Nankai Trough fault zone and wall rock sediments show mainly velocity-strengthening behavior, with exceptions at very low and very high shearing velocities. Frictional experiments on analog seismogenic fault zone rock showed that lithification processes and probably sample fabric influences the stability of fault rocks. The majority of scientific studies tested powdered samples at effective normal stresses much higher than in-situ. Consequently, the above discussed results can only be regarded as rough estimates of the in-situ strength and stability of fault zone sediments.

In the manuscripts shown in the following chapters, direct and rotary shear friction experiments are presented that test intact and powdered fault zone material including new core samples from Site C0010 and samples representing lithologies already tested in earlier studies. The experiments were performed at sliding velocities from 0.01 – 30 $\mu\text{m/s}$ under effective normal stresses of 2 – 18 MPa.

2.2 Manuscript 1 (EPSL submitted): Friction experiments under in-situ stress reveals unexpected velocity-weakening in Nankai accretionary prism samples

A. Roesner¹, M.J. Ikari¹, D.M. Saffer², K. Stanislawski¹, A.M. Eijsink¹, A.J. Kopf¹

¹MARUM—Center for Marine Environmental Sciences and Faculty of Geosciences, University of Bremen, Bremen, Germany

²Department of Geosciences, Pennsylvania State University, University Park, Pennsylvania 16802, USA

Abstract

The Nankai Trough hosts diverse fault slip modes, ranging from slow slip events to megathrust earthquake ruptures. We performed laboratory friction experiments on samples collected by the Integrated Ocean Drilling Program offshore Kii Peninsula, Japan. This study systematically investigates the effect of effective normal stress on frictional strength and the velocity-dependence friction for natural fault zone and wall rock samples collected from depths of 270 to ~450 meters below seafloor (mbsf), and over a range of sliding velocities spanning from 0.01 – 30 $\mu\text{m/s}$. We tested both powdered and intact specimens at estimated in-situ effective stresses, as well as at higher stresses representing deeper portions of the megasplay fault (Sites C0004, C0010) and the frontal thrust zone (Sites C0007, C0006). The coefficient of sliding friction μ_s varies between 0.22 – 0.53 and correlates inversely with clay content. Direct measurements of cohesive strength show that on average 11 % of the shear strength, and up to ~30 % for some specimens, can be attributed to sliding cohesion. Friction coefficient and the velocity-dependent friction parameter $a - b$ do not show a dependence on effective normal stress. The lowest μ_s values are observed for samples from Sites C0007 and C0010. All samples show a combination of velocity-strengthening and velocity-weakening behavior, but intact samples tested under in-situ effective normal stress and low shearing velocities ($< \sim 1 \mu\text{m/s}$) exhibit consistently large velocity-weakening behavior. The observed velocity-weakening behavior is related to the induration state of the material, which affects the real area of contact along shear surfaces. This is supported by direct measurements of cohesive strength, showing that higher cohesion values in intact samples correspond with a more pronounced evolutionary effect in velocity step tests that, in turn, map to lower $a - b$ values. We propose that fault zones in the Nankai subduction zone are likely to be velocity-weakening, and thus potentially able to host the nucleation of unstable slip, from seismogenic depths to

the seafloor. We also find that testing disaggregated fault zone samples and employing effective stresses exceeding those in-situ lead to overestimation of the RSF parameter $a - b$, emphasizing the importance of testing intact samples under in-situ conditions in laboratory friction studies.

Introduction

Megathrust earthquakes at convergent plate boundaries release 90 % of the global seismic moment (Lay et al., 2005), and the resulting strong ground motion and potential geohazards such as tsunamis and (submarine) landslides are a threat to heavily populated coastal areas. A better understanding of earthquake fault mechanics is fundamental to the development of successful earthquake and tsunami mitigation strategies for these coastal areas. Onshore and offshore drilling projects around the world have targeted active fault systems at plate boundaries to investigate earthquake mechanics and hazards (Chester et al., 2013; Kinoshita et al., 2009).

The **Nankai Trough Seismogenic Zone Experiment** (NanTroSEIZE) is a multi-expedition International Ocean Discovery Program (IODP; formerly Integrated Ocean Drilling Program) drilling project designed to investigate fault mechanics and seismogenesis of the Nankai Trough subduction zone offshore Kii Peninsula, Japan (Figure 5 A). Devastating tsunamigenic earthquakes have been documented in the Nankai Trough dating back 1300 years, with recurrence intervals of ~90 – 150 years (Ando, 1975b). In the last century, two large megathrust earthquakes occurred in the Nankai Trough region: the 1944 Tonankai (Mw 8.1) and 1946 Nankaido (Mw 8.3) events (Figure 5 A). The Tonankai earthquake produced a large tsunami, potentially linked to slip on shallow parts of a major out-of-sequence thrust fault (OOST) within the accretionary prism, which is often called the “megasplay fault” (Park et al., 2002; Strasser et al., 2009) (Figure 5 B). The hypothesis of active coseismic slip along the megasplay fault is supported by theoretical modelling results by Kame et al. (2003), who showed based on fault geometry that seismic rupture would follow the megasplay fault, and by Sakaguchi et al. (2011), who presented evidence for paleo-frictional heating in fault core samples. Recently, slow earthquakes, during which the fault slips faster than plate convergence rates but slower than coseismic slip rates, have been documented in the shallow parts of the Nankai Trough subduction zone. One example are slow slip events with fault slip velocities of 0.008 – 0.23 $\mu\text{m/s}$, and with durations of ~2 – 15 days (Figure 5 B) (Araki et al., 2017; Obara and Kato, 2016). Very low-frequency earthquakes (VLFs) have also been documented along the Nankai Trough within the accretionary prism (Ito and Obara, 2006b; Sugioka et al., 2012). These VLFs occur along the shallow reaches of major faults such as the décollement and the megasplay, and in at least some cases may accompany slow slip events (Kaneko et al., 2018). Thus, the Nankai Trough accretionary prism hosts a wide variety of fault slip modes, from slow earthquakes to megathrust earthquake ruptures.

The mode of fault slip is controlled by the frictional properties of faults, the elastic properties of the wall rock, and the in-situ stress state. Fault frictional behavior is often described in terms

Three different velocity regimes have been previously tested in laboratory friction experiments on NanTroSEIZE fault zone material: (1) ultra-low, plate-rate velocities of 2×10^{-9} – 2×10^{-8} m/s (6.3 – 63 cm/y) (Ikari and Kopf, 2017), (2) low to intermediate velocities of 3×10^{-8} – 3×10^{-3} m/s (Ikari et al., 2013b; Ikari and Kopf, 2017; Ikari and Saffer, 2011; Tsutsumi et al., 2011), and (3) fast slip velocities that approach coseismic rates, 0.03 – 1.3 m/s (Tsutsumi et al., 2011; Ujiie and Tsutsumi, 2010). These experiments were performed under effective normal stresses ranging from 0.6 – 25 MPa on predominantly megasplay fault samples from IODP Site C0004, and on a few frontal thrust zone samples from IODP Site C0007. Experiments at low effective normal stresses show that ultra-low velocities resulted in mostly velocity-weakening friction (Ikari and Kopf, 2017), and extreme weakening at high velocities due to thermally-activated dynamic processes (Ujiie and Tsutsumi, 2010). However, samples sheared at low to intermediate velocities and tested at higher effective normal stresses showed mostly velocity-strengthening. Additionally, all of the above mentioned experiments assumed that cohesive strength has a minor effect on well-developed slip surfaces; however, some work has shown that cohesion plays a significant role in clay rich sediment throughout the shearing process (Ikari and Kopf, 2011).

Here, we present results from laboratory friction experiments from slow to intermediate shearing velocities on phyllosilicate-rich fault zone material from the Nankai Trough accretionary prism (IODP Sites C0004, C0010, C0006, C0007) (Figure 5). Through experiments under stresses representative of those up to a few km below the seafloor, we investigate the strength, stability and cohesion of the hemipelagic fault zone and wall rock sediments. A particular focus of this study is the comparison between intact and powdered fault zone material under in-situ stresses.

Geological setting and experimental samples

Nankai trough subduction zone

The Nankai Trough is one of the best studied subduction zones in the world, by means of numerous drilling expeditions (Deep Sea Drilling Project, DSDP; Ocean Drilling Program, ODP; Integrated Ocean Drilling Program and International Ocean Discovery Program IODP), geophysical surveys and seismological studies (Figure 5). Our study is focused on the Kumano transect, an IODP drilling transect that is part of the NanTroSEIZE project (Figure 5 B) (Tobin and Kinoshita, 2006b). Along the Nankai Trough, the Philippine Sea Plate subducts to the northwest beneath the Amurian microplate at a rate of ~ 6.5 cm/a (Miyazaki and Heki, 2001). A wide accretionary complex forms through off-scraping of hemipelagic Shikoku Basin and overlying trench-fill sediment deposited on the Philippine Sea Plate (Moore et al., 2009)

(Figure 5 B). The accretionary complex can be divided into an inner and outer accretionary prism separated by the megasplay fault (Kimura et al., 2007; Park et al., 2002). The frontal thrust zone close to the trench is characterized by a complex deformation history in the last 0.78 Ma (Screaton et al., 2009).

Megasplay fault

The megasplay fault (Figure 5 B) is a major landward-dipping OOST that branches from the décollement ~55 km landward from the trench (Park et al., 2002; Strasser et al., 2009). It represents a major mechanical discontinuity between the “inner wedge” on its landward side and the “outer wedge” on its seaward side (Kimura et al., 2007). Slip along the megasplay has constructed a continuous outer ridge (forearc high) along strike.

Four IODP drilling expeditions (314, 316, 319 and 365) targeted the megasplay fault to acquire logging-while-drilling (LWD) data and core samples from Sites C0004 and C0010, which are separated by ~3.5 km along strike. At IODP Site C0004 the megasplay fault is recognized as a brecciated zone at 256 – 315 mbsf, whereas at Site C0010 the fault zone is identified at a depth of ~407 mbsf as a sharp discontinuity between more compacted and fractured thrust wedge hanging wall material, and less compacted and deformed footwall sediments. The highly fractured and brecciated megasplay fault interval (“fault bounded package”) at Site C0004 is composed of ash-bearing hemipelagic mud with scattered volcanic ash layers. The sediments are, on average, composed of 60 % clay minerals, 20 % quartz, 18 % feldspar, and 2 % calcite (Expedition 316 Scientists, 2009a). Megasplay fault samples from Site C0010 were not recovered due to challenging hole conditions and the narrower and more localized nature of the fault (Kopf et al., 2017; Saffer et al., 2017c), but the hanging wall and footwall hemipelagic mudstones were sampled within ~10 m of the fault zone. The hanging wall is, on average, composed of 65 % clay minerals, 17 % quartz, 13 % feldspar, and 5 % calcite, whereas the footwall is on average composed of 55 % clay minerals, 22 % quartz, 22 % feldspar, and 1 % calcite. The footwall is dominated by slightly coarser-grained and less deformed sediments than the fractured claystone of the hanging wall (Kopf et al., 2017; Saffer et al., 2017c).

Frontal thrust zone

The frontal thrust zone (Figure 5 B) is dominated by a shallowly dipping (7 – 8°) 6 km-long frontal thrust fault that causes underplating of Shikoku Basin and trench wedge sediments (Screaton et al., 2009). The incoming sediment column consists of a ~1.3 km thick trench sediment wedge overlying 1.1 km of Shikoku Basin sediments that contain thick mudstones

interbedded with turbidite layers (Moore et al., 2009; Screateon et al., 2009). Near the trench, a proto-thrust zone characterized by diffuse faulting forms within these sediments.

Two IODP drilling expeditions (314 and 316) drilled the shallow frontal thrust zone to acquire LWD data and core samples from Sites C0006 and C0007. At Site C0006, the plate-boundary thrust fault was not cored, but rather a highly deformed interval in the hanging wall from 230 – 545 mbsf. This broad zone comprises accreted trench wedge and Shikoku Basin sediments consisting of 46 % clay minerals, 23 % quartz, 30 feldspar, and 1 % calcite (Expedition 316 Scientists, 2009b). At Site C0007, several thrust branches were cored. The deepest of these is overlain by a zone of concentrated deformation at a depth of 399 – 446 mbsf. These accreted Shikoku basin sediments are on average composed of 65 % clay minerals, 20 % quartz and 15 % feldspar (Expedition 316 Scientists, 2009c).

Samples tested in this study (Table 2) are chosen to be compositionally representative of the megasplay and frontal thrust fault/fracture zones. At Site C0010, the fault zone proper was not cored, therefore we tested the samples from the hanging and footwall cored nearest to the megasplay fault (± 10 m), assuming that these samples bound the likely mineralogic composition of the fault.

Table 2: Sample and sample location details.

Fault type and Location	Sample ID	State	Depth [mCSF]	Clay ¹ [%]
Frontal thrust fault zone III	C0007D29R01	powder	437.25	64
Frontal thrust fault zone III	C0007D26R01	intact	408.89	66
Frontal thrust fracture zone	C0006E37X08	powder/intact	295.55	38
Megasplay fault	C0004D29R03	powder	276.89	61
Megasplay fault	C0004D32R02	powder/intact	289.74	59

¹clay mineralogy data from shipboard measurements

Experimental methods and procedure

We conducted experiments in a *GIESA RS5* direct shear apparatus (see e.g. Ikari and Kopf, 2017, 2011 for more details) at room temperature of ~ 21 °C (Figure 6 B). The cylindrical samples were tested in a stainless steel shearing assembly with a sample diameter of 25 mm and ~ 25 mm initial sample height. They were tested as powdered fault zone material; five samples were also tested as intact fault zone material (Table 2). Intact samples were carefully trimmed from whole-round cores as cylinders aligned with the core axis, whereas powdered samples were initially dried at room temperature, pestled to powder, sieved to a grain size fraction < 125 μm and mixed with deionized water in a ratio of 2:1 to form a stiff paste. Intact samples were tested under effective normal stresses (σ'_n) of 2.1 – 4.1 MPa to represent the

in-situ conditions at the depth of coring, calculated from shipboard bulk density measurements assuming hydrostatic pore water pressure. The powdered, fluid-saturated samples were tested under these same normal stresses, and additionally at 10 MPa and 17 MPa. For all experiments, the sample cell was flooded with simulated seawater with a salinity of ~3.5 %. Samples were loaded by a vertical piston to the desired normal stress, and allowed to consolidate until the change in sample height became negligible (at least 24 hours). Pore water pressure was not measured, but we assume full pore water pressure dissipation once further vertical displacement ceases. In this case the applied normal stress equals the effective normal stress (pore water pressure = 0 MPa). Horizontal and vertical sample displacement, load point displacement and horizontal and vertical load were continuously measured at a sampling rate of 0.2 – 5 Hz depending on the shearing velocity (Figure 6 B).

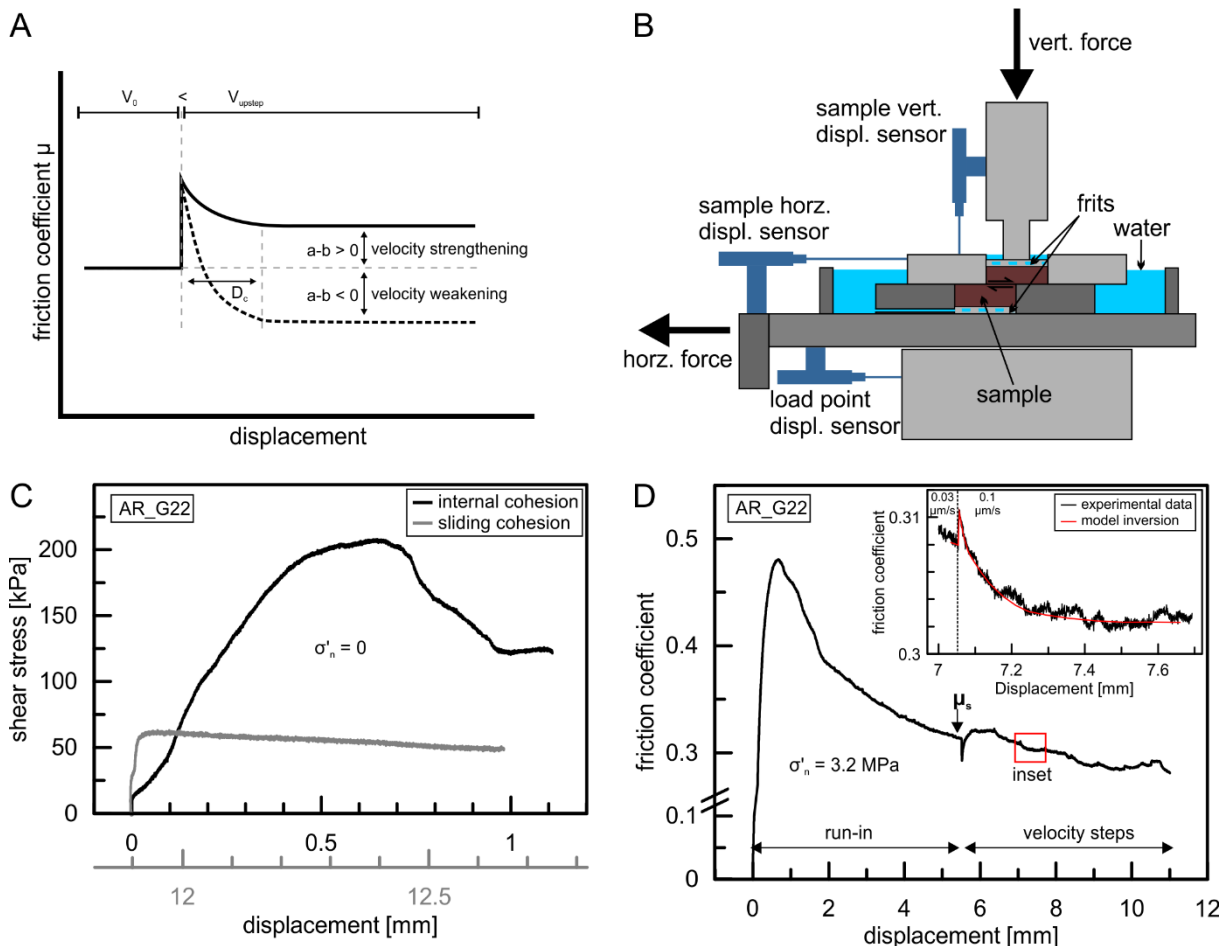


Figure 6: (A) Schematic diagram illustrating the change in friction coefficient after a velocity step in the framework of the Rate- and State Friction law. Velocity-strengthening $a - b > 0$ (solid) and velocity-weakening behavior $a - b < 0$ (dashed). (B) Schematic diagram of the shear device used in this study where the dark grey part moves to the left under constant vertical force while monitoring displacement and shear force. (C) Data example of cohesive strength tests. (D) Data example of a velocity step test on an intact sample, divided into Run-in and velocity stepping sequence. μ_s illustrates the coefficient of sliding friction and the red box indicates the velocity step shown as inset. The inset shows the experimental data and the respective RSF model inversion; for this velocity step, the sample is velocity-weakening.

The following order of tests was applied for each sample: (1) a cohesion test (Figure 6 C), in which the shear strength is measured under zero effective normal stress; (2) shearing under normal load including a velocity-stepping sequence (Figure 6 D); and (3) and another cohesion test. For the first cohesion test, powdered samples were first consolidated to the desired effective normal stress and then unloaded and sheared (1 $\mu\text{m/s}$) until failure ($\sim 0.5 - 1.0$ mm horizontal displacement), whereas intact samples were sheared immediately with no initial loading. Afterwards, the sample holder was reset to its original position and normal load was applied to the sample. The subsequent shearing experiment started with 5 mm of “run-in” at a velocity of 10 $\mu\text{m/s}$. The “run-in” allows the development of a fault surface that has attained a steady state shear strength. The velocity stepping sequence (velocities of 0.1-0.3-1-3-10-30 $\mu\text{m/s}$) was then initiated, with incremental fault displacements of 0.7 – 1 mm at each velocity. For some experiments, two lower velocities (0.01 and 0.03 $\mu\text{m/s}$) were also tested. After the velocity step test, the shear stress on the sample was relieved and the normal load was then removed to perform the second cohesion test. With increasing shear displacement the sediment to sediment contact area between the upper and lower sample halves decreases (Figure 6 B). Therefore, we corrected the measured shear stress in cohesion experiments by calculating the contact area of two overlapping circles and assuming negligible adhesion at the sediment-to-metal interfaces. In addition, we corrected for friction between the metal-metal interfaces. Two samples of C0004D 32R-2 (one intact and one powdered) were impregnated with low viscosity epoxy resin after shearing for microstructural analysis. Thin sections were cut parallel to the shear direction and were analyzed with a *LEICA DMRX* microscope.

The shear strength of rocks and sediments is often expressed by the Coulomb-Mohr failure criterion:

$$\tau = \mu * \sigma'_n + c \quad (6)$$

where τ is the shear stress at failure, μ coefficient of internal friction, σ'_n is the effective normal stress, and c is the cohesion (Handin, 1969). When testing sliding on a pre-existing fault surface, many friction studies assume that the cohesion is negligible, which simplifies Equation (6) to:

$$\mu_s = \frac{\tau}{\sigma'_n} \quad (7)$$

with μ_s being the coefficient of sliding friction (Figure 6 D). Previous studies by Ikari and Kopf (2015, 2011) have shown that the cohesion can be directly measured by shearing samples without applying normal load, and furthermore that sediments containing a high percentage of clay minerals maintain a significant amount of cohesion even on sliding surfaces. Consequently, the measured shear strength consists of both a frictional and cohesive component. To distinguish our two cohesion tests we name the cohesion measured before a

velocity step test “internal cohesion c_i ” and the one measured after “sliding cohesion c_s ”. To be consistent with previous studies we present our data in terms of friction coefficient (Equation (7)) and do not subtract the sliding cohesion from the shear stress. However, we still evaluate our measured values of cohesion. We normalize the measured cohesion by the (maximum) effective normal stress to calculate the cohesion coefficient χ (Ikari and Kopf, 2015):

$$\chi_i = \frac{c_i}{\sigma'_n} \quad \text{and} \quad \chi_s = \frac{c_s}{\sigma'_n} \quad (8)$$

The cohesion coefficient has the advantage of being directly comparable to the friction coefficient.

In order to evaluate the velocity-dependence of friction we use the rate- and state-dependent constitutive laws for frictional sliding with two state variables (e.g. Dieterich, 1981, 1979; Marone, 1998a). We model our experimental velocity steps with an inverse modelling technique using a least-squares method (Reinen and Weeks, 1993; Saffer and Marone, 2003):

$$\mu = \mu_o + a \ln\left(\frac{V}{V_o}\right) + b_1 \ln\left(\frac{V_o \theta_1}{Dc_1}\right) + b_2 \ln\left(\frac{V_o \theta_2}{Dc_2}\right) \quad (9)$$

$$\frac{d\theta_i}{dt} = 1 - \frac{V \theta_i}{Dc_i}, i = 1, 2 \quad (10)$$

where a , b_1 , and b_2 are dimensionless constants, θ_1 and θ_2 are state variables having units of time, which can be interpreted as the average lifetime of surface contacts (Dieterich and Kilgore, 1994), and Dc_1 and Dc_2 are critical slip distances over which friction evolves to a new steady state. μ_o is the steady state friction coefficient at the initial sliding velocity V_o and V is the new fault slip velocity (Figure 6 A). We used the “Dieterich/aging/slowness” evolution law Equation (10), in which θ_i may evolve over time even for truly stationary contact (Dieterich and Kilgore, 1994; Marone, 1998a). If the data is well described by one state variable, we set $b_2 = \theta_2 = 0$; however, in some cases the data is clearly better described by two state variables, where we define $b = b_1 + b_2$.

When steady-state sliding conditions are reached, Equations (9) and (10) can be reduced so that we can describe the velocity-dependence of friction with the parameter $a - b$:

$$a - b = \frac{\Delta\mu_{ss}}{\ln\left(\frac{V}{V_o}\right)} \quad (11)$$

Positive $a - b$ values indicate velocity-strengthening friction, whereas negative $a - b$ values describe velocity-weakening friction (Figure 6 A). Velocity-strengthening faults tend to slide stably and inhibit rupture nucleation, whereas velocity-weakening is a prerequisite for earthquake nucleation (Dieterich, 1981; Marone, 1998a; Scholz, 1998).

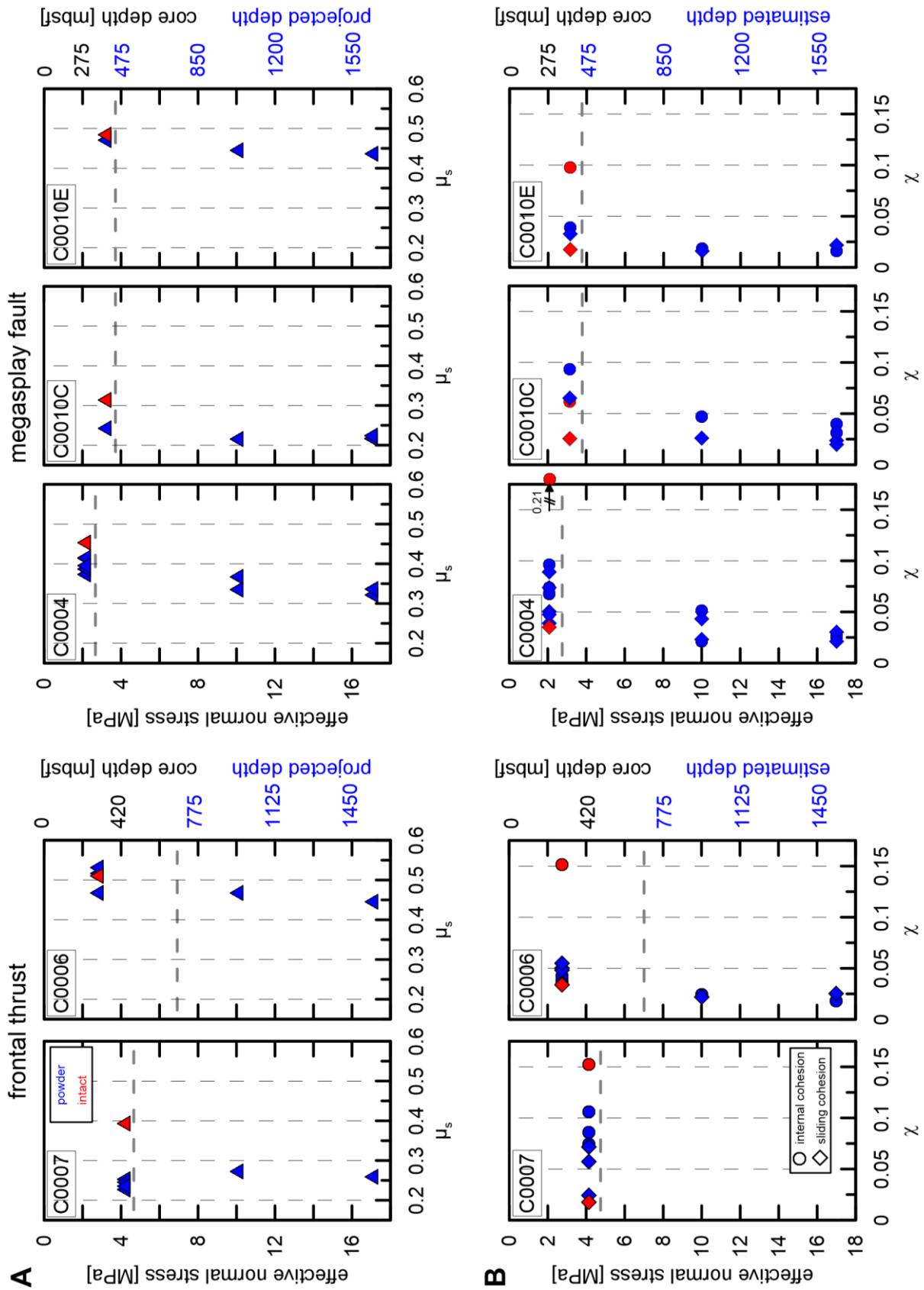


Figure 7: Both (A) coefficient of sliding friction and (B) cohesion coefficient as a function of effective normal stress, simulating different depth levels for the fault zone samples from frontal thrust Sites C0007 and C0006 as well as for the megasplay fault Sites C0004 and C0010. Below the bottom of coring (gray dashed lines) the projected depth is extrapolated from effective normal stress calculations from shipboard bulk density measurements on cored intervals.

Results

Friction-displacement curves of intact samples show a peak in friction within the first 2 mm of shearing (Figure 6 D), whereas a peak in friction in powdered samples is only observed in the weakest of our samples. In contrast, the friction of the stronger powdered samples ($\mu_s > \sim 0.33$) increases gradually without exhibiting a peak during the run-in. For all experiments, measured coefficients of sliding friction vary from $\mu_s = 0.22$ to 0.53 (Figure 7 A). The frontal thrust fault zone sample from C0007 and the hanging wall sample of the megasplay fault from C0010C exhibit the lowest μ_s values of $\sim 0.2 - 0.3$ over the entire range of effective normal stresses tested. In contrast, C0006, C0004 and C0010E samples show higher μ_s of 0.30 to 0.55, with the highest values measured in C0006 under in-situ stresses. Neither the frontal thrust nor megasplay fault samples show a significant trend with increasing effective normal stress. The coefficient of sliding friction shows a good reproducibility for repeated tests (e.g. C0007 at 4.1 MPa) at all effective normal stresses. μ_s of intact samples tested under in-situ effective normal stresses is larger than or similar to their (averaged) powdered equivalent (Figure 8 A). We calculate the percentage of strength loss due to sample powdering as

$$\mu_{loss} = \frac{(\mu_{s_intact} - \mu_{s_powder})}{\mu_{s_intact}} * 100 \quad (12)$$

Strength loss increases with clay content, with samples from C0007 and C0010C showing the largest strength loss (up to 38 %) (Figure 8 B). We observe that the coefficient of sliding friction decreases drastically (Figure 8 A) and strength loss increases exponentially as a function of increasing bulk clay content (Figure 8 B).

Measured internal cohesion coefficient χ_i varies from 0.02 – 0.20, whereas the sliding cohesion coefficient χ_s exhibits smaller values of 0.02 – 0.09 for the majority of our experiments (Figure 7 B). Sliding and internal cohesion coefficients both decrease with increasing effective normal stress, indicating that cohesion contributes little to the shear strength at larger effective normal stresses, as would be expected for brittle/frictional materials. Generally, intact samples show higher internal cohesive strength than the equivalent powdered samples. After establishment of a shear surface the large internal cohesion of intact samples drops to a small sliding cohesion, even smaller than the sliding cohesion for equivalent powdered samples. Thus, the difference between internal and sliding cohesion coefficient is much larger in intact samples than in powdered samples (about three times larger). The sliding cohesion of powdered samples represents 4 – 30 % of the measured shear strength with an average of ~ 12 % (Table 3 supplementary material). In contrast, for intact samples it is 6 % of the measured shear strength. The cohesive proportion of the shear strength decreases with

increasing effective normal stress from 14 to 8 % for powdered samples. Repeated experiments show a significant scatter in internal and sliding cohesion values (Figure 7).

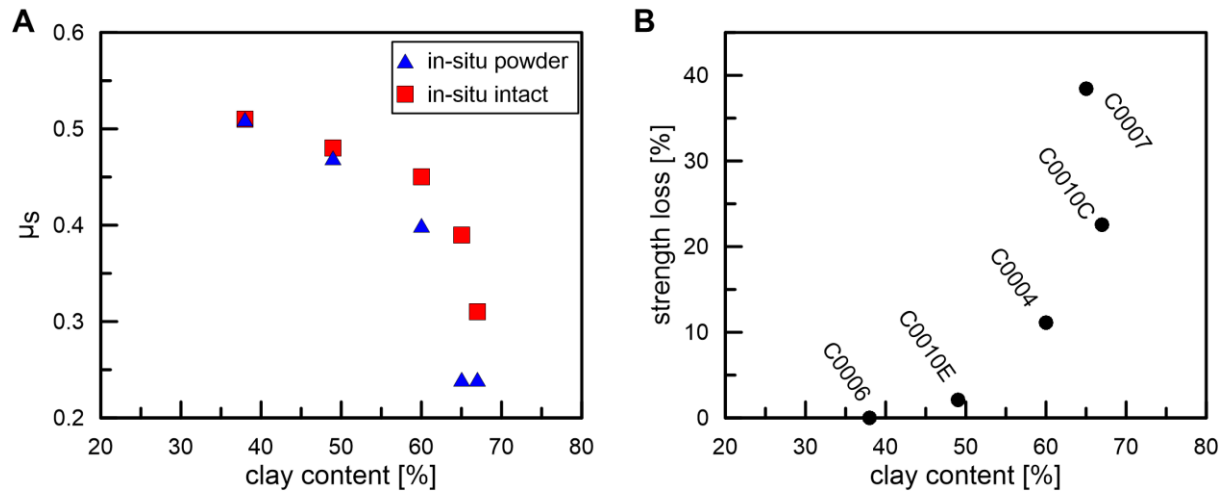


Figure 8: (A) Inverse correlation of coefficient of sliding friction vs. clay content. (B) percentage of strength loss between intact and powdered sample state vs. clay content.

Samples from all of the fault settings exhibit some velocity-weakening behavior at low effective normal stresses, with the most pronounced velocity-weakening occurring in intact samples under estimated in-situ stress conditions (Figure 9). The largest contrast in the RSF parameter $a - b$ is observed in the hanging wall sample from C0010C, where the intact sample is velocity-weakening but the equivalent powdered sample is mostly velocity-strengthening. This difference is less obvious comparing the intact and powdered C0010E footwall samples under in-situ stress conditions (Figure 14 supplementary materials). The megasplay fault zone samples show a larger difference between the RSF parameter $a - b$ in powdered and intact states than those from the drill sites in the frontal thrust region. Neither sets of powdered samples show a significant trend in $a - b$ values as a function of effective normal stress. However, taking intact samples into account, a slight tendency of increasing $a - b$ with effective normal stress is visible. The scatter in $a - b$ of repeated experiments decreases with increasing effective normal stress, e.g. samples from C0004 (Figure 9). There is a slight overall trend of increasing $a - b$ as a function of increasing slip velocity; mostly velocity-weakening is observed at velocities $\leq 0.1 \mu\text{m/s}$, whereas all samples show velocity-neutral to velocity-strengthening behavior at $30 \mu\text{m/s}$ (Figure 9).

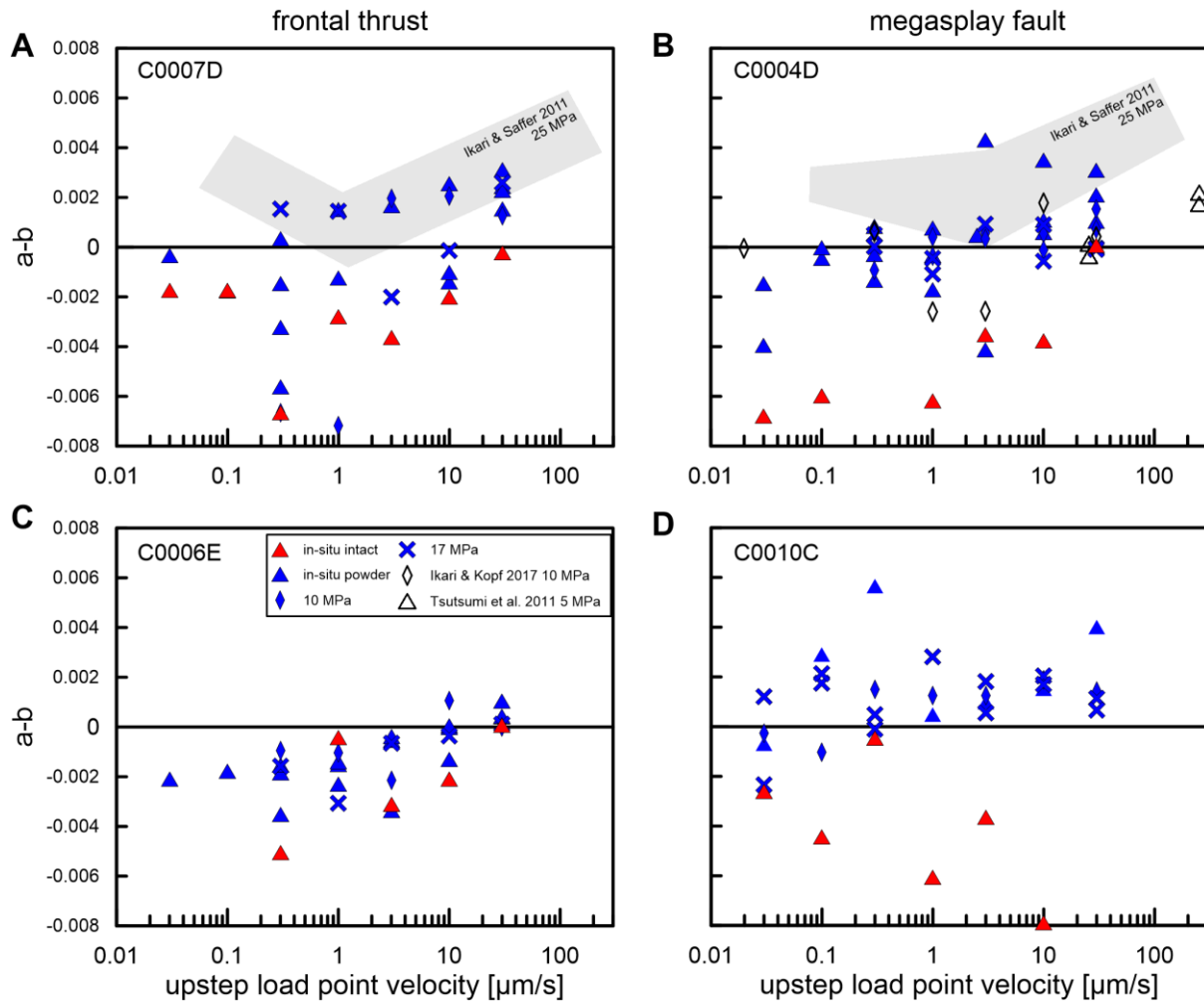


Figure 9: Rate-dependent friction parameter $a - b$ as a function of upstep load point velocity for the frontal thrust and megasplay fault sites. C0010E (footwall) is not shown. Gray area illustrates fault zone material tested by Ikari and Saffer (2011). Samples from Tsutsumi et al. (2011) were tested in a ring-shear apparatus; only data without calcite are shown.

Considering $a - b$ as a function of sliding velocity, each of the tested samples in this study have unique characteristics, with no clear distinction between those from the frontal thrust region and megasplay fault zone. For example, experiments on C0007 powdered samples under in-situ stress show $a - b$ values which transition from velocity-weakening to velocity-strengthening with increasing shearing velocity. This transition from velocity-weakening to velocity-strengthening as a function of sliding velocity is employed in numerical modeling studies as a “cut-off” velocity (Shibazaki and Iio, 2003). This is most clearly apparent in the 10 MPa experiment at a shearing velocity of $\sim 2 \mu\text{m/s}$. In contrast, the 17 MPa experiment reveals a minimum value of $a - b$ at $3 \mu\text{m/s}$ rather than a single trend. The fracture zone sample from Site C0006 shows velocity-weakening behavior, with a tendency towards velocity-strengthening at higher shearing velocities. The transition velocity for all powdered C0006 samples is $\sim 20 \mu\text{m/s}$. The powdered megasplay fault zone samples from C0004 tested under in-situ stress conditions exhibit a large scatter in $a - b$ values. At low velocities of

0.01 – 1 $\mu\text{m/s}$ velocity-weakening dominates, whereas at higher velocities velocity-strengthening is dominant. In contrast, the experiments conducted at 10 and 17 MPa consistently show $a - b$ values close to zero. All powdered hanging wall samples from Site C0010 show velocity-strengthening behavior for velocities $< 0.1 \mu\text{m/s}$. In contrast, the intact sample shows the most prominent velocity-weakening behavior, with the tendency for lower $a - b$ values at higher shearing velocity. The velocity-step tests also show that with increasing effective normal stress, slip-weakening is observed at in-situ effective normal stresses, which evolves to slip-neutral behavior by 17 MPa effective normal stress (Figure 15 and Table 3 supplementary materials).

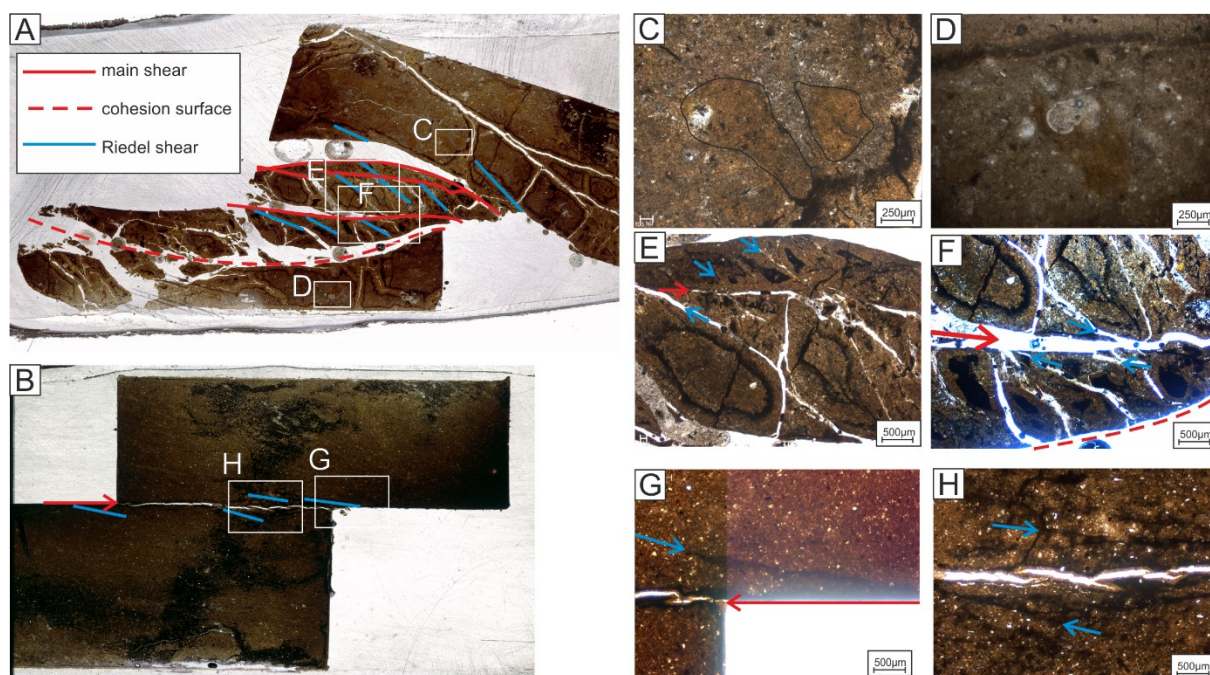


Figure 10: Microstructural analysis of (A) intact sample AR_G25 C0004D32R2 and (B) equivalent powdered sample AR_G26 C0004D32R2. Close-ups of the intact sample show: (C) lithic fragments, (D) intact microfossil (white arrow), (E) and (F) close-ups of the shear zone, with the main shear surfaces and possible Riedel shear surfaces indicated by red and blue arrows, respectively. Close-ups of the powdered sample show (G) Riedel shear in a homogeneous matrix and (H) the main shear zone.

Microstructural analyses of an intact sample (Figure 10A) and a powdered aliquot (Figure 10 B) from Site C0004, sheared at the same experimental conditions, show differences in deformation structures and their distribution. The intact sample is characterized by a heterogeneous appearance with no clear pre-existing foliation and includes large lithic fragments (diameter $>500 \mu\text{m}$) (Figure 10 C) and intact microfossils (diameter $\sim 300 \mu\text{m}$) (Figure 10 D). The powdered sample has a more homogenous matrix in which only fragments of fossils can be found (diameter $<100 \mu\text{m}$) (Figure 10 G). Drying of the intact sample opened several cracks, which preferentially form along shear surfaces. The multiple shear surfaces include one originating from the initial cohesion test, which is distinguished from the shear surface formed under normal load because it is located deeper in the sample cell. Oblique

cracks bend into the fault surface with a shallow angle typical of Riedel fractures related to shearing (Figure 10 E and F), but the possibility of them being formed along pre-existing weak zones is not excluded. In contrast, the powdered sample shows one narrow, through-going shear zone with internal Riedel shear structures and no distinguishable shear surface that developed earlier during the cohesion test (Figure 10 G and H).

Discussion

Frictional strength

The coefficient of sliding friction for the samples tested in our study shows a clear inverse correlation with total clay content, which ranges between 38 – 67 % (Table 2) (Expedition 316 Scientists, 2009a, 2009b, 2009c; Saffer et al., 2017c) (Figure 8 A). This is consistent with several previous studies, which have shown that frictional weakness is associated with the presence of clay minerals (Logan and Rauenzahn, 1987; Lupini et al., 1981; Saffer and Marone, 2003; Tembe et al., 2010).

Because the fault zone itself was not sampled at Site C0010, we tested samples from both the hanging wall and footwall within ~10 m of the interpreted fault zone. The hanging wall at Site C0010 has a lower coefficient of sliding friction than the footwall, which can be explained by the difference in clay content. Moreover, the internal cohesion in the hanging wall is smaller than in the footwall. On this basis, we suggest that the megasplay fault localized within materials derived from the hanging wall sediment at Site C0010.

Although Ikari and Saffer (2011) showed that megasplay fault samples from Site C0004 are consistently stronger than frontal thrust zone samples from C0007, our sample of analogous materials from Site C0010C shows the opposite. In fact, it is slightly weaker than the sample from C0007. This means frictional strength can vary significantly over short distances along strike at the same tectonic location, for example within the ~4 km distance between Sites C0004 and C0010. One explanation could be the difference in bulk clay content (7 %) (Table 2) between the samples from Sites C0004 and C0010, which makes the sample from Hole C0010C as weak as the frontal thrust sample from C0007.

Our data shows decreasing coefficient of sliding friction with both increased clay content, and due to sample disaggregation (Figure 8 A). With increasing bulk clay content, we observe that the coefficient of sliding friction decreases from 0.50 to 0.22. A remarkable observation from our experiments is the large shear strength loss (μ_{loss}) of up to ~38 % from intact to powdered state under similar stress conditions. The samples with the highest clay content show the largest μ_{loss} , whereas the shear strength of the sample with the lowest clay content of 38 % is

unaffected by disaggregation (Figure 8 B). The observed μ_{loss} could be interpreted as strengthening (or structure) effect (Leroueil and Vaughan, 1990) of initial lithification (predominantly compaction) from originally hemipelagic loose sediment to early diagenetic hemipelagic mudstones, which happens for sediment with clay contents >50 %. However, we do not observe a correlation between cohesive strength and either clay content or μ_{loss} , so the cause of μ_{loss} remains speculative.

Velocity dependence of sliding friction

Our data show that sediments from both the frontal thrust and megasplay regions exhibit velocity-weakening behavior at low effective normal stress (<~10 MPa), consistent with a limited number of previous studies that have shown rate-weakening in phyllosilicate gouges restricted to low normal stresses (Ikari et al., 2015; Ikari and Kopf, 2017; Saffer et al., 2001). Specifically, our experiments show that intact fault zone samples sheared under in-situ stress conditions exhibit the lowest $a - b$ values, and these values are lower than for the equivalent powdered samples. We suggest that the intact nature of the samples is responsible for low $a - b$ values due to contact asperity interactions on the shear surface.

Shear surfaces created during experiments are not ideally flat, therefore the real area of contact, which is the sum of individual asperities on the shear surface, is smaller than the nominal contact area defined by the sample dimensions (Figure 11). The real area of contact may be on the order of 1 % or less of the nominal contact area at room temperature (Aharonov and Scholz, 2018; Dieterich and Kilgore, 1996a; Dieterich and Kilgore, 1994). Frictional behavior is controlled by stresses at the asperity contacts and therefore by changes in real contact area. Differences in sample homogeneity affect the real area of contact, where heterogeneous samples have an initially smaller area of real contact than homogenous samples (Figure 11), due to a wider grain size distribution and angularity of the individual grains. Our microstructural analysis revealed that the grain size in the intact samples is up to five times larger than that of the equivalent powders (Figure 10).

More evidence suggesting that real area of contact plays a controlling role can be found by examining the cohesion data. Compaction and cementation over millions of years causes higher internal cohesion in intact samples. Even after establishing a mature shear surface (run-in), this means that for our intact samples, the high internal cohesion away from the shear surface (in the “wall rock”) is preserved during shear. This cohesion effect prevents relative motion and rearrangement of grains in intact samples (Figure 11). On the actual shear surface, the real area of contact is therefore smaller for intact samples, which also results in low sliding cohesion. In contrast, the powdered samples show smaller internal cohesion and higher sliding

cohesion, suggesting that grain rearrangement along the shear surface maximizes the real area of contact during shearing (Figure 11).

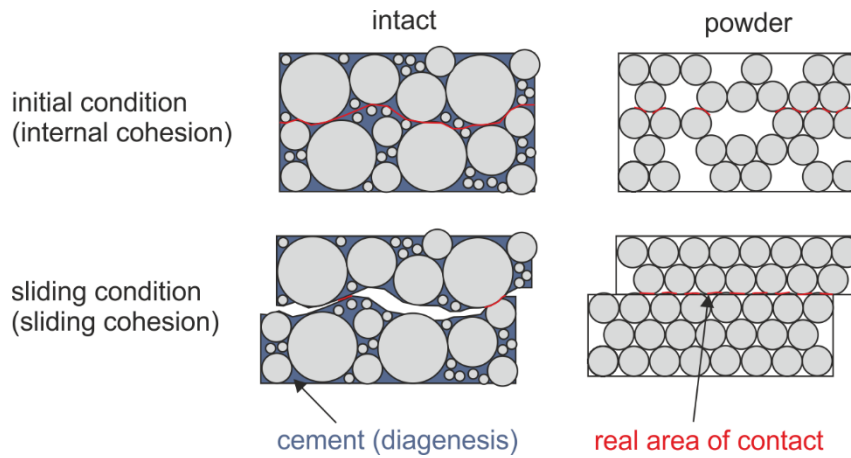


Figure 11: Conceptual model of the real area of contact in intact and powdered samples.

Previous studies have linked the evolution effect of friction, as quantified by the RSF parameter b , to the ability of the real area of contact to grow with time. Velocity-weakening friction arises because at a faster slip velocity, the duration of contact area growth and therefore the maximum real area of contact is limited (Dieterich and Kilgore, 1996a; Dieterich and Kilgore, 1994; Ikari et al., 2016a). For example, Saffer and Marone (2003) tested synthetic mixtures of smectite clay and quartz and observed rate-weakening friction and large values of the parameter b at low normal stress, and rate-strengthening at higher normal stresses, accompanied by decrease in values of b . This dependence on normal stress was interpreted to reflect the initial real area of contact, where at high normal stress clay grains lie flat and the contact area saturates, so that b is small and velocity-strengthening occurs. In our experiments, we observe that intact samples tested under in-situ stresses have a clearly larger b compared to powdered samples and samples at larger effective normal stresses, but this difference is not observed for the a values (Figure 12). This demonstrates that sample disaggregation and increasing effective normal stresses above the in-situ condition clearly favor velocity-strengthening behavior, because reducing the cohesion imparted by lithification causes the material to maximize its real area of contact (i.e. limited the capacity for contact area growth) (Figure 11). Incorporating data from Ikari and Saffer (2011) tested at 25 MPa supports the tendency for $a - b$ values to increase with effective normal stresses. This explains why previous studies conducted at effective normal stresses much higher than the in-situ stresses on powdered and intact subduction zone material from the Nankai Trough (e.g. Kumano and Muroto transect) are dominated by velocity-strengthening behavior (Ikari and Saffer, 2011; Saffer et al., 2012a).

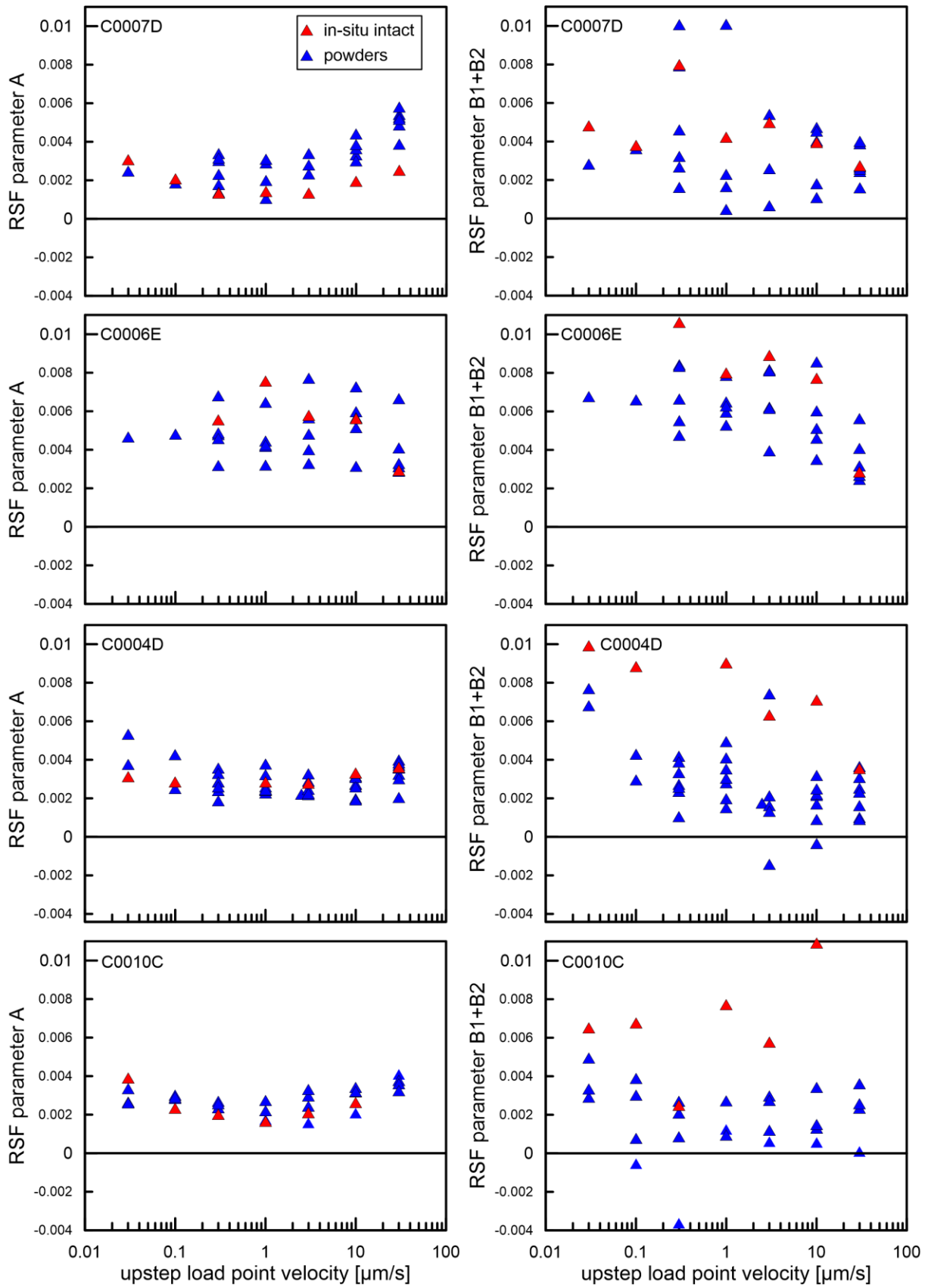


Figure 12: Values of the RSF parameter a and b as a function of upstep load point velocity for samples from Sites C0004, C0006, C0007, C0010.

To our knowledge, few studies have compared intact and powdered versions of the same sample material in velocity stepping experiments and analyzed the influence of lithification on the RSF parameter $a - b$ (Carpenter et al., 2015b, 2012; Ikari et al., 2011a; Trütner et al., 2015). A similar study was conducted by Trütner et al. (2015) who observed exclusively velocity-strengthening behavior for powdered samples and a mixture of velocity-strengthening and velocity-weakening for intact samples (Figure 13). They tested argillaceous samples from the Shimanto Belt, an exhumed accretionary wedge onshore Japan, at high effective normal stresses (81 – 117 MPa), corresponding to a depth of ~9 – 13 km in the modern active Nankai Trough. Their observations were explained by porosity loss and cementation due to lithification in the intact samples. Saffer et al. (2012a) tested intact “wafers” of porous sediment incoming to the modern Nankai Trough, and found only velocity-strengthening behavior, but they tested their samples at effective normal stresses much higher than the in-situ values (>20 MPa). Ikari et al. (2011a) observed smaller $a - b$ values for intact samples of Berea Sandstone, Indiana Limestone and illite shale than for the powdered equivalent samples tested under 50 MPa effective normal stress. In addition, the sandstone and limestone were found to be velocity-weakening as intact samples whereas the equivalent powder was velocity-strengthening. Those studies emphasize the occurrence of velocity-weakening behavior in intact sample material tested under stress conditions close to those in-situ, particularly for cases where the burial depth is shallow and in-situ stresses are low. However, in some cases a significant difference in $a - b$ for intact and equivalent powdered samples was not observed; this was attributed to the extraordinarily high clay content of the fault gouge (>~70 – 80 wt% smectite) (Carpenter et al., 2015b, 2012).

Implications for fault slip in the Nankai accretionary prism

Our results for intact samples tested under simulated in-situ stress conditions in this study show that the Nankai Trough has the potential for unstable slip under near surface conditions (<2 km). Trütner et al. (2015) showed that intact samples from the Shimanto complex, an ancient exhumed analogue for the seismogenic Nankai megathrust (Kimura et al., 2012), tested under stresses representative for depths greater than ~9 km also show some velocity-weakening behavior (Figure 13). For the depth window of ~2 – 9 km, no intact samples are currently available. Some previous studies have attempted to address this issue by testing samples recovered at shallow depths at stresses much higher than those experienced in-situ (Ikari and Saffer, 2011; Saffer et al., 2012a), or by simulating the evolution of stresses and composition with depth via combining data from a suite of synthetic gouges (Ikari et al., 2007). Such studies report predominantly velocity-strengthening behavior; however, our data indicate that testing powdered fault zone samples under higher than in-situ stresses can result in

artificially high $a - b$ values. We suggest that these previously published $a - b$ values may overestimate the tendency for rate-strengthening behavior; and expect that intact samples recovered from 2 – 9 km depth tested under in-situ stresses would result in low, likely negative $a - b$ values. Both shallow and deeper portions of the Nankai accretionary prism have the potential to host unstable slip, based on data from this study and from Trütner et al. (2015). Therefore, we propose that the entire Nankai plate boundary may be frictionally unstable (Figure 13). This would promote the propagation of coseismic slip from seismogenic depths up to and along the megasplay fault as well as along the frontal thrust zone, possibly to the seafloor. This hypothesis is supported by vitrinite reflectance results from fault zone cores, which document frictional heating in megasplay fault and frontal thrust zone cores (Sakaguchi et al., 2011).

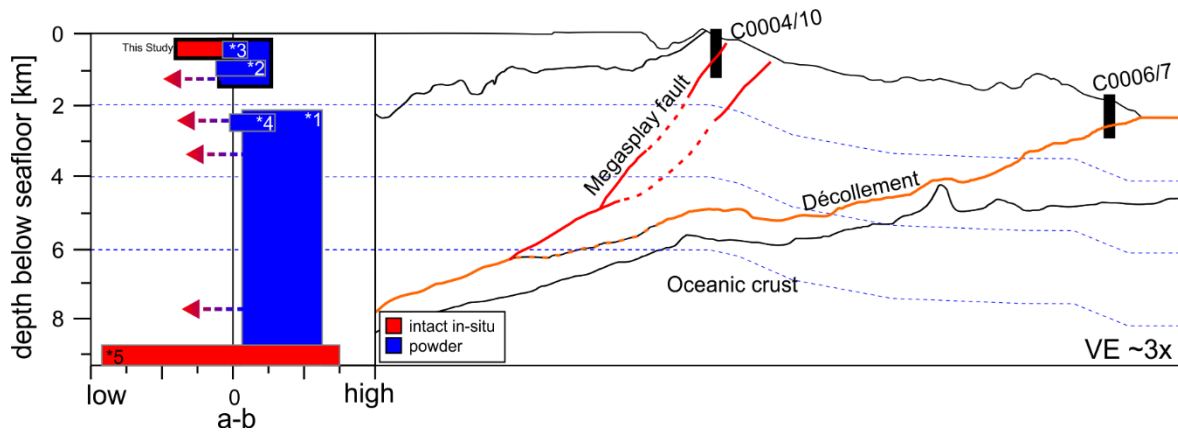


Figure 13: Variations of RSF parameter $a - b$ with depth are shown together with a cross section of the Kumano transect showing the main tectonic characteristics. Data from intact and powdered Nankai Trough subduction zone sediments are shown *1 Saffer et al. (2012a), *2 Ikari and Kopf (2017) (only modelled steps), *3 Tsutsumi et al. (2011) (calcite free samples), *4 Ikari and Saffer (2011) and *5 Trütner et al. (2015). The tested effective normal stresses were converted into depth below seafloor to indicate the approximated accretionary prism depth range that was simulated by the different studies. Thick black outline indicates data of this study.

Because our data show that velocity-weakening might be a phenomenon much more common in subduction zone settings than reported in previous studies, it suggests that unstable slip could also nucleate at shallow depths. Velocity-weakening fault rock is mandatory for earthquake nucleation, but, in the context of a simple spring-slider analogy, the criterion for nucleation of unstable slip is described by a force imbalance. This force imbalance is defined by the relative values of the loading system stiffness k and the fault's rheological critical stiffness k_c , which in turn depends on RSF parameters and effective normal stress (Dieterich, 1986; Scholz, 1998):

$$k < k_c = \frac{(b - a)\sigma'_n}{D_c} \quad (13)$$

Since velocity-weakening might be omnipresent from seismogenic to shallow depths, the instability criterion controls unstable slip in the Nankai Trough. Periodic slow slip events are thought to occur at the transitional boundary from stable to unstable sliding expressed as $k/k_c \approx 1$ (Gu et al., 1984; Leeman et al., 2016). The critical slip distance (D_c) decreases with increasing shear localization, and reduces the minimum length a patch has to slip before instability and therefore increases the tendency for slip instability (Leeman et al., 2016). Increasing effective normal stress (e.g., due to burial depth) also favors instability, whereas fluid overpressure reduces the effective normal stress and therefore promotes stable or transitional slip behavior. This is in good agreement with slow earthquake observations in overpressured sediment along the Nankai Trough (Kitajima and Saffer, 2012). The growing coverage of offshore seismic and geodetic networks along the Nankai Trough revealed shallow seismicity and slow earthquakes above the seismogenic zone towards the trench (Araki et al., 2017; Obara and Kato, 2016; Sugioka et al., 2012). Our data could explain the recently reported occurrence of slow earthquakes (such as slow slip events, VLFs and tremor) in the shallow parts of the Nankai subduction zone.

Conclusion

This study provides a comprehensive dataset of frictional properties for natural samples from four different IODP Sites along the Kumano transect offshore Japan, tested under shallow depth conditions. Fault zone samples from the frontal thrust zone (C0006, C0007) and megasplay fault (C0004, C0010) were sheared under effective normal stresses ranging from in-situ (~ 2 MPa) up to 17 MPa in a direct shear configuration. Fault zone samples from C0007 and C0010C have the lowest friction coefficient, whereas fault zone samples from C0006, C0004 and C0010E are stronger. The strengthening effect of lithification observed in intact samples relative to powdered samples is only seen in samples with clay mineral content >50 wt%. Our experimental results indicate that cohesive strength might account for a significant portion of fault strength even after a well-defined slip zone has been formed. The cohesive strength imparted by lithification affects the real area of contact along shear surfaces, by favoring large values of the rate-dependent parameter b measured in velocity step experiments, shifting $a - b$ to lower values. All samples show a mixture of velocity-strengthening and velocity-weakening behavior, but intact samples tested under in-situ effective normal stress exhibit predominantly velocity-weakening behavior. We propose that powdered fault zone samples and testing at stresses higher than those in-situ overestimates the RSF parameter $a - b$, and that fault zones in the Nankai subduction zone may be velocity-weakening from seismogenic depths up to the seafloor. The velocity-weakening behavior over a wide depth interval would promote coseismic slip propagation from seismogenic depth up to

the seafloor along the megasplay fault and/or décollement, and also the nucleation of slow slip events or VLFs. Our data also emphasize the importance of intact samples tested under in-situ conditions in friction studies.

Acknowledgments

This work used samples and shipboard data from the Integrated Ocean Drilling Program (IODP). We would like to thank the crew and the technicians (Marine Works Japan) of D/V Chikyu for their effort and support during the drilling expeditions. We would like to thank the working group Petrology of the Ocean Crust (University of Bremen) for accessing their petrological microscope. Prof. Dr. Michael Strasser (University of Innsbruck) kindly provided intact core samples for this study. This project has received funding from the European Research Council (ERC) under the European Union's Horizon 2020 research and innovation programme (grant agreement No 714430 to MJI) as well as from the University of Bremen, the Deutsche Forschungsgemeinschaft (DFG KO2108/24-1 to AK), and the Alexander von Humboldt foundation to DMS.

Author Contributions

A. Roesner, A.J. Kopf, M.J. Ikari and D.M. Saffer designed the project and the experimental program. A. Roesner performed all laboratory experiments except for two, which were completed by D.M. Saffer. Preparation of thin sections and microscopic analysis was done by A. Eijsink and A. Roesner. A. Roesner in collaboration with K. Stanislawski processed the data. A. Roesner did the data evaluation, figure preparation, wrote the first version of the manuscript, and led the revision process. M.J. Ikari and A. Eijsink revised the manuscript. K. Stanislawski, D.M. Saffer, A.J. Kopf commented on the manuscript. A.J. Kopf supervised and funded the project.

Supplementary materials

Results velocity step test Site C0010E - footwall

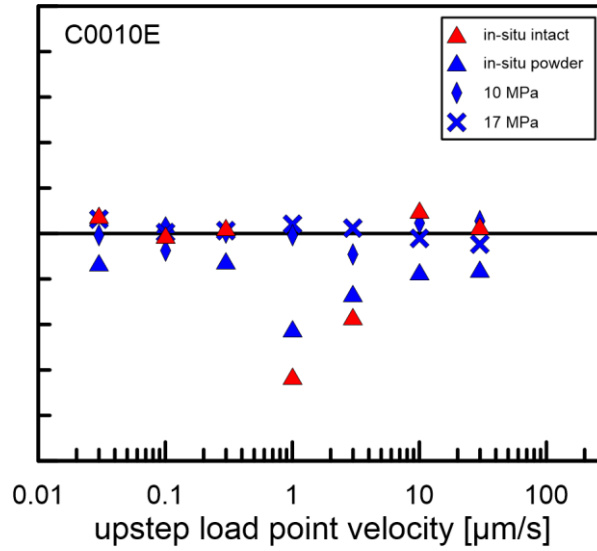


Figure 14: Rate-dependent friction parameter $a - b$ as a function of upstep load point velocity for the samples from the megasplay fault footwall Site C0010.

Slip-weakening

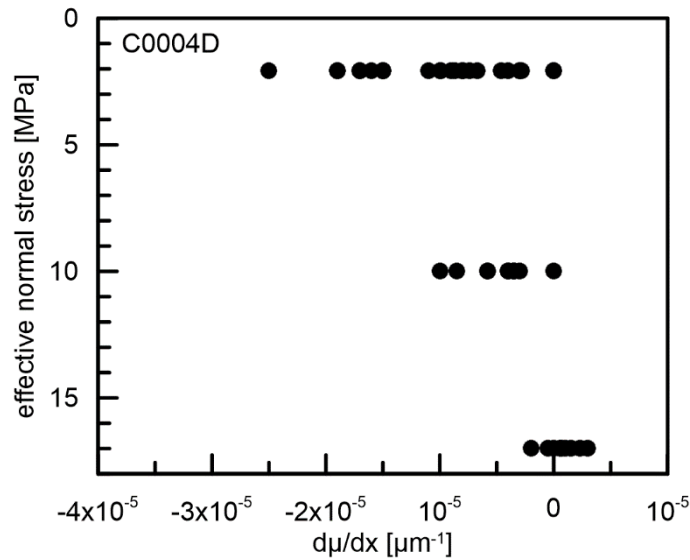


Figure 15: Effective normal stress as a function of $d\mu/dx$ for all experiments on C0004 samples.

Overall experimental table

Table 3: Summary of experiments.

The comprehensive experimental data table is uploaded to <https://zenodo.org/> and can be found under the digital object identifier: 10.5281/zenodo.3490686.

2.3 Manuscript 2 (in preparation): Slip dependent weakening revealed for a shallow megasplay fault in the Nankai subduction zone

A. Roesner¹, M.J. Ikari¹, A. Huepers¹, A.J. Kopf¹

¹MARUM - Center for Marine Environmental Sciences, University Bremen, Germany

Abstract

The Nankai Trough megasplay fault likely hosts different modes of fault slip from slow to megathrust earthquakes, and is responsible for related phenomena such as tsunamis and submarine landslides. All types of slip events require some kind of frictional weakening process in order to nucleate and propagate. We tested fluid-saturated powdered megasplay fault samples in a direct shear apparatus under effective normal stresses from 2 – 18 MPa to investigate the velocity- and slip dependence of friction of the megasplay fault. The velocity-stepping tests showed an evolution from velocity weakening at low effective normal stress, to velocity strengthening at high effective normal stresses. All experiments revealed strong slip-weakening behavior, with the slip dependence having a much larger effect on friction than the velocity dependence. The friction slip dependence is also controlled by the effective normal stress, showing large weakening at low effective normal stresses and smaller weakening at higher effective normal stresses. Therefore, frictional weakening mechanisms on the megasplay fault become more effective at shallow depths. This may amplify seafloor deformation by shallow coseismic slip and could increase the tsunamigenic potential of the fault zone.

Introduction

Active subduction zones host a variety of deformation phenomena, ranging from aseismic creep, to various forms of slow and transient slip, to megathrust earthquakes. The Nankai Trough subduction zone offshore SW Japan has a long history of documented large-magnitude megathrust earthquakes with recurrence intervals of 90 – 150 a (Ando, 1975a). In recent years, a comprehensive spectrum of fault slip modes including very low frequency earthquakes (VLFs) (Ito and Obara, 2006b; Obara and Ito, 2005; Sugioka et al., 2012), slow slip events (SSEs) (Araki et al., 2017; Hirose et al., 2010; Nakano et al., 2018), and tectonic tremor (Annoura et al., 2017; Ide, 2012) have been documented in the outer accretionary prism up to the trench (Figure 16). In the last century, two megathrust earthquakes with $M_w > 8$ occurred in the Nankai Trough (Ando, 1982; Tanioka and Satake, 2001) (Figure 16 A). One of these, the 1944 Tonankai earthquake, triggered a tsunami with an average wave height of 6 – 8 m along the Kumano coast (Ichinose et al., 2003). Over the last 400 years, five megathrust earthquakes generated devastating tsunamis of different intensity that hit the coastline along the Nankai Trough (Ando, 1975b). Frictional heating documented by vitrinite reflectance in ocean drilling samples of a major out of sequence thrust fault and the toe of the Nankai accretionary prism suggests coseismic slip extended close to the seafloor in older and undocumented earthquakes (Sakaguchi et al., 2011). The type occurrence of shallow fault slip events are clearly important for evaluating earthquake and tsunami hazards (Polet and Kanamori, 2000), but the frictional properties remain subject to debate (Bilek and Lay, 2002; Faulkner et al., 2011; Marone and Scholz, 1988; Seno, 2002).

Fault slip behavior is controlled by the frictional properties of the fault and the elastic properties of the surrounding wall rock, which is often expressed in the rate and state friction (RSF) framework that describes frictional stability of rocks and sediments. Within this framework, decreasing frictional strength in response to an accelerating fault slip is called velocity weakening, whereas the opposite is termed velocity strengthening behavior. Velocity strengthening faults inhibit earthquake nucleation and favor steady creep. In contrast, velocity-weakening behavior of fault zone sediment is a prerequisite for earthquake nucleation and favors coseismic slip along the fault zone.

RSF theory assumes steady-state sliding conditions, but experimental studies often show a slip dependence superimposed on the friction record during velocity step tests (Blanpied et al., 1998; Ikari et al., 2013b; Ito and Ikari, 2015). These long-term slip weakening/strengthening trends are often neglected in the frictional stability analysis (Blanpied et al., 1998). Ikari et al. (2013b) analyzed the slip dependence in natural fault zone samples and showed that slip-weakening friction could allow the occurrence of slow earthquakes. Furthermore, velocity

perturbations e.g. by coseismic rupture could induce slip weakening causing natural faults to become unstable (Ito et al., 2017; Ito and Ikari, 2015). Ito and Ikari (2015) showed that slip dependence of friction can overwhelm the velocity dependence of friction. Consequently, both slip and velocity dependence can affect the stability of a fault zone and must be considered to assess the potential for coseismic slip up to seafloor and therefore the risk for tsunamigenesis.

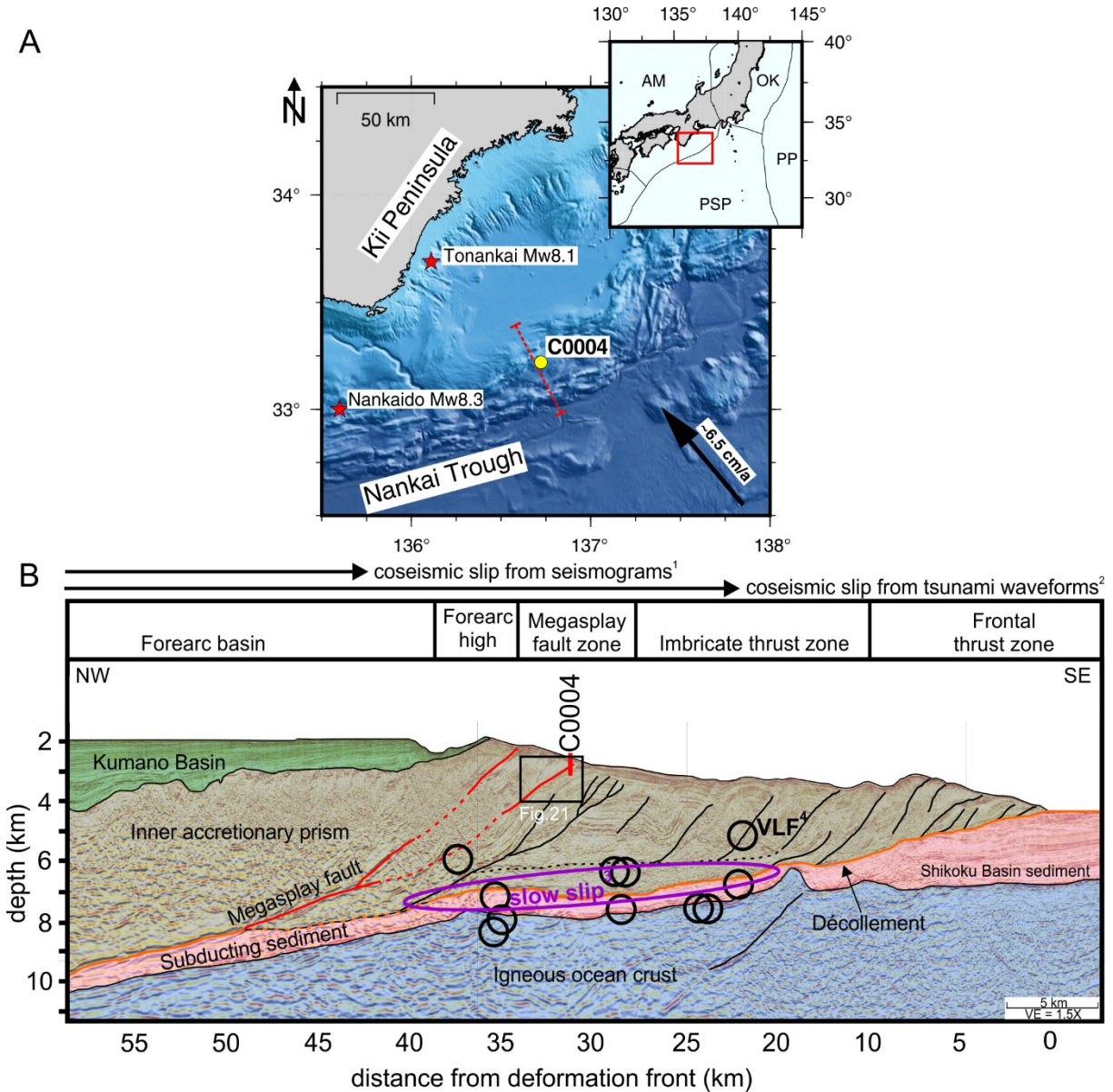


Figure 16: (A) Bathymetric map showing drill Site C0004 as well as the location of the seismic cross section (red dashed line) shown in Figure 16 B. Red stars indicate epicenters of the last two megathrust earthquakes in the study area. Am – Amurian Plate, OK – Okhotsk Plate, PSP – Philippine sea Plate and PP – Pacific Plate. (B) Interpreted seismic cross section of the Kumano transect after Moore et al., 2009. Black arrows indicate the coseismic slip during the Tonankai earthquake ¹Kikuchi et al. (2003) and ²Tanioka and Satake (2001). The purple ellipse locates slow slip areas ³Araki et al. (2017), black circles indicate very low frequency earthquakes (VLF) ⁴Sugioka et al. (2012).

Here, we use velocity stepping and constant velocity experiments under simulated near surface conditions (equivalent to $< \sim 2 - 3$ km below seafloor) to investigate the slip- and velocity-dependence of friction for a phyllosilicate-rich sample from the megasplay fault zone

in the Nankai Trough accretionary prism (Figure 16). The observed frictional behavior is then discussed in terms of different modes of fault slip and potential geohazards originating on the megasplay fault.

Geological setting and experimental sample

The Nankai Trough subduction zone is characterized by the subduction of the Philippine Sea plate under the Amurian microplate at a convergence rate of 6.5 cm/a (Miyazaki and Heki, 2001; Yokota et al., 2016). Offscraping of the incoming sediment cover led to the formation of a >100 km wide accretionary prism. The prism can be separated into an inner, stronger accretionary wedge and a weaker outer wedge, which is offset by a major out of sequence thrust fault (“megasplay fault”) (Kimura et al., 2007; Park et al., 2002). The megasplay fault branches upward from the deformation front at ~55 km from the plate boundary thrust up to the seafloor seaward of the outer ridge (Figure 16 B).

The shallow branches of the megasplay fault were drilled during IODP Expeditions 316 and 319 at Sites C0004 and C0010. We focus on samples from Site C0004 (Figure 16) where a wide fracture zone hosting the megasplay fault was sampled. IODP Site C0004 is well characterized by numerous friction studies testing fault zone and wall rock sediment (e.g. Ikari and Saffer, 2011; Tsutsumi et al., 2011; Ujiie and Tsutsumi, 2010; Ikari and Kopf, 2017). The hanging wall is composed of overriding accretionary prism sediment, whereas the footwall comprises underthrust slope sediment (Kimura et al., 2011). The fault zone spans from 256 to 315 mbsf and the deformed interval is composed of ash-bearing hemipelagic mud with some volcanic ash layers. The fault zone material on average is composed of 20 % quartz, 18 % feldspars, 2 % calcite and 60 % clay minerals (Expedition 316 Scientists, 2009a).

Experimental methods and procedure

We tested a sample from within the fault zone from 277 mbsf (sample C0004D29R3), which has a mineralogical composition of 15 % quartz, 17 % feldspars, 50 % phyllosilicates and 18 % other minerals below 10 %. The mineralogical composition was determined by X-ray diffraction (XRD) analysis following Vogt et al. (2002). Due to limited amount of core material, we re-used the sample for each experiment in this study. Possible effects of sediment recycling may include a slight increase in the amount of detected amorphous silica, most likely due to wear from preparation with a mortar and pestle as well as experimental shearing (C. Vogt, personal communication). Re-analyzing the sample after the experimental study showed a mineralogical composition of 18 % quartz, 19 % feldspars, and 42 % phyllosilicates, and 20 % other minerals below 10 %, including 8 % amorphous silica.

The sample material was dried in an oven at $\sim 60^\circ\text{C}$, powdered with a mortar and pestle and sieved to a grain size of $< 180\ \mu\text{m}$. The powder was mixed with deionized water in a ratio 2 to 1 to form a stiff paste and placed in a stainless steel shearing assembly with a sample diameter of 25.4 mm and height of 25 mm. Experiments were conducted in a direct shear configuration (GIESA RS5) at a room temperature of $\sim 21^\circ\text{C}$. For all experiment the sample holder was flooded with simulated seawater with a salinity of 3.5 %. (Figure 17 A).

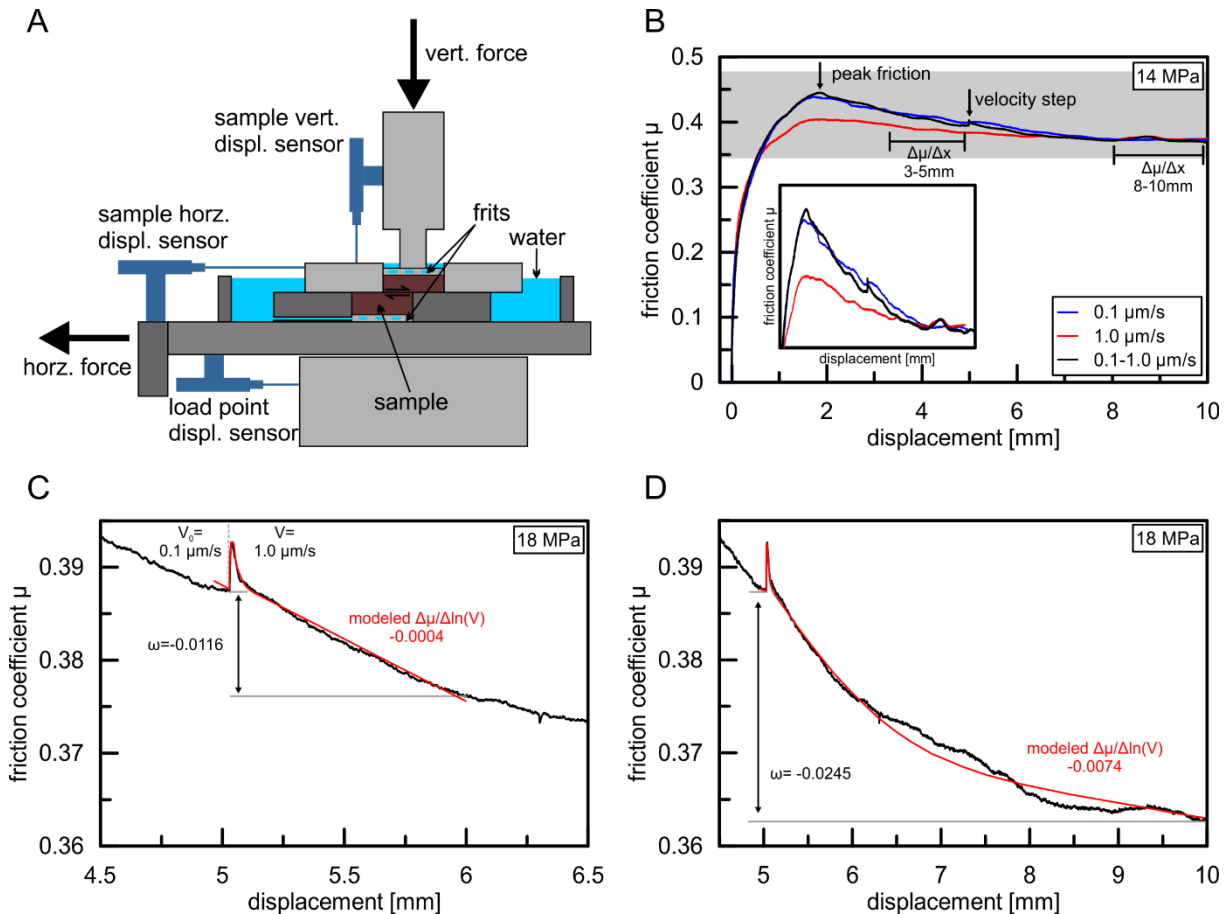


Figure 17: (A) Schematic diagram of the shear device used in this study where the dark grey part moves to the left under constant vertical force while monitoring displacement and shear force. (B) Data example of one set of experiments at 14 MPa effective normal stress, gray background indicates data shown in inset. (C) Velocity-step modeled over 1 mm. (D) Velocity-step modeled over 5 mm.

The upper and the lower part of the shearing assembly are displaced relative to each other, which enforces localized shear in the cylindrical sample. The bottom and upper end of the sample are connected via porous frits to an open water reservoir that ensures pore water drainage during the consolidation periods. The samples were consolidated for 24 hours via a vertical piston which applied normal stresses σ_n of 2, 4, 6, 10, 14 and 18 MPa. Changes in sample height became negligible after 24 hours of consolidation, thus we assume complete dissipation of pore water pressure in excess of hydrostatic. Consequently, the applied normal stress equals the effective normal stress σ'_n . For every tested effective normal stress, we performed one velocity-step experiment and two constant velocity experiments (no velocity

step). In the velocity-step experiments the samples were sheared in total 10 mm with an initial sliding velocity $V_0 = 0.1 \mu\text{m/s}$ for the first ~ 5 mm (run-in) followed by a velocity step increase to $V = 1.0 \mu\text{m/s}$. During the constant velocity experiments, shearing velocity ($0.1 \mu\text{m/s}$ and $1.0 \mu\text{m/s}$ respectively) was held constant for 10 mm of displacement.

The results are reported in terms of the coefficient of sliding friction μ_s , which is defined as the ratio of measured shear stress τ and applied effective normal stress. Cohesion is often neglected in experimental friction studies, but recent studies showed that cohesive strength can be significant on mature clay rich shear surfaces (Ikari and Kopf, 2015, 2011). Therefore, our reported coefficient of sliding friction includes both cohesive and frictional strengths and does not distinguish between them.

The friction data from a velocity step test can be quantified as (Dieterich, 1979; Marone, 1998a):

$$\mu = \mu_o + a \ln\left(\frac{V}{V_0}\right) + b_1 \ln\left(\frac{V_0 \theta_1}{Dc_1}\right) + b_2 \ln\left(\frac{V_0 \theta_2}{Dc_2}\right) \quad (14)$$

$$\frac{d\theta_i}{dt} = 1 - \frac{V \theta_i}{Dc_i}, i = 1, 2 \quad (15)$$

where a , b_1 , and b_2 are dimensionless constants, θ_1 and θ_2 are state variables having units of time and Dc_1 and Dc_2 are critical slip distances over which friction evolves to a new steady state. μ_o is the reference friction coefficient associated with the reference sliding velocity V_0 prior to the velocity step. If the experimental data is well described by one state variable, we set $b_2 = 0$; however, in some cases the data is clearly better described by two state variables, where we define $b = b_1 + b_2$. To evaluate our velocity step data and extract the RSF parameters, we modeled our velocity steps with an inverse modeling technique using a least-squares method established by Reinen and Weeks (1993).

Under steady-state sliding conditions the RSF law shown in Equations 1 and 2 reduces to:

$$a - b = \frac{\Delta\mu_{ss}}{\ln\left(\frac{V}{V_0}\right)} \quad (16)$$

where μ_{ss} is the friction coefficient at steady state sliding and the parameter $a - b$ quantifies the friction velocity-dependence. Positive $a - b$ values describe velocity-strengthening behavior that favors stable fault creep, and coseismic slip is resisted due to energy consumption by strengthening. In contrast, negative $a - b$ values describe velocity-weakening behavior, which is a prerequisite for earthquake nucleation and a favorable condition for coseismic slip.

The RSF equations assume steady-state sliding conditions (friction is independent of displacement) before and at the end of a particular velocity step. In most experiments, we observe a trend of slip dependence superimposed on the data which we commonly remove before the inversion (Blanpied et al., 1998; Ikari et al., 2013b). There is no standardized method how to remove a superimposed trend on the data. Commonly, a linear fit is applied to the velocity step data to account for a superimposed trend, this praxis involves already some degree of interpretation, especially when the trend changes before, after or during a particular velocity step. Commonly slip distances for individual velocity steps in step tests are < 1 mm to perform multiple velocity steps during an experiment. Here, we compare results of RSF modeling applied over the commonly used distance of approximately 1 mm and over an extended distance of 5 mm (e.g. Ito and Ikari, 2015) (Figure 17 C&D).

To investigate the slip dependence of friction we measured the long-term trends in the friction data following the procedure of Ito and Ikari (2015). The slip dependence of friction is measure as a linear fit to the friction data over 3 to 5 mm and 8 to 10 mm total slip displacement (Figure 17 B). The slip dependence of friction is expressed as:

$$\eta = \frac{\Delta\mu}{\Delta x} \quad (17)$$

where x is the horizontal displacement. The first fitting window precedes all velocity steps, whereas the second fitting window follows the velocity step in sufficient distance (~ 3 mm) to be not biased by the evolutionary effect of the velocity step. This fitting procedure was done for both constant and velocity-step experiments to allow comparison. We also determined the net change in frictional strength over 1 and 5 mm displacement following the velocity step, denoted as ω :

$$\omega = \frac{\Delta\mu_i}{\ln\left(\frac{V}{V_0}\right)} \quad (18)$$

where μ_i is the instantaneous coefficient of friction. The net change measurement ω includes the effects of both the velocity- and slip dependence of friction (Figure 17 C&D).

Results

The experimental data exhibit a peak in friction coefficient between 1 and 3 mm horizontal displacement, followed by decreasing frictional strength over millimeter-scale slip distance (Figure 17 B). The peak friction coefficient in our experiments varies from 0.4 – 0.5 over the range of tested effective normal stresses and velocities (Figure 18 and Table 4). Peak friction for shearing velocity of 0.1 $\mu\text{m/s}$ decreases from 0.50 to 0.44 with increasing effective normal stress from 2 – 6 MPa, and remains nearly constant from 6 – 18 MPa. The peak friction

measured at a shearing velocity of 1.0 $\mu\text{m/s}$ is systematically smaller than the measurements at 0.1 $\mu\text{m/s}$, showing a decrease in peak friction from 0.46 to 0.40 between 2 – 6 MPa and also remaining nearly constant from 6 – 18 MPa.

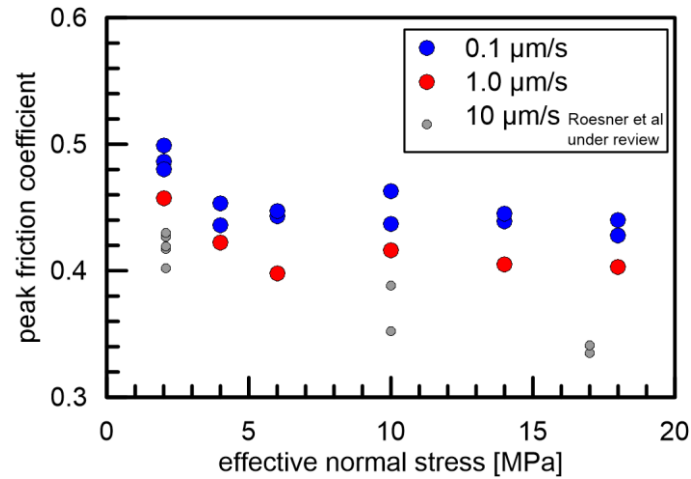


Figure 18: Peak friction as a function of effective normal stress. Blue circles represent constant velocity and velocity-step experiments.

The velocity step experiments show mainly weakening, either expressed as velocity-weakening or net weakening (Figure 19). Inverse model results of velocity step data over 1 mm show $a - b$ values of $-0.005 - 0.002$, with velocity-weakening at low effective normal stresses transitioning to velocity strengthening at 10 MPa effective normal stresses.

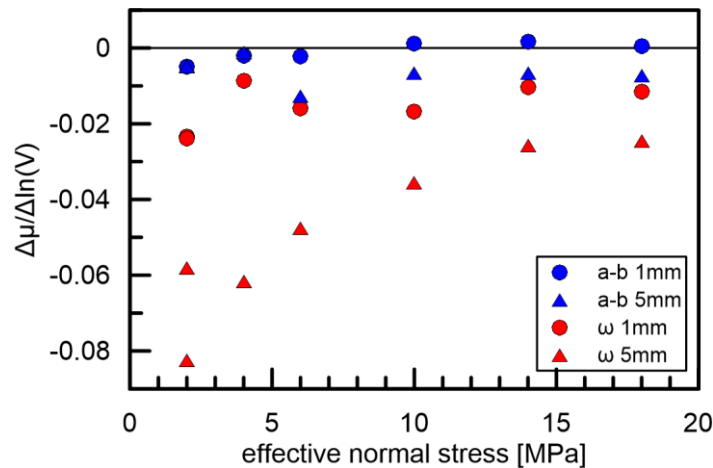


Figure 19: Results of velocity-stepping experiments showing modelled velocity-dependence and net changes.

When the inverse model is applied over 5 mm displacement following the velocity step, strictly velocity weakening ($a - b = -0.013 - -0.002$) independent of effective normal stress is observed. In comparison, net changes in friction coefficient exhibit larger absolute values of weakening. Net weakening measured 1 mm following the velocity steps ranges from $\omega = -0.025 - -0.010$, which decreases slightly as a function of effective normal stress. The largest net weakening is measured at 5 mm displacement beyond the velocity step ($\omega = -0.09 - -0.03$),

which represent the largest values of weakening of any kind in this study (Figure 19). Net weakening at 5 mm correlates inversely with effective normal stress.

All experiments show slip weakening ($\eta < 0$) over the tested range of horizontal displacement and effective normal stresses (Figure 20 A&B). With increasing effective normal stress slip weakening decreases from $\eta = -0.016 - -0.024$ at 2 MPa to $\eta = -0.004 - -0.016$ at 18 MPa for 3 – 5 mm horizontal displacement (Figure 20 A). Slip weakening is more pronounced at lower velocities (Figure 20 A). At larger horizontal displacements of 8 – 10 mm, the slip weakening decreases from $\eta = -0.014 - -0.016$ at 2 MPa to $\eta = -0.001 - -0.004$ at 18 MPa. At high effective normal stresses, neutral η values are observed indicating steady state frictional behavior.

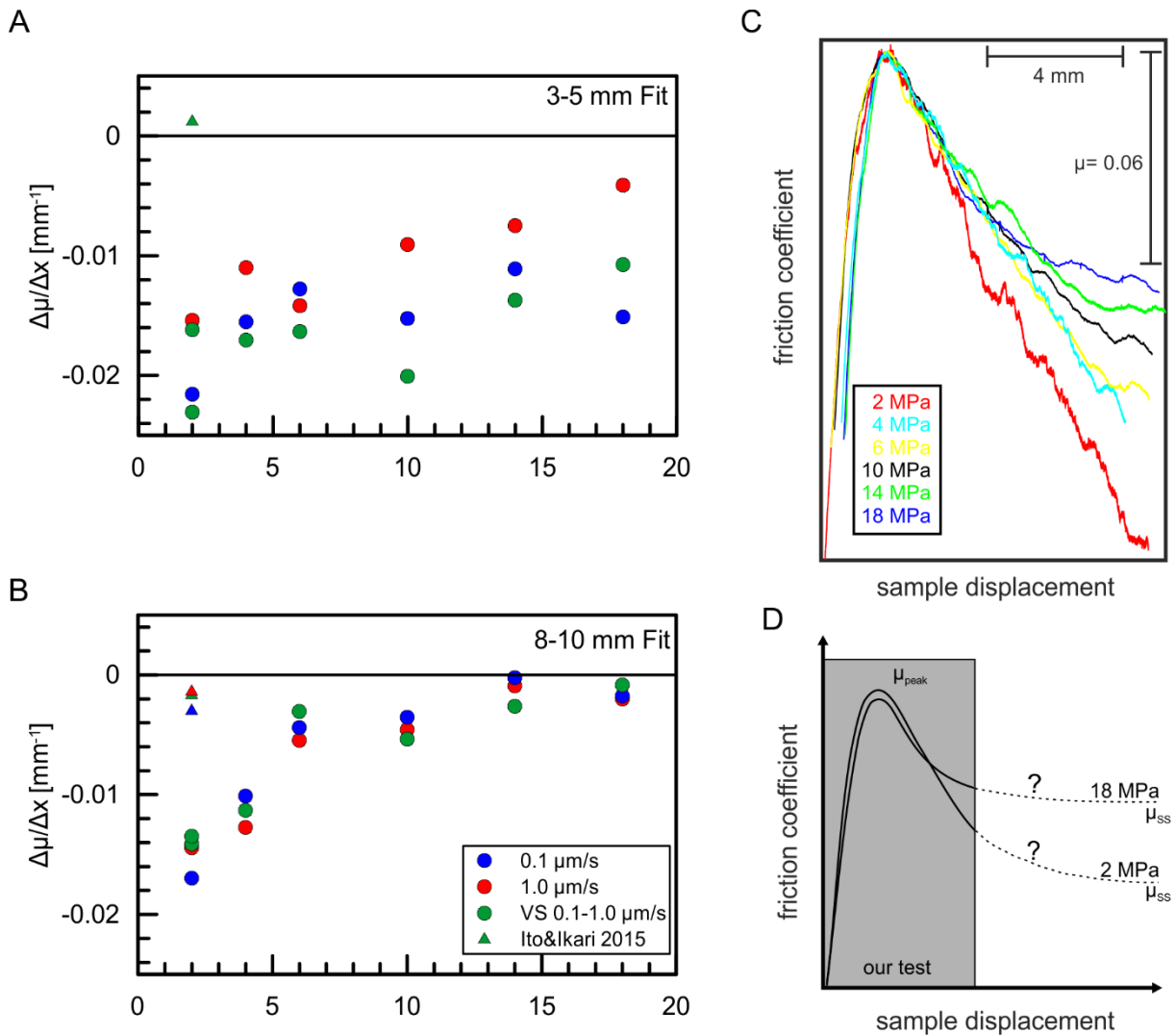


Figure 20: Slip dependence of friction as a function of effective normal stress in velocity-step and constant velocity experiments. Slip dependence between 3 – 5 mm (A) and 8 – 10 mm (B) displacement. (C) Friction-displacement curves for 0.1 $\mu\text{m/s}$ graphically normalized by peak friction to illustrate slip weakening behavior from peak friction to “steady state”. (D) Conceptual model of slip weakening behavior under varying effective normal stress. Gray represents data from our direct shear tests with 10 mm maximum displacement.

Neither sliding velocity nor velocity perturbations (velocity step tests) systematically affect the weakening behavior at large displacements of the fault zone material (Figure 20 B). At high effective normal stresses, friction reaches steady state, whereas at low effective normal stresses steady state friction is not reached within 10 mm of shear displacement (Figure 20 C).

Discussion

Evolution of frictional behavior

Friction coefficient-displacement curves in our study show behavior typical of overconsolidated clays, which are characterized by a peak in shear strength followed by soil softening to a steady state friction. This behavior originates from initial soil compaction followed by volume dilation after the yield point is passed (Mitchell and Soga, 2005). However, our samples are normally consolidated because we use disaggregated sample powder, so that the applied stress in our experiments equals the maximum stress experienced by the sample. Normally consolidated clays show ductile deformation accompanied with volume compaction in shear experiments (Mitchell and Soga, 2005). A peak in shear stress has been reported in different natural and analog fault gouges under various testing conditions (e.g. Haines et al., 2013; Ikari et al., 2015; Saffer et al., 2001; Saffer and Marone, 2003). We explain the apparent overconsolidation in our samples with secondary consolidation creep within the 24 h of consolidation, which took place after primary consolidation was finished (Mitchell and Soga, 2005; Terzaghi et al., 1996).

Tenfold sliding velocity differences from 0.1 – 1.0 – 10 $\mu\text{m/s}$ shifts the coefficient of peak friction of the fault zone sediment systematically to lower values (Figure 18). Peak friction analysis is rarely documented in frictional studies evaluating earthquake related processes at slow sliding velocities. Buijze et al. (2017) observe decreasing peak friction with increasing velocity (0.1 – 10⁴ $\mu\text{m/s}$) for halite and halite-muscovite mixtures at room temperature and humidity. In contrast, simulated clay mineral-rich fault gouge tested under various sliding velocities (0.048 – 4.8 $\mu\text{m/s}$) and temperature did not show a peak in friction (Moore et al., 1986). Increasing pore water pressure during shear loading could reduce the effective stress, causing a smaller shear strength (Mitchell and Soga, 2005). This effect would be more pronounced at higher shearing rates because of the limited time for pore water drainage. On the other hand, shear failure is a dilatant phenomenon, which would cause a reduction in pore fluid pressure (e.g. Beeler, 2007; Marone et al., 1990). In our direct shear configuration, we cannot measure pore water pressure but we assume that our samples are in a dilatational regime. Thus, it is not clear what material properties cause the difference in peak friction values with increasing sliding velocity.

In all our experiments, we observe decreasing friction from peak friction at ~ 2 mm towards the end of the test at 10 mm shear displacement. Within the limits of our experimental set-up, we approach nearly steady state sliding conditions at 18 MPa effective normal stress (Figure 20 C). With decreasing effective normal stress slip weakening expressed by more negative η increases (Figure 20 B). Thus, the friction-displacement curves after peak friction show a convex curvature at high effective normal stress, whereas at low effective normal stress the curves can be described by a linear decrease in friction (Figure 20 C). Since the gouge is seeking for steady state friction, at low effective normal stresses the displacement between peak and steady state friction must be larger. In addition, the steady state friction coefficient is most likely smaller at low effective normal stresses, due to more pronounced slip weakening (Figure 20 D).

The evolution from peak to steady state shear strength is often explained by shear band formation and alignment of sediment particles. Conceptual models such as the March strain model (March, 1932) are used to describe the preferred orientation of plate-shaped bodies under uniaxial deformation. Experimental evidence for fabric intensity development under differential stresses of <10 MPa are presented by, for example, Sintubin et al. (1995) and Tullis (1976), whereas at compressional stresses >10 MPa the fabric intensity is nearly unaffected (Haines et al., 2009). However, high normal stresses have a strong effect on fabric intensity development under shear (Haines et al., 2009). Shearing of phyllosilicates causes preferred alignments of clay particles resulting in inter-particle sliding in narrow shear bands (D'Ignazio and Lämsivaara, 2015). The oriented clay particles reduce the friction coefficient of the sediment and increase the fabric intensity. Fabric intensity increases with effective normal stress at similar shear strains (Haines et al., 2009). The testing geometry of the biaxial testing apparatus used in the experiments by Haines et al. (2009) allows the formation of boundary and Riedel shears within in the 2 – 3 mm thick gouges (Haines et al., 2009), whereas our testing geometry (direct shear apparatus) forces shear localization. The shear surface in the direct shear geometry can probably be best compared to the boundary shears in the biaxial shear apparatus (Haines et al., 2009). Despite the different shearing geometry, the effect of effective normal stresses on fabric intensity development in our shear zones is likely similar, where low effective normal stresses cause a slowly-developing fabric intensity which, in our experiments, does not reach steady state. In contrast, at high effective normal stresses clay particles re-orientate faster (smaller slip distance) allowing steady state fabric, and thus steady-state friction, to be achieved within a shorter displacement (Figure 20 D).

Our friction experiments indicate that at a specific normal stress, the slip dependence of friction η becomes smaller with progressive slip (Figure 20). Thus, effective normal stress controls the total slip amount necessary to achieve steady state friction. Ito and Ikari (2015) and (2017)

suggested that velocity perturbations induce slip-weakening, by comparing η of constant velocity with velocity-step test data. Ito and Ikari (2015) data show a perturbation effect for upstep sliding velocities $\geq 10 \mu\text{m/s}$, whereas for tests at $1.0 \mu\text{m/s}$ they did not observe such an effect, similar to our experiments at $1 \mu\text{m/s}$ (Figure 20 B). Therefore, we conclude that velocity perturbations only affect the slip dependence of friction for upstep sliding velocities $> 10 \mu\text{m/s}$. In our experiments, friction changes induced by the velocity steps do not affect the general trend of slip weakening in our experiments (Figure 17 B & 20). Comparing friction data with and without velocity perturbations indicates that for slip distances of 5 mm, weakening is primarily due to the slip dependence (Figure 17 B & 20). Mathematically the RSF equations produce a good fit to the experimental data, but the RSF law specifically quantifies velocity-induced frictional changes. Consequently, the $a - b$ values derived for 5 mm displacement following the velocity step can potentially largely underestimate the amount of weakening (Figure 19). Our modelled velocity step data show that short velocity steps are important to minimize potential artefacts of slip dependence in RSF modeling and isolate the velocity dependence. Moreover, short displacements enable better linear detrending, since most RSF laws are coupled with a linear detrending equation to account for slip dependent background trends. However, slip dependence of friction expressed as slip weakening in our phyllosilicate-rich fault gouge is an important weakening mechanism as can be seen by the frictional net change measurements. To fully quantify the slip dependence of friction shear displacements until steady state friction are necessary.

Implication to natural fault zones

We observe slip dependent weakening in all our experiments over the range of effective normal stresses tested. Stresses from 2 – 18 MPa simulate shallow depth (up to 2 – 3 km bsf) conditions along the megasplay fault (Figure 21). Megathrust earthquakes nucleating at seismogenic depths, such as the Nankaido or Tonankai earthquakes, produce coseismic slip that propagates onto preexisting fault zones such as the megasplay fault (Kame et al., 2003; Sakaguchi et al., 2011). The slightly higher peak friction at effective normal stresses between 2 – 6 MPa allows the sediment to store more potential energy; increasing the fracture energy at shallow depth (Faulkner et al., 2011). Coseismic slip propagating updip along the megasplay fault experiences progressively decreasing effective normal stress, and thus encounters fault segments with increasing slip weakening behavior (Figure 21). In addition, our velocity step test results are in agreement with former frictional studies showing at shallow depth mixtures of weakening and strengthening behavior (Ikari and Kopf, 2017; Tsutsumi et al., 2011) (Figure 19 & 21). Once the stabilizing peak friction is overcome weakening at coseismic slip speeds imply that coseismic rupture propagates easily through the clay rich fault gouge

(Faulkner et al., 2011; Ujiie and Tsutsumi, 2010). Consequently, shallow depth conditions along the megasplay fault amplify coseismic slip, increasing the likelihood for large seafloor displacements. Similar to coseismic slip, SSEs nucleating at deeper portions of the megasplay fault or the plate boundary thrust might propagate updip, due to the pronounced slip weakening at shallow depths (Araki et al., 2017). In the shallow part of the accretionary prism, the sediment slip behavior is dominated by the slip dependence and not by the velocity dependence of friction (Figure 21); also observed in simulate fault gouge tested at 2 MPa effective normal stress by Ito and Ikari (2015). Our data show that even velocity-strengthening sediment could favor coseismic slip up to seafloor due to its pronounced slip weakening behavior. Increasing fracture energy and pronounced slip weakening behavior at shallow depth could be favorable for large seafloor displacements. This is in agreement with mechanical data by Stipp et al. (2013) suggesting surface breaks after the deformation of the structurally weak shallow hanging wall megasplay fault sediments. Thus, tsunamigenesis is likely during a large-magnitude megathrust earthquake that induces seafloor displacements comparable to the Tonankai earthquake in the rupture areas of the former Tonankai and Nankaido megathrust earthquakes.

Our experiments also suggest that large slip weakening should be expected at effective normal stresses <2 MPa, which are depths relevant for submarine landslide occurrence e.g. $\sim 0 - 200$ mbsf. Evidence for sediment mass transports in the shallow megasplay fault zone (Figure 16 B) have been identified in seismic and bathymetric data but also in core samples (Kanamatsu et al., 2014; Strasser et al., 2011). These mass-wasting events occurred at times of enhanced megasplay fault activity (Strasser et al., 2011) and could be triggered by dynamic loading (earthquake shaking) similar to mass wasting events triggered by the Tohoku-Oki earthquake in the Japan trench (Ikari et al., 2011b; Strasser et al., 2013). Landslide acceleration, velocity and runout is controlled by the loss of resistance forces within a soil mass. The reduction from peak to steady state strength leads to the propagation of the shear surface. The enhanced slip dependence at low effective normal stresses would promote long landslide run-outs because the slip weakening is more dramatic. In addition, the expected low steady-state friction would reduce the sliding resistance.

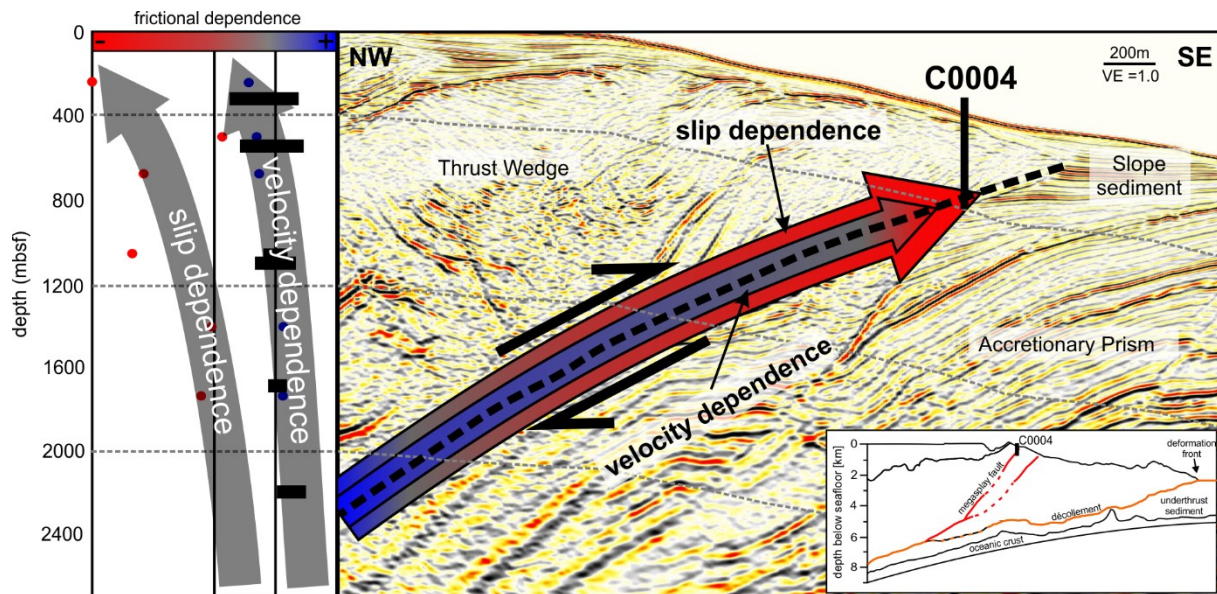


Figure 21: Seismic cross section of Site C0004 showing frictional dependence at shallow depth. Slip dependence is the controlling parameter for weakening in megasplay fault sediment (indicated by the bold arrow). Red and blue circles show experimental data of this study whereas the black boxes show velocity step test results from (Roesner et al under revision; Ikari and Kopf, 2017; Ikari and Saffer, 2011; Ujiie and Tsutsumi, 2010). Depth is extrapolated from effective normal stress calculations from shipboard bulk density measurements on the cored interval.

Conclusions

The RSF framework is a powerful tool to model velocity dependence of experimental data. Nevertheless, by removing superimposed trends from the frictional data important information describing fault gouge behavior under shear are not considered. Consequently, a combination of slip and velocity-dependent analysis is necessary for a comprehensive frictional analysis. The weakening in C0004 megasplay fault samples is caused by velocity and slip dependent weakening but slip weakening is dominant over millimeter scale displacement. The magnitude of slip weakening and the slip weakening distance from peak to steady-state depend on the effective normal stress. The slip weakening distance is larger under low effective normal stresses, so that the frictional weakening is more pronounced. Sediments characterized by large slip-weakening in the shallow accretionary prism may foster seafloor deformation caused by coseismic slip or updip propagation of SSEs. Therefore, megasplay fault sediment at shallow depth are favorable for tsunamigenesis. The extrapolation of our result to depths relevant for landslide occurrence may explain long landslide run outs due to pronounced slip weakening mechanism and low steady state friction.

Acknowledgments

This study used samples drilled by the D/V Chikyu from the Integrated Ocean Drilling Program (IODP). We would like to thank the staff, the drilling personnel, and the technicians (Marine Works Japan) for their effort and support during the drilling expedition. XRD measurements were done by Dr. Christoph Vogt in the research group crystallography of the University of Bremen. We thank Gregory F. Moore (University of Hawaii) for providing the seismic image of the megasplay fault. This project has received funding from the European Research Council (ERC) under the European Union's Horizon 2020 research and innovation programme (grant agreement No 714430 to MJI) as well as from the University of Bremen and the Deutsche Forschungsgemeinschaft (DFG KO2108/24-1 to AK).

Author Contributions

A. Roesner conceived the project. Together with M.J. Ikari and A. Huepers he designed the experimental program. A. Roesner performed all experiments and processed the data. A. Roesner did the data evaluation, figure preparation, wrote the first version of the manuscript, and led the revision process. M.J. Ikari, A. Huepers and A.J. Kopf revised the manuscript. A. Kopf supervised and funded the project.

Supplementary materials

Table 4: Summary of experiments.

The comprehensive experimental data table is uploaded to <https://zenodo.org/> and can be found under the digital object identifier: 10.5281/zenodo.3490686.

2.4 Manuscript 3 (in preparation): Frictional healing of the Nankai frontal thrust and megasplay fault- Bridging the gap between laboratory and in-situ data

A. Roesner¹, M.J. Ikari¹, K. Stanislawski¹, A.J. Kopf¹

¹MARUM - Center for Marine Environmental Sciences, University Bremen, Germany

Abstract

Every 4 – 15 months repeating slow slip events (SSEs) accompanied with very low frequency tremor have been documented along the plate boundary thrust in the Nankai Trough. Repeating SSEs, similar to regular earthquakes, need a re-strengthening mechanism within the interseismic period to release stress in a repetitive nature. Frictional healing experiments on Nankai Trough megasplay fault and frontal thrust zone sediments were performed in a rotary shear apparatus with hold times up to 106 s. Tests were run at two shearing rates (0.01 and 10 $\mu\text{m/s}$) representing the upper and lower bound of documented SSEs slip velocities in the Nankai Trough. Log-linear healing rates of the megasplay fault sediment are ~ 2.5 larger than healing rates of the frontal thrust zone. The low velocity healing experiments are better described by a power-law relation than by the log-linear fit, resulting in larger healing at extrapolated SSE recurrence intervals than by log-linear law. Stress drops derived from extrapolated laboratory healing rates exceed SSE stress drops by one to two orders of magnitude. The discrepancy can be either explained by an overestimation of the healing rate, overestimations of vertical normal stress on the plate boundary thrust or the underestimation of the seismic moment of the SSEs.

Introduction

Earthquakes are sudden releases of strain energy along a fault or a fault zone system accumulated often over decades or centuries. Considering geological time scales, earthquakes are repetitive events that can be described by an earthquake cycle, which can be subdivided into an interseismic and coseismic period (Kanamori and Brodsky, 2001). During the interseismic period, strain accumulates along the locked fault by plate convergence, whereas during the coseismic period the fault ruptures and releases the stored energy either as fracture, thermal or radiated energy (Kanamori and Rivera, 2006). Following a rupture event, the slip deficit accumulates again and loads the fault system. Repetitive rupture events at the same fault patch are only possible due to fault re-strengthening (healing) (Dieterich, 1972; Marone, 1998b; Marone and Saffer, 2015). Shallow fault healing inferred from repeated seismic surveys after the Mw 7.3 Landers earthquake on the Johnson Valley fault in California have been documented by Vidale and Li (2003). The phenomenon of frictional healing might be explained by contact area growth and/or chemical cementation between two (sliding) surfaces as a function of time which was analyzed in laboratory friction experiments (Dieterich, 1972; Dieterich and Kilgore, 1994; Marone, 1998b; Rabinowicz, 1951).

Laboratory derived healing rates can be determined in slide-hold-slide (SHS) shear experiments (Dieterich, 1972; Marone and Saffer, 2015). First, the sediment is sheared at a constant velocity until steady state. At steady state, the driving velocity is stopped for a defined time interval, referred to as hold time, until sliding is reinitiated. The resulting peak in shear strength, which exceeds the previous steady state strength, is interpreted as healing (Marone and Saffer, 2015). Many studies have shown, that healing follows a log-linear relationship with increasing hold time (e.g. Carpenter et al., 2016; Dieterich, 1972; Richardson and Marone, 1999). In most instances, experimental studies explore hold times between 3 and 10^4 s, which can be extrapolated to interseismic periods under the assumption of log-linear healing behavior (Marone, 1998b). Testing at unconventionally long hold times of up to 10^6 s revealed accelerated healing rates in fault zone and wall rock core samples from the San Andreas Fault Observatory at depth (SAFOD) (Ikari et al., 2016b). Healing at these long hold times is better described by a power-law relation (Ikari et al., 2016b). Accelerated healing rates enable faults to re-strengthen much faster than expected from the originally proposed log-linear law, and thus reducing predicted recurrence intervals between consecutive earthquakes. Deviations from simple log-linear healing are also shown by numerical simulations of fault healing of up to 3000 days by (Marone, 1998b), where differences between short and long term healing were identified. The differences in short and long term healing are comparable to changes in stress drop magnitudes for repeating earthquakes measured at the San Andreas fault (Marone,

1998b; Marone et al., 1995; Vidale et al., 1994). Lower healing rates and stress drops up to 100 days were explained by afterslip on the fault zone (Marone, 1998b).

During the last two decades a variety of fault slip modes between plate rate and coseismic earthquake slip, such as slow slip events (SSEs), very low frequency earthquakes (VLFs), episodic tremor and slip and low frequency earthquakes were explored by geodetic and seismological studies. Compared to ordinary earthquakes these events have much longer durations but occur often together at the same time and on the same fault patch (Araki et al., 2017; Ide et al., 2007). Similar to ordinary earthquakes, these events can show a repetitive nature following a cyclic behavior of strain accumulation and release.

Araki et al. (2017) documented reoccurring SSEs in shallow portions of the Nankai Trough subduction zone by pressure transients measured with deep sea borehole observatories (Figure 22). Very low frequency tremor recorded by ocean bottom seismometers accompanied the SSEs (Araki et al., 2017) (Figure 22). The SSEs last for days to several weeks and recur every 4 to 15 months. Araki et al. (2017) reports a period of 8 – 15 months between repetitive SSEs but the shortest recurrence interval is 4 months based on the data they provided. These events were explained by 1 – 4 cm of slip on the plate interface beneath the inner accretionary prism (Araki et al., 2017). Similar to regular earthquakes the fault zone has to re-strengthen between repeating SSEs to release energy. In addition to in-situ measurements, laboratory SSEs have been documented in frictional experiments in Nankai Trough megasplay fault gouge sheared at a plate-rate velocity (Ikari, 2019). The relative short SSE recurrence interval compared to regular earthquakes of up to 15 months makes the strengthening mechanism and resulting SSE stress drop an interesting target for long-term SHS laboratory healing studies on Nankai Trough fault zone sediment.

In this paper, we present SHS experiments performed in a ring shear apparatus sheared at slip velocities comparable to SSEs velocities in the Nankai Trough subduction zone. Time-dependent frictional strengthening of Nankai Trough megasplay fault and frontal thrust zone sediments was measured for hold times up to 10^6 s. By means of a power-law and log-linear fit, healing rates were extrapolated to hold times equivalent to recurrence intervals of documented SSEs in the Nankai Trough, allowing to compare laboratory derived stress drops to those derived for the SSEs. This analysis bridges the gap between laboratory small-scale experiments and in-situ long-term measurements.

Geological setting and experimental samples

The Nankai Trough is one of the best-studied subduction zones in the world and has been target of multiple Integrated Ocean Drilling Program and International Ocean drilling program

(IODP) expeditions. Along the Nankai Trough the Philippine Sea Plate subducts northwestward beneath the Amurian Microplate with a convergence rate of ~ 6.5 cm/a (Miyazaki and Heki, 2001; Seno et al., 1993) (Figure 22). Historical sources document earthquake activity for over 1300 years along the Nankai Trough. In 1944 and 1946 the last two megathrust earthquakes (Tonankai Mw 8.1 and Nankaido Mw 8.3) hit the Japanese coast (Ando, 1982; Kikuchi et al., 2003).

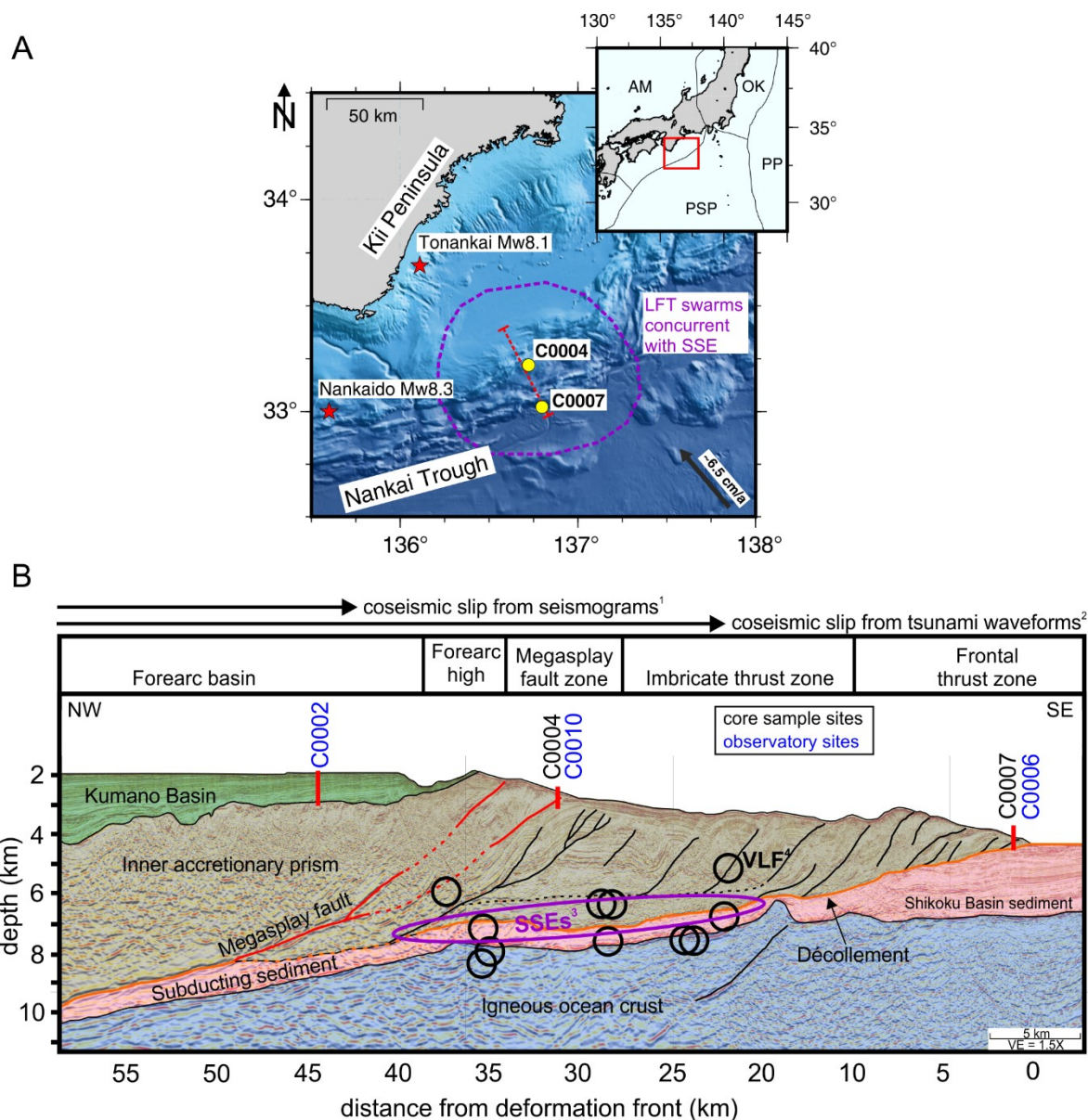


Figure 22: (A) Bathymetric map showing drill sites as well as the location of the seismic cross section (red dashed line). Red stars indicate epicenters of the last two megathrust earthquakes in the region. Am – Amurian Plate, OK – Okhotsk Plate, PSP – Philippine sea Plate and PP – Pacific Plate, LFT – Low frequency tremor (B) Interpreted seismic cross section with coseismic slip propagation inferred from seismograms (Kikuchi et al., 2003) and tsunami waveforms (Tanioka and Satake, 2001). Documented VLFs by Sugioka et al. (2012) and SSE by Araki et al. (2017).

These earthquakes ruptured most likely portions of the plate boundary thrust and a major out-of-sequence thrust fault system (Kikuchi et al., 2003; Sakaguchi et al., 2011; Tanioka and

Satake, 2001). The rupture area of the megathrust earthquakes coincides spatially with the SSEs documented by Araki et al. (2017) (Figure 22). SSEs were detected by pressure perturbations measured with permanent Long Term Borehole monitoring systems (LTBMS) installed at C0002 and C0010. Nowadays, also Site C0006 is equipped with a LTBMS. All LTBMS are connected to a real-time cabled network.

Along the Nankai Trough an extensive >100 km wide accretionary prism has been formed that can be subdivided in an inner and an outer prism (Figure 22 B). The inner prism consists of older accreted sediments, which are separated by an out-of-sequence thrust fault, often named the “megasplay fault”, from the younger outer prism sediments (Kimura et al., 2007; Park et al., 2002). The megasplay fault branches upward from the plate boundary thrust fault 55 km landward from the deformation front. In our study we tested fault zone sediment from IODP Sites C0004 (megasplay fault) and C0007 (frontal thrust zone). At Site C0004, a brecciated and fractured zone composed of ash-bearing hemipelagic mud with scattered volcanic ash layers from 256 to 315 mbsf was interpreted as the megasplay fault zone (Expedition 316 Scientists, 2009a). The fault bounded package on average consists of 60 % clay minerals, 20 % quartz, 18 % feldspar, and 2 % calcite (Expedition 316 Scientists, 2009a). At Site C0007, a zone of concentrated deformation was cored at a depth of 399 – 446 mbsf. These accreted Shikoku basin sediments are on average composed of 65 % clay minerals, 20 % quartz and 15 % feldspar (Expedition 316 Scientists, 2009c). Table 5 summarizes the composition of the two tested samples (C0004D29R03 and C0007D28R02) from ~276 mbsf (C0004) and ~429 mbsf (C0007). Sample mineralogical composition was determined by X-Ray-Diffraction (XRD) measurements in a Phillips X’Pert Pro multipurpose diffractometers (for detailed information, Ikari et al., 2016b).

Methods

Fault zone sediments were powdered with a mortar and pestle and sieved to a grain size diameter <180 µm. The powder was dried and afterwards mixed in a ratio of ~2:1 with deionized water to form a stiff paste, which was pressed into the sample cell. The initially approximately 6 mm thick samples were sheared in an annular sample holder with an inner diameter of 10 mm and outer diameter of 25 mm at room temperature (Figure 23 E). Simulated sea water with a salinity of 3.5 % flooded the sample holder that the sample is fully submerged to imitate ocean conditions. The sample is hydraulically connected with the water reservoir.

The experiments were performed in a rotary shear apparatus manufactured by Wykenham Ferrance capable of shear speeds from ~0.001 to 1000 µm/s and a maximum vertical stress up to 4 MPa (Figure 23 E) (Kopf, 2013). The fault zone samples were consolidated to the

maximum of 4 MPa effective normal stress by incremental loading via a lever-arm system to simulate shallow depth conditions along the plate boundary thrust fault. The pore water pressure was not controlled, but assumed to be hydrostatic due to sufficient excess pore water drainage when changes in vertical displacement became negligible. SHS experiments were performed at different sliding velocities (10 and 0.1 $\mu\text{m/s}$) representing the potential lower and upper SSEs velocities in the Nankai Trough subduction zone (Araki et al., 2017). Every experiment started with a “run-in” to establish steady-state frictional sliding on a mature shear surface, followed by the SHS sequence (Figure 23). After shearing with a constant velocity, the motor was held stationary (0 $\mu\text{m/s}$) for a defined time interval t_h (hold time) before shearing was resumed at the initial velocity (Figure 23). We tested hold times between 10 and 10^6 s.

The shear strength of rocks and sediment is often expressed by the Coulomb-Mohr failure criterion:

$$\tau = \mu * \sigma'_n + c \quad (19)$$

where c is the cohesion, μ coefficient of internal friction, σ'_n is the effective normal stress and τ is the shear stress at failure (Handin, 1969). Cohesion is often neglected in experimental friction studies, but recent studies showed that cohesive strength can be significant on mature clay rich shear surfaces (Ikari and Kopf, 2015, 2011). The measured shear stress includes both frictional and cohesive strengths, thus the coefficient of sliding friction μ_s also does not distinguish between them:

$$\mu_s = \frac{\tau}{\sigma'_n} \quad (20)$$

Figure 23 D illustrates the frictional response of a SHS sequence where the sample relaxes during the hold period due to elastic relaxation of the rotary shear apparatus and creep within the sample (e.g. Carpenter et al., 2016). The frictional decrease due to relaxation creep is described by the difference between frictional strength at steady state pre-hold and at the end of the hold period, expressed as $\Delta\mu_c$ (Figure 23 D). In contrast, frictional healing $\Delta\mu$ is quantified by the difference between steady state friction pre-hold and peak friction upon re-shear post-hold. Both $\Delta\mu_c$ and $\Delta\mu$ were evaluated as functions of time to derive frictional healing and relaxation rates.

We derived a frictional healing rate β by describing our data with a log-linear relationship in the form of

$$\Delta\mu = \beta \log_{10}(t_h) \quad (21)$$

(e.g. Dieterich, 1972). We also computed creep relaxation rates by replacing $\Delta\mu$ with $\Delta\mu_c$ (e.g. Carpenter et al., 2016). In addition, we fitted the power-law for phyllosilicate rich sediment proposed by Ikari et al. (2016b) to our data:

$$\Delta\mu = At_h\omega \quad (22)$$

where ω is the healing rate and A an empirical constant.

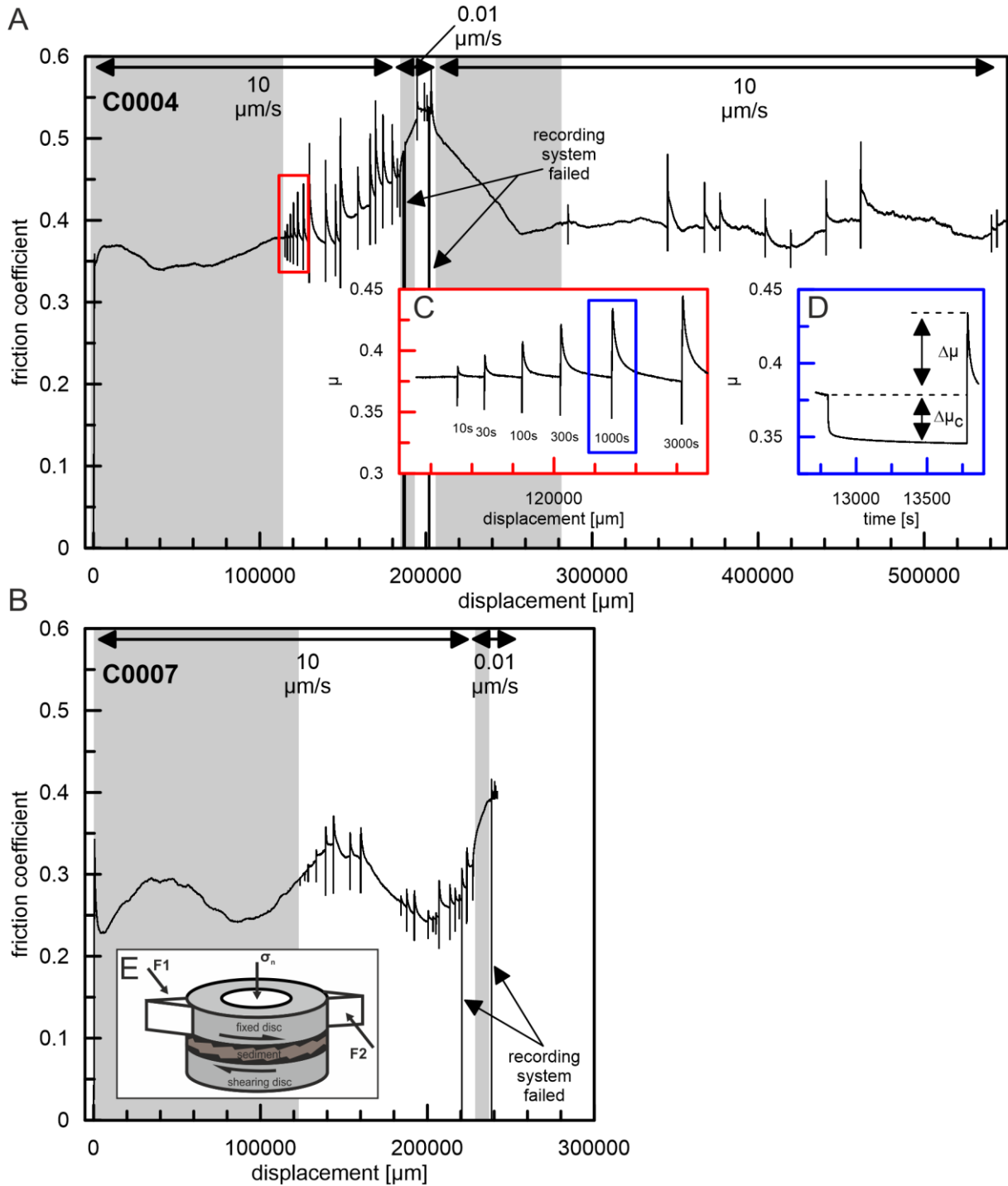


Figure 23: (A) and (B) showing experimental data for fault zone sediment from IODP Site C0004 and C0007. Gray shadings illustrate the “run-in” whereas white illustrates the SHS sequences. (C) Zoom of the first six holds indicates $\Delta\mu$ increases with hold time. (D) Experimental data of a 1000 s hold showing measurement of creep relaxation and frictional healing. (E) Schematic diagram of the rotary shear apparatus. Powdered fault gouge is sandwiched between grooved steel forcing rings and consolidated from the top. $F1$ and $F2$ = force sensors, σ_n = normal load.

Equally, we computed creep relaxation rates by replacing $\Delta\mu$ with $\Delta\mu_c$. For all our experiments, we calculated the coefficient of determination R^2 to evaluate the goodness of the fit to our experimental data.

Richardson and Marone (1999) documented experimentally a displacement dependence on $\Delta\mu$, where healing for equal hold times increased with cumulative displacement. To account for this effect we performed 100 s reference holds at the beginning, in the middle, and at the end of each experiment. Our 100 s reference holds show no systematic effect on frictional healing $\Delta\mu$ with cumulative displacement, thus we conclude $\Delta\mu$ is independent of displacement in our experiments.

Results

The megasplay fault sample (C0004) exhibits a small initial peak in friction between 0.5 – 1 mm of displacement followed by a strain hardening trend superimposed on the SHS sequence at 10 and 0.01 $\mu\text{m/s}$. No strain hardening was observed for the SHS sequence after 250 mm of displacement (Figure 23 A). In contrast, the frontal thrust zone sample (C0007) shows a more pronounced peak friction followed by frictional oscillation superimposed on the dataset (Figure 23 B). This variability is an experimental artefact caused by the rotary shear apparatus due to misalignment between the lower and upper sample holder (Fig.2 E). We therefore express the coefficient of sliding friction as a range (Table 5). The background frictional strength of megasplay fault sediment is 0.34 – 0.44 at 10 $\mu\text{m/s}$ to 0.5 – 0.54 at 0.01 $\mu\text{m/s}$. Generally, the frontal thrust zone is weaker with a coefficient of sliding friction between 0.23 – 0.33 at 10 $\mu\text{m/s}$ and 0.36 – 0.40 at 0.01 $\mu\text{m/s}$ (Figure 23 A&B, Table 5).

Both frictional healing $\Delta\mu$ and creep relaxation $\Delta\mu_c$ increase with hold time and sliding velocity (Figure 23 C and 24). The log-linear healing rates of the megasplay fault sediment ($\beta = 0.025$ and 0.01) exceed the healing rates of the frontal thrust zone sediment ($\beta = 0.009$ and 0.005) (Figure 24), with coefficients of determination $R^2 > 0.90$ for all log-linear fits (Table 5). Creep relaxation rates show a larger variability in R^2 (0.57 – 0.91) than the healing rates. The two fault zone samples show larger log-linear relaxation at 10 $\mu\text{m/s}$ than at 0.01 $\mu\text{m/s}$. The healing data at a sliding velocity of 0.01 $\mu\text{m/s}$ are better fitted with the power-law relation generating $R^2 > 0.97$, whereas at a sliding velocity of 10 $\mu\text{m/s}$ the goodness of fit is similar to the log-linear relation. For creep relaxation, the power-law provides always a better fit with larger R^2 (Figure 24 & Table 5).

At recurrence intervals of documented SSEs along the Nankai Trough, the extrapolated laboratory derived healing $\Delta\mu$ varies between 0.05 – 0.15 for 0.01 $\mu\text{m/s}$ and between

0.15 – 0.26 for 10 $\mu\text{m/s}$ at site C0004. At site C0007 extrapolated healing for SSEs recurrence intervals are much smaller 0.02 – 0.07 for 0.01 $\mu\text{m/s}$ and 0.05 – 0.08 for 10 $\mu\text{m/s}$.

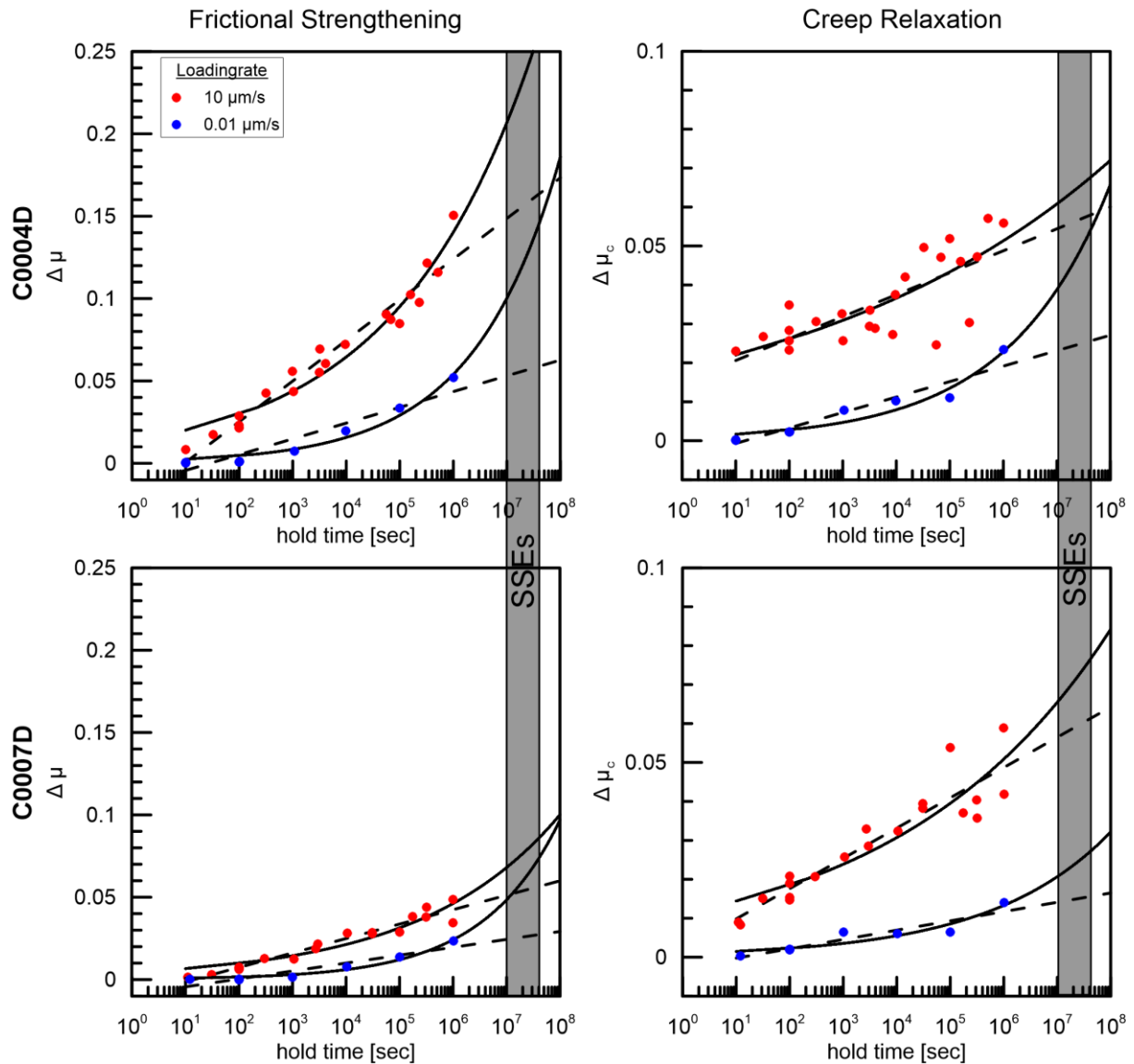


Figure 24: SHS parameters $\Delta\mu$ and $\Delta\mu_c$ are plotted against the logarithm of hold time. The log-linear and power-law are fitted to the data and are extrapolated to the recurrence interval (4 – 15 months) of natural occurring SSEs in the Nankai Trough subduction zone. Coefficient of determination for the fits is given in Table 5. All test were done at 4 MPa effective normal stress.

Discussion

Frictional strength and healing rates

Frictional properties of fault gouge are primarily controlled by sediment composition. Recent studies show that phyllosilicate content often controls frictional strength, stability and healing rate (e.g. Brown et al., 2003; Byerlee, 1978; Carpenter et al., 2016). Surprisingly, the coefficient of sliding friction increases with phyllosilicate content in our two samples (Table 5). The mineral

composition for both samples is nearly identical, only the phyllosilicate and amorphous silica content differs. Thus, the amorphous silica has to have an influence on the frictional properties of our sample. Altered vitric ash is abundant in Nankai Trough input and accretionary prism sediments accountable for high amorphous silica contents in XRD measurements (Hüpers et al., 2015). The frontal thrust zone sample is characterized by ~40 % phyllosilicates and over 20 % amorphous silica (Table 5). Vitric ash was documented in smear slides above and below the tested samples. The frontal thrust zone sediment shows a lower coefficient of sliding friction compared to the phyllosilicate rich megasplay fault sediment (Figure 23). This contradicts results from Brown et al. (2003) who measured high friction coefficients in vitric ash bearing samples from the Ashizuri and Muroto drilling transect. Vitric ash alteration products have small friction coefficients, thus an explanation could be the alteration of vitric ash in a two-stage process to silica gel and in the end to smectite (Berger et al., 1987; Hodder et al., 1993). The measured coefficient of sliding friction alternates or shows a strain hardening trend in both experiments with displacement (Figure 23). The coefficients of sliding friction at 10 $\mu\text{m/s}$ are in good agreement with megasplay fault and frontal thrust zone sediments tested under various normal stress in a direct shear configuration by *Roesner et al under review*. The friction coefficients measured at 0.01 and 10 $\mu\text{m/s}$ suggest velocity weakening behavior.

Log-linear healing and creep relaxation rates scale with frictional strength, which is in agreement with previous studies (Carpenter et al., 2016). The stronger megasplay fault sample (C0004) shows higher healing and creep relaxation rates compared to weaker frontal thrust zone sample (C0007). Consequently, the mineralogical composition controls to a first order the healing and relaxation behavior of the fault gouges. The observed log-linear healing rates are high for phyllosilicate-dominated sediment. The observed healing rates of $\beta = 0.025$ (C0004) and $\beta = 0.009$ (C0007) at 10 $\mu\text{m/s}$ are up to three times larger than documented healing rates for phyllosilicate rich fault gouge tested under 20 MPa effective normal stress and 10 $\mu\text{m/s}$ by Carpenter et al. (2016). Previously, published log-linear healing rates ($\beta = 0.005 - 0.008$) derived from C0004 fault gouge and wall rock sediments tested in a biaxial configuration at 25 MPa and a sliding velocity of 11 $\mu\text{m/s}$ are 3 to 5 times smaller than in our measurements (Ikari et al., 2012). In contrast, C0007 healing rates ($\beta = 0.003 - 0.007$) measured under the same testing conditions are only slightly smaller than our measured healing rates. The observed inverse correlation of log-linear healing rates and effective normal stresses is consistent with experimental data on calcite rich sediments showing that increasing effective normal stress reduces healing (Carpenter et al., 2015a; Tesei et al., 2014). The difference in the megasplay fault sample is much more pronounced than for the frontal thrust zone sample. Therefore, we speculate that the effect of effective normal stress on healing rates is larger within phyllosilicate rich sediment.

Our data show that especially for low sliding velocities (0.01 $\mu\text{m/s}$) time dependent friction is better described by a power-law relationship with hold time. Frictional healing and creep relaxation fits show larger R^2 for a power-law fit than for a log-linear fit (Table 5). It is not clear which material properties cause this enhanced healing at long hold times and low sliding velocities. Similar frictional healing behavior has been observed by Ikari et al. (2016b) for SAFOD wall rock and fault gouge samples, but in contrast, to our observations their creep relaxation rates still follow a log-linear law. In addition, Carpenter et al. (2015a) observed power-law healing behavior in calcite rich sediment at 1 MPa effective normal stresses at hold times up to 10^4 s. Healing behavior documented in high-speed velocity SHS experiments do not follow a log-linear law either (Yao et al., 2013). At seismic slip rates, healing could be divided in an initial rapid healing (an order of magnitude larger than in our experiments) explained by rapid cooling of the gouge and an gradual healing following the log-linear relationship. Based on our results and the previously cited studies we conclude that fault zone healing processes are more complex and cannot be described by a single log-linear healing law. Especially at low effective normal stress and low sliding velocity, healing of phyllosilicate rich sediment is better described by a power-law fit. The possibility of power-law healing could have a significant effect on the expected time dependent stress changes of a seismogenic fault system. Healing rates are used to explain recurrence intervals between repetitive slip events or to calculate stress drops. “Traditionally” log-linear healing behavior would underestimate healing when a power-law relation is the more appropriate fit to the data. This inaccuracy might overestimate recurrence intervals or underestimate the stress drop (Ikari et al., 2016b).

Bridging the gap between in-situ and laboratory measurements

Along the plate boundary thrust fault eight repetitive SSEs have been documented by pressure transients in borehole observatories installed along the Kumano drilling transect between 2011 and 2016 (Araki et al., 2017) (Figure 22 B). Araki et al. (2017) used a simple dislocation model to define source parameters such as fault displacement, slip patch size and source locations. The observed pressure transients could be modelled by 1 – 4 cm slip on the plate boundary thrust fault on a rectangular 400 – 1600 km^2 large patch. Based on the modeled source parameters a seismic moment of $\sim 4 \cdot 10^{16}$ – $\sim 3.2 \cdot 10^{17}$ Nm was calculated (Araki et al., 2017). We calculate an in-situ stress drop $\Delta\sigma$ based on the proposed source parameters by Araki et al. (2017). The average stress drop was calculated following the expression by (e.g. Kanamori and Anderson, 1975; Kanamori and Brodsky, 2004):

$$\Delta\sigma = C \frac{M_0}{A^{\frac{3}{2}}} \quad (23)$$

where M_0 is the seismic moment, A is the rupture area and C depends on the shape of the rupture patch. We used $C = 2.53$ for a rectangular patch with an aspect ratio of 1 (Noda et al., 2013). $\Delta\sigma_{SD}$ is of the order of 0.013 MPa comparable to the lower limit of globally compiled SSE stress drops by Gao et al. (2012) and to the megasplay fault laboratory SSEs reported by Ikari (2019).

Based on our experimental healing data we calculate predicted stress drops ($\Delta\mu * \sigma'_v$) as a function of recurrence time for both the log-linear and the power-law healing relation up to 100 months (Figure 25). For that we used an averaged vertical effective normal stress σ'_v of 6 MPa proposed by Kitajima and Saffer (2012) for the overpressured zone along the plate boundary thrust, which spatially overlaps with hypocenters of very low frequency earthquakes (Sugioka et al., 2012) and the simulated fault slip for SSEs by Araki et al. (2017). Derived stress drops for the megasplay fault zone are larger than for the frontal thrust zone because of the larger healing rates (Figure 25). At low recurrence intervals, log-linear healing predicts slightly higher stress drops than the power-law healing relation, whereas at recurrence intervals of the repeating SSEs power-law healing inferred stress drops are much larger than those of log-linear healing. Consequently, SSE stress drop calculations derived from log-linear healing are lower bounds and power-law healing mark the upper bound. The in-situ stress drop derived from the dislocation model is one to two orders of magnitudes smaller than the stress drops calculated from the experimental healing data (Figure 25).

Differences in stress drops could be explained by the low effective vertical stress of 4 MPa applied to the sample. Higher effective normal stresses, closer to in-situ conditions proposed by Kitajima and Saffer (2012), would reduce the healing rate (Carpenter et al., 2015a; Tesei et al., 2012). Calculated stress drops with the healing rates proposed by Ikari et al. (2012) derived at 25 MPa effective normal stress for megasplay fault and frontal thrust zone samples are still one order of magnitude higher than the in-situ stress drops derived from the seismic moment analysis. Reducing the vertical effective stress from 6 to 1 MPa reduces the calculated stress drops by approximately one order of magnitude being in the range of the in-situ stress drops. On the other hand, the seismic moments derived by Araki et al. (2017) are based on a simple dislocation model using a single tapered slipping patch. The location of the slipping patch was determined via a forward model until model parameters best agreed with the borehole pressure data. The limited amount of data (two locations) did not allow for an inversion because it would have been a severely underdetermined problem. Consequently, the distribution of slip is most likely more complex and might be not well described by the simple model. A larger seismic moment and therefore a larger stress drop would be expected from a larger fault displacement or a larger fault patch size. In addition, a more rigid sediment would increase the seismic stress drop but Araki et al. (2017) used a rigidity of 10 GPa which is already an upper bound for

shallow accretionary prism sediment (Jeppson et al., 2018). Most likely, an interplay of all describe reasons above contribute to the discrepancy of laboratory and in-situ SSE stress drop.

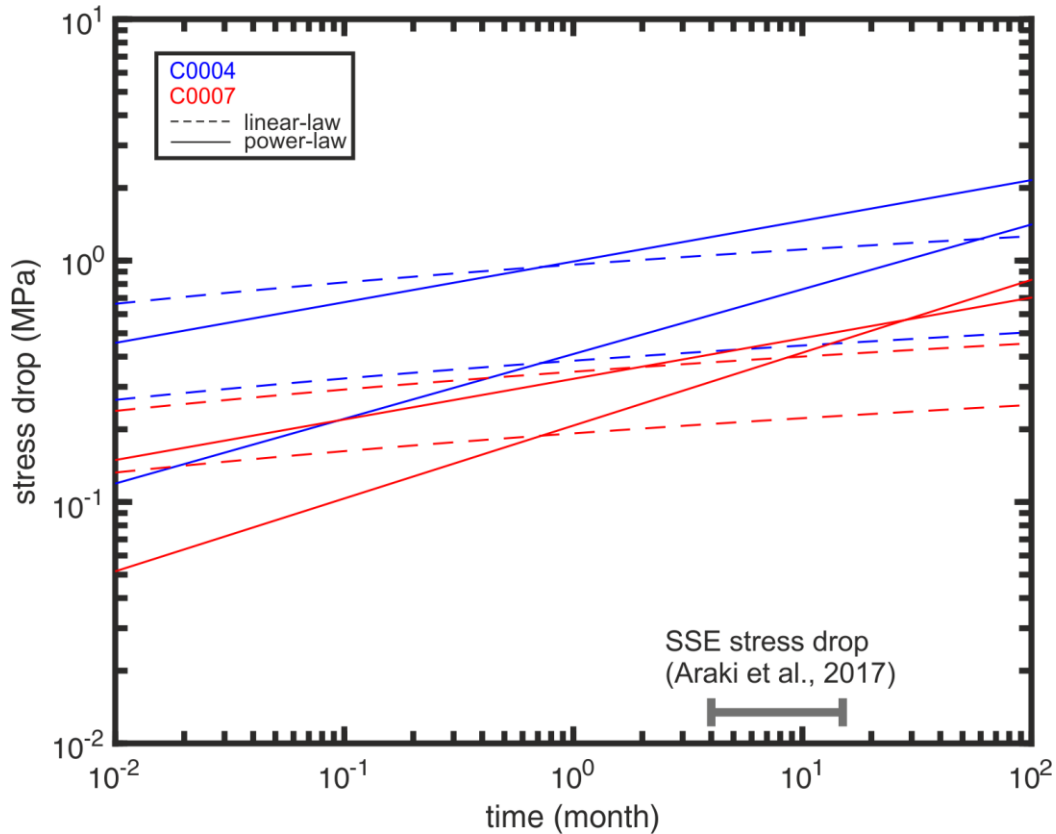


Figure 25: Predicted SSE stress drops as a function of recurrence interval based on the log-linear and power-law healing relations on megasplay fault and frontal thrust zone samples. Blue line in-situ stress drops based on seismic moment calculated by Araki et al. (2017). Experimental derived stress drops are an order of magnitude higher than in-situ derived stress drops.

Conclusions

We show that the coefficient of sliding friction is higher in the megasplay fault sample than in the frontal thrust zone samples. Both samples show higher coefficient of sliding friction for the lower bound SSE velocity tested. The classic log-linear law, mostly used to describe healing and creep relaxation behavior, does not necessarily describe long-term laboratory healing data derived from hold times up to 10^6 s sufficiently. Especially at low sliding velocities and low effective normal stresses, experimental SHS data are better fitted with a power-law than with a log-linear law. The power-law shows accelerated healing for long hold periods, suggesting that faults regain strength faster within the interseismic period than expected from log-linear healing. The accelerated healing would increase the expected stress drop of repeating SSEs. SSE stress drops are one to two orders of magnitudes lower than the stress drop predictions based on laboratory healing experimental data. This discrepancy arises most likely due to an

interplay of various reasons i) overestimated laboratory healing rates ii) overestimated effective vertical stress on the plate boundary fault and iii) underestimated seismic moment of in-situ SSEs.

Table 5: Sample details and experimental data in bold larger R^2 .

Sample	velocity ($\mu\text{m/s}$)	log-linear					power-law					composition			
		μs	β	R^2	β_c	R^2	$\Delta\mu_{SSE}$	ω	A	R^2	ω_c		A_c	R^2	$\Delta\mu_{SSE}$
C0004	10	0.34- 0.44	0.025	0.95	0.006	0.57	0.151- 0.166	0.1686	0.0137	0.95	0.0735	0.0186	0.60	0.207- 0.261	50 % clays, 15 % quartz, 17 % feldspars, 4 % carbonates
	0.01	0.50- 0.54	0.010	0.91	0.004	0.91	0.056- 0.062	0.2683	0.0013	0.97	0.2296	0.0009	0.94	0.098- 0.141	
C0007	10	0.23- 0.30	0.009	0.95	0.008	0.86	0.053- 0.058	0.1682	0.0045	0.91	0.1097	0.0112	0.82	0.068- 0.085	39 % clays, 13 % quartz, 17 % feldspars, 2 % carbonates, 22 % amorphous silica
	0.01	0.36- 0.40	0.005	0.90	0.002	0.86	0.026- 0.029	0.3019	0.0004	0.97	0.1922	0.0009	0.88	0.052- 0.078	

Acknowledgements

We thank A.M. Eijsink and A. Hüpers for fruitful discussions, which significantly improved the manuscript. In this work samples from IODP expeditions were tested, thus we would like to thank the crew and the scientist onboard D/V Chikyu and all funding countries. This work was supported by the European Research Council (ERC) under the European Union's Horizon 2020 research and innovation programme (grant agreement No 714430 to MJI) as well as from the University of Bremen and the Deutsche Forschungsgemeinschaft.

Author Contributions

A. Roesner and K. Stanislowski designed the project and planned the experimental program. K. Stanislowski performed the “fast” A. Roesner the “slow” sliding velocity SHS experiments in the rotary shear apparatus. A. Roesner processed the data, prepared the figures, wrote the first version of the manuscript, and led the revision process. K. Stanislowski, M.J. Ikari, and A.J. Kopf revised the manuscript. A. Kopf supervised and funded the project.

3 Long-term borehole monitoring studies

3.1 Introduction

Long-term in situ hydrologic and geophysical measurements in borehole observatories have been recognized as a key element in the IODP Science Plan between 2013 and 2023. Data time series provided by long-term observatories are of major importance toward understanding strain and fault slip at plate boundaries, the fluxes of volatiles and chemical budgets at subduction systems, heat loss from the earth, and the role of fluids in mechanical, chemical, biological, and thermal processes beneath the seafloor. Over the last three decades, long-term observations of pore pressure, temperature, and fluid chemistry in sealed ODP/IODP boreholes have produced a wealth of data that have significantly advanced our understanding of subseafloor deformation and hydrogeology. For example, monitoring of pore pressure and temperature coupled with continuous sampling of pore waters for chemical analysis have provided constraints on fluid flow systems associated with globally significant transport of heat and solutes (e.g. Becker and Davis, 2004; Davis and Becker, 2001; Davis and Becker, 1994; Fisher et al., 1997). Direct measurement of ambient pore pressure attested the key role of fluids in affecting fault mechanical behavior (e.g. Becker et al., 1997; Foucher et al., 1997). The analysis of tidally driven pressure changes has provided a powerful means to quantify formation and fluid elastic and hydrologic properties in many settings – and potentially to resolve changes in formation properties associated with strain events (e.g. Davis et al., 2000; Wang et al., 1998; Wang and Davis, 1996).

3.1.1 History of borehole observatories in ocean drilling

Long-term borehole monitoring in ocean drilling can be traced back into the late 80s, where the initial 'Circulation Obviation Retrofit Kit' (CORK) had literally been sketched on a dinner napkin. At that time, it had been recognized that drilling disturbances strongly affect the thermal and hydrological system of the formation surrounding the borehole. Reliable measurements of formation temperature and pressure are only possible in sealed 'equilibrated boreholes' that prevent exchange between ocean bottom water and surrounding formation. Figure 26 A shows an early conceptual design of a borehole seal sitting inside the casing and re-entry cone, whereas Figure 26 B shows a complete CORK configuration measuring temperature and pressure in oceanic crust covered with sediment. The first CORK was installed on ODP Leg 139 in summer 1991 in a sediment filled valley of the northern Juan de Fuca Ridge (Davis et

al., 1992). This 'original' CORK is a single seal CORK consisting of a CORK body sealing the casing hanger system at the top of borehole, a pressure housing comprising data logger and batteries, pressure gauges and a sensor string in the sealed borehole. Initially two pressure gauges were installed one above the pressure housing as a reference pressure measuring oceanographic noise and one below measuring averaged fluid pressure in the sealed borehole. A tubing connecting the sealed borehole with a valve at the wellhead allows fluid sampling via a submersible. Depending on the ocean floor setting a completely cased borehole with perforated sections is used in a subduction zone setting, whereas in oceanic crust covered by sediment casings are only used in upper sedimentary section into uppermost basement.

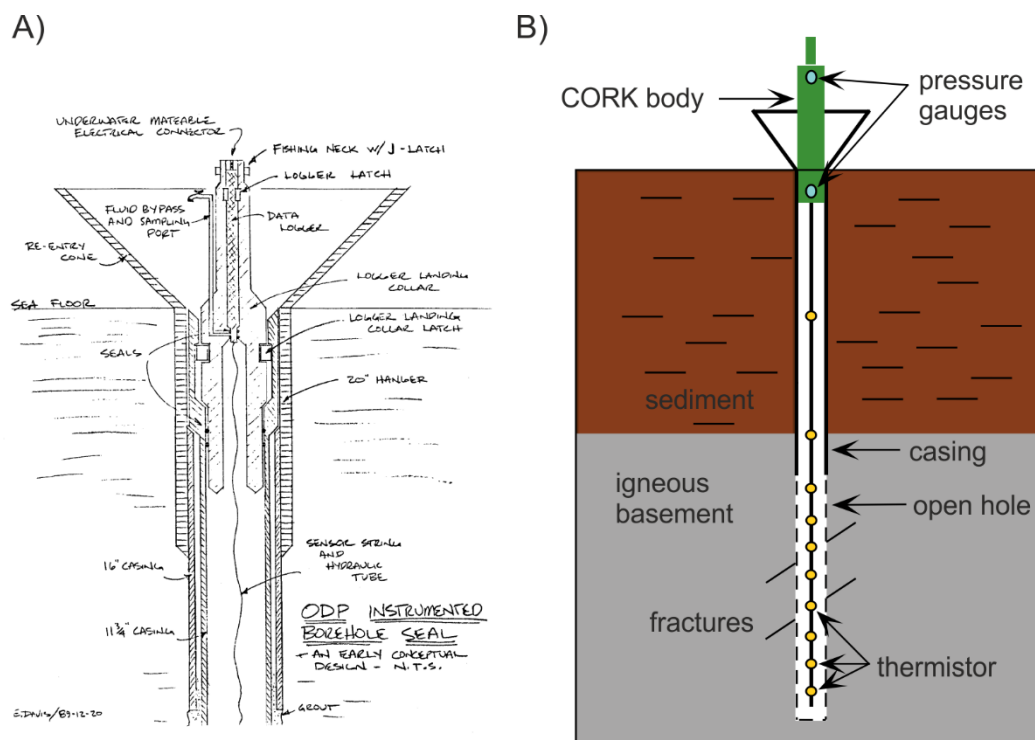


Figure 26: (A) Early conceptual design of a borehole seal from October 1989. (B) Single seal CORK configuration including pressure gauges and thermistor string (modified from Becker and Davis, 2005).

The single seal CORK had the shortcoming of measuring averaged formation pressure signals from the entire open hole or perforated casing sections. The advanced CORK and the CORK-II are the next generation CORKs capable of measuring formation pressure in multiple separately isolated intervals (Jannasch et al., 2003; Shipboard Scientific Party, 2002). Multilevel monitoring is achieved by inflatable packers attached outside to the casing (advanced CORK) or by inflatable packers attached to the instrument hanger (CORK-II) sitting inside the casing.

The original, advanced and CORK-II requires operational time on a drillship and to overcome this disadvantage the wireline CORK was developed. It can be set up by a multifunctional research vessel in a previously drilled reentry hole. The wireline CORK is also equipped with

multi-packers to isolate different formation intervals (Becker et al., 2004; Becker and Davis, 2005).

All CORKs have in common an underwater mateable connector installed at the wellhead for data download and reprogramming of the data logger. This can be done either with a submersible or with a remotely operated vehicle.

Previously described CORK designs were developed during the ODP phase that began in 1985 and ended in 2004. More recent long-term borehole monitoring system developments include the SmartPlug and GeniusPlug that were installed during the subsequent IODP phase (Kopf et al., 2011b). The SmartPlug is an autonomous borehole observatory that is installed immediately beneath a retrievable casing packer seal. The instrumental reference pressure sensor measures above the casing packer, whereas the second pressure sensors measures the formation pressure beneath. In addition, temperature is monitored beneath the casing packer. The packer is placed immediately above the perforated casing to minimize the borehole volume. The GeniusPlug is structurally identical to the SmartPlug but hosts also an OsmoSampler unit at the bottom of the instrument (Kopf et al., 2011b) for long-term autonomous fluid sampling. OsmoSamplers utilize the principal of an osmotic pump for fluid sampling. Installation and recovery (for data download) is done by a drill ship.

A next generation of borehole observatories is termed Long-Term Borehole Monitoring System (LTBMS). These complex observatories are comparable to the CORK-II design (Kitada et al., 2013; Kyo et al., 2014; Saffer et al., 2017b). Similar to the CORK-II the LTBMS lands installed in a cased borehole is capable of multilevel pore pressure measurements, depending on the amount of packers used. In contrast to the CORK-II design, the LTBMS incorporates sophisticated downhole electronics and is also able to measure volumetric strain, tilt and seismic wave speed (Kinoshita et al., 2018b). The instrument package including a volumetric strainmeter, a tilt sensor, a three-component geophone, a broadband seismometer and a temperature digitizer is installed on an integrated instrument carrier that is part of the backbone of the observatory string. The instrument package is installed in the deeper portions of the borehole where they are cemented to provide a better coupling with the surrounding formation. A good coupling is important for the data quality and the signal to noise ratio because it prevents fluid flow in the borehole. Nowadays, three LTBMSs are operated in the real-time DONET network (Becker et al., 2018).

3.1.2 Borehole observatories along the Nankai Trough

Along the Nankai Trough subduction zone five long-term borehole observatories are presently in operation. Two advanced CORKs have been installed in 2001 along the Muroto transect and three LTBMS in 2010/16/18 along the Kumano transect (Figure 2).

Muroto drilling transect

Two advanced CORKs have been installed during ODP Leg 196 at Sites 808 and 1173 along the Muroto drilling transect. These two CORKs were installed in the toe of the accretionary prism and 12 km seaward in the incoming sediments. Multilevel pore water pressure measurements aim to understand hydrological properties and the state of the shallow accretionary prisms and the incoming sediments. At the toe, Site 808, a configuration with two packers and six screens should measure pore water pressure transients at the décollement and overlying sediments. A four packer configuration with five screens was implemented at Site 1173 spanning the sediments of the projected décollement (Mikada et al., 2002).

Strain events of different duration and magnitude have been resolved by the two CORKs (Davis et al., 2013; Davis et al., 2009; Davis et al., 2006). In 2004 a Mw 7.5 earthquake triggered co-seismic and post-seismic formation pressure increases indicating contraction in the incoming sediments at Site 1173. At the same time deformation caused dilation on the plate interface reflected by decreasing pore pressure just above the décollement at Site 808 (Davis et al., 2009). Pore pressure transients concurrent with VLFs have been observed at both sites (Davis et al., 2013). Triggered local slip following the Tohoku-Oki earthquake reveal a fragile stress state in the shallow accretionary prism close to the trench (Davis et al., 2009).

Kumano drilling transect

The LTBMSs are part of the long-term NanTroSEIZE operations aimed understanding the mechanical and hydrological behavior of the Nankai Trough subduction megathrust. The first LTBMS measuring pressure at four depth intervals was installed at Site C0002 in the Kumano Basin sediment and the underlying upper accretionary prism strata (Expedition 332 Scientists, 2011). The second LTBMS measuring pressure at three depth intervals was installed at Site C0010 at the megasplay fault (Kopf et al., 2017). The third LTBMS measuring pressure at two depth intervals was installed at Site C0006 in the overriding plate at the toe of the accretionary prism (Becker et al., 2018). Before the second LTBMS installation, the autonomous SmartPlug and GeniusPlug were installed at Site C0010 in the megasplay fault in 2009/10. Pore pressure monitoring along the Kumano transect focuses on three main scientific objectives: (i) document ambient pore pressures at several depth intervals, (ii) provide constraints on formation elastic

and hydraulic properties from the response to tidal loading at the seafloor, and (iii) record hydraulic transients related to strain and/or episodic fluid flow.

First scientific results were published by Hammerschmidt et al. (2013a) and Hammerschmidt et al. (2013b) based on the 15 month long pore pressure and temperature record from the SmartPlug. The observatory detected pressure transients associated with meteorological, seismological and tsunamigenic events. Passing seismic waves induced strain that might have increased the permeability of the formation (Hammerschmidt et al., 2013a). Hydraulic and elastic properties of the formation can be derived from the loading efficiency (attenuation factor of tidal signals in the formation compared to the seafloor). Based on this the hydraulic diffusivity could be determined which is larger than the measured hydraulic diffusivity in core samples, because of the presence of large scale fractures accounted for in the in-situ borehole measurement (Hammerschmidt et al., 2013b). No deformation event along the megasplay fault was captured within the short recording time.

GeniusPlug and LTBMS data are presented in the manuscripts shown in the following chapter. These results are based on much longer time series (~6 years) compared to the short SmartPlug time series and reveal deformation at different time scales.

3.2 Manuscript 4 (JGR published): Near-field observations of an offshore Mw 6.0 earthquake from an integrated seafloor and subseafloor monitoring network at the Nankai Trough, southwest Japan [co-authorship]

L. M. Wallace¹, E. Araki², D. Saffer³, X. Wang⁴, **A. Roesner**⁵, A. Kopf⁵, A. Nakanishi², W. Power⁴, R. Kobayashi⁶, C. Kinoshita⁷, S. Toczko², T. Kimura², Y. Machida², and S. Carr⁸

¹Institute for Geophysics, University of Texas at Austin, Austin, Texas, USA

²JAMSTEC, Yokohama, Japan

³Department of Geology, Pennsylvania State University, University Park, Pennsylvania, USA

⁴GNS Science, Lower Hutt, New Zealand

⁵MARUM, University of Bremen, Bremen, Germany

⁶Graduate School of Science and Engineering, Kagoshima University, Kagoshima, Japan,

⁷Disaster Prevention Research Institute, Kyoto University, Kyoto, Japan

⁸Bigelow Laboratory for Ocean Sciences, East Boothbay, Maine, USA

Abstract

An Mw 6.0 earthquake struck ~50 km offshore the Kii Peninsula of southwest Honshu, Japan on 1 April 2016. This earthquake occurred directly beneath a cabled offshore monitoring network at the Nankai Trough subduction zone and within 25 – 35 km of two borehole observatories installed as part of the International Ocean Discovery Program's NanTroSEIZE project. The earthquake's location close to the seafloor and subseafloor network offers a unique opportunity to evaluate dense seafloor geodetic and seismological data in the near field of a moderate-sized offshore earthquake. We use the offshore seismic network to locate the main shock and aftershocks, seafloor pressure sensors, and borehole observatory data to determine the detailed distribution of seafloor and subseafloor deformation, and seafloor pressure observations to model the resulting tsunami. Contractual strain estimated from formation pore pressure records in the borehole observatories (equivalent to 0.37 to 0.15 μ strain) provides a key to narrowing the possible range of fault plane solutions. Together, these data show that the rupture occurred on a landward dipping thrust fault at 9 – 10 km below the seafloor, most likely on the plate interface. Pore pressure changes recorded in one of the observatories also provide evidence for significant afterslip for at least a few days following the main shock. The earthquake and its aftershocks are located within the coseismic slip region of the 1944 Tonankai earthquake (Mw ~8.0), and immediately downdip of swarms of very low

frequency earthquakes in this region, illustrating the complex distribution of megathrust slip behavior at a dominantly locked seismogenic zone.

Introduction

Investigating earthquakes and contemporary plate boundary deformation at offshore subduction zones has been a perennial challenge, due to the technical limitations and great expense of undertaking continuous, real-time monitoring of such processes in the submarine environment. Recent devastating earthquakes and tsunami generated in the outer forearc of subduction zones, such as the 2011 Mw 9.0 Tohoku-Oki and 2004 Mw 9.2 Sumatra earthquakes, underscore the need to monitor active deformation and seismicity in these regions and to integrate these data into earthquake and tsunami analyses, as well as early warning systems (Lay and Kanamori, 2011). DONET (Dense Oceanfloor Network System for Earthquakes and Tsunamis) is a network of seismometers and absolute pressure gauges (APGs) installed on the seafloor offshore southwest Japan to monitor the Nankai Trough subduction zone (Kaneda, 2014; Kawaguchi et al., 2015) (Figure 27 and 28). DONET is used in Japan's tsunami and earthquake early warning system, and it represents one of the first dense offshore subduction zone monitoring networks to continuously stream data to land. Ocean bottom seismometers (OBS) enable better location of offshore earthquakes and aftershocks, while the APGs record seafloor pressure changes due to vertical deformation of the seafloor in earthquakes, as well as passage of tsunami waves. Two borehole observatories are also installed within the DONET footprint at Sites C0002 and C0010 (Figure 28), as part of the Integrated Ocean Drilling Program's (IODP; now the International Ocean Discovery Program) NanTroSEIZE project. The borehole observatories provide critical information on crustal deformation through changes in formation pore pressure, which can be used as a sensitive proxy for volumetric strain as well as a recorder of other hydrological, thermal, and deformation processes (Davis et al., 2009; Wang, 2004).

The Mw 6.0 Mie-ken Nanto-oki earthquake occurred ~50 km offshore the Kii Peninsula of southwest Japan at 02:39 UTC (11:39 A.M., local time) on 1 April 2016. The earthquake occurred directly beneath DONET and was strongly felt on board the Drilling Vessel Chikyu, which was in the area for IODP Expedition 365. The aims of Expedition 365 were to (a) retrieve an existing temporary observatory from IODP Site C0010 (Figure 28) and (b) install a new long-term borehole monitoring system in the same hole. It was fortuitous that the earthquake happened only a few hours before the temporary observatory was due to be retrieved, and data from the event were recorded by the instruments. Initial National Research Institute for Earth Science and Disaster (NIED) (<http://www.bosai.go.jp/e/>) locations placed the earthquake ~50 km SE of the town of Shingu, at a depth of 13 km, while Japanese Meteorological Agency (JMA) locations placed it at 28.7 km depth. Although JMA uses DONET data in their earthquake locations, their locations for offshore earthquakes are biased by the large number of land stations, as well as use of a velocity model that is not well-resolved offshore. The global

centroid moment tensor (CMT) solution (Dziewonski et al., 1981; Ekström et al., 2012) suggests a reverse faulting event, at 17.8 km depth, on a plane dipping either 14° (striking 236°) or 76° (striking 42°) (Figure 27). Note that all depths discussed in this paper are in kilometers below sea level, unless specified otherwise.

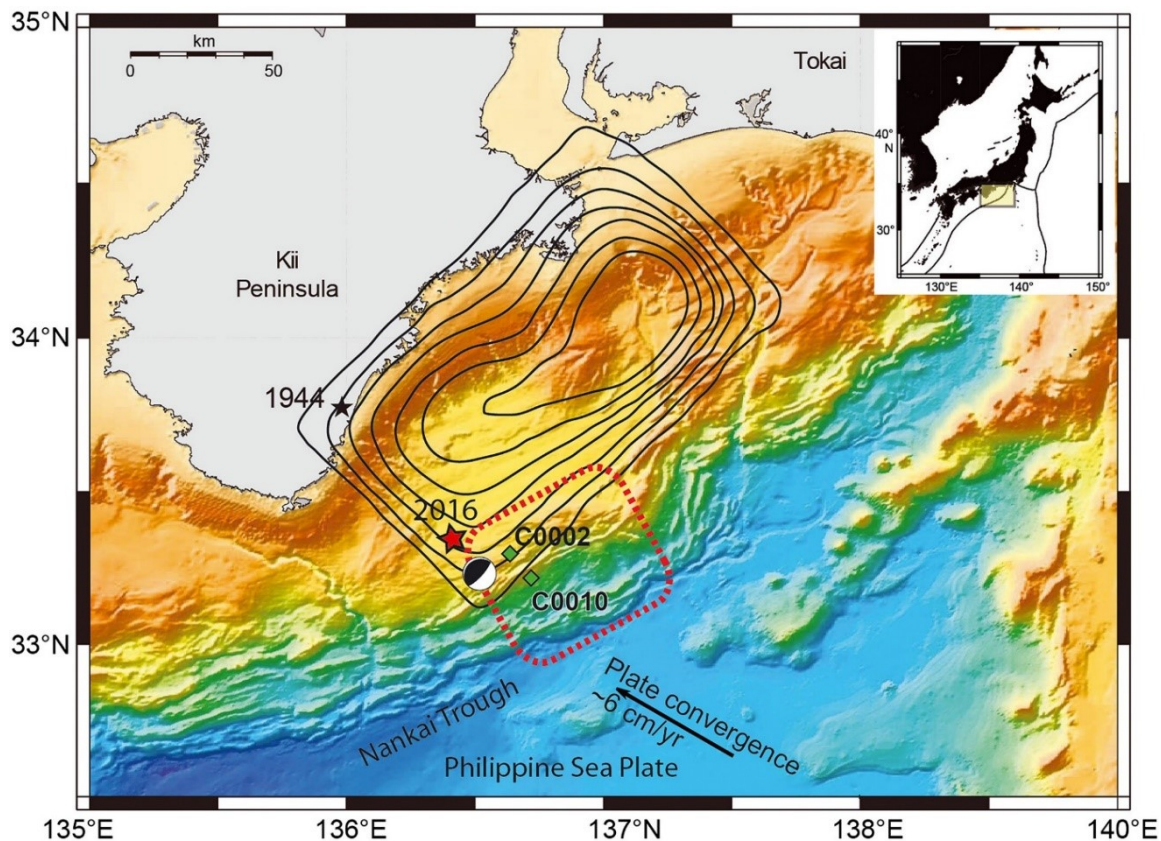


Figure 27: Regional tectonic setting of Kii Peninsula region and the Nankai Trough. Black contours (0.5 m intervals) show rupture area of 1944 Tonankai earthquake (Kikuchi et al., 2003) (see black star for epicenter). Red star shows our relocation of the 2016 Mie-Ken Nanto-Oki Mw 6.0 earthquake. Beach ball shows the Global CMT (Dziewonski et al., 1981; Ekström et al., 2012) location and focal mechanism solution for the earthquake (note the global CMT location is seaward of our relocation). Red dashed lines show region of very low frequency earthquakes identified by Ito and Obara (2006b). Green squares are IODP borehole observatories.

The region of the 1 April Mw 6.0 earthquake is where the Philippine Sea Plate subducts northwestward beneath southwest Japan along the Nankai Trough at $\sim 6 \text{ cm yr}^{-1}$ (DeMets et al., 2010; Miyazaki and Heki, 2001) and is the site of historic great (Mw 8+) subduction earthquakes, such as the 1944 Tonankai earthquake (Figure 27) (Ando, 1975b). In the region of the 1 April hypocenter, the subduction interface is located at $\sim 10 - 12 \text{ km}$ below sea level

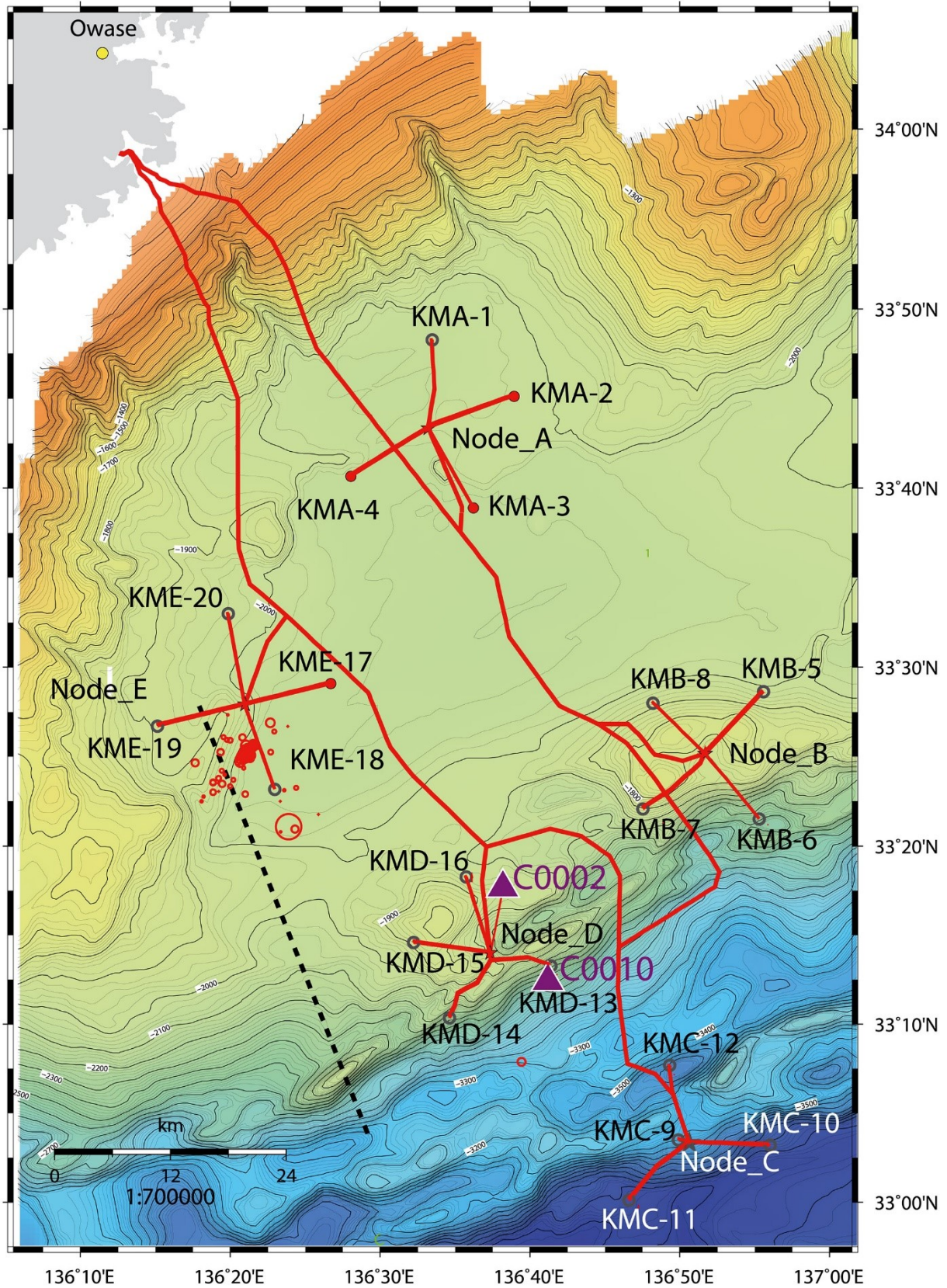


Figure 28: Map of the DONET network in the region of the Mie-ken Nanto-oki earthquake sequence (earthquake locations are red circles, scaled for magnitude). Purple triangles are IODP drill sites with borehole observatories. Black dashed line shows location of seismic velocity cross section in Figure 30.

(km bsl) and dips to the NNW at $\sim 8^\circ$ (Moore et al., 2014). Thus, the JMA and CMT preliminary earthquake locations (based on largely on land seismic network data) with a 18 – 29 km deep hypocenter placed the main shock within the subducting Philippine Sea Plate; the NIED location is shallower, at ~ 13 km, closer to the plate interface. We show from a detailed and integrated analysis of the DONET seismological data, seafloor pressure records (deformation and tsunami models), and the IODP borehole observatory data that the earthquake and its aftershocks occurred at 11 – 14 km, on a low-angle, landward dipping thrust fault, consistent with the plate interface. The borehole observatory data are critical to differentiate between the possible fault focal plane solutions, which is difficult to determine uniquely from the seafloor data and to provide a record of afterslip from the event. The offshore DONET data provide key constraints on both the slip model for the earthquake and the hypocenter and aftershock locations. Finally, we discuss the implications of this earthquake in the context of the earthquake cycle and megathrust behavior at the Nankai Trough.

Seismological analysis

Hypocenters of the foreshock, main shock, and aftershock events were located using P wave arrival records from DONET seafloor accelerometers. We analyzed accelerometer data from the stations above and around the source region. Determination of the hypocenter location was performed using the HYPOMH program (Hirata and Matsu'ura, 1987) with a 1-D seismic structure model. The velocity model used in this study (Figure 29) is based on Airgun-OBS seismic surveys, and the 1-D seismic structure used is a slice from the 2-D model in Figure 30 at the main shock location. Because accuracy of the location depth is critical in our analysis, we use the most reliable seismic structure models available in the region, which are from marine seismic surveys conducted in 2004 by R/V Kaiyo and 2011 by R/V JAMSTEC Kairei. The P wave seismic model shown in Figure 29 is derived from the seismic models of Kamei et al. (2012) and a new velocity model for the area by Nakanishi (Figure 30; see supporting information for more details on the velocity model). In our analysis, we used only P wave arrival picks to determine hypocenters to avoid introducing uncertainty from shear wave velocity structure, particularly for the upper few kilometers comprising recent sediment fill in the Kumano Basin. Correction to the P wave arrival time is applied to minimize offset between observed and calculated travel times for each station for all earthquakes. The resulting station corrections for the P wave arrivals are within the range -0.2 to 0.2 s for all stations, and travel time residuals for the earthquakes are within 0.1 s for most events and stations, justifying the use of the 1-D seismic model.

We located 164 local earthquakes in the period from 3 h before the main shock to 48 h after the main shock (see supporting information Table 7). Of these, 61 events were listed in the

JMA (Japan Meteorological Agency) catalog. The magnitude of the earthquakes is determined from earthquake duration (Tsumura, 1967). There are not significant differences between our magnitudes and those of the JMA catalog, whereas the magnitude estimated using the velocity seismogram (Watanabe, 1971) tends to be greater by ~ 0.46 , probably due to amplification from the soft seafloor sediment. Aftershock magnitudes are smaller than M 2.3. Our analysis covers earthquakes greater than approximately M 0.7, while JMA the catalog contains events only above M 1.3.

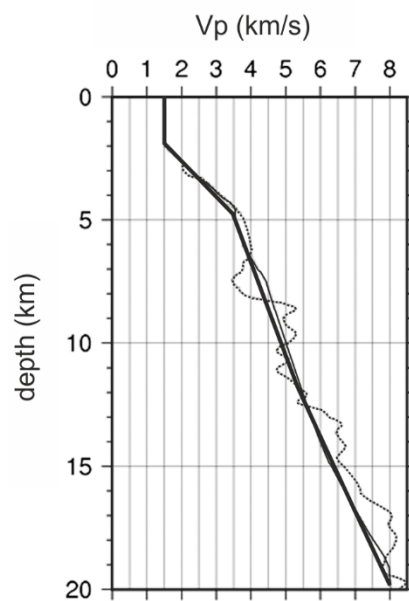


Figure 29: One-dimensional P wave velocity model used in the earthquake relocations (thick solid line). Reference seismic models from marine seismic surveys in Figure 30 (thin solid line, see supporting information) and Kamei et al. (2012) (more detailed dashed line) (modified after Wallace et al., 2016a).

The main shock (Mw 5.9) is located at 11.4 km depth at 33.35°N and 136.4°E . Many of the aftershocks are distributed approximately 10 km down dip of the main shock at 13 – 14 km depth (Figure 30) and are aligned roughly parallel to the strike of the subduction zone (Figure 28). The aftershock activity initiated soon after the main shock, although most of the aftershocks began approximately an hour after the main shock (Figure 30). There are a few small earthquakes observed slightly updip of the main shock during the 3 h period prior to the main shock, which we consider to be foreshocks. The foreshocks, main shock, and aftershocks are situated on a plane along the contour of $V_p \sim 5.5$ km/s to 5.8 km/s (Figure 30), near the location of the subduction interface picked from multichannel seismic images (black lines on Figure 30; see discussion in supporting information), consistent with the interpretation that they occurred at or near the plate interface rather than in the lower plate. The uncertainties on the plate interface location in the region of the earthquakes are estimated to be approximately ± 1.1 km (see discussion in supporting information). We also suggest the possibility that

aftershock activity was induced (and offset) downdip of the main shock by possible afterslip propagating down dip along the interface, from the main shock into the aftershock region.

Deformation models from seafloor and borehole pressure changes

Absolute pressure gauges (APGs) are widely used to measure pressure due to the overlying water column at the seafloor and to measure formation pore pressure in borehole observatories. Changes in pressure measured by APGs on the seafloor have been used to determine meter-scale vertical deformation of the seafloor during earthquakes (Iinuma et al., 2012) and volcanic unrest events (Chadwick Jr et al., 2012). More recently, it has been demonstrated that APGs can resolve centimeter-level deformation during offshore slow slip events (Davis et al., 2015; Ito et al., 2013; Wallace et al., 2016b). APG data also show changes in formation pore pressure when used as part of borehole observatories and provide a sensitive measure of volumetric strain during earthquakes and other transient deformation events, as well as responses to other forcing processes, including ocean tidal loading and hydrologic perturbations (Davis et al., 2009; Sawyer et al., 2008; Scretton et al., 2000; Wang and Davis, 1996).

Figure 31 and 32 show the seafloor and borehole pressure records from nearby DONET and IODP borehole (C0002 and C0010) observatory sites before, during and immediately following the earthquake. The effect of tides is removed from the borehole pressure data by subtracting a colocated seafloor reference pressure from the borehole pressure data, scaled by the 1-D tidal loading efficiency in the formation at each site and accounting for a small observed phase lag (<1.5 min) at Site C0010 (Wang and Davis, 1996). Pore pressure in the formation at Site C0002 increased coseismically by 2.1 kPa, while C0010 (which is farther seaward of the main shock) experienced a smaller pressure increase of 0.7 kPa (Figure 32). Seafloor pressures measured at C0002 and other DONET sites nearby (Figure 31) indicate a small (<5 mm) upward displacement of the seafloor, indicating that the pressure changes observed in the formation reflect volumetric strain (Davis et al., 2009; Wang, 2004), rather than vertical movement of the seafloor. The coseismic increases in pore pressure suggest that contraction was induced by the earthquake at both sites. The relationship between pore pressure change and volumetric strain is a function of the rock or sediment matrix compressibility, the fluid compressibility, and the formation porosity (Davis et al., 2009; Wang, 2004).

We use sediment properties reported from laboratory tests on core samples acquired at several drill sites that sampled the same formations where pressure is monitored at Sites C0002 and C0010 (Guo et al., 2011; Saffer et al., 2011). At C0010, the pressure to strain

conversion factor is 4.7 kPa/ μ strain and 5.7 kPa/ μ strain at C0002. The observed pressure changes correspond to coseismic volumetric strains of -0.37 μ strain at C0002 and -0.15 μ strain at C0010 (following a notation where compressive strain is negative). The pressure continued to increase by 0.63 kPa at C0002 (equivalent to -0.11 μ strain) for up to 2 days following the earthquake, which we suggest is due to afterslip, most likely in the region of the aftershocks (or between the main shock and aftershocks, Figure 30). The temporary observatory at Site C0010 had to be retrieved from the borehole by IODP Expedition 365 several hours after the 1 April earthquake, so we are unable to evaluate if a similar postseismic signal is observed at this site. We note that these strains should be considered lower bounds. If fluid compressibility is higher than in the ideal case, for example, due to the effects of dissolved gas in the pore fluid, the pressure to strain conversion factor would be smaller, leading to lower sensitivity to strain and larger estimated contraction at both sites (Wang et al., 1998).

The seafloor pressure changes (Figure 31) range from an 80 – 1000 Pa increase (0.8 – 10 cm subsidence) at the DONET sites closest to the epicenter, to possible small pressure decreases (~40 Pa or 0.4 cm uplift) at some DONET sites southeast of the main shock. A small tsunami (<2 cm) was generated by the earthquake, which can be seen in the pressure records of the DONET sites at 2 – 7 min following the main shock (Figure 31). We removed oceanographic noise from the seafloor pressure records by using a 30 s fourth-order Bessel low-pass filter and by subtracting synthetic tides computed from the tidal constituents obtained for each station using BAYTAP-G (Tamura et al., 1991). In order to isolate centimeter-level deformation signals during long-term transient events (such as slow slip events), it is important to correct for oceanographic noise (Wallace et al., 2016b). However, because the coseismic displacement occurred over a very short time, oceanographic noise from longer-term processes such as eddies, currents, and tides will not affect our estimates of coseismic seafloor pressure changes. The root-mean-square pressure changes over 13 min segments during a 2 h period prior to the earthquake are equivalent to 1.5 – 2.4 mm water depth, suggesting uncertainties in station displacement on the order of 2 mm.

We invert the vertical seafloor displacements for parameters of the earthquake fault plane using the code TDefnode (McCaffrey, 2009). TDefnode applies simulated annealing to simplex minimization to invert surface displacements and GPS time series for interseismic, coseismic, and other sources of transient deformation. In our case, we do not use the time-dependent or interseismic capabilities of TDefnode and only invert the static earthquake offsets at the DONET sites for parameters describing the coseismic deformation source in the Mw 6.0 earthquake. We assume uniform slip on a single plane and invert for latitude, longitude, depth, slip, strike, dip, and rake of the fault plane. To narrow the range of potential fault models, we constrain the location of the center of the fault plane to be within 5 km of the main shock

location (see section Seismological analysis). We also tested a suite of different models that constrain the fault plane parameters to be within various depth and dip ranges to better assess the range of models that can fit the data (Table 6; these are discussed below).

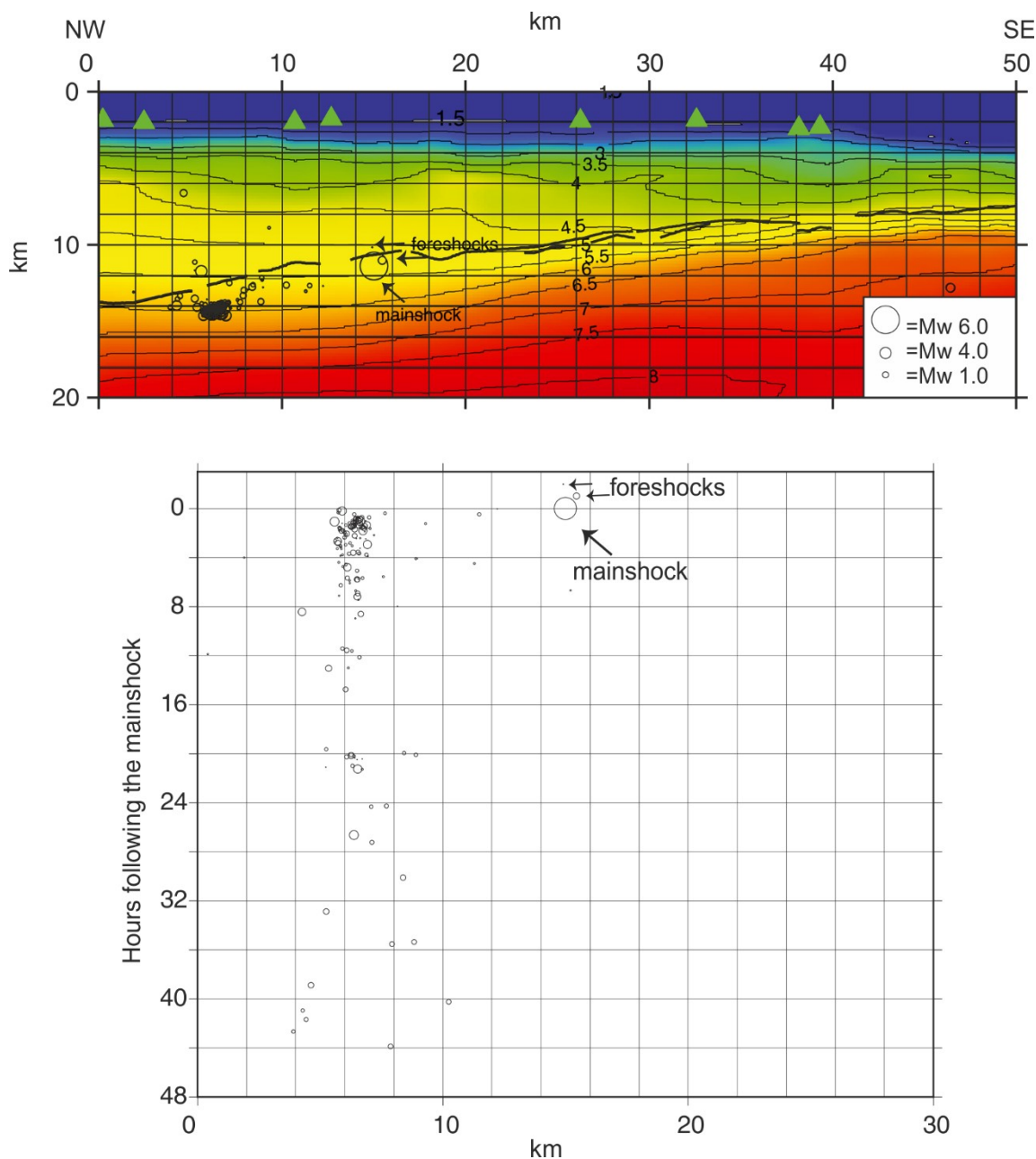


Figure 30: **(top)** Cross section of earthquake locations and aftershocks projected onto the V_P seismic model (see supporting information) and **(bottom)** time history of the earthquakes in the cross section with respect to the origin time of the main shock. P wave velocity contours labeled in km/s. Cross-section location shown in Figure 28. The plate interface (black lines) is determined from interpretation of multichannel seismic data and is in part derived from Park et al. (2002). Depth (y axis) in Figure 30 (top) is in kilometers below sea level. Green triangles show nearby DONET sites projected onto cross section (modified after Wallace et al., 2016a).

We assume a uniform elastic half-space, using the equations of Okada (1992, 1985). To calculate the M_w for the earthquake in our coseismic slip inversions, we assume a shear

modulus of 18 GPa (determined from a V_P of 5 km/s at ~ 10 km depth in the region of the earthquake, and assuming a V_P/V_S of 1.9 and a bulk density of 2650 kg m^{-3}) (Kamei et al., 2012). Williams and Wallace (2015) showed that elastic property variations at subduction zones can have a large influence on inversions of slow slip events at subduction zones. For example, when near-field data (e.g., directly above the slow slip) is available, inversions with realistic elastic properties can produce up to 30 % lower slip than those obtained using uniform half-space models. Based on the Williams and Wallace (2015) study, we expect that the anticipated effect of using a model with spatially variable elastic properties would be to lower the magnitude of slip on the fault in the earthquake by up to 30 %. Our inversions do not include variations in bathymetry/topography. This is an appropriate assumption in the Kumano Basin region as the seafloor is essentially flat, and there will be minimal influence on the inversion results from topography. We consider the seafloor as the surface of the half-space in our models and thus report our fault plane location results in kilometers below the seafloor (Table 6).

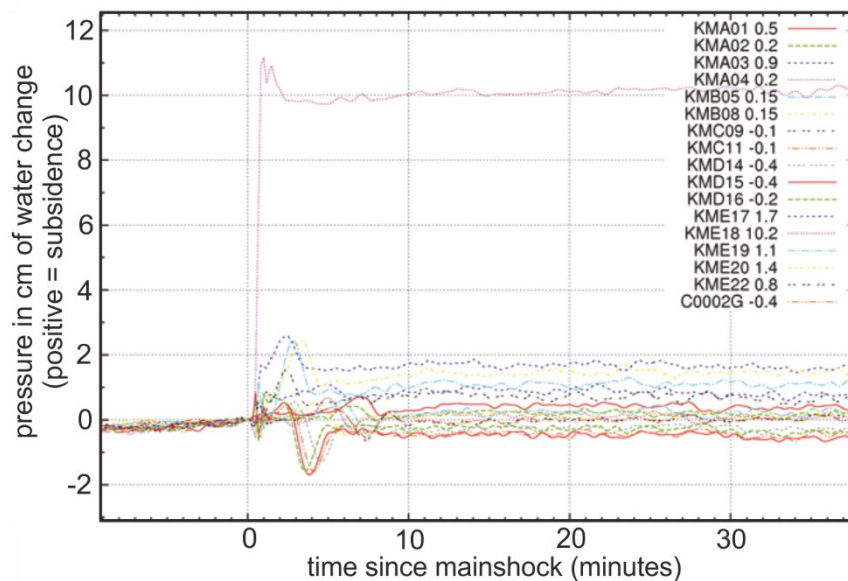


Figure 31: Seafloor pressure changes observed at DONET sites and C0002 observatory. Data shown in terms of equivalent water depth of the pressure change (y axis). Positive values (pressure increase) indicate subsidence. Time is shown on the x axis in minutes after the main shock (modified after Wallace et al., 2016a).

Two models (A and B; Table 6) that fit the seafloor displacement data best yield an Mw of 6.1 – 6.2. Model A (reduced chi-square, $\chi_n^2 = 0.37$) involves ~ 1.5 m of slip on a 16° dipping, 209° striking thrust fault, centered at 3.1 km below the seafloor. The second solution ($\chi_n^2 = 0.37$) has a more steeply dipping (64°) northeast striking (41°) plane and a similar amount of slip, centered at 6.4 km below the seafloor. Both of these models fit the large (~ 10 cm) subsidence observed at site KME-18 extremely well (Figure 33 A and B). However, both of these models predict extensional strain at the borehole observatory sites C0002 and C0010,

which is at odds with the 2.1 kPa and 0.7 kPa pressure increases observed (respectively) at those sites that indicate contraction. The pressure data from the borehole observatories are instrumental in allowing us to rule out both Models A and B. Moreover, the fault planes for Models A and B are much shallower than the main shock location suggests (section Seismological analysis).

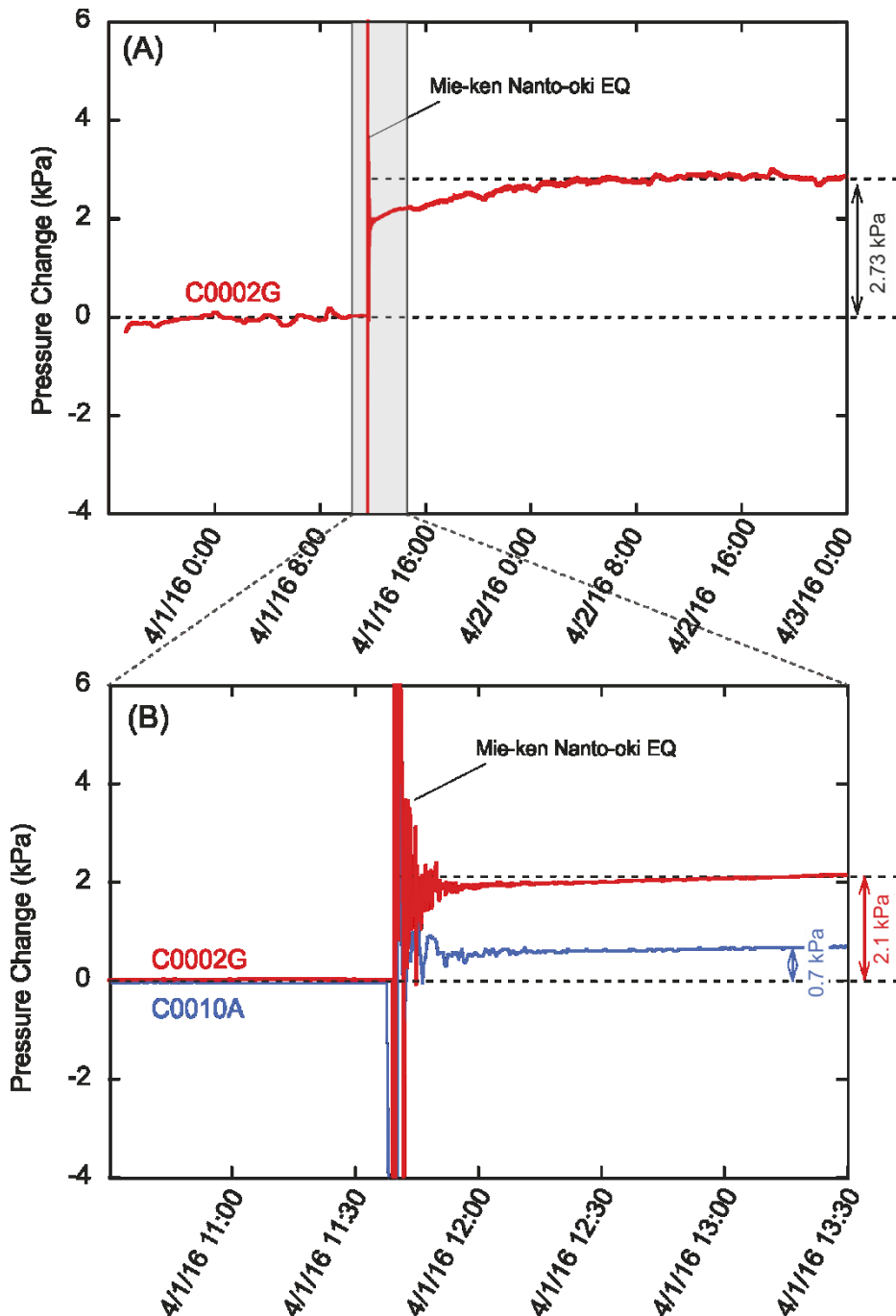


Figure 32: Borehole pressure changes during the 1 April earthquake. (A) Pressure data at C0002 from the ~2 day period surrounding the earthquake. (B) Zoom in on the time of the earthquake (gray box in A) showing pressure records from C0002 (red) and C0010 (blue). Note that the temporary observatory at C0010 was retrieved only several hours after the earthquake (on IODP Expedition 365), so it is not shown in Figure 32 A (modified after Wallace et al., 2016a).

We also test models with deeper slip planes, more consistent with the ~12 km below sea level (or ~10 km below the seafloor) main shock location discussed in the section Seismological analysis. First, to assess the influence of fault plane depth on the fit to the seafloor data, we undertake an inversion where the depth of the center of the fault plane is constrained to lie between 6 and 12 km below seafloor (bsf). In this scenario, we obtain a best fitting fault plane at 6 km depth, striking 207° and dipping 11°, with $\chi_n^2 = 0.50$ (Model C). The slightly increased misfit to the seafloor pressure data with this model (compared to Model A) is mostly at site KME-18, which is the site close to the main shock where 10 cm of subsidence is observed (Figure 33 C).

To explore models fitting the seafloor displacement data that place the fault plane at similar depths to the main shock, we run an additional inversion (Model D) where the depth is constrained to lie between 9 and 11 km below the seafloor, corresponding to the depth of the main shock and aftershocks, as well as to the plate interface beneath the earthquake epicenter. This model produces a significantly worse fit to the data (Figure 33 D), with $\chi_n^2 = 1.45$. However, the large misfit is due to the fact that we are unable to fit the large subsidence at KME-18 (a misfit of ~5 cm in Model D) with this deeper fault plane. It is clear that the fit to KME-18 degrades significantly with increasing depth of the fault plane source and that the large 10 cm displacement at KME-18 cannot be fit well with a fault plane deeper than ~6 km. We run a similar inversion (Model E), but without including the vertical displacement inferred from KME-18, and we obtain a similar fit to the rest of the seafloor data ($\chi_n^2 = 0.51$) as for Models A through C. Although Models D and E cannot reproduce the large (~10 cm) observed seafloor pressure increase at station KME-18, they do predict significant subsidence (~4.5 cm or approximately 50 % of the observed pressure change) at this site. Models C, D, and E all predict contraction at the borehole observatory Sites C0002 (-0.50 to -0.55 μ strain) and C0010 (-0.11 to -0.20 μ strain) and agree extremely well with the estimated strains of -0.37 and -0.15 μ strain at these sites (respectively). Overall, the uncertainties on the depth and dip of the earthquake source are large when using seafloor displacement on its own, as a range of depths and dips can fit the seafloor deformation data (Table 6). To further narrow the range of possible models, we rely on integration with earthquake locations, tsunami data, and the borehole pressure data, as discussed here and in section “Integrated interpretation of seismological, geodetic, and tsunami modeling data”.

KME-18 is the closest site to the earthquake and experienced peak ground accelerations of 0.61 g (horizontal) and 0.07 g (vertical) during the event. It is possible that the 10 cm of subsidence observed at KME-18 could be influenced by other factors, such as site instability and settling or rotation of the instrument into soft surface sediment.

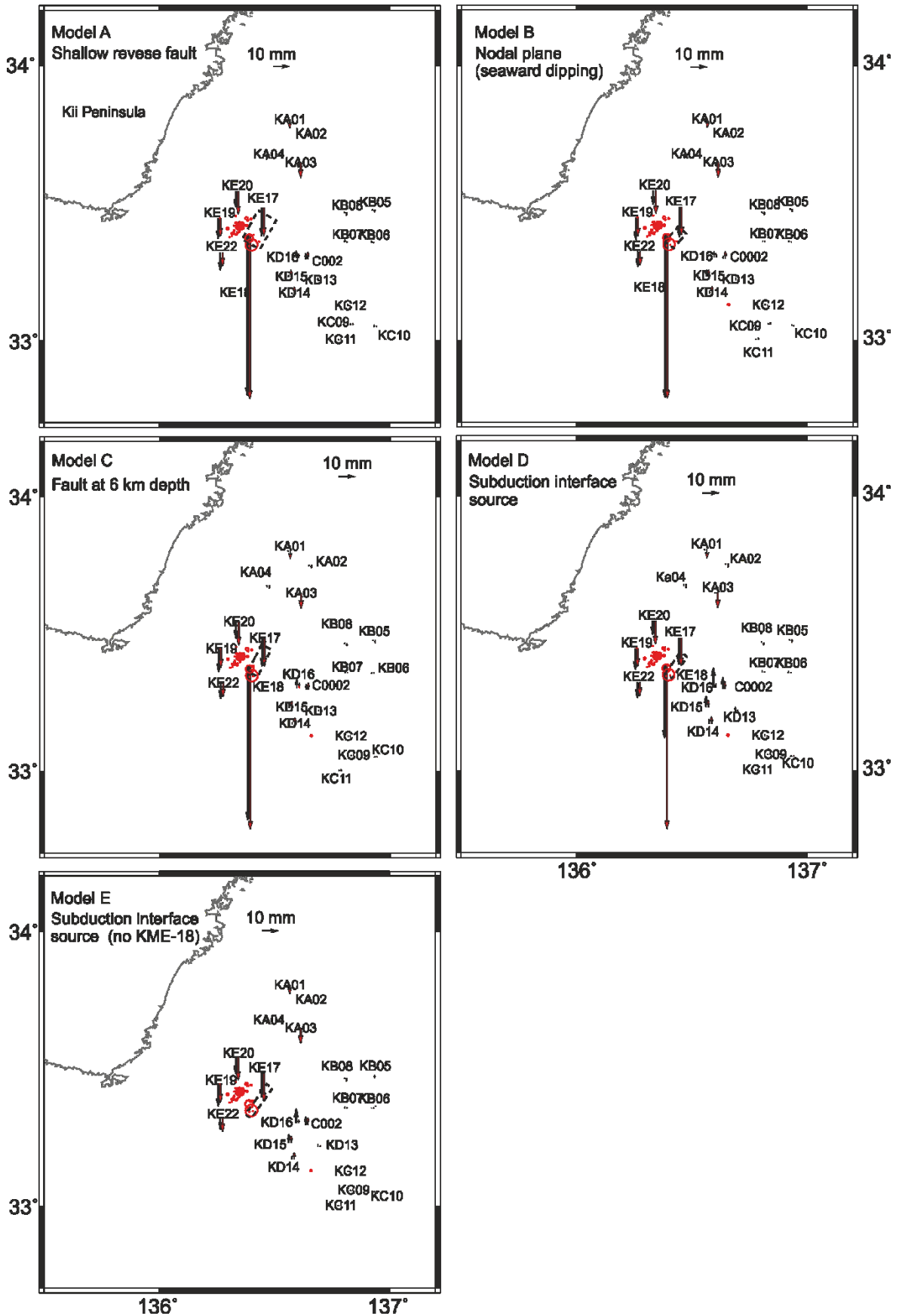


Figure 33: Results of dislocation Models A–E (see Table 6). Dashed outline shows the fault plane; red dots are the earthquake and aftershocks. Red arrows show observed displacements; black arrows are model displacements (modified after Wallace et al., 2016a).

Chadwick et al. (2006) show that tilting of absolute pressure gauges about a vertical axis can cause large pressure changes, $\sim 7 - 10$ kPa over 180° of tilt, due to the influence of the orientation of the Earth's gravitational field on the Paroscientific pressure sensors. Thus, much of the observed ~ 1 kPa pressure increase at KME-18 could be explained by tilting of the APG on the order of $10 - 30^\circ$. Whether or not such tilting of the sensor occurred during the earthquake at this site is unknown.

Tsunami modeling

A small passing tsunami wave is clearly observed in the DONET seafloor pressure data during the hour following the Mie-ken Nanto-oki earthquake (Figure 31). To help assess the suitability of the different deformation models discussed in section "Deformation models from seafloor and borehole pressure changes", we undertake modeling of tsunami wave propagation for a subset of these models. Modeling of tsunami generation and propagation was undertaken using COMCOT (Cornell Multigrid Coupled Tsunami). COMCOT was originally developed by the wave research group of Cornell University, USA, starting in the early 1990s (Cho, 1995; Wang, 2008). It has subsequently been under continued development at the Institute of Geological and Nuclear Science (GNS Science), New Zealand, since 2009 (Wang and Power, 2011). COMCOT is capable of simulating the entire lifespan of a tsunami, including its generation by seabed displacement, transoceanic propagation, coastal runup, and inundation. It uses modified explicit staggered leap-frog finite difference schemes to solve the linear and nonlinear shallow water equations in either spherical or Cartesian coordinates. The implementation of a two-way nested grid scheme allows the model to efficiently deal with the large variations in spatial and temporal scales that occur during tsunami evolution (Cho, 1995; Wang, 2008; Wang and Power, 2011).

For the current study a single bathymetric grid, interpolated from the GEBCO-08 30 arc sec global database, was used to simulate tsunami generation and propagation at 15 arc sec resolution (approximately 300 m at the latitude of the epicenter). Two hours of tsunami propagation was calculated for each source model, using the linear shallow water equations with the assumption of vertical wall boundary conditions at the coastlines. Seafloor displacements used as boundary conditions to drive tsunami generation were calculated for the selected source models shown in Table 6, using Okada's analytical equations (Okada, 1985). The tsunami model calculates water surface time histories, which we convert into simulated bottom pressure recordings at the DONET sensor locations. The coseismic vertical displacement at each sensor location was subtracted from the corresponding water surface time history (to account for the change in pressure resulting from the change in elevation of the pressure gauge).

As fault Models A and B are ruled out by the borehole pressure data (see section “Deformation models from seafloor and borehole pressure changes”), we only show tsunami model results from fault source Models C and D (e.g., Table 6) (Figure 34 B and C). Models D and E are very similar and therefore produce similar overall tsunamis, so we do not show Model E here. Although Model C fits the large displacement at KME-18 well, this model and other similar models with a shallow fault (e.g., <7 km) produce tsunami with larger amplitudes (5 cm or more) and shorter wavelengths (Figure 34 B) than observed (Figure 34 A). This is due to the larger amplitude and shorter wavelength seafloor displacements predicted by the shallower fault source model. With the exception of the large coseismic subsidence at KME-18, tsunami models generated by source Model D (Figure 34 C) match the observed seafloor pressure data very well and produce longer wavelength, lower amplitude waves than the shallower fault Model C. The maximum tsunami amplitude is typically ~2.0 – 2.5 cm in Model D, comparable to the 1.5 – 2.0 cm tsunami observed on the DONET pressure sensors following the main shock (Figure 34). The overall wave arrival patterns are also similar, with an initial increase in wave height at DONET sites in the KME group (downdip of the main shock) during the first few minutes following the earthquake. In contrast, sites in the KMD group of DONET sites (seaward of the uplifted zone) experienced an initial decrease in wave height approximately 2.5 – 3 min following the earthquake. The model also reproduces a ~1 cm peak and trough observed at the KMC group of sites at 5 – 7 min following the main shock (compare Figure 34 A and C).

Table 6: Summary of models and fit to the seafloor vertical deformation data, and predicted volumetric strain at boreholes (last two columns in μ strain, positive is dilatation, negative is contraction)^a.

Model	Lat.	Long.	Depth (km bsf)	Dip (deg)	Strike (deg)	Rake (deg)	Slip (m)	Length (m)	Width (km)	χ_n^2	C0002 (μ s)	C0010 (μ s)
A	33.405	136.434	3.1	16	209	98	1.5	13.4	8.7	0.37	+0.27	+0.19
B	33.375	136.423	6.4	64	41	115	1.5	7.9	10	0.37	+0.08	+0.12
C	33.405	136.434	6	11	207	98	1.5	12.3	4.5	0.5	-0.53	-0.11
D	33.385	136.434	9.8	5	215	95	1.5	10.6	3.4	1.45	-0.50	-0.20
E	33.384	136.434	9.8	18	215	85	1.4	15	3.1	0.51	-0.55	-0.15

^aFor reference, the plate interface is located 9 – 10 km below the seafloor in this area and dips westward at ~7° (Figure 30). Our preferred model (D) is in bold. Although Model D produces a worse fit to the seafloor data (due to misfit at site KME-18), it fits the other data sets (earthquake locations, borehole pressure data, and tsunami data) better than Models A–C (see discussion in section “Integrated interpretation of seismological, geodetic, and tsunami modeling data”). Model E is an inversion without including KME-18, with results similar to Model D (note the comparable fit to the data between E and A–C). Models A and B predict dilatation at the C0002 and C0010, which contradicts the contractional strain observed there, thus ruling out A and B. All of these models have moment magnitudes between 5.9 and 6.1. χ_n^2 = reduced chi-square statistic. km bsf = km below seafloor.

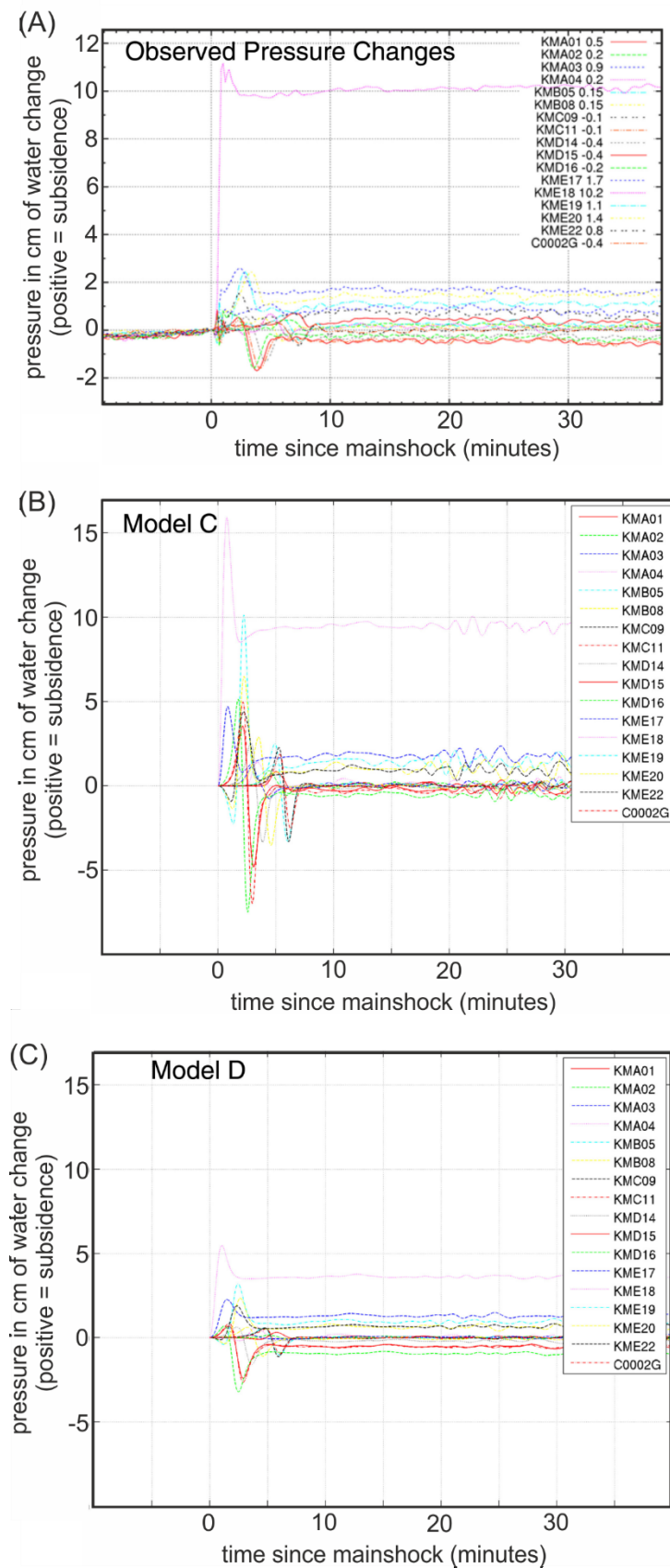


Figure 34: Tsunami model plots shown in terms of water level changes predicted at the seafloor sensors, compared to observed data. (A) Observed pressure data (see also Figure 31); (B) Model C upper plate fault model; (C) Model D subduction interface model (modified after Wallace et al., 2016a).

Discussion

Integrated interpretation of seismological, geodetic, and tsunami modeling data

With the exception of the large (~10 cm) subsidence at KME-18, our diverse seismological, seafloor displacements, borehole pressure, and tsunami observations yield results that are highly consistent with each another. Such data are not typically available for offshore earthquakes and can provide a much higher fidelity picture of an offshore Mw 6.0 earthquake than is usually possible. Overall, locations of the main shock and aftershocks of the Mie-ken Nanto-oki earthquake point to a location on the plate interface. The earthquake locations combined with the agreement between the tsunami models from source Model D (Figure 33 D and 34 C) and the observed seafloor pressure data (Figure 31 and 34 A) lead to our preference of the Model D fault plane (Figure 33 D and Table 6), which coincides with the plate interface (Figure 30). Contraction of 0.37 and 0.15 μ strain observed in the formation at IODP Sites C0002 and C0010 (respectively) requires a deeper (>5 km deep), landward dipping plane and is consistent with models placing the main shock slip on the plate interface (Table 6, Models D and E).

The aftershocks occur in a cluster that is offset ~3 – 7 km NW of and ~1 – 2 km deeper than the main shock (Figure 28 and 30). This suggests a possible model wherein the main shock ruptured a portion of the interface 11–12 km deep (~9 – 10 km bsf) and produced a sequence of aftershocks just downdip of the rupture area at ~13 – 14 km on the same fault plane (e.g., the plate interface) (Figure 30). There also appears to be a horizontal gap between the main shock and aftershocks (Figure 28 and 30), which we speculate could be the site of afterslip that propagated downdip immediately following the main shock, and triggered the intense aftershocks that began an hour later. The foreshocks are located slightly SE (updip) of the main shock (Figure 30), suggesting that the entire foreshock-main shock-aftershock sequence propagated downdip along the plate interface. All of the best fitting deformation models (Figure 33) suggest a fault with its southwestern edge coincident with the main shock location, indicating that the Mw 6.0 rupture may have initiated in the southwest and propagated along strike to the northeast.

The continued increase in pore pressure observed at C0002 in the 2 days following the earthquake suggests afterslip following the main shock (Figure 32). The continued contractional strain following the earthquake is ~0.11 μ strain, equivalent to ~30 % of the signal that was observed during the main shock. If this pore pressure change reflects volumetric strain in response to afterslip in the aftershock and/or main shock source area or on

immediately surrounding fault patches, it likely involves several to a few tens of cm of slip on the plate boundary. Afterslip of ~30 % of the main shock slip following an earthquake is not unexpected, and similar ratios of afterslip to main shock slip have been observed for a range of subduction interface earthquakes (Melbourne et al., 2002). It is unlikely that the postseismic pressure increase at C0002 is related to poroelastic deformation, as this would produce a decrease in pore pressure due to drainage of the initial (coseismic) increase in pressure. We note that vertical deformation of the seafloor due to afterslip is not resolvable by the DONET seafloor pressure gauges. We do not record a postseismic pressure transient at Site C0010, as the borehole instruments were removed from C0010 within a few hours after the earthquake.

Implication for the subduction zone earthquake cycle in the Tonankai region

The source area of the Mw 6.0 Mie-ken Nanto-oki earthquake last ruptured in the 1944 Mw 8.0 Tonankai earthquake (Figure 27). Great earthquakes recur here approximately every 100 – 200 years, as documented by historical records for the last >1300 years (Ando, 1975b). According to models based on GPS data, the plate interface in this region is currently interseismically locked (Mazzotti et al., 2000; Yokota et al., 2016) and elastic strain is being accrued in the surrounding crust. Moreover the occurrence of the Mie-ken Nanto-oki earthquake suggests that interseismic strain accumulation was occurring in the source region of the 1 April earthquake. Seismic reflection data place the subduction megathrust ~9 – 11 km beneath the seafloor (Moore et al., 2014; Park et al., 2002) in the region of the earthquake. The location of the main shock at ~9 – 10 km below the seafloor, combined with the seafloor and subseafloor geodetic data and tsunami modeling, indicate that the earthquake is located on or very close to the plate interface, with the aftershocks occurring further downdip along the interface (Figure 30).

Seismicity near the subduction interface is rare in this portion of the Nankai Trough. To our knowledge, there has been no notable interface seismicity (Mw >5.0) since the 1944 earthquake and its aftershocks. Two different source models for the 1944 Tonankai earthquake exist, based on seismological data (Ichinose et al., 2003; Kikuchi et al., 2003), both of which show that the 1 April Mw 6.0 earthquake occurred within the 1944 rupture area (see Figure 27 for 1944 slip distribution of Kikuchi et al. (2003)). Although not shown in Figure 27, the model of 1944 Tonankai earthquake slip from Ichinose et al. (2003) suggests a relatively large amount of slip (2 – 3 m) in the region adjacent to (or possibly within) the source area of the 2016 Mw 6.0 earthquake. Previous OBS deployments show that although microseismicity rates are relatively high near the trench axis, they are extremely low in the rupture area of the 1944

earthquake (Obana et al., 2004). Obana et al. (2004) attribute this lack of seismicity to a large, fully locked asperity that ruptures in earthquakes similar to the Mw 8.0 Tonankai earthquake. We do not yet know what role the Mw 6.0 Mie-ken Nanto-oki earthquake plays in the earthquake cycle in this part of the Nankai Trough, or if it could represent a foreshock of the next Tonankai earthquake. However, given the relative quiescence of this part of the plate interface in recent decades, the situation should certainly be monitored closely.

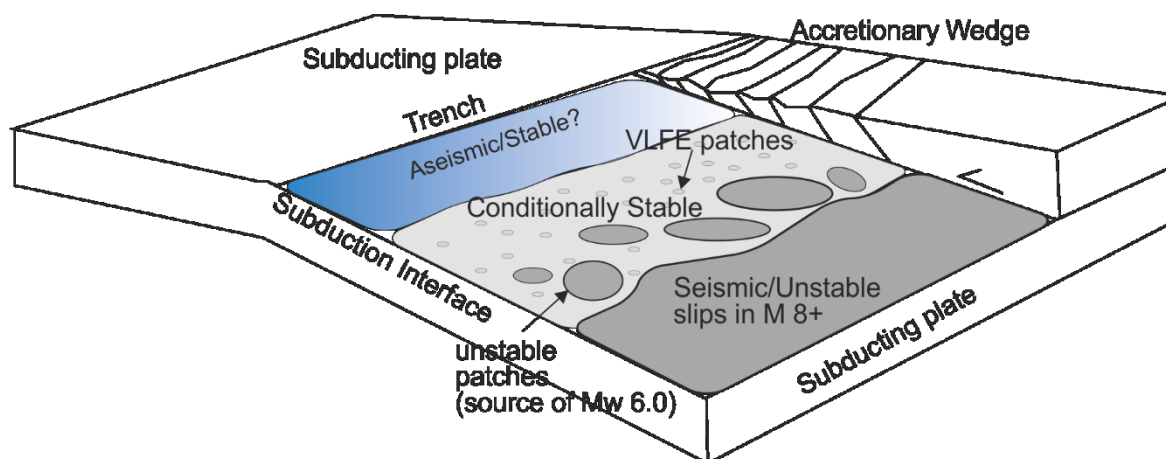


Figure 35: Cartoon schematic of possible heterogeneity of plate interface properties and slip behaviors beneath the outer forearc at the offshore Nankai Trough (modified after Wallace et al., 2016a). We suggest that earthquakes similar to the 1 April 2016 Mw 6.0 earthquake may rupture moderate-sized unstable patches within the updip transition from the large seismogenic patch (that likely ruptures in great earthquakes) to a conditionally stable region characterized by very low frequency earthquakes (VLFES) (Obana and Kodaira, 2009; Obara and Ito, 2005; Sugioka et al., 2012) and possible slow slip.

The Mw 6.0 earthquake occurred just downdip of recent swarms of very low frequency earthquakes (VLFES) and tremor activity (Obana and Kodaira, 2009; Obara and Ito, 2005; Sugioka et al., 2012), which are thought to represent possible slow slip events on the plate interface. One possible model explaining this family of events is that the plate interface in the region of the VLFES and the Mw 6.0 earthquake slips in a spatially and temporally heterogeneous manner, rather than simply being characterized as an extensive and uniform locked seismogenic zone that ruptures only in great earthquakes. In particular, the rupture area of the 2016 Mw 6.0 earthquake may represent a moderate-sized asperity located in the transition from the VLFE and SSE region, to the broadly locked Mw 8.0 earthquake source zone further downdip (Figure 35). We expect that this asperity may rupture occasionally in moderate-sized events like the 1 April 2016 earthquake but that it may also rupture collectively with the larger asperities in Mw 8.0 earthquakes, like the 1944 Tonankai earthquake

Conclusion

Access to offshore seismological and deformation data greatly enhances our ability to resolve the location and mechanisms of earthquakes relevant to the subduction earthquake cycle at

the Nankai Trough. Initial locations of the Mw 6.0 Mie-ken Nanto-oki earthquake were based on land network data, and most of these placed the earthquake deeper (within the subducting slab and further offshore) than the seafloor network data suggest. Together, the ocean bottom seismometer data, seafloor and subseafloor geodetic data, and tsunami modeling converge on a plate interface source for the earthquake. If offshore data were not available for this earthquake, it is possible that it would be classified as an intraslab earthquake, rather than a subduction interface event. The close agreement between observed and modeled coseismic volumetric strain at IODP observatories C0002 and C0010, as well as their sensitivity to afterslip, further demonstrates the value of downhole pressure sensing as a monitoring tool for strain accumulation and release, especially in the offshore and near-trench region. Our results suggest the possibility that many offshore subduction margin earthquakes previously thought to be located within the subducting plate may in some cases be located on the interface, particularly when information about these events is based only on data from global and/or shore-based networks that provide limited aperture and azimuthal coverage, and which lack sensitivity to offshore deformation. Offshore monitoring networks similar to DONET are critically needed at subduction zones elsewhere to properly evaluate possible precursors to megathrust earthquakes and tsunamis.

Acknowledgements

We thank the German Science Foundation (DFG-grants KO2108/8-1 and KO2108/15-1) for funding the GeniusPlug work, NSF grants OCE-0623633 and OCE-1334436 to Saffer supporting the pressure instrumentation at C0002, and the Integrated Ocean Drilling Program (IODP) for the efforts during Expeditions 315, 319, 332 and 365 to drill and instrument Sites C0002 and C0010. The seismic survey performed in 2011 is part of a project entitled “Research on Evaluation of Linkage between Tokai/Tonankai/ Nankai Earthquakes,” funded by the Japanese Ministry of Education, Culture, Sports, Science, and Technology (MEXT). This paper was improved by insightful reviews from Takeshi Sagiya and one anonymous reviewer. The data for this paper are available by contacting the corresponding author at llwallace@utexas.edu.

Author Contributions

Laura Wallace as first author wrote the manuscript about earthquake hypocenter localization with offshore observatory data. I participated in the IODP expedition 365 during which the GeniusPlug borehole observatory was recovered. As onboard observatory specialist, I was responsible for the pressure and temperature data acquisition. Besides the technical

assistance, I processed the borehole pressure data shown in Figure 32 and provided the figure for this manuscript. Since, the initial draft was written onboard D/V Chikyu I participated heavily in discussions regarding the interpretation of the borehole and seafloor pressure data. Finally, I reviewed and commented on the drafts before submission.

Supplementary materials

Introduction

This supplementary material provides details on how the seismic velocity model used for earthquake relocations is derived. A caption for Table 7 of the earthquake sequence locations is also provided.

Derivation of the seismic velocity model used for earthquake relocations

First-arrival tomography was used to derive the seismic velocity model used in the earthquake relocations and Figure 4. The initial model was constructed by simplifying and smoothing the previous results around the seismic profile (Kodaira et al., 2006). We also used time-migrated multi-channel seismic reflection (MCS) sections, where available, to provide a priori information about the shallow structure from the ocean floor down to the top of the oceanic crust, or the acoustic basement.

We use the GeoCT-II software package, which is based on the algorithm of Zhang et al. (1998). In this software the first-arrival refraction travel times and ray paths are calculated by the shortest raypath-tracing method, using graph theory to expand a wavefront by finding the shortest paths, with an optimized node distribution (Zhang and Toksöz, 1998). This method is characterized by a regularized nonlinear inverse problem that minimizes misfits of the average slowness and the apparent slowness (Zhang and Toksöz, 1998). Forward calculations are done on a 0.1 km x 0.1 km grid and inversions on a 0.2 km x 0.2 km grid. All first-arrival refraction traveltimes were picked from all wide-angle OBS sections. The inversion was iterated until the root mean square of traveltimes residuals became smaller than the observed uncertainty, that is, less than 0.05 s.

To examine the reliability of the final model in terms of its resolution and uncertainty, we conducted travel time fitting and checkerboard tests. These tests are commonly used to assess model reliability in tomographic studies. In our data, the calculated travel times fit the observed travel times within uncertainties of the observed travel times (± 0.05 s) with a few exceptions. We also followed the checkerboard test method described by Zelt and Barton (1998). For the model of the entire profile, we calculated theoretical travel time data from the initial model with an anomaly pattern of positive and negative regions based on the observed source-receiver geometry. The lateral anomaly pattern is a $\sin(x)$ and $\sin(z)$ function with a peak anomaly value of ± 5 % of the background velocity. The theoretical travel time data were inverted by the same method as was used to obtain the final model by using the same initial model. The grid size of

the checkerboard anomaly was generally 10 km (horizontal) x 5 km (vertical). For the model of the entire profile, the area over which rays corresponding to the travel time data used for the travel time tomography passed can be resolved with structural variation of 10 km x 5 km, according to the recovered anomaly pattern.

Comparison with the MCS section

Two-way travel time (TWT) of interpreted reflector as the subducting plate interface can be picked from the time-migrated MCS section previously acquired along the same line as the seismic profile Park et al. (2002). To obtain the depth of the subducting plate interface, the picked TWT is converted to depth using our seismic velocity model and superimposed on the seismic velocity model shown in Figure 30. The interface was picked from the MCS section with uncertainties of approximately ± 0.15 s in the main shock and aftershock area. Considering both the uncertainties in the plate interface picking and the velocity model (discussed earlier in this section), the depth uncertainty for the interface is estimated at less than ± 1.1 km.

Table 7: Table of foreshock, mainshock, and aftershock locations and their uncertainties for the Mie-ken Nanto-oki earthquake sequence. The mainshock is the third event on the list, at 2:39:08. Times and dates are in UTC time. Horizontal and vertical location uncertainties (rows 4, 6, 8) are in km. Mdur refers to magnitudes determined using Tsumura's duration formula, while MI refers to magnitudes determined from Watanabe's velocity amplitude formula (see discussion of these formulas and their differences in the manuscript).

Date	Time	Lat.	Lat. σ (km)	Long.	Long σ (km)	Depth	Depth σ (km)	Mdur	MI
04.01.2016	00:40:57	33.36144	1.41	136.4341	2.41	10.161	1.49	0.18	0.26
04.01.2016	01:37:32	33.34779	0.38	136.4078	0.41	11.006	0.57	1.46	0.19
04.01.2016	02:39:08	33.34999	0.35	136.401	0.35	11.371	0.53	5.5	5.9
04.01.2016	02:40:47	33.37369	1.07	136.3915	0.97	12.662	1.15	0.11	3.92
04.01.2016	02:47:51	33.4257	0.41	136.3598	0.44	14.25	0.55	0.94	1.88

This decimated table is only for illustration purpose. The full table with all events can be found online.

3.3 Manuscript 5 (Science published): Recurring and triggered slow-slip events near the trench at the Nankai Trough subduction megathrust [co-authorship]

E. Araki,^{1*} D. M. Saffer,^{2*} A. J. Kopf,³ L. M. Wallace,^{4,5} T. Kimura,¹ Y. Machida,¹ S. Ide,⁶ E. Davis,⁷ **IODP Expedition 365 shipboard scientists**

¹Japan Agency for Marine-Earth Science and Technology (JAMSTEC), Yokusuka, Japan.

²Department of Geology, Pennsylvania State University, University Park, Pennsylvania, USA

³MARUM - Center for Marine Environmental Sciences, Bremen, Germany.

⁴GNS Science, Lower Hutt, New Zealand.

⁵University of Texas Institute for Geophysics, Austin, TX 78758, USA.

⁶Department of Earth and Planetary Science, The University of Tokyo, Tokyo, Japan.

⁷Pacific Geoscience Centre, Geological Survey of Canada, Sidney, Canada.

Abstract

The discovery of slow earthquakes has revolutionized the field of earthquake seismology. Defining the locations of these events and the conditions that favor their occurrence provides important insights into the slip behavior of tectonic faults. We report on a family of recurring slow-slip events (SSEs) on the plate interface immediately seaward of repeated historical moment magnitude (Mw) 8 earthquake rupture areas offshore of Japan. The SSEs continue for days to several weeks, include both spontaneous and triggered slip, recur every 8 to 15 months, and are accompanied by swarms of low-frequency tremors. We can explain the SSEs with 1 to 4 centimeters of slip along the megathrust, centered 25 to 35 kilometers (km) from the trench (4 to 10 km depth). The SSEs accommodate 30 to 55 % of the plate motion, indicating frequent release of accumulated strain near the trench.

Over the past several years, geodetic and seismic observations have revealed a continuous spectrum of slow earthquake behaviors, in which failure occurs on time scales ranging from seconds to years, fundamentally changing the way fault slip behavior is understood (Beroza and Ide, 2011; Dragert et al., 2001; Obara, 2002; Obara and Kato, 2016; Schwartz and Rokosky, 2007; Sugioka et al., 2012; Wallace et al., 2016b). These phenomena span from normal earthquakes to low-frequency tremors (LFTs) and very-low-frequency earthquakes (VLFEs), characterized by a higher abundance of low frequency energy in radiated seismic waves than for a typical earthquake (Beroza and Ide, 2011; Ito and Obara, 2006a; Shelly et al., 2006), and further to slow-slip events (SSEs), in which slip occurs over weeks to months (Beroza and Ide, 2011; Dragert et al., 2001; Schwartz and Rokosky, 2007; Wallace et al., 2016b). SSEs can be large, with a moment equivalent to moment magnitude (M_w) >6 earthquakes (Beroza and Ide, 2011; Wallace et al., 2016b), and in some cases may precede and trigger damaging interplate earthquakes (Kato et al., 2012; Obara and Kato, 2016). Slow earthquakes are observed in a wide range of geologic and tectonic settings but occur most commonly at subduction plate boundaries (Beroza and Ide, 2011; Schwartz and Rokosky, 2007). Despite their importance for fault dynamics and associated earthquake and tsunami hazards, the patterns of strain accumulation and release in slow earthquakes, their relationship to large, damaging earthquakes, and the underlying physical mechanisms that dictate observed variations in fault slip behavior all remain poorly understood. This is primarily due to the lack of direct constraints on in situ conditions and rock properties, as well as a dearth of continuous observations to resolve deformation offshore near the trench (Obara and Kato, 2016; Saffer and Wallace, 2015; Schwartz and Rokosky, 2007; Wallace et al., 2016b).

Slow earthquakes are most commonly documented near the lower edge of the seismogenic zone that fails episodically in earthquakes (Dragert et al., 2001; Obara, 2002; Schwartz and Rokosky, 2007; Shelly et al., 2006; Wallace et al., 2016b). Observations of SSEs and related phenomena updip of a large, locked seismogenic zone are far less common. Shallow SSEs have been detected at a number of subduction zones (Davis et al., 2015; Davis et al., 2013; Dixon et al., 2014; Obana and Kodaira, 2009; Ozawa et al., 2007; Wallace et al., 2016b; Yamashita et al., 2015), some possibly reaching the trench itself, primarily at margins where the plate boundary appears to be mostly creeping (Obana and Kodaira, 2009; Wallace et al., 2016b) or where the seismogenic zone is extremely heterogeneous (Davis et al., 2013; Dixon et al., 2014; Ozawa et al., 2007). However, there is minimal constraint on shallow SSE recurrence or the distribution of slip, especially in the shallowest areas closest to the trench where onshore geodetic networks lack resolution. Although a few isolated VLFE swarms and LFTs have been observed in this environment and identified as thrusting events along the plate interface or within the upper plate (Obana and Kodaira, 2009; Obara and Kato, 2016; Sugioka

et al., 2012), the extent of such events and their connection to patterns of fault locking and slip remain unknown. Among the outstanding questions are whether SSEs are commonplace on the shallowest reaches of subduction megathrusts and how they are related to VLFEs, LFTs, and large, damaging earthquake ruptures (Obara and Kato, 2016).

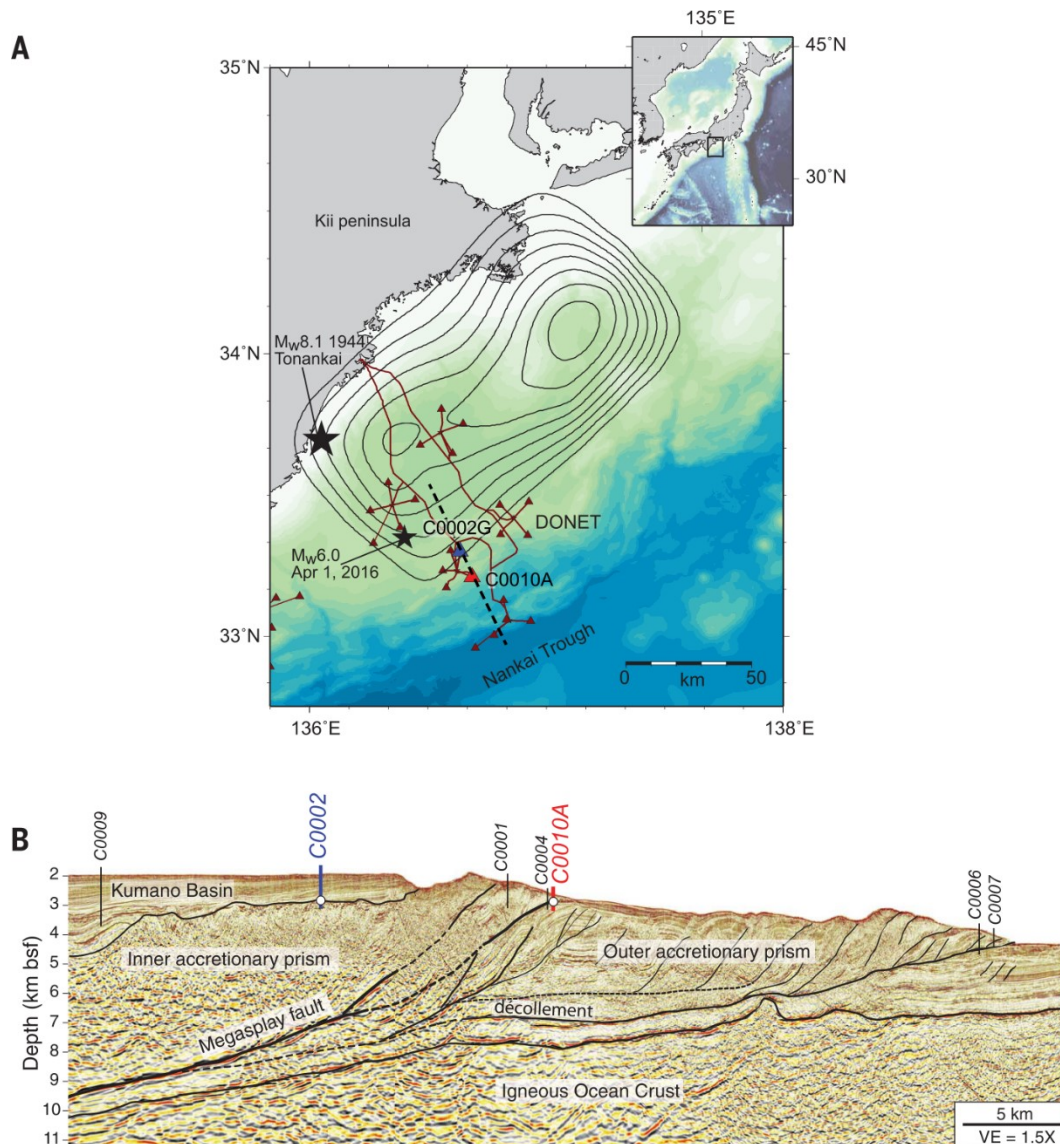


Figure 36: Map and seismic cross section showing borehole observatories and seafloor sensor network. (A) Map showing the DONET network (brown line; seafloor sensors denoted by brown triangles) and IODP boreholes (blue, C0002G; red, C0010A). Black contours (0.5-m interval) and the large black star indicate the rupture area and epicenter of the 1944 Tonankai earthquake (21). The epicenter of the Mw 6.0 earthquake on 1 April 2016 (Wallace et al., 2016a) is indicated by the smaller star. The dashed line shows the location of the seismic section in (B). (Inset) Zoomed-out view of area. (B) Seismic line showing NanTroSEIZE drill sites. White circles indicate the depth of pore-pressure monitoring intervals at the observatory boreholes C0002G (931 to 980 m) and C0010A (389 to 407 m). bsf, below seafloor; VE, vertical exaggeration.

Similarly, little is known about their role in accommodating long-term plate motion, particularly in strain accumulation and release near the trench where seafloor deformation is intimately linked to tsunamigenesis (Fujiwara et al., 2011). Because the shallowest megathrust is

accessible by drilling and high-resolution imaging, documentation of slow earthquakes there presents an important opportunity to characterize the in situ conditions and rock properties and thus to probe the underlying mechanics of these events (Saffer and Wallace, 2015).

We report on observations from an array of borehole and seafloor instruments at the Nankai Trough offshore of Honshu, Japan. Our instruments captured a series of repeating SSEs and associated tremor swarms over a ~6-year period from 2011 to 2016. The Nankai Trough is formed by northwestward subduction of the Philippine Sea plate beneath the Eurasian plate at ~6.5 cm/year (Figure 36) (Miyazaki and Heki, 2001; Yokota et al., 2016). Over most of its depth extent, the plate interface is interseismically locked, as defined by geodetic studies and a history of recurring large earthquakes and tsunamis, including the 1944 Mw8.1 Tonankai event in which coseismic rupture extended to within 30 to 40 km of the trench (Kikuchi et al., 2003; Yokota et al., 2016). Previous work in this region has documented multiple VLFE and LFT swarms between the trench and the shallow termination of estimated coseismic rupture in the Tonankai earthquake (Obana and Kodaira, 2009; Obara and Kato, 2016; Sugioka et al., 2012), raising the possibility that slow slip may occur updip of the seismogenic zone. The Integrated Ocean Drilling Program and the International Ocean Discovery Program (IODP) NanTroSEIZE (Nankai Trough Seismogenic Zone Experiment) project installed subseafloor borehole observatories at two drill sites above the plate interface (holes C0002G and C0010A) (Figure 36 and 39) (Kopf et al., 2016; Kopf et al., 2011a). The two holes are separated by 11 km in the dip direction and straddle the shallow limit of estimated coseismic slip in the Tonankai earthquake. We report pore-fluid pressure measurements within isolated depth intervals containing fine-grained and low-permeability sediments at the two observatories. Variations in formation pore pressure in these sealed intervals provide a robust proxy for volumetric strain (Davis et al., 2015; Davis et al., 2013). The borehole observatories are part of an extensive offshore observatory, the Dense Oceanfloor Network System for Earthquake and Tsunamis (DONET) (Figure 36 A), which includes a dense array of seafloor seismometers and pressure gauges linked to shore by a submarine cable (Kaneda et al., 2015). The observatory facilitates the detection and location of LFTs and VLFEs offshore (To et al., 2015) (Figure 40).

We found eight strain transients from the formation pore-pressure records (Table 8). The strain transients included a variety of styles and event durations, all of which were caused by regional deformation, as they were synchronous at the two sites. The events lasted from a few days to several weeks, and some were accompanied by LFT swarms (Figure 37 and 38 and 41). The patterns of strain included: (i) mixed polarity, with a dilatation of ~0.05 to 0.24 microstrain (μ strain) (pore-pressure decrease of 0.26 to 1.35 kPa) at hole C0002G and a contraction of similar magnitude (0.13 to 0.15 μ strain, pressure increase of 0.62 to 0.71 kPa) at hole C0010A

(four events); (ii) contraction at both sites (0.04 to 0.07 μ strain, corresponding to pressure increases of 0.22 to 0.34 kPa) (two events); and (iii) dilatation at both sites (0.38 to 0.5 μ strain; pressure decreases of 1.8 to 2.72 kPa) (two events) (Figure 37 B and 41 A). One event began with a mixed-polarity signal (October 2015) (Figure 37 C), but after \sim 11 days the sign of strain at the more trenchward borehole (hole C0010A) reversed. Both sites were then characterized by dilatation for the remaining \sim 3-week duration of the mixed event.

The character of the two exclusively dilatation events is distinct from the mixed-polarity and compressional events, in that the volumetric strains are larger (Figure 38), and the events immediately follow the Mw 9.1 Tohoku-Oki (March 2011), Mw 6.0 Mie-ken Nanto-Oki, and Mw 7.0 Kumamoto (April 2016) earthquakes. This suggests that the SSEs were triggered by either static stress changes or dynamic stress changes from passing seismic waves. Although we cannot rule out the possibility of static triggering, dynamic triggering is most consistent with the large distances from the hypocenters of the Tohoku- Oki and Kumamoto earthquakes, the expected larger magnitude of dynamic relative to static stress changes, and widely observed magnitude distance thresholds for earthquake triggering (Freed, 2005; Gomberg and Davis, 1996). Triggering is well documented for normal earthquakes and tremors (Beroza and Ide, 2011; Freed, 2005; Gomberg and Davis, 1996; Schwartz and Rokosky, 2007), but observations of triggered SSEs are comparably rare (Itaba and Ando, 2011).

Low-frequency tremors accompany the strain events but are restricted primarily to one region trenchward of both drill sites and a second region \sim 20 km along strike to the northeast (Figure 37 and 41). The locations of these LFTs are broadly consistent with those of well-located LFTs and VLFES in the region from previous studies and clearly extend to the trench (Figure 37 and 41) (Obana and Kodaira, 2009; Obara and Kato, 2016; Sugioka et al., 2012). Some of the borehole pore-pressure transients are associated with energetic LFT swarms (e.g., October 2015 and April 2016), whereas others are accompanied by weaker activity. In most cases, LFT activity is generally concurrent with the strain transients in the boreholes (Figure 37 A and B, and 41). However, in some events (December 2012 and October 2015) (Figure 37 C and 41 C), LFT swarms initiate days after the strain transient begins. In the October 2015 case, the strain event observed in the boreholes begins on 10 October, whereas the LFT swarm initiates on 21 October—at the time of the reversal in sign of the strain signal at hole C0010A—and is localized mainly seaward of the borehole (Figure 37 C).

The concurrent LFT swarms and strain events at the two boreholes, together with their quasi regular recurrence, suggest that they represent SSEs on the subduction plate interface below (Davis et al., 2015; Davis et al., 2013; Obara and Kato, 2016; Sugioka et al., 2012).

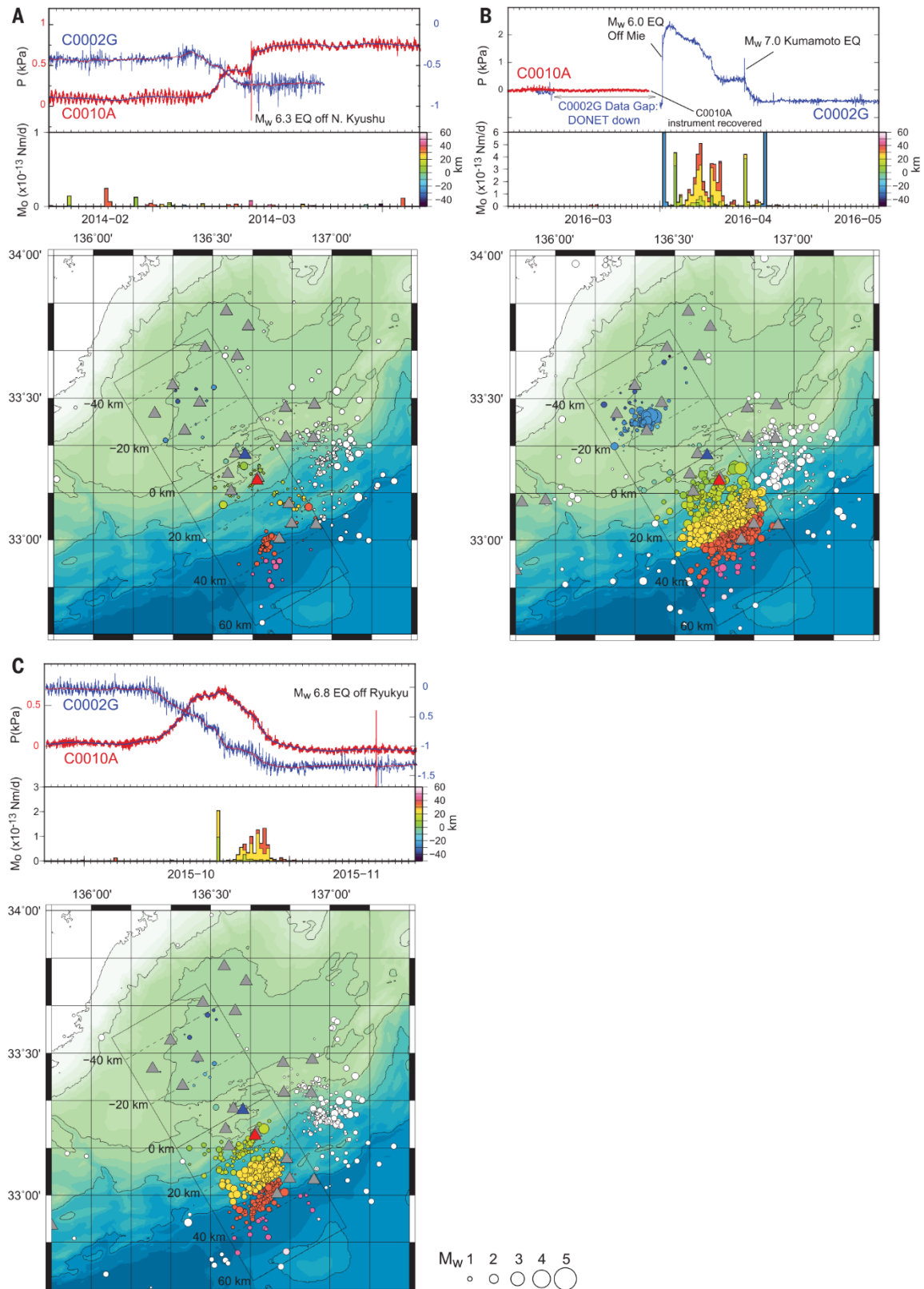


Figure 37: Formation pore-pressure and LFT records for three example SSEs. (A) March 2014, (B) April 2016, and (C) October 2015. In all examples, the top panel shows porepressure records (red, hole C0010A; blue, hole C0002G) filtered to remove oceanographic signals (see supplementary materials). Thin trace lines in the top panels of (A) and (C) show smoothed data using a 12-hour window. The middle panels show the seismic moment release rate (Mo) [in Newton meters per day (Nm/day)] for LFTs, binned by color to indicate position relative to hole C0002G (distances as shown in maps below). Migration of LFTs is suggested in both (B) and (C) (primary moment release shifts to shallower depths,

shown by warmer colors, over the duration of the swarms). Bottom panels show locations and magnitudes of LFTs (colors same as in middle panels, white for outside the square area), as well as DONET seafloor stations used to locate LFTs (gray triangles). For the April 2016 event (B), abrupt dilatation (decrease in pressure) initiates at the time of the Kumamoto earthquake; however, the preceding periods of rapid dilatation on 7 and 10 April do not correspond to any regional $M_w > 4.0$ earthquakes.

To explore this interpretation, we use a simple dislocation model to define the source locations, slip-patch widths, and fault displacements on the interface that are most consistent with the borehole data (Okada, 1992). We can explain the observed patterns of strain with ~ 1 to 4 cm of slip on the megathrust occurring on a 20- to 40-km wide patch, for all eight events. The polarity of the strain signal is dictated by the position of the patch relative to the boreholes (Figure 38 and 42). The best fit for mixed-polarity events requires 1 to 2 cm of slip centered below and between the two sites (25 to 36 km from the trench, ~ 4 to 6 km below seafloor). When contraction occurred at both sites, we found that a similar slip was required but needed to be centered farther landward (> 36 km from the trench, $> \sim 6$ to 7 km below seafloor). The dilatational signals potentially triggered by regional earthquakes required a slip patch centered seaward of both sites (< 24 km from the trench, $< \sim 4$ km depth) and larger slip (2 to 4 cm) relative to the other events (Figure 38 and 42). For the October 2015 event, the magnitude of strain and its reversal in sign partway through the sequence (Figure 37 C) are most consistent with a net slip of 2 to 4 cm and migration of slip from a region between the two boreholes toward the trench over ~ 3 weeks. The delayed onset of LFTs during the event and its localization to the region seaward of hole C0010A indicate that this SSE initiated silently and probably activated LFTs only upon reaching the area closer to the trench (Figure 37 C).

Based on our data, we suggest that periodic SSEs occur along the outermost reaches of the megathrust every 8 to 15 months (Figure 38). Because the strain transients appear to repeat at relatively short intervals and the required deformation at the borehole sites is equivalent to that caused by centimeters of slip on the plate interface, these SSEs most plausibly reflect slip on the megathrust. If the deformation were distributed elsewhere, we cannot reconcile the required displacement with long-term slip on the plate boundary of ~ 6.5 cm/year. Additionally, the signs of strain at the two boreholes, in combination with the locations of LFTs (Figure 37), are not well explained by slip on normal faults or on the megasplay fault in the upper plate, although these modes of deformation have been suggested for isolated events on the basis of inferred seafloor displacements and the focal mechanisms of VLFs following the Tohoku-Oki earthquake (Suzuki et al., 2016; To et al., 2015).

The fault slip amounts we determined from dislocation models require that these SSEs accommodate ~ 30 to 55 % (~ 11 to 22 cm) of the total plate convergence budget (~ 39 cm) over the 6-year observation period. Slip rates for the SSEs, based on the estimated ranges of total displacement and the duration of each event, are ~ 0.1 to 2 cm/day, comparable to those

documented for isolated shallow SSEs observed on other subduction megathrusts (Davis et al., 2013; Dixon et al., 2014; Saffer and Wallace, 2015; Wallace et al., 2016b). The two likely triggered SSEs exhibited larger slip and were centered farther seaward than the six spontaneous ones (Figure 38 and 42).

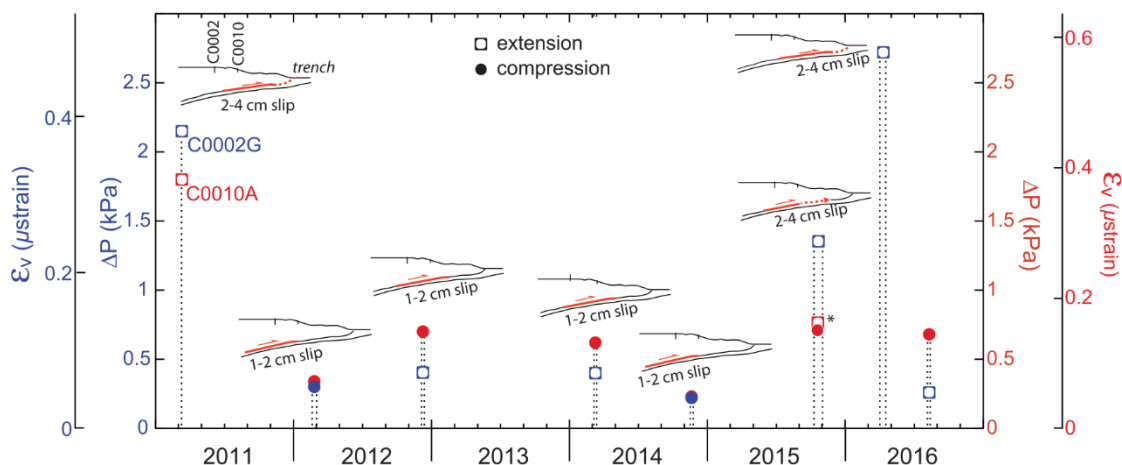


Figure 38: Summary of pressure and strain transients at holes C0002G (blue) and C0010A (red). Dashed vertical lines indicate the duration of each event. Those characterized by pressure increase (compressional strain; solid circles) at both boreholes are most consistent with 1 to 2 cm of slip centered >36 km from the trench, as shown in schematic cross sections for each event (compare with Figure 42 A). Those characterized by dilatation (extension; open squares) at hole C0002G and compression at hole C0010A are most consistent with 1 to 2 cm of slip centered 24 to 38 km from the trench, and those by dilatation at both boreholes are consistent with slip of 2 to 4 cm centered <27 km from the trench. The October 2015 event (denoted by the asterisk) exhibited extension only at hole C0002G, and initial compression followed by dilatation at hole C0010A. ϵ_v , volumetric strain; ΔP , change in pressure.

Our observations also allow us to illuminate the spatiotemporal relationships between SSEs and LFTs. The location and timing of primary slip slip we deduced from strain at the boreholes were not always coincident with LFTs. All of the spontaneous SSEs exhibited either compression at both boreholes or mixed polarity, indicating that the main slipping patch lies landward of hole C0010A. Yet LFT swarms were restricted mainly to the area 10 to 20 km trenchward of the boreholes (Figure 37 and 41). In comparison, events that exhibited primary slip nearest the trench (e.g., April 2016) were accompanied by many LFTs in that same region (Figure 37 B and C). In the October 2015 event, the onset of LFTs at the time of strain sign reversal and the inferred migration of slip updip of hole C0010A provide additional evidence that LFTs do not fully map the slipping region. Instead, tremor appears to be activated by the SSE (rather than slip being driven by cascading tremor), and much of the slip occurs without any radiated seismic energy. The total seismic moment from tremor is on the order of 5×10^{13} Newton meters (N m) (Figure 37 C), whereas the moment expected for 2 to 4 cm of slip in the tremor patch of area 400 to 1600 km² (rectangular patch of 20- to 40-km dimension) would be $\sim 4 \times 10^{16}$ to 3.2×10^{17} N m (Mw 5.0 to 5.6), assuming a rigidity of 10 GPa for the near-trench

region. Finally, the recurrence of LFTs restricted to particular areas (near the trench and in a patch along strike to the northeast) (Figure 37 and 41) suggests that their occurrence is controlled by the presence of small-scale asperities, likely related to local fault frictional, compositional, hydraulic, or geometric properties that persist over multiple SSE cycles (Shelly et al., 2007).

Our data provide evidence for repeated SSEs associated with tremor in the outer reaches of a subduction megathrust. The SSE source areas coincide with locations of previously observed LFTs and VLFs (Obara and Kato, 2016; Sugioka et al., 2012), within a region of the megathrust characterized by anomalously low seismic velocity and elevated pore-fluid pressure. This picture is consistent with models suggesting that SSEs and slow earthquakes originate in areas of very low effective stress (Liu and Rice, 2007; Saffer and Wallace, 2015). The SSEs are arguably the clearest example of slow slip directly trenchward of a strongly locked seismogenic zone, along a megathrust that produces large earthquakes, raising the possibility that SSEs may also be common at similar subduction zones that host large or giant earthquakes, such as Cascadia (Wallace et al., 2016b; Yamashita et al., 2015).

The regularity and relatively short recurrence of these SSEs, taken together with evidence for dynamic triggering, suggest that the outer subduction megathrust is mechanically weak and highly sensitive to perturbations. The SSEs account for a large proportion of the total plate convergence budget over the 6-year monitoring period. If this pattern is sustained over longer time scales, it implies that the shallow portion of the megathrust is unlikely to store substantial interseismic strain between large subduction earthquakes, consistent with relatively weak interplate coupling in this area over decadal time scales deduced from geodetic data (Yokota et al., 2016). If these newly observed near trench SSEs are a mechanism for periodic and frequent release of accumulated strain, the hazards associated with shallow earthquake rupture and tsunami generation in this region may be reduced. Continued offshore monitoring is critical for revealing longer-term patterns of strain accumulation and release, as well as possible links between shallow SSEs and large, damaging earthquakes (Wallace et al., 2016a).

Acknowledgement

This work was supported by Japan Society for the Promotion of Science KAKENHI grant JP15H05717, NSF grants NSF-OCE 0623633 and NSF-OCE 1334436, and Deutsche Forschungsgemeinschaft grant KO2109/25-1. The borehole pore-fluid pressure data used for this research are openly available from JAMSTEC (join-web.jamstec.go.jp/join-portal/en/) and The Pennsylvania State University (offshore.geosc.psu.edu); the data set is also available from

the National Environmental Information Center. Seafloor seismometer data are available from JAMSTEC on request.

Author Contributions

First author E. Araki wrote the manuscript about SSE detection based on borehole pressure data. I participated in the IODP expedition 365 where the GeniusPlug borehole observatory was recovered. As onboard observatory specialist, I was responsible for the pressure and temperature data acquisition. Besides technical assistance, initial data processing was done by myself. I reviewed and commented on the paper drafts before submission.

Supplementary materials

IODP Expedition 365 shipboard scientists

Name	Affiliation
Achim J. Kopf	MARUM-Center for Marine Environmental Sciences University of Bremen
Demian M. Saffer	Department of Geosciences The Pennsylvania State University
Sean Toczko	Center for Deep Earth Exploration Japan Agency for Marine-Earth Science and Technology Research and Development Center for Earthquake and Tsunami Japan Agency for Marine-Earth Science and Technology
Eiichiro Araki	Research and Development Center for Earthquake and Tsunami Japan Agency for Marine-Earth Science and Technology
Stephanie Carr	Bigelow Laboratory for Ocean Sciences Research and Development Center for Earthquake and Tsunami Japan Agency for Marine-Earth Science and Technology
Toshinori Kimura	Research and Development Center for Earthquake and Tsunami Japan Agency for Marine-Earth Science and Technology
Chihiro Kinoshita	Kyoto University
Reiji Kobayashi	Kagoshima University Departments of Earth and Environmental Sciences Research and Development Center for Earthquake and Tsunami Japan Agency for Marine-Earth Science and Technology
Yuya Machida	Research and Development Center for Earthquake and Tsunami Japan Agency for Marine-Earth Science and Technology
Alexander Rösner	MARUM-Center for Marine Environmental Sciences University of Bremen
Laura M. Wallace	GNS Science, New Zealand

Materials and methods

The borehole observatory at Hole C0002G, installed in 2010, comprises an integrated suite of instruments, including formation pore-fluid pressure sensing within two hydraulically isolated depth intervals (757 – 780 and 931 – 980 m below sea floor; mbsf), a thermistor array, and a volumetric strainmeter, tiltmeter, and broadband seismometer (Figure 39) (Kopf et al., 2011a). The upper pressure sensing interval is composed of mudstones with interbedded sands and silts, whereas the lower interval lies within a uniform mudstone section. At Hole C0010A, a simpler temporary observatory was installed during the same drilling expedition, designed to monitor only formation pore fluid pressure and temperature in an interval spanning 389 – 407 mbsf, within a fault zone that is capped by a few hundred meters of relatively uniform mudstone (Kopf et al., 2016; Kopf et al., 2011a). This temporary instrument package was retrieved in April 2016, and replaced with a permanent observatory similar in configuration to that at Hole C0002G (Kopf et al., 2016).

We focus specifically on the pore pressure measurements, because: (1) they are the only dataset available at both boreholes before April 2016; and (2) the borehole tilt and strain record in Hole C0002G exhibits high noise levels in the long-period range related to a problem with the integrity of the cement and the instrument, and we thus consider it unreliable. The strainmeter at Hole C0010A, which was deployed in late April 2016, appears to be functioning properly and recorded the event we observed in pore pressure records during July – August 2016. Although this single event was observed in both the pore fluid pressure and strain datasets, a reliable strainmeter record was not available during the most of our observation

period. At Hole C0002G, the pressure records from the two monitored intervals exhibit the same response to the SSEs. We report pressure records only from the deeper of the two because the more uniform and lower permeability mudstone there results in less noise relative to the upper interval, which is affected by local fluid flow in permeable (sandy and silty) horizons.

At both boreholes, we take advantage of a co-located reference pressure sensor at the seafloor to remove tidal and other oceanographic loading from the formation porefluid records with high precision, in order to extract signals related to volumetric strain or hydrologic transients (Davis et al., 2015; Davis et al., 2013). This is accomplished by: (1) scaling the seafloor pressure variations by an amplitude damping factor (known as the loading efficiency) governed by formation and fluid elastic properties defined at the dominant tidal period; and (2) subtracting these variations from the formation pressure (Davis et al., 2015). We also account for phase lag between the ocean tidal signal and formation pressure signals by shifting the scaled seafloor pressure prior to subtraction. The phase lag at these depths is caused by the finite time required for fluid to flow from the formation into the sensing volume and equilibrate pressure in the observatory (Davis et al., 2015; Davis et al., 2013). Contributions to the formation signals are also expected from earth tidal strain. At Hole C0002G, there is no resolvable phase lag, whereas at Hole C0010A there is a small lag (between 90 – 120 seconds). With a sampling interval of 30 s for the majority of the deployment (until June 2016 when the borehole was connected to the DONET cable), we are unable to account for this small phase lag perfectly, and as a result there is a small residual tidal signal even in the corrected pressure records (on order of ± 0.1 kPa). In general, the very small phase lag provides evidence of good hydraulic communication between the formation and sensing volume of the observatory.

We then relate formation pore fluid pressure changes to volumetric strain using the approach of Davis et al. (2013) and Wang (2004), and constrained by measurements of the sediment physical properties within each monitoring interval. The resulting pressure-to-strain conversion factors of 4.7 kPa/ μ s (C0010A) and 5.7 kPa/ μ s (C0002G) are highly consistent with observed step changes in pore pressure at the two boreholes in response to static strain from a well-characterized nearby M6 earthquake in April 2016 (the Mie-Ken Nanto-Oki event); this event provides a unique and valuable field calibration of the pressure-strain conversion (Wallace et al., 2016a). This approach allows us to resolve < 0.05 μ strain (0.25 kPa), corresponding to < 1 cm of slip on the plate interface (Figure 42). The formation pressures are more sensitive to buried fault slip than seafloor pressure gauges, which can distinguish vertical motions on the order of ~ 1 cm, depending on the level of oceanographic noise and the duration of the deformation (Suzuki et al., 2016; Wallace et al., 2016b). We note that the values of volumetric

strain we report, which are defined by pore pressure changes, should be considered minima. This is because any drainage – and thus dissipation of the pressure signal - over the length of the events (days to weeks), would lead to an underestimate of the true undrained response in the formation.

Low frequency earthquakes (VLFs and LFTs) were detected using broadband seismographic records from DONET seafloor stations (Figure 36 A). In the study area, observed VLFs (0.04 – 0.08 Hz band) always accompanied LFT (2 – 8 Hz band) (see example in Figure 40). Because the signal amplitude in the LFT frequency band tends to be much larger than in the VLFE band for stations near the source, LFT were more readily identified than VLFE using the DONET network. Hence, we identified and located LFTs for the observation period using an envelope cross correlation method (Ide, 2012) in the 2 – 8 Hz band using all available DONET vertical and horizontal broadband seismic records. Seismic moment (M_0) of each LFT event was also evaluated from the amplitude of ground motion, assuming a relationship of earthquake energy: $E_s/M_0 = 10^{-5}$ (Ide and Yabe, 2014).

To define fault slip models that are consistent with our borehole observations of strain, we use a simple dislocation model that includes a single tapered slipping patch (Okada, 1992) (Figure 42 A). We undertake a suite of forward models to determine the general location of the slipping patch that best agrees with the data. Given that we only have data from two sites, we do not invert the data for slip, as this is a severely underdetermined problem. The primary objective of these models is to constrain the general width and position of potential SSE slip patches and the fault displacements required to reproduce observed volumetric strain at the two drill holes. Although the detailed distribution of slip is likely to be more complex than a single tapered patch (Dixon et al., 2014; Wallace et al., 2016b), these simple models provide robust first-order constraints on the location and amount of primary slip that would lead to the magnitude and sign of strain at the two monitoring locations. Moreover, more complex slip models would be underdetermined given our spatially limited data.

We explore scenarios with 1, 2, and 4 cm of slip on fault patches with widths of 20 and 40 km, and consider a range of slip patch locations (defined by the up-dip edge of slip) spanning from 1 to 40 km landward of the trench (Figure 42). We restrict our analysis to these patch widths, because initial models illustrate that larger slip patches would not reproduce the observed sign of strain in most of the events without breaching the trench, whereas smaller (i.e. 10 km-wide) patches require larger displacements to produce the observed strain, in turn leading to seafloor vertical displacements >1 cm, which would be detectable but are not observed in absolute pressure gauge data at the seafloor during our observation period. We note that this contrasts with a possible large isolated SSE hypothesized to have occurred along the splay fault,

postulated on the basis of long-term (>7 month duration) gradual pressure changes observed at three local seafloor pressure sensors in the DONET node along northeast of the boreholes (Suzuki et al., 2016). Because predicted volumetric strains are insensitive to dip-slip motion out of plane, it is clear that our data reflect fault slip on the interface below (i.e. along the transect containing) the boreholes (cf. Figure 37; Figure 41), but provide little constraint on the persistence of slip patches alongstrike.

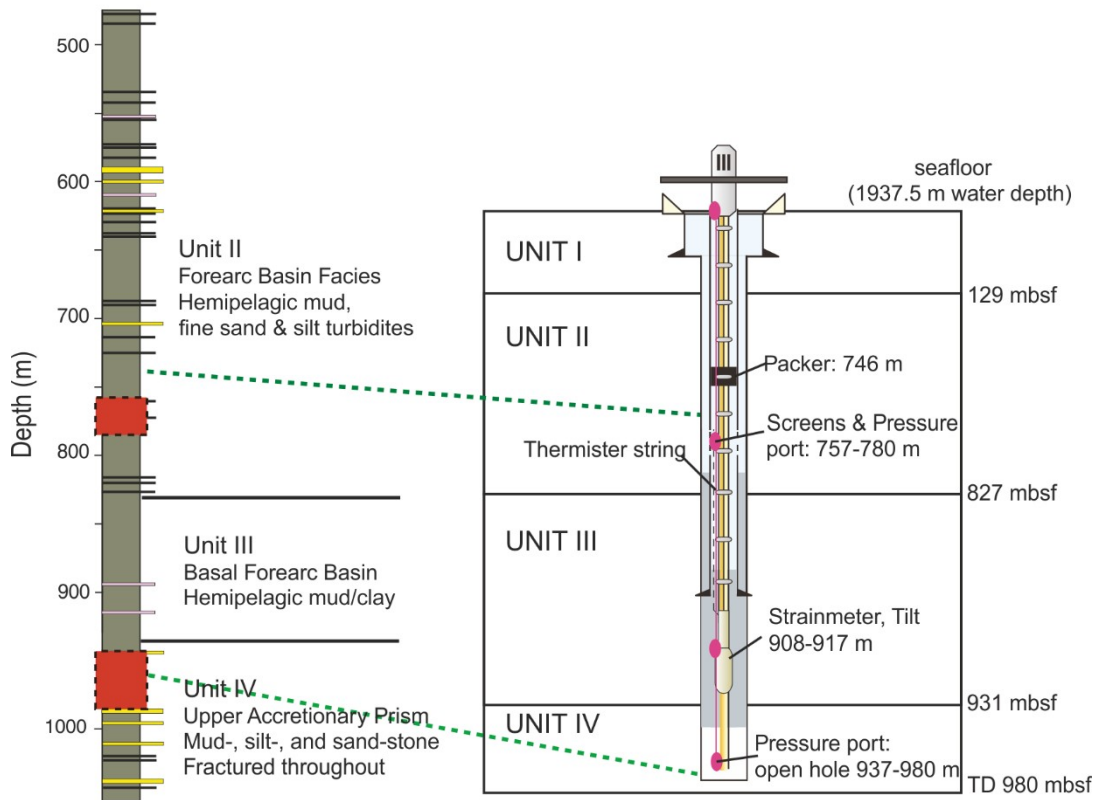
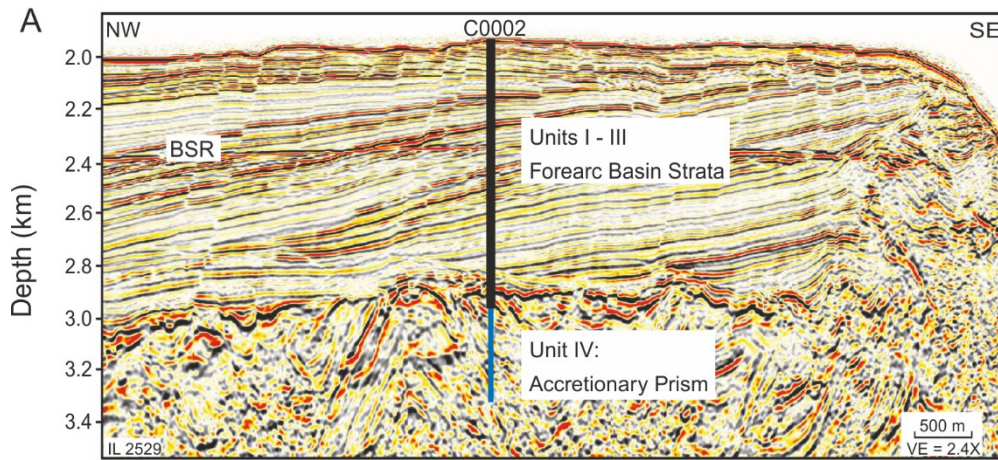
Table 8: Summary of borehole pressure signals and SSE characteristics.

Dates	Polarity	ΔP_{C0002} (kPa) ^a	ΔP_{C0010} (kPa)	Slip (cm)	Location (km landward of trench) ^b
Mar 11-13, 2011	Dilatation	-1.8	-2.15	02. Apr	<24
Feb 14-May 6, 2012	Contraction	0.3	0.34	01. Feb	>36
Dec 5-14, 2012	Mixed	-0.43	0.7	01. Feb	25-36
Mar 6-19, 2014	Mixed	-0.4	0.62	01. Feb	25-36
Nov 19-Dec 1, 2014	Contraction	0.22	0.23	01. Feb	>36
Oct 8-Nov 4, 2015 ^c	Mixed/Dilatation	-1.35	0.71/-0.72	02. Apr	25-36 / <24
Apr 3-18, 2016	Dilatation	-2.72	N/A	02. Apr	<24
Aug 10-24, 2016	Mixed	-0.26	0.68	01. Feb	25-36

^acontractional volumetric strains correspond to positive pressure changes; dilatational strains correspond to negative pressure changes.

^blocation reported as the center of slip patch of 20-40 km width (c.f. Figure 42).

^cOctober-November 2015 event exhibited a reversal in strain polarity at Site C0010. Two values are reported, representing the peak pressure increase at each borehole and the slip patch location corresponding to the mixed-polarity phase (first value), followed by those corresponding to the dilatational phase (see Figure 37 C).



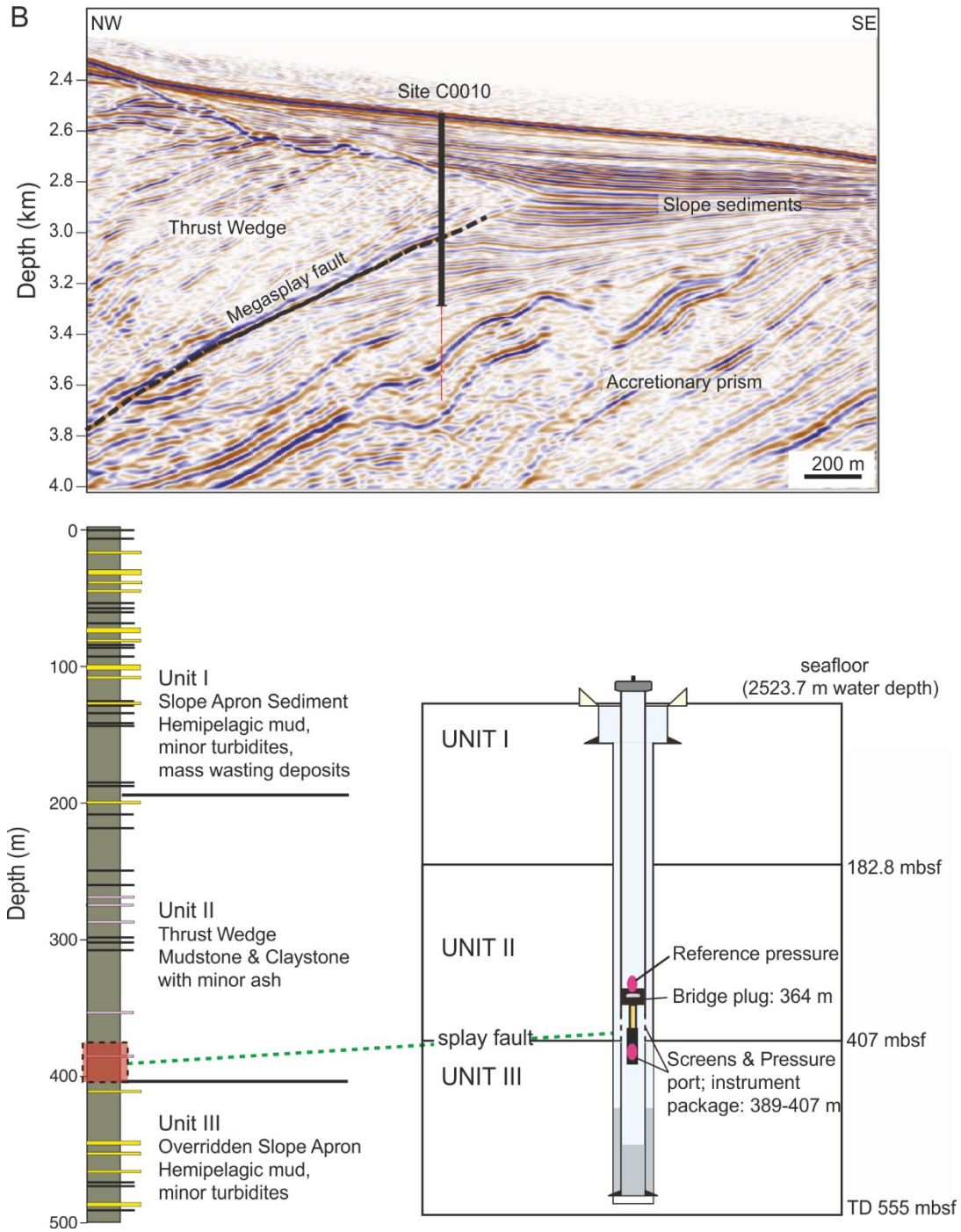


Figure 39: Seismic section showing location of borehole observatory installations (top), schematic stratigraphic column (lower left) and borehole completion diagram (lower right) for: (A; preceding page) Hole C0002G and (B; above) Hole C0010A (Kopf et al., 2016; Kopf et al., 2011). In the stratigraphic columns, gray indicates clay- and mudstone, black indicates silt, yellow indicates sand, and pink indicates ash. Both observatories include formation pressure ports and a hydrostatic reference pressure sensor (at the wellhead in (A) and above the instrument package in (B)) used to remove oceanographic signals (modified after Araki et al., 2017).

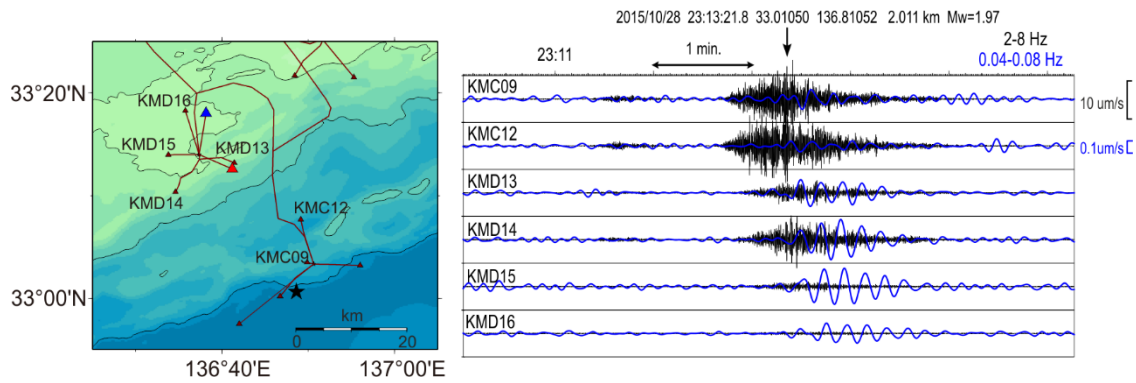
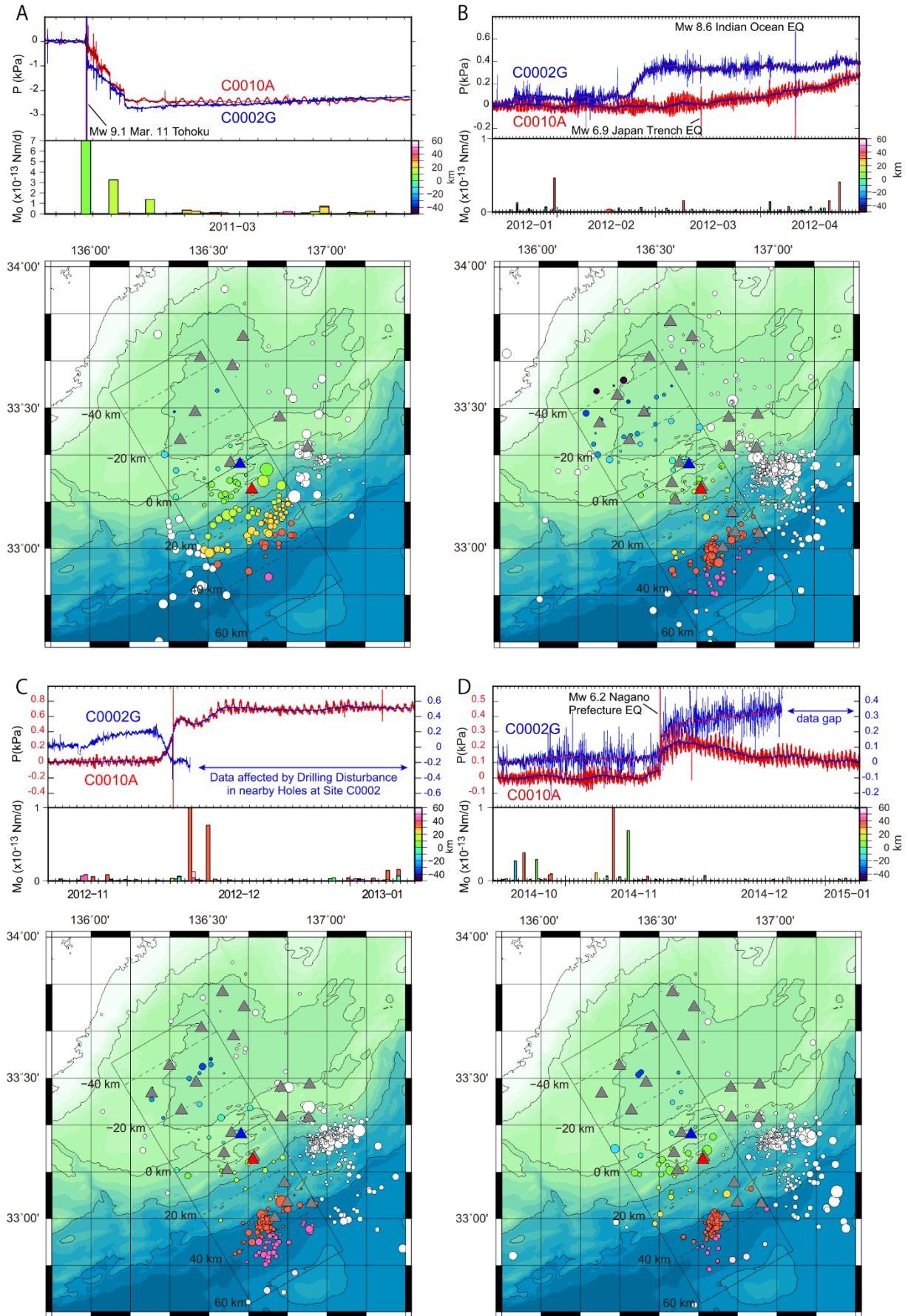


Figure 40: An example of very low frequency earthquake (VLFE) and low frequency tremor (LFT) event identified by DONET seafloor stations. Vertical component records filtered in two frequency bands (0.04 – 0.08 Hz (blue) and 2 – 8 Hz (black)) are overlain (note different scales). The LFT event was located near station KMC09 (shown by black star in map at left), and the event clearly exhibits both low frequency (0.04 – 0.08 Hz) and high frequency (2 – 8 Hz) seismic waves propagating from the same region at the same time (modified after Araki et al., 2017).



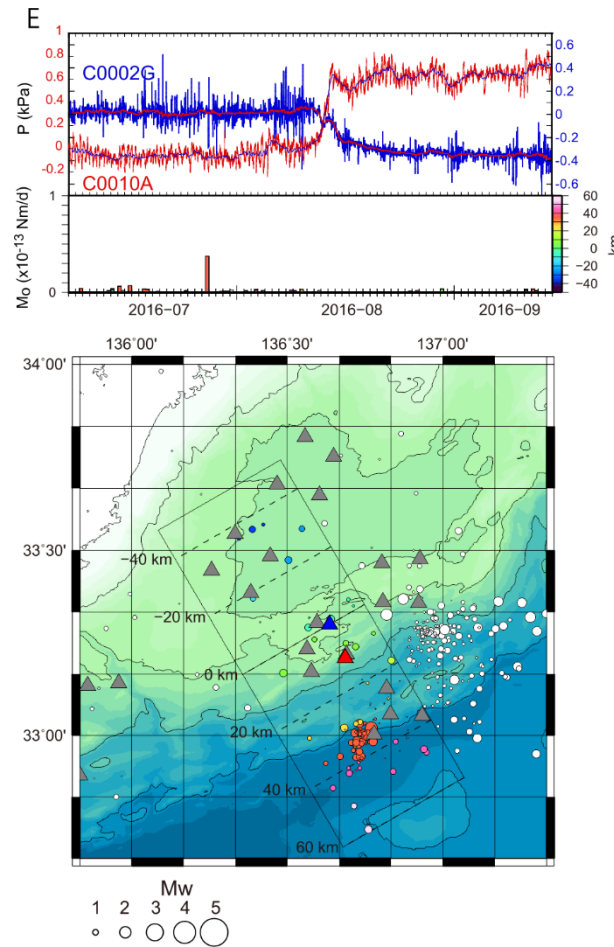


Figure 41: Formation pore pressure and LFT records for remaining SSEs not shown in Figure 37 in main text. Panels A – D are shown on preceding page; E is directly above. (A) March 2011; (B) Feb. 2012; (C) Dec. 2012; (D) Nov. 2014; (E) Aug. 2016. In all examples, top panel shows pore pressure records (Hole C0010A = red; Hole C0002G = blue) filtered to remove oceanographic signals. Thin lines in figures (A) and (C) show smoothed data using a 12 h window. Second panel shows seismic moment release rate (Nm/day) for LFT, binned by color to indicate position relative to Hole C0002G (distances as shown in map, lower panel in each figure). Migration of LFT is evident for the March 2011 SSE following the Tohoku earthquake (panel A). Bottom panel shows locations and magnitudes of LFT using the same color legend as the second panel, and DONET seafloor stations used to locate LFT (gray triangles).

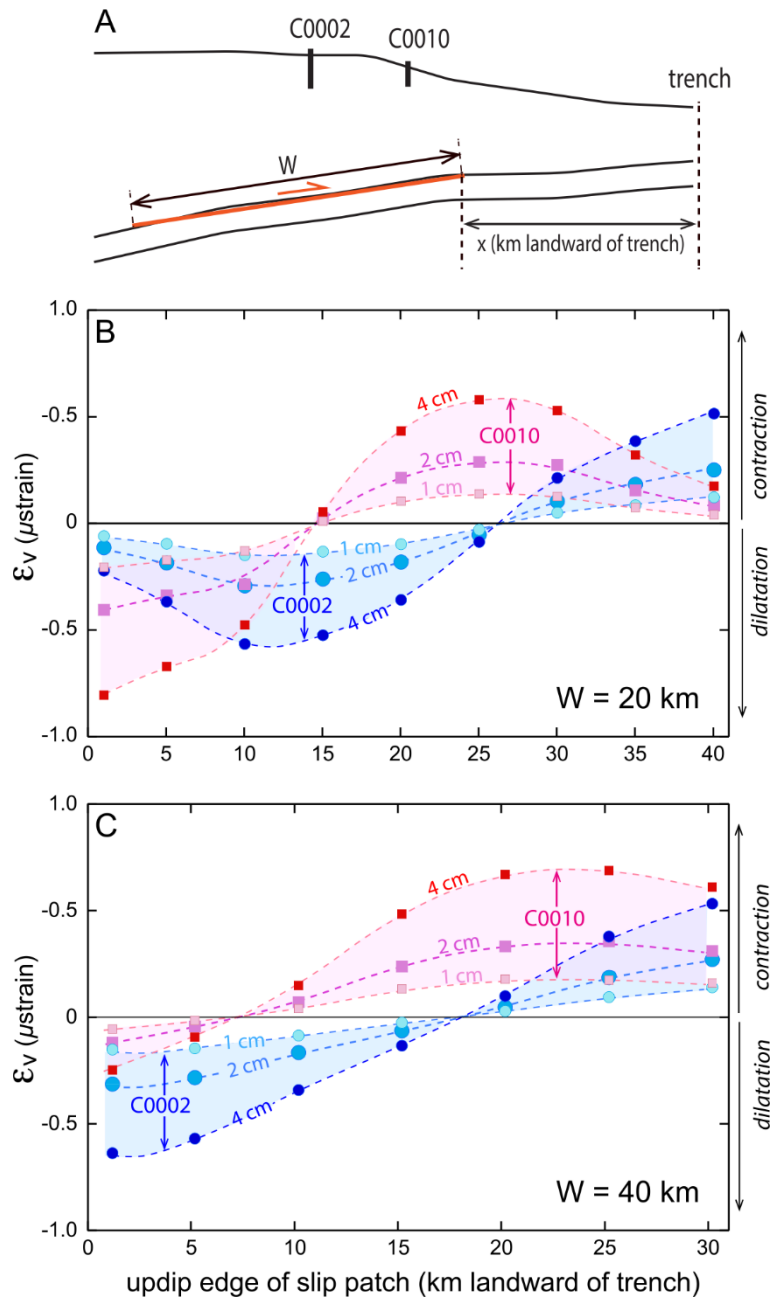


Figure 42: (A) Schematic of elastic dislocation models. (B) and (C) Predicted volumetric strain at the two borehole monitoring intervals for (B) a 20 km and (C) a 40 km wide slipping patch (as measured in the dip direction) and for slip of 1, 2, and 4 cm (as labeled). For all models, slip is assumed to be pure dip-slip and to occur on the plate interface, with dip of 6° , and a uniform Poisson's ratio of 0.35. Volumetric strain for most of the events ranges from 0.04 to 0.16×10^{-6} . For the two largest pressure transients interpreted to indicate extensional strain at both boreholes, the volumetric strain ranges from 0.38 to 0.48×10^{-6} (cf. Figure 38 in main text) (modified after Araki et al., 2017).

3.4 Manuscript 6 (JGR published): Changes in Physical Properties of the Nankai Trough Megasplay Fault Induced by Earthquakes, Detected by Continuous Pressure Monitoring [co-authorship]

C. Kinoshita¹, D. Saffer², A. Kopf³, **A. Roesner**³, L.M. Wallace^{4,5}, E. Araki⁶, T. Kimura⁶, Y. Machida⁶, R. Kobayashi⁷, E. Davis⁸, S. Toczko⁶, and S. Carr⁹

¹Disaster Prevention Research Institute, Kyoto University, Kyoto, Japan

²Department of Geosciences, The Pennsylvania State University, University Park, PA, USA

³MARUM, University of Bremen, Bremen, Germany

⁴Institute for Geophysics, University of Texas, Austin, TX, USA

⁵GNS Science, Lower Hutt, New Zealand

⁶JAMSTEC, Yokohama, Japan

⁷Graduate School of Science and Engineering, Kagoshima University, Kagoshima, Japan

⁸Pacific Geoscience Centre, Geological Survey of Canada, Sidney, Canada

⁹Bigelow Laboratory for Ocean Sciences, East Boothbay, ME, USA

Abstract

One primary objective of Integrated Ocean Drilling Program Expedition 365, conducted as part of the Nankai Trough Seismogenic Zone Experiment, was to recover a temporary observatory emplaced to monitor formation pore fluid pressure and temperature within a splay fault in the Nankai subduction zone offshore SW Honshu, Japan. Here we use a 5.3 year time series of formation pore fluid pressure, and in particular the response to ocean tidal loading, to evaluate changes in pore pressure and formation and fluid elastic properties induced by earthquakes. Our analysis reveals 31 earthquake-induced perturbations. These are dominantly characterized by small transient increases in pressure (28 events) and decreases in ocean tidal loading efficiency (14 events) that reflect changes to formation or fluid compressibility. The observed perturbations follow a magnitude-distance threshold similar to that reported for earthquake-driven hydrological effects in other settings. To explore the mechanisms that cause these changes, we evaluate the expected static and dynamic strains from each earthquake. The expected static strains are too small to explain the observed pressure changes. In contrast, estimated dynamic strains correlate with the magnitude of changes in both pressure and loading efficiency. We propose potential mechanism for the changes and subsequent recovery, which is exsolution of dissolved gas in interstitial fluids in response to shaking.

Introduction

Crustal deformation induced by seismic events produces wide-ranging hydrological effects, in some cases at distances of several tens to hundreds of kilometers, inducing changes in well water levels; changes in spring discharge and chemistry, liquefaction, and geyser; and mud volcano eruptions (Rudolph and Manga, 2010; Wang and Manga, 2010). In some cases, induced damages are unexpected and larger than caused by the main shock (Greene et al., 1991; Yasuda et al., 2013). Additionally, although they are not as widely observed, transient changes in fluid pressure and permeability along fault zones (Fulton and Brodsky, 2016; Kitagawa and Kano, 2016; Xue et al., 2013) are of particular importance for understanding possible earthquake or slip triggering phenomena, because fluid redistribution within faults changes effective stresses (Mulargia and Bizzarri, 2014).

Montgomery and Manga (2003) summarized mechanisms that produce earthquake-induced changes in hydrological systems, all of which depend on the magnitude of static or dynamic strains. Static strains represent elastic or permanent deformation of the crust produced by fault slip, and dynamic strains are caused by temporary (oscillatory) crustal deformation associated with the passage of seismic waves. These can produce compression and extension of rock formations and interstitial pores, ultimately affecting formation properties such as permeability, storage coefficient, and compressibility. In addition to dynamic strains, ground shaking may generate transient local hydraulic gradients that force water flow in fractures and pore throats, mobilizing fine particles and leading to changes in permeability and compressibility (Brodsky et al., 2003; Candela et al., 2014; Elkhoury et al., 2011). Monitoring of crustal deformation and estimating changes in rock properties constitute one key strategy to characterize such hydrological perturbations.

In this study, we use continuous monitoring of formation pore fluid pressure in a sealed borehole to define changes in rock properties within a fault zone in the Nankai subduction zone, located offshore southwest Honshu in Japan (Figure 43). The borehole observatory was installed at Integrated Ocean Drilling Program (IODP) Site C0010 as part of the Nankai Trough Seismogenic Zone Experiment (Kopf et al., 2011a). The observatory hole (Hole C0010A) crosses a major out-of-sequence splay thrust fault (termed the “megasplay”) at a depth of 407 m below seafloor (bsf) (Figure 43 B and 44). This fault branches from the plate interface below and has been hypothesized to slip coseismically in historical great earthquakes (Mw 8 class) (Ando, 1975b; Ichinose et al., 2003; Kikuchi et al., 2003). In addition, very low frequency earthquakes and slowslip events have been observed in this area at depths <10 – 12 km and may occur on the deep reaches of the megasplay fault (Araki et al., 2017; Ito and Obara, 2006b; Sugioka et al., 2012).

We use a time series of formation pore pressure from within the fault zone to investigate three phenomena: (1) formation pressure responses to ocean tidal loading as indicators of formation hydraulic properties, (2) step changes in formation pressure induced by earthquakes, and (3) associated changes in the tidal loading efficiency, as a measure of changes in formation and/or fluid poroelastic properties. We then explore possible mechanisms for the earthquake-induced changes in pore pressure and loading efficiency by considering the effects of static and dynamic strains.

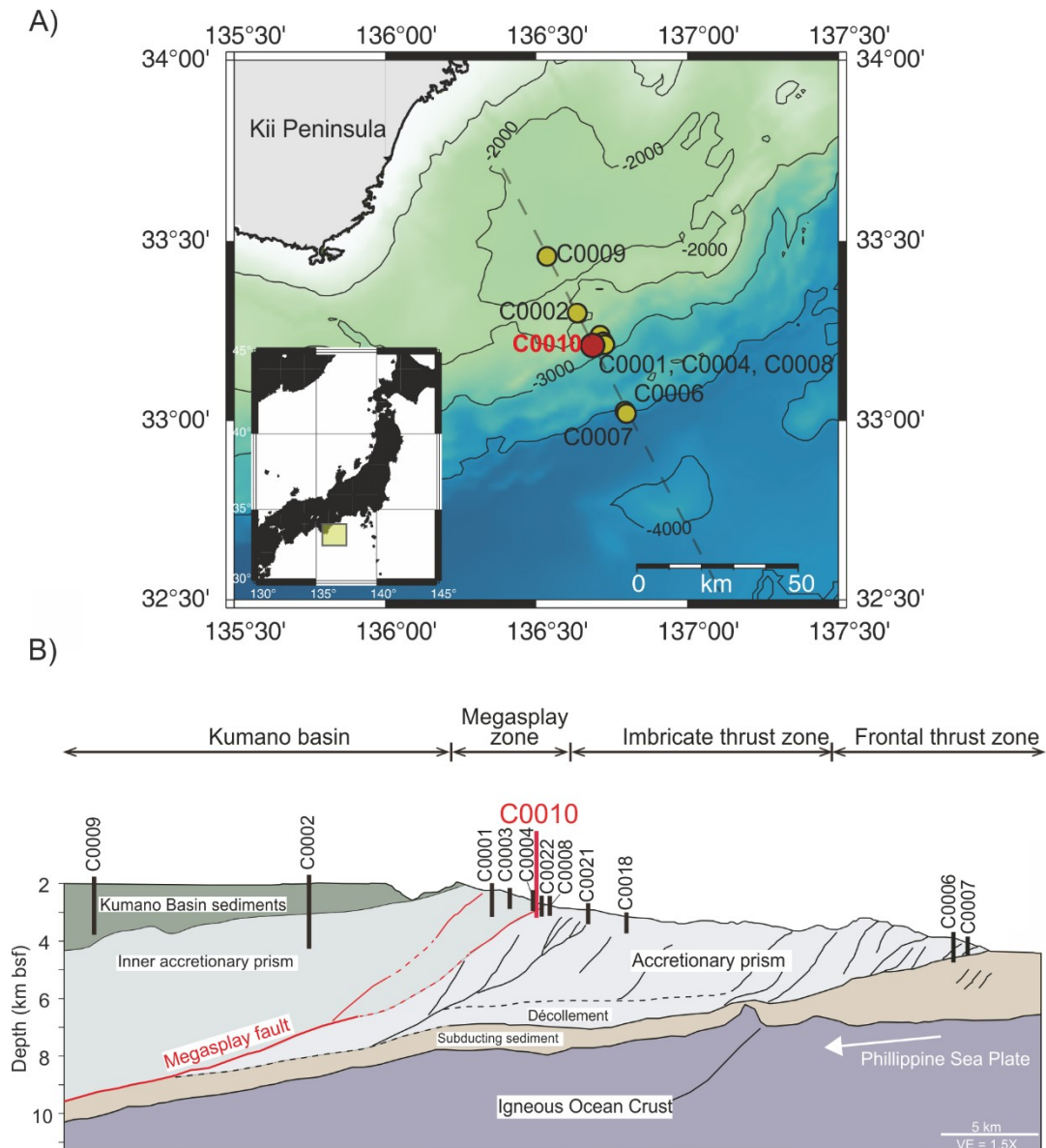


Figure 43: Location of NanTroSEIZE drillsites (modified from Kopf et al., 2016). **(A)** Map of the drilling sites (circles). We focus on analysis of data from a temporary observatory installed at Site C0010 (red circle), which penetrates the shallow megasplay fault at 407 mbsf. **(B)** Schematic image of cross section along gray dashed line in (A) (modified after Kinoshita et al., 2018a).

Geological Setting

Nankai Trough Subduction Zone

The Nankai trough is one of the best-studied subduction zones globally, with numerous drilling efforts, geophysical surveys, and earthquake studies aimed at understanding the margin's structure, earthquake processes, hydrogeology, and tectonic history (Hirose et al., 2010; Kinoshita et al., 2009; Moore et al., 2007; Strasser et al., 2009). The Nankai Trough is located offshore southwest Honshu Japan, where the Philippine Sea Plate subducts northwestward beneath the Eurasian Plate at ~6.5 cm per year (Miyazaki and Heki, 2001; Seno et al., 1993). Offscraping of trench fill and hemipelagic sediments of the Shikoku Basin on the Philippine Sea Plate has formed a wide accretionary prism with well-developed fold-and-thrust belt structures (Aoki et al., 1983; Moore et al., 2009; Park et al., 2000) (Figure 43 B). The megasplay fault forms a boundary between the active outer accretionary prism and a less active inner prism that is overlain by Pleistocene sediments of the Kumano Basin.

IODP Site C0010 intersected the megasplay fault near its updip termination, at a depth of 407 m bsf (Saffer et al., 2010). The borehole penetrated three lithological units as defined on the basis of logging while drilling and coring (McNeill et al., 2010). These are thought to represent the regional geology of the shallow megasplay and include (i) Pleistocene slope sediments (Unit I, 0 – 182.8 mbsf) composed of hemipelagic mud and minor turbidite interbeds, (ii) a thrust wedge (Unit II, 182.8 – 407 mbsf) composed of Pleistocene clay and mudstones uplifted by movement on the fault, and (iii) overridden Pleistocene slope sediments (Unit III, >407 mbsf) composed of hemipelagic mud.

Borehole Observatory Configuration and Deployment

Hole C0010A was drilled in 2009 during IODP Expedition 319, in 2,524 m water depth, and to a total depth of 555 mbsf. The borehole crosses the megasplay fault at 407 mbsf (Saffer et al., 2010). The borehole was completed by installing casing with screens spanning the depth interval from 387 to 409 mbsf, allowing hydraulic access to the fault zone (Figure 44). At the time the hole was drilled and completed, an initial temporary instrument package (termed a "SmartPlug") was suspended in the hole below a retrievable packer (a bridge plug) that was set within the casing and above the screened interval (Saffer et al., 2010). The bridge plug served to isolate the monitoring interval from the overlying ocean, and the instruments initially recorded formation pressure and temperature at the depth of the screens, as well as an overlying ocean reference pressure from August 2009 until December 2010 (Kopf et al., 2011a). This instrument package was recovered in 2010 as part of IODP Expedition 332 and

replaced with a “GeniusPlug” having fluid sampling capabilities (Kopf et al., 2011b). Analysis of the SmartPlug deployment records has provided initial information about formation pressure and temperature responses to earthquakes, as well as preliminary estimates of formation properties (Hammerschmidt et al., 2013a; Hammerschmidt et al., 2013b). However, these analyses are limited by the short duration of the deployment and by partial decoupling of the reference pressure sensor from the overlying ocean by a cap at the wellhead, which led to incomplete accounting for oceanographic and tidal signals (Hammerschmidt et al., 2013a; Hammerschmidt et al., 2013b).

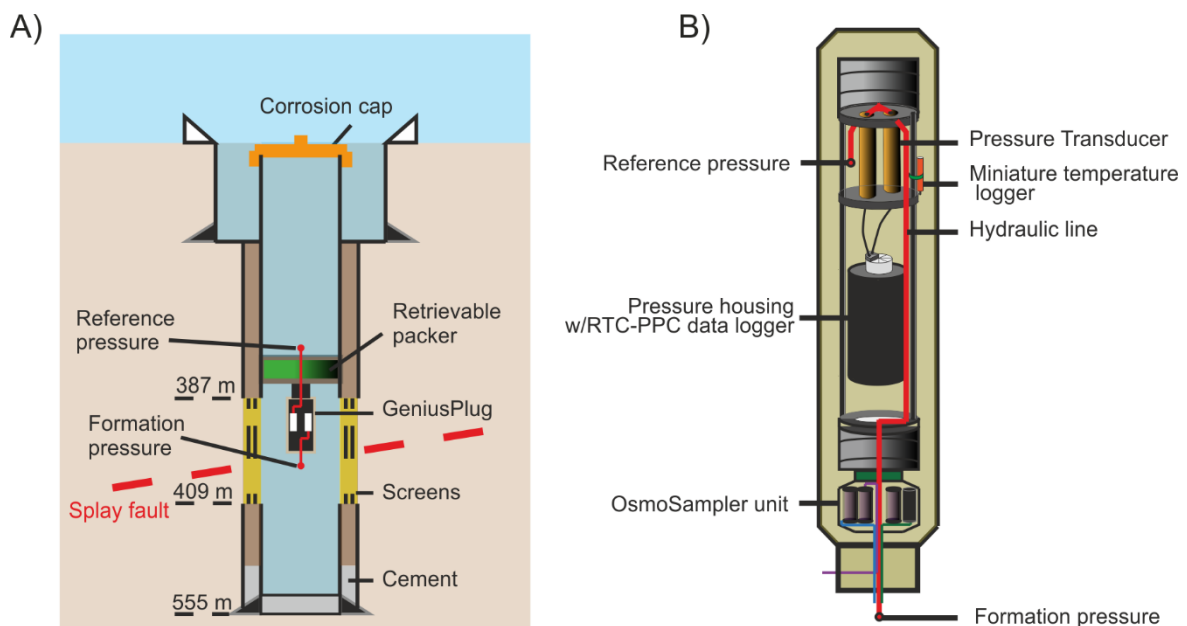


Figure 44: Schematic images of (A) Hole C0010A and (B) GeniusPlug (modified from Kopf et al., 2016). (A) The total depth of borehole is 555 mbsf, and it crosses the megasplay fault at 407 mbsf. Screened casing joints provide access to the formation over a zone spanning 387 – 409 mbsf. (B) The GeniusPlug is equipped with two pressure sensors (for formation and reference pressures) and three different temperature sensors (modified after Kinoshita et al., 2018a).

Like the Smartplug, the GeniusPlug included two pressure sensors, a “downward looking” sensor to record formation pore pressure in the screened interval and an “upward looking” sensor to measure an oceanographic reference pressure, both with a sampling interval of 30 s (Figure 44 B). In addition, the observatory was equipped with three temperature sensors, primarily for compensation of the pressure transducers (Hammerschmidt et al., 2013a; Hammerschmidt et al., 2013b; Kopf et al., 2011a), and an ~30 cm long extension at its lower end housing a fluid sampling and in situ microbiological experiment designed to collect a time series of samples for geochemical and microbiological research (Kopf et al., 2011b). Here we restrict our analysis to the pressure time series.

Methods

Ocean tidal loading results in periodic variations in total stress at the seafloor. The formation response to this transient oceanographic loading includes an elastic component, which is instantaneous and characterized by amplitude damping that depends on formation and pore fluid stiffnesses; and a diffusive component generated at boundaries (i.e., the seafloor or at the top and base of layers in the subsurface having differing elastic properties) (Wang and Davis, 1996). The amplitude damping results from contributions from both the elastic and diffusive responses and is described by a 1-D loading efficiency (γ), given by the ratio of the amplitude of variations in formation pressure to that of the ocean tidal loading at the seafloor. The diffusive component of the response can also result in phase lags or leads of pore fluid pressure in the formation relative to the oceanographic signal, but for typical sediment hydraulic diffusivities, this effect becomes negligible by a few tens of meters away from boundaries at dominant ocean tidal frequencies.

An added complication arises in the measurement of pressure in sealed borehole observatories, in which both amplitude damping and phase lags may also be generated by the transfer of fluid mass between the formation and the borehole sensing volume, necessary to measure and record pressure changes (Sawyer et al., 2008). This effect is governed by the hydraulic diffusivity of the formation, which controls the rate of fluid movement into and out of the borehole, and by the ratio of formation to instrument compliance, which defines the pressure change associated with a given fluid mass transfer (Hammerschmidt et al., 2013b; Sawyer et al., 2008).

As described in detail in the following sections, we define the overall average tidal loading efficiency and use the observed in-phase formation pressure to seafloor loading to provide bounds on formation hydraulic diffusivity. We then determine a time series of small but clearly resolved variations in pressure and loading efficiency over the 5.3 year deployment and evaluate the relationship between these perturbations and regional earthquakes.

Removal of Tidal and Oceanographic Signals

The GeniusPlug monitored pressure continuously from its initial deployment on 6 November 2010 until recovery of the instruments on 3 April 2016 (Kopf et al., 2016; Kopf et al., 2011a). The monitoring period included both the installation and recovery of the GeniusPlug, during which there are large pressure excursions related to the drillstring operations in the hole. To avoid these effects and the transient equilibration following initial deployment, we limited our analysis to the time window from one week following the end of installation (13 November 2010) until the time of recovery. The pressure data are dominated by the diurnal ocean tidal

signal with an amplitude of approximately 10 kPa, along with a semidiurnal component of roughly half this amplitude (Figure 45 A). The tidal signal is far larger than transient changes in pressure associated with earthquakes or other tectonic phenomena, and analyses of the latter therefore require that the effects of ocean tides be removed.

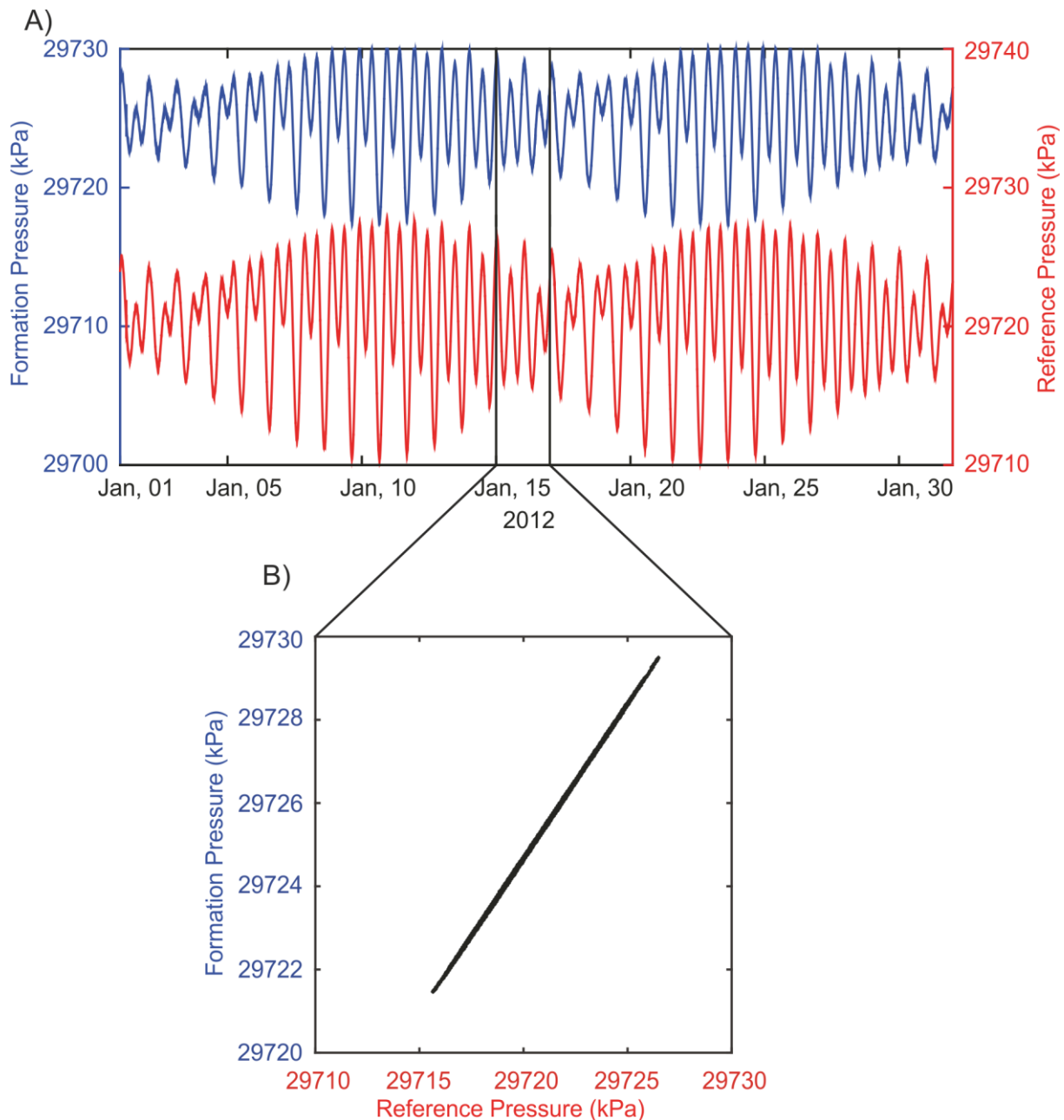


Figure 45: Example of tidal and oceanographic signals in the observed pressures. (A) Time series observed pressures from Jan.1 - Feb.1, 2012. The blue and red lines show formation and reference pressures, respectively. (B) Example of loading efficiency estimation for a 2 day time window which includes both diurnal and semi-diurnal components. The slope of relationship between formation and reference pressures indicates the loading efficiency (modified after Kinoshita et al., 2018a).

We observe essentially no phase lag in formation pressure relative to the reference pressure, which simplifies the removal of tidal signals (Davis et al., 2013; Davis et al., 2009; Wang and Davis, 1996). In this case, we simply remove the tidal effects from the formation pressure

directly to define a corrected pressure (P_{corr}) using the upward looking reference pressure and accounting for amplitude damping by the 1-D loading efficiency (Davis et al., 2013; Davis et al., 2009):

$$P_{corr} = P_{form} - \gamma P_{ref} \quad (24)$$

where P_{form} and P_{ref} are the formation and reference pressures, respectively.

Identification of Regional Earthquakes and Definition of Pressure Changes

Guided by previous work that demonstrates a clear relationship between hydrologic signatures and earthquake magnitude and distance (Manga et al., 2016; Wang, 2007), we identify earthquakes to compare with the observatory data by focusing on regional events with epicenters located between latitude 25 – 45° and longitude 125 – 150° (epicentral distances <1,200 km), and having moment magnitude (M_w) ≥ 6.0 . We also consider events with M_w 4.0 – 5.9 having with epicentral distances <300 km. Aftershocks of the 2011 M_w 9.0 Tohoku earthquake from 11 – 14 March 2011 are not considered because it is difficult to distinguish individual events, especially given the relatively coarse sampling interval (30 s). If multiple earthquakes occurred on the same day, we selected the larger M_w event for our analysis. We use earthquake data from the F-net Catalog (based on the F-net Broadband Seismograph Network; Fukuyama, 1998), which includes a focal mechanism for each event; we use these focal mechanisms to predict the theoretical static volumetric strain for each event as described in section “Responses to Earthquakes”.

After removal of tidal and oceanographic signals Equation (24), clear step changes in pressure are apparent and correspond to regional and large global seismic events (Figure 46 A). However, there are still local trends in the data related to recovery from drilling perturbations and to instrument drift. In order to define the magnitude of individual pressure steps, we detrended the data by assuming a constant drift rate defined over a moving three-month window (Polster et al., 2009). For data prior to 27 December 2010 (less than three months after the start of data collection), a one-month window was used instead. To define the size of pressure steps, we calculated a 10 min average of detided and detrended pressure before and after each event (Figure 47).

Definition of Tidal Loading Efficiency (γ)

In most analyses, loading efficiency is assumed to remain constant over time and is used to remove tidal and oceanographic signals from pressure records as described above

(Hammerschmidt et al., 2013b; Sawyer et al., 2008). However, the loading efficiency reflects the formation's elastic and hydraulic properties and therefore can vary over time due to tectonic or other processes. This has been recognized in the analysis of groundwater observations in terrestrial wells, and combined observations of amplitude damping and phase lag have been used in several studies to define variations in formation hydraulic diffusivity caused by earthquakes (Elkhoury et al., 2006; Kinoshita et al., 2015).

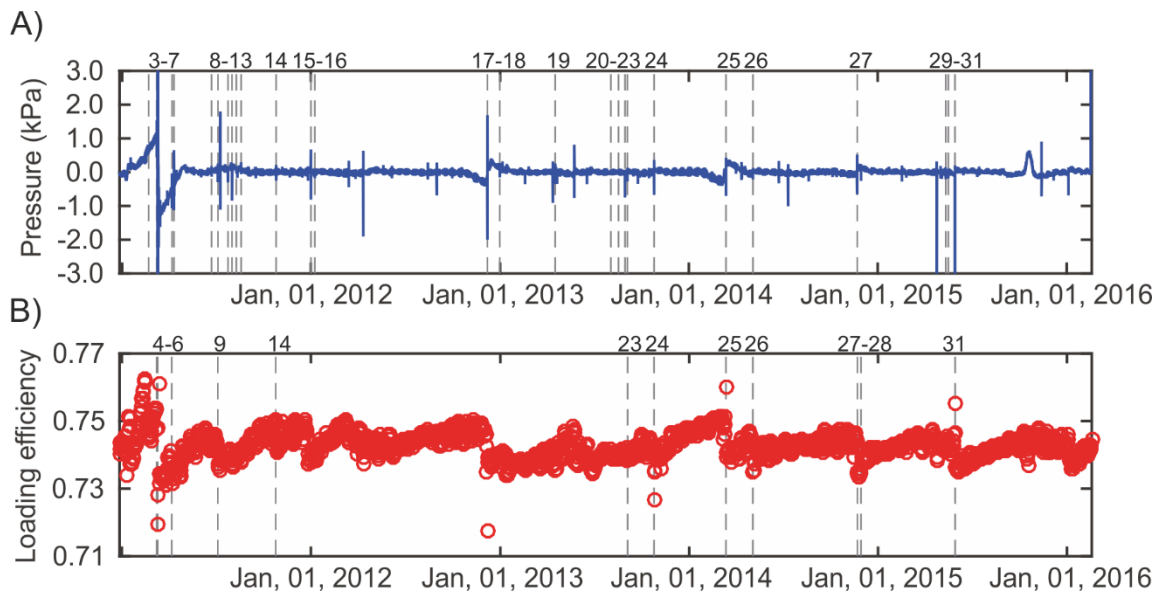


Figure 46: Time series of (A) pressure and (B) loading efficiency. (A) Detided and detrended formation pressure, corrected as described in the text. The dashed lines indicate the timing of earthquakes that produced detectable changes in pressure and/or loading efficiency. The numbers above dashed lines correspond to the events listed in Table 10 (modified after Kinoshita et al., 2018a).

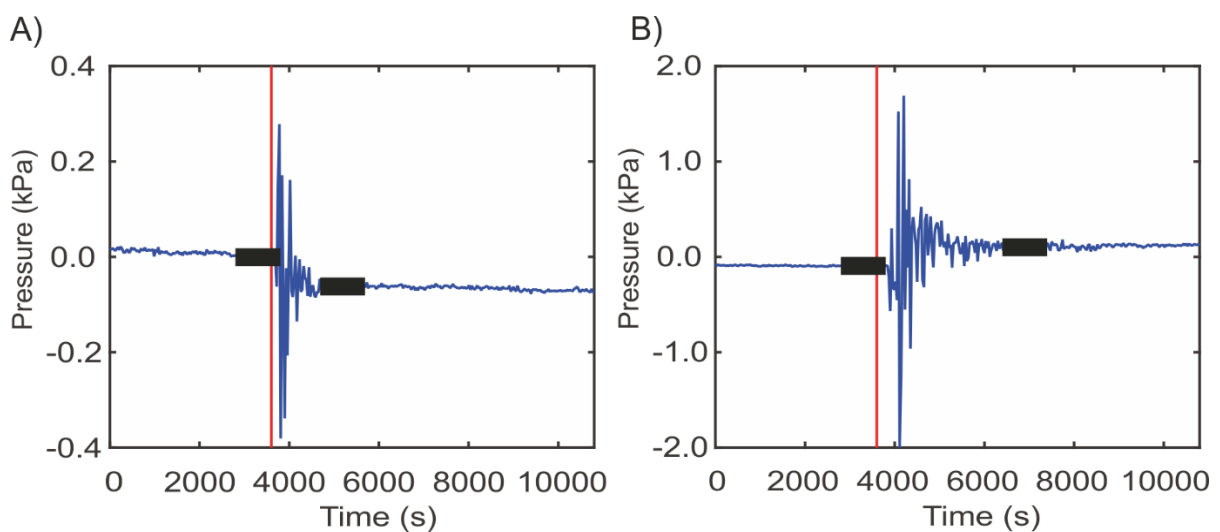


Figure 47: Examples of pressure step changes. (A) Example of pressure decrease in response to an earthquake on Nov. 30, 2010 (Mw 6.7; Table 10). (B) Example of pressure increase (earthquake on Dec. 7, 2012; Mw 7.3; Table 10). The black lines show the periods used to define a 10 minute average before and after the event. The red line is origin time of the earthquake (modified after Kinoshita et al., 2018a).

To explore potential temporal variations in loading efficiency, we computed γ on a daily basis by crossplotting the reference and formation pressures for each 24 hr window (Figure 45 B); this captures the diurnal variations in both data sets. For this analysis, we first applied a low-pass filter (cutoff frequency 10^{-4} Hz) to the pressures to extract the tidal frequencies and remove any perturbations induced by seismic waves.

Results and Discussion

The overall amplitude damping and phase lag (if present) responses to cyclic loading provide information about formation hydraulic properties (Sawyer et al., 2008; Wang and Davis, 1996). In addition, shifts in these quantities over time reflect hydrological perturbations in the formation or to the well completion that yield insights into transient hydrological and deformation processes (Elkhoury et al., 2006).

Phase and Amplitude Responses: Constrains on Formation Properties

Our analysis reveals essentially no phase lag within the limits of our 30 s sampling interval, and an overall value of $\gamma = 0.74 \pm 0.008$ (2σ), with small but clearly resolvable changes superimposed on the time series (Figure 46 B). The loading efficiency we obtain is similar to that of $\gamma = 0.73$ reported by Hammerschmidt et al. (2013b) using pressure records from the previously deployed SmartPlug. The standard deviation in any given single year of the time series is slightly smaller than that for the entire data set ($2\sigma = \sim 0.006$), and we consider this as a detection limit for resolving changes in loading efficiency that occur over short timescales (i.e., those associated with earthquakes). To identify transient changes in loading efficiency that could be linked to individual earthquake or other events, we apply an additional criterion that the loading efficiency must recover.

Loading Efficiency and Formation and Fluid Compressibilities

Generally, the lack of phase lag in formation pressure relative to the reference pressure signifies good hydraulic coupling between the formation and observatory (Gibson, 1958; Sawyer et al., 2008). This is consistent with the placement of the hydraulic screens spanning a fractured and presumably permeable interval associated with and immediately above the megasplay fault (Kopf et al., 2016; Kopf et al., 2011a). Unrestricted hydraulic communication between the formation and well should also lead to near-zero amplitude damping of the formation's response to periodic loading as measured in the borehole sensing volume (Hammerschmidt et al., 2013b; Sawyer et al., 2008). This lends confidence that the loading

efficiency of 0.74 observed in the borehole is correctly representative of that of the formation. The formation's 1-D loading efficiency is given by (Sawyer et al., 2008; Wang, 2004)

$$\gamma = \frac{\beta'_f}{\beta'_f + n\beta_w} \quad (25)$$

where

$$\beta'_f = \frac{1 + \nu}{3(1 - \nu)} \beta_f \quad (26)$$

and β_f and β_w are the formation and fluid volumetric compressibilities (Pa^{-1}), respectively; β'_f is the 1-D vertical formation compressibility (Pa^{-1}); n is fractional porosity; and ν is the Poisson's ratio (all variables and their values are listed in Table 9). However, for values of sediment compressibility consistent with values measured on core samples from equivalent depths of the monitoring interval and assuming pure seawater as pore filling phase, γ determined from Equations (25) and (26) would be >0.95 (Davis et al., 2009; Wang and Davis, 1996).

In order to explain the observed value of $\gamma = \sim 0.74$, the required formation compressibility would be >10 times smaller than measured in laboratory experiments for sediments from the megasplay, or for similar porous lithologies elsewhere in the Nankai system or in other marine settings (Guo et al., 2011; Wang and Davis, 1996). Alternatively, the presence of a small amount of either free or dissolved gas in the interstitial fluids could lead to decreased loading efficiency (Wang et al., 1998; Wang and Davis, 1996). This occurs because the compressibility of gas is much higher than that of seawater. To evaluate this possibility, we modify Equations (25) and (26) and to consider the effects of gas compressibility and solubility (Wang et al., 1998). In this case, the term $n\beta_w$ in Equation (25) is replaced by β_{w+g} (Wang et al., 1998):

$$\begin{aligned} \beta_{w+g} &= \frac{1}{V} [V_w \beta_w + V_g \beta_g + \chi V_\chi (\beta_g - \beta_w - \beta_\chi)] \\ &= (1 - n_g) \beta_w + n_g \beta_g + (1 - n_g) \chi (\beta_g - \beta_w - \beta_\chi) \end{aligned} \quad (27)$$

where V is volume (m^3), β is compressibility (Pa^{-1}), χ is volumetric solubility, and the subscripts, w , g , and χ represent water, gas, and dissolved gas, respectively. For the formation properties listed in Table 9, at the P-T conditions of the observatory monitoring interval, a volumetric gas content of $\sim 0.5\%$ would be sufficient to explain the observed loading efficiency. The presence of dissolved and possibly free gas in the in situ pore fluids is

supported by the observation of abundant free gas in the geochemical sampling coils of the GeniusPlug upon recovery and depressurization (Saffer et al., 2017a).

Hydraulic Diffusivity

The lack of phase lag also allows us to define a lower bound on formation hydraulic diffusivity. We follow the approach of Sawyer et al. (2008), who considered measured pressure variations in a borehole in response to periodic fluctuations of formation pressure to reflect radial flow of fluid into and out of the sensing volume from the surrounding rock (supplementary materials; see also Gibson, 1958). In this model, the measured amplitude and phase response to pressure fluctuations in the formation depend on the hydraulic diffusivity of the formation, the frequency of the fluctuations, and the ratio of formation and sensing volume compressibilities (Figure 48) (Hsieh et al., 1987; Sawyer et al., 2008).

One of the important developments of Sawyer et al. (2008) was the consideration of the formation and instrument compressibility ratio (β_D), which governs the response of the pressure monitoring system (the sealed borehole volume) to fluid mass exchange with the formation. The formation-instrument compressibility ratio is given by

$$\beta_D = \frac{\pi r_{SO}^2 H \beta_f}{\beta^* V} \quad (28)$$

where r_{SO} is the screened casing outer radius (m), β_f is formation compressibility (Pa^{-1}), β^* is the effective instrument compressibility (Pa^{-1}), and V is the sensing volume (m^3). For the borehole configuration at Hole C0010A, β^* is given by the aggregate compressibility of the fluid and steel weighted by their contributions to the sensing volume (Sawyer et al., 2008; all variables and their values are listed in Table 9 and Figure 56).

Generally, there is a time delay between pressure change in formation and pressure in the observatory because of the effects of wellbore storage (β^*V). Above some threshold frequencies, pressure in the observatory cannot equilibrate with variations in real formation pressure, leading to damping of the amplitude response and phase lag (Figure 48); at frequencies below this threshold, the response of measured pressure is correct. This frequency dependence of the amplitude-phase response allows us to place bounds on the formation hydraulic diffusivity at the scale of the volume sampled by the observatory response. Because the volume of formation interrogated by the tidal response depends on the formation properties, as well as any layering and geometry, we do not know it precisely, but estimate that the observatory response represents the properties of the fault zone and surrounding sediments over a distance of tens to ~100 m from the borehole (e.g., Wang and Davis, 1996).

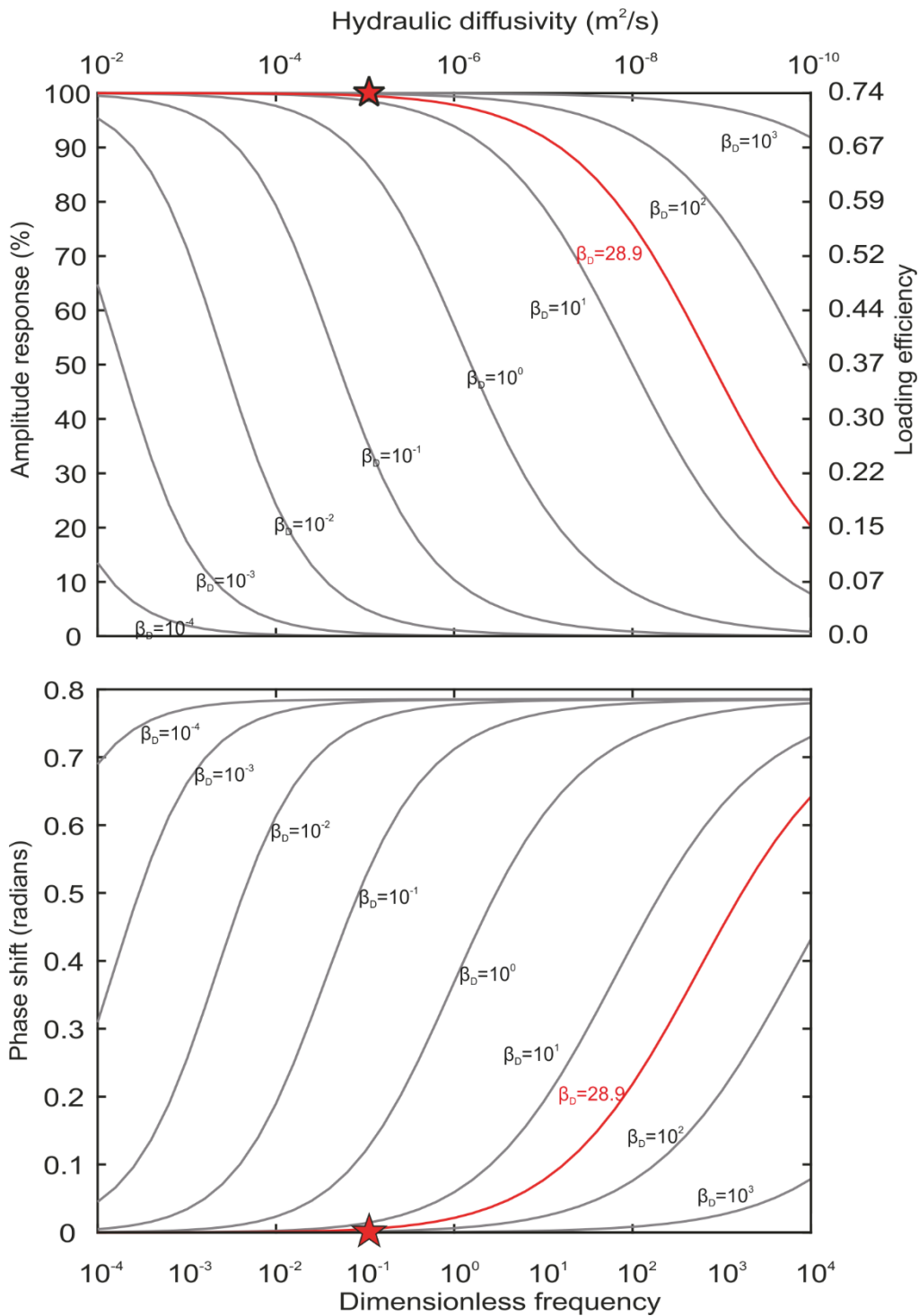


Figure 48: Predicted amplitude (A) and phase lag (ζ) in formation pressure relative to reference pressure versus hydraulic diffusivity (top axis) and dimensionless frequency (bottom axis; $f_D = \frac{r_{so}^2 f}{c}$). Several values of formation and instrument compressibility ratio (β_D) are shown; for a given period, hydraulic diffusivity can be estimated from a known compressibility ratio and observed phase lag and/or amplitude damping. Red stars show our observations, reflecting 100 % amplitude response relative to the formation (which is in turn damped by a factor of 0.74 relative to the seafloor), zero phase lag. For our calculated $\beta_D = 28.9$ (supplementary materials), this yields a hydraulic diffusivity $9.1 \times 10^{-6} \text{ m}^2 \text{ s}^{-1}$ (modified after Kinoshita et al., 2018a).

For the formation-instrument compressibility ratio of our system ($\beta_D = \sim 29$), a hydraulic diffusivity $> 9.1 \times 10^{-6} \text{ m}^2 \text{ s}^{-1}$ is required to explain the lack of phase lag. As noted above, the lack of phase lag also requires a 100 % amplitude response—that is, that there is no damping between the formation and borehole (cf. Figure 48), consistent with our interpretation that the observed loading efficiency ($\gamma = 0.74$) is best explained as a true formation response possibly caused by a small amount of gas.

For a formation compressibility of $7.0 \times 10^{-9} \text{ Pa}^{-1}$ (Saffer et al., 2011), this hydraulic diffusivity corresponds to a shallow splay fault permeability $> 6.4 \times 10^{-13} \text{ m}^2$. A similar, but less complete, analysis of the previously deployed SmartPlug data yielded an estimated lower bound for hydraulic diffusivity of $> 1.5 \times 10^{-5} \text{ m}^2 \text{ s}^{-1}$ (Hammerschmidt et al., 2013b). For comparison, Dugan and Daigle (2011) performed the Constant Rate-of-Strain Consolidation tests for core samples from the thrust wedge (Unit II) at Site C0004, located 3.5 km away along-strike, and obtained a matrix permeability more than 2 to 3 orders of magnitude lower than ours, of $3.8 \times 10^{-15} - 1.6 \times 10^{-16} \text{ m}^2$. This difference is likely due to the fact the borehole screens samples a larger volume that includes fractures (e.g., Boutt et al., 2012), and the fact that the Constant Rate-of-Strain Consolidation tests measured vertical permeability.

The lower bound of fault zone permeability we obtain is generally consistent with the range of values reported for other subduction fault zones (Saffer, 2015). For example, Fisher and Zwart (1997) measured in situ permeabilities of $6.0 \times 10^{-16} - 1.6 \times 10^{-13} \text{ m}^2$ for the Barbados accretionary complex décollement zone in a series of drillstem packer experiments. Screaton et al. (2000) reported a value of $1.2 \times 10^{-14} \text{ m}^2$ for the Barbados décollement from cross-hole tests over a distance of $\sim 45 \text{ m}$. Reported permeabilities of $6.0 \times 10^{-14} - 1.6 \times 10^{-11} \text{ m}^2$ for the frontal thrust fault of the Oregon accretionary prism were reported by Screaton et al. (1995) from drillstem packer experiments similar to those of Fisher and Zwart (1997). The reported field observations, though sparse, are also consistent with large-scale fault permeabilities estimated from numerical modeling studies at several margins, including Costa Rica (Spinelli et al., 2006; $\geq 10^{-14} \text{ m}^2$) Barbados (Bekins et al., 1995; 10^{-14} m^2 at steady state and $10^{-13} - 10^{-11} \text{ m}^2$ in transient simulations), and Nankai (Skarbek and Saffer, 2009; $10^{-15} - 10^{-13} \text{ m}^2$). The configuration of the observatory (i.e., screened interval spanning the splay fault), taken together with the lower bound on permeability we obtain, suggests that our permeability estimate represents the properties of fault zone.

Responses to Earthquakes

Changes and Recovery of Formation Pressure and Loading Efficiency

From 187 earthquakes that met the magnitude-distance criteria, 31 events produced changes either in pore pressure and/or loading efficiency. We detected individual events based on the definition described in section “Methods”. In some cases, changes in tidal loading efficiency precede earthquake occurrence by as much as a few days (events #15 – 19). The origin of these changes in loading efficiency is not clear, and we do not consider these changes in our analysis, which is focused on responses to earthquakes. The magnitude of pressure steps ranges from 10 to 230 Pa (tens to hundreds of times larger than the precision of pressure measurements of ± 0.7 Pa). Changes in loading efficiency range from 0.003 to 0.029. We detected 28 events associated with pressure steps and 25 of these are increases. In contrast, 13 of 14 events, changes in loading efficiency are decreases. In several cases, events resulted in only a change in pressure, and 11 of the 31 events produced changes in both pressure and loading efficiency (Table 10).

Global compilations document a magnitude-distance threshold for a wide range of hydrologic effects from earthquakes, including changes in groundwater level, increase in streamflow, and liquefaction (Matsumoto et al., 2003; Wang and Manga, 2010). Our observations follow a similar pattern, with detectable changes in both formation pressure and loading efficiency following a systematic trend in which responses appear to be controlled by earthquake magnitude and epicentral distance (Figure 49). Smaller earthquakes, or more distal larger earthquakes, do not lead to observed perturbations in either pressure or loading efficiency.

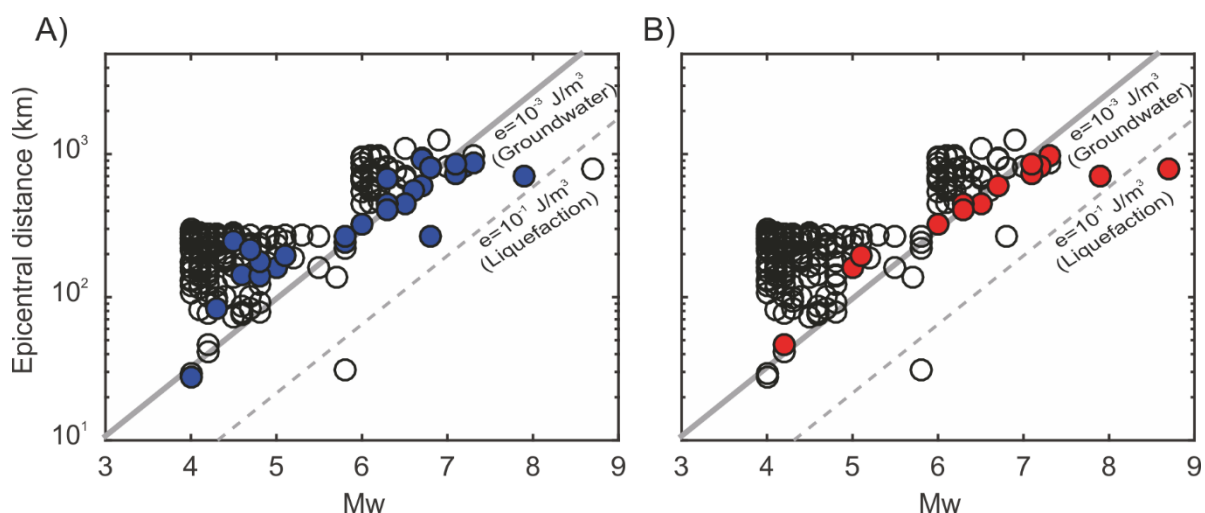


Figure 49: Earthquake magnitudes and epicentral distances from Site C0010. Blue and red circles show events which produce detectable changes in (A) pressure and (B) loading efficiency; black circles show events that did not produce detectable perturbations. The gray solid and dotted lines represent the thresholds for groundwater level changes and liquefaction, respectively (Wang and Manga, 2010) (modified after Kinoshita et al., 2018a).

Wang et al. (2006) suggested that seismic energy density (SED), defined as the maximum seismic energy available in a unit volume to do work on rock or sediment (Wang and Manga, 2010), is the primary factor governing the magnitude-distance threshold. They suggested that in their global catalog of hydrologic perturbations, the thresholds for changes in groundwater level and liquefaction correspond to SED of $\sim 10^{-3}$ and $\sim 10^{-1}$ J/m³, respectively (Figure 49). Our data suggest that a similar threshold applies to changes in pressure and loading efficiency along the megasplay and that it is most similar to the threshold for changes in water levels (10^3 J/m³), whereas the SED associated with liquefaction responses in the global data set is generally higher than that encountered at our site for most events. Note that the SED threshold for water level changes in the global compilation shown in Figure 49 is defined by events having epicentral distance of 24 – 10,800 km and seismic magnitude (Mw) of 4.7 – 9.3; the SED for liquefaction is defined for events having epicentral distance <480 km and seismic magnitude (Mw) >4.8 (Wang and Manga, 2010).

The recovery of changes in both pressure and loading efficiency following earthquakes is also observed clearly, and generally exhibits a systematic increase in recovery time with increased magnitude of perturbation (Figure 50). We define the recovery time as the time required after the earthquake for the value of pressure or loading efficiency to return to its prior value. If a large earthquake occurred before pressure or loading efficiency recovery was complete, we report a minimum recovery time, because we cannot distinguish the effects of first and second events; if there was no subsequent event, the recovery time of first event could have been longer than observed. It is also possible that the recovery from a second earthquake includes effects of the earlier event; however, in this case we assume that the recovery time is not strongly affected by the preceding event because the perturbation caused by the first event has mostly decayed.

Recovery of loading efficiency is generally slower than pressure recovery. For the largest change in pressure (231 Pa), recovery takes ~ 108 days, whereas the smallest detectable change in pressure (13 Pa) recovers in as little as 3.6 hr (Figure 50 A and Table 10). In contrast, the largest changes in loading efficiency ($\Delta \gamma = 0.012 - 0.029$) recover over times of ~ 50 to >130 days, and the smallest observable changes ($\Delta \gamma = 0.003$) recover in less than one day (Figure 50 B and Table 10). We hypothesize that the differences in recovery times for pressure and loading efficiency reflect a difference in processes. In the case of pressure, regional fluid flow reequilibrates pressure head relatively rapidly. In contrast, recovery of loading efficiency depends on recovery of the formation and/or fluid elastic properties, which is related to reestablishment of dissolved gas in the fluid, and to pore structure and grain contacts.

Our observations of changes in pressure and loading efficiency are similar to numerous observations of reduced seismic wave velocity and subsequent time-dependent recovery following earthquakes in a range of geological settings (Li et al., 2003; Schaff and Beroza, 2004). Our observed responses are also similar to reported abrupt permeability increases following earthquakes, and their gradual recovery preevent conditions (Elkhoury et al., 2006). For example, Nakata and Snieder (2011) reported that shear wave velocity decreased at the time of the 2011 Tohoku earthquake and recovered logarithmically with time. The similar nature and time dependence of recovery in these systems suggest that the processes that affect rock and fluid properties as a result of earthquakes, and the controls on their recoveries, may be similar across a range of environments.

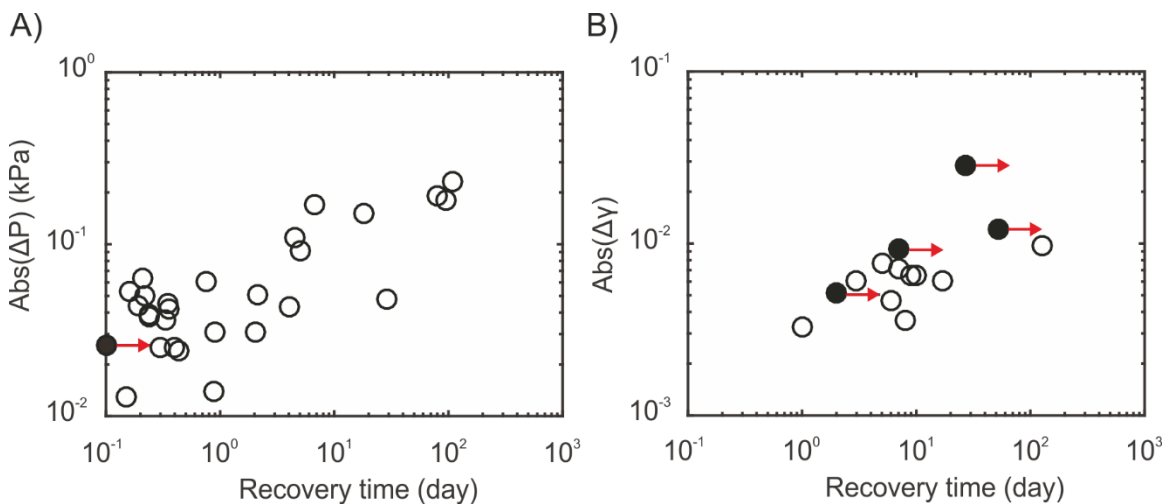


Figure 50: Recovery times for changes in (A) pressure and (B) loading efficiency. The solid circles indicate events for which subsequent large earthquakes interfered with the recovery. Consequently, only a lower bound on recovery time can be estimated (Table 10) (modified after Kinoshita et al., 2018a).

Relationship of Perturbations to Static and Dynamic Strains

To investigate potential mechanisms for the observed perturbations in pore pressure and loading efficiency, we evaluate the static and dynamic strains expected for the earthquakes listed in Table 10. We estimate the static volumetric strain theoretically, based on solutions of Okada (1992) and the focal mechanisms reported by F-net (the National Research Institute for Earth Science and Disaster Prevention).

Dynamic strain is often determined by using peak ground velocity (PGV); however, we were unable to use local seismic data from nearby instruments in the seafloor DONET observatory (Dense Oceanfloor Network system for Earthquakes and Tsunamis) because seismic data are only available for small portion of our study period (after October in 2014). Instead, we estimate dynamic strains using the integrated “pressure energy density” (PED) for each event over a 30 min window of the pressure records, which provides a proxy for the integrated dynamic strain. Generally, formation pressure records seismic waves (“hydroseismograms”) (Roeloffs,

1996), and the magnitude of pressure fluctuations depends on the earthquake magnitude and epicentral distance, in the same manner as a seismometer’s response.

To verify the utility of PED as a proxy for strain energy in light of the low pressure sampling rate, we assess the relationship between PED and PGV for events during the time interval when DONET data are available at the closest ocean bottom seismometer (Site KMD 13, located 1.2 km to the Northeast of Hole C0010A). PGV was defined from the ocean bottom seismometer record by filtering for frequencies of 0.1 – 10 Hz. We document a clear correlation between PGV and PED (Figure 51) indicating that PED provides a viable proxy for dynamic strain. We note that the PED likely underestimates the strain energy because the 30 s sampling interval does not allow detection of energy at frequencies >0.016 Hz.

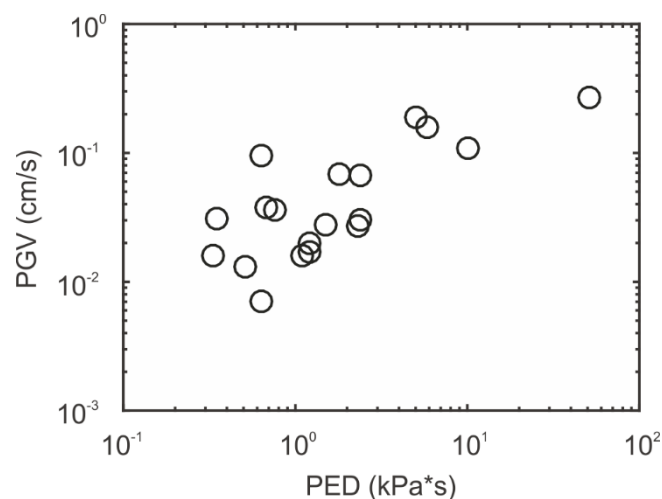


Figure 51: Assessment of relationship between PED (pressure energy density) and PGV (peak ground velocity). PED and PGV were estimated for the earthquakes listed in Table 11, from the time period when DONET ocean bottom seismometer data were available (modified after Kinoshita et al., 2018a).

Figure 52 shows the relationship between changes in pressure and loading efficiency and predicted static strains and PED (as a proxy for volumetric strain), respectively. We find that there is a clear trend in which larger PED produces larger changes in both pressure and loading efficiency (Figure 52 B and D), whereas any correlation between expected static volumetric strain and the observed hydrological perturbations is less clear (Figure 52 A and C).

To further investigate the possible role of static strain in driving the hydrological changes, we compute the expected pore pressure response to the predicted static volumetric strain for each earthquake shown in Figure 52. We assume a conversion factor of 4.7 kPa μ strain⁻¹, as reported by Wallace et al. (2016a) and Araki et al. (2017), and based on the formulation of Wang (2004). This conversion factor is in excellent agreement with the observed pressure changes associated with a well-constrained Mw 6.0 earthquake nearby, which provides a “field calibration” of the formation response (Wallace et al., 2016a). Our analysis demonstrates that the predicted changes in pressure are tens to hundreds of times smaller than those observed

(Figure 53). This difference cannot be explained by local trends of pressure or instrument drift and suggests that static strains are unlikely to be a factor in causing the pressure changes. The Okada (1992) model predicts static strains in the case of a uniform elastic half-space, and therefore, there is undoubtedly some error associated with the fact that our observatory data are obtained in shallow intervals within a poorly consolidated mudstone. However, we note that a recent detailed analysis of well-characterized regional April 2016 Mw 6.0 earthquake located down-dip of the observatory, and for which the slip distribution and magnitude are well constrained, predicts static strains using steps, observed in the observatory records (Wallace et al., 2016a). This “field calibration” suggests that the Okada (1992) model provides a reasonable approximation of expected static strains for the events we analyze.

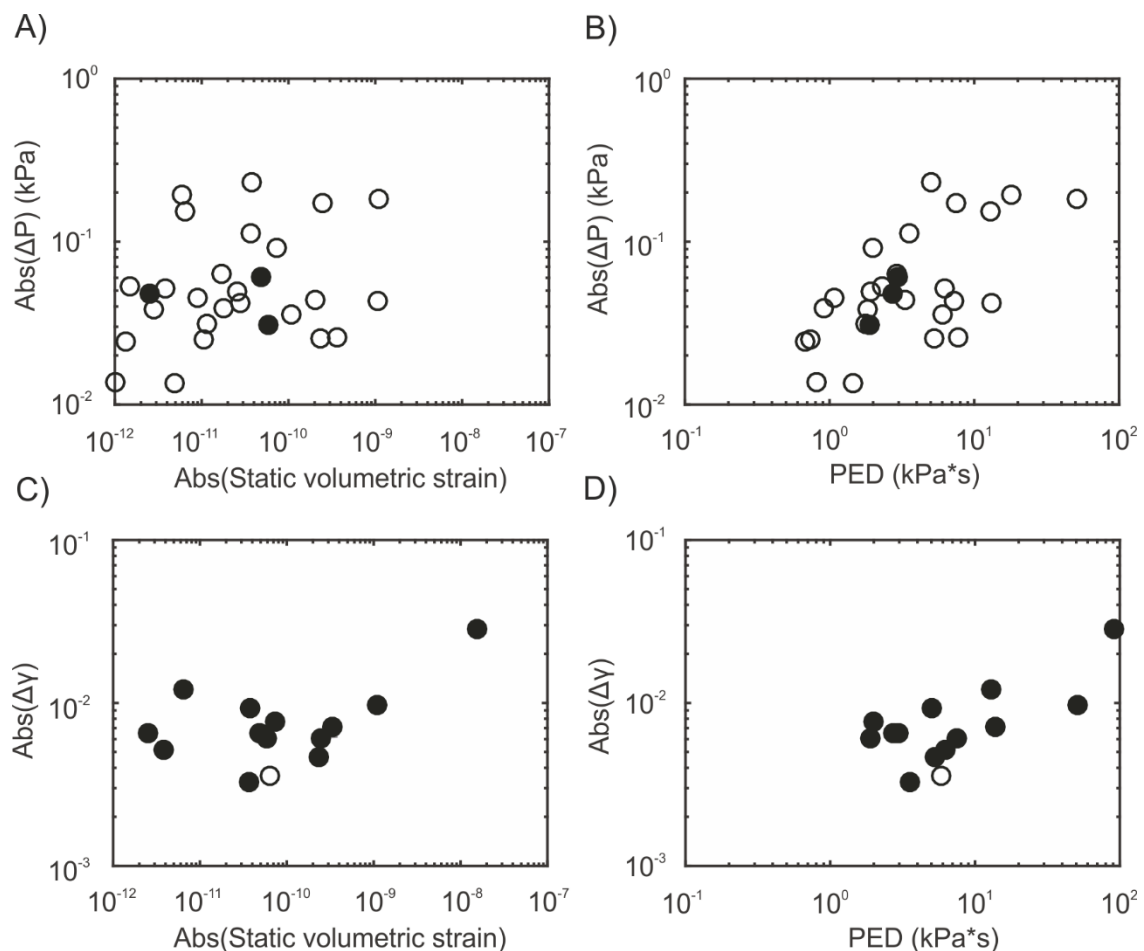


Figure 52: Relationship between hydrologic perturbations and static and dynamic strains. Panels (A) and (B) show changes in pore pressure versus (A) theoretical static volumetric strain and (B) pressure energy density (PED). Panels (C) and (D) show changes in loading efficiency versus (C) theoretical static volumetric strain and (D) PED. Open and solid circles represent increases and decreases in pressure or loading efficiency, respectively (modified after Kinoshita et al., 2018a).

Moreover, the stronger correlation between dynamic strain (or PED as a proxy) and the observed changes shown in Figure 52 provides additional support for the interpretation that the perturbations we observe reflect responses to dynamic strains associated with surface wave passage (e.g., Hammerschmidt et al., 2013a). This interpretation is also consistent with

global observations indicating that dynamic strain is a primary driver for triggering of earthquakes and mud volcano eruptions, and to changes in groundwater level (Kilb et al., 2000; Kitagawa et al., 2006; Manga and Wang, 2007).

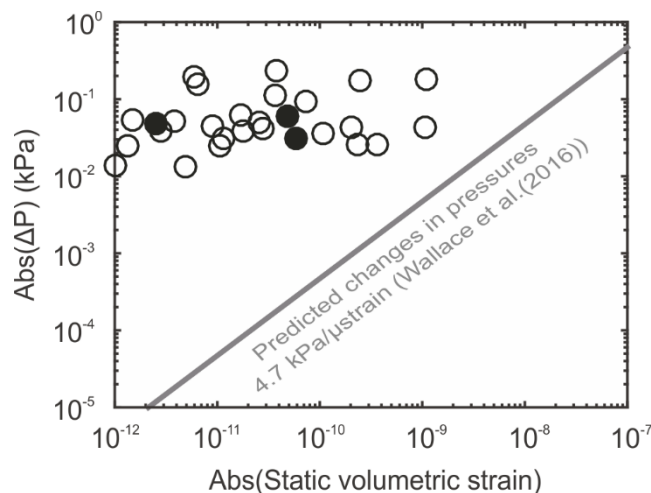


Figure 53: Comparison of observed changes in pressure (symbols; open = pressure increases; solid = pressure decreases), and predicted pressure changes (gray line) on the basis of calculated static strains for each earthquake listed in Table 10 (modified after Kinoshita et al., 2018a).

Mechanisms for Changes in Pressure and Loading Efficiency

In almost all cases, the perturbations we document represent increases in pressure and decreases in loading efficiency. Many, but not all, of these occur in response to the same earthquakes (Table 10). We suggest potential mechanisms to explain these observations (Figure 54) in which dissolved gas exsolves in response to dynamic shaking. In this scenario, interstitial water contains dissolved gas (in addition to ~0.5 % free gas), and as seismic waves pass, a modest amount of dissolved gas exsolves. Because the compressibility of free gas is much larger than that of dissolved gas, this phenomenon would produce decreases in loading efficiency (cf., Equations (25) and (27)). In our case, an increase in compressibility of the gas-water mixture (β_{w+g}) by ~15 % (corresponding to an increase from ~0.5 % to ~1 % by volume of free gas) would be required to explain the observed changes in γ . We posit that the exsolution of this small amount of additional gas may be triggered by fluctuations of pressure accompanying dynamic strain, wherein pressure reductions allow rapid (essentially instantaneous) exsolution of the gas. In contrast, the redissolution of this gas would not be instantaneous. As a result, the short-lived pressure increases associated with dynamic strain would not modify the fluid properties immediately, and the net effect of shaking on loading efficiency would be to lower it. Recovery of the loading efficiency would then occur over longer timescales in the wake of shaking.

The difference in timescales of recovery for loading efficiency and pressure suggests that at least in part, these two responses reflect different underlying processes. In some cases,

loading efficiency recovers more slowly than pressure (event #25 in Table 10; see also supplementary materials, Figure 55), whereas in a small number of cases the opposite is true (event #14). On average, the time required for recovery of loading efficiency is somewhat longer than that for pressure (compare Figure 50 A and B). One possible interpretation of this pattern is that the pressure increase and initial decrease in loading efficiency both reflect gas exsolution, as described above. The recovery loading efficiency would then depend on the time-dependent redissolution of gas. The recovery of pressure would be controlled by the combined effects of gas redissolution and pressure dissipation due to drainage; because these processes would act in concert to affect pressure, the pressure recovery would occur more rapidly than the loading efficiency recovery, which depends exclusively on the local fluid and rock properties. The exsolution and expansion of gas would also potentially enhance the drainage effect if the changes in fluid volume induce fracturing. Alternatively, the strong sensitivity of loading efficiency to small changes in free gas content could result in a protracted recovery simply because even small amounts of remaining free gas—even if insufficient to maintain an observable pressure increase could lead to observable reductions in fluid compressibility.

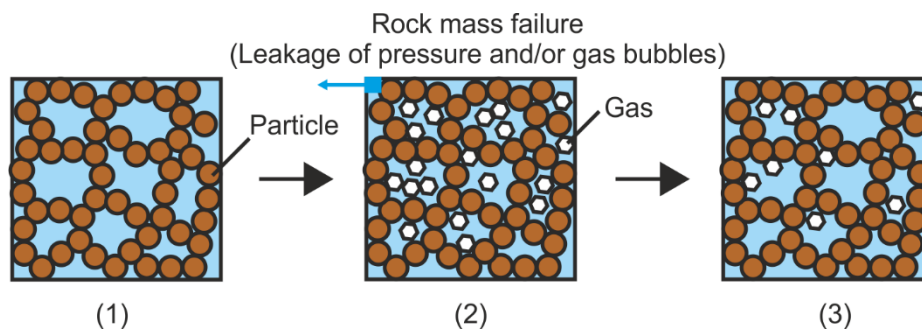


Figure 54: Schematic of potential mechanisms explaining the suite of observations. Originally, (1) interstitial water contains dissolved gas and (2) seismic wave passage leads to gas exsolution under drained conditions that drives pressure increase and loading efficiency increase. This is followed by (3) recovery associated with time-dependent dissolution of gas accompanied by possible drainage and dissipation of pressure (modified after Kinoshita et al., 2018a).

Given the observation of abundant gas bubbles in the GeniusPlug fluid sampling coils upon recovery (Saffer et al., 2017a), we suggest that this mechanism is the most plausible to explain both the overall low loading efficiency (as discussed in section “Loading efficiency and formation and fluid compressibilities” above) and the perturbations and recoveries associated with dynamic strains. The existence of methane was also confirmed by core samples obtained at Site C0004; for example, the sample at 400 mbsf shows the volumetric gas content of ~0.2 % (Kinoshita et al., 2009).

In a small subset of events, changes in pressure and loading efficiency show the opposite trends, implying that other processes may also play a role in the response of the formation or borehole sensing system to seismic events. Only one event led to an increase in loading

efficiency (requiring a decrease in stiffness). There is no clear aspect of this earthquake that distinguishes it from the others; it is a Mw 4.2 earthquake located 46 km away, and although it exceeds our detection threshold, the magnitude of the change in loading efficiency is small and detectable pressure change was not confirmed. In this case, it may be possible that only disaggregation of sediment particles occurred, and perturbations in pore pressure equilibrated very rapidly. In a small number of cases, decreases in pressure without changes in loading efficiency were also observed. In these cases, no changes in loading efficiency were detected, suggesting that formation elastic properties were not affected.

Summary

We investigated a time series of formation pressure monitored continuously within a major fault zone in the active Nankai Trough accretionary complex. Our analysis shows that the pressure record provides a highly sensitive measure of hydrological perturbations associated with earthquakes, and reveals several small but detectable changes in both formation pore fluid pressure and poroelastic properties.

One key observation is that there is essentially no phase lag in formation pressure relative to the seafloor reference pressure, yet the amplitude of the pressure response in the observatory is damped by a factor of ~ 0.74 . This can be explained by a combination of rapid fluid pressure diffusion between the formation and the borehole (suggesting high hydraulic diffusivity), and a small amount of dissolved gas in the interstitial waters, that increases the compressibility of pore fluids and thus decreases the formation loading efficiency. This explanation differs somewhat from previous interpretations of the pressure response (Hammerschmidt et al., 2013a; Hammerschmidt et al., 2013b), which attributed both effects to limited fluid mass transport between the formation and borehole (e.g., Sawyer et al., 2008) but were not able to reconcile the clear amplitude damping and lack of any phase lag. On the basis of our interpretation, we find a lower bound on formation (fault zone) hydraulic diffusivity of $9.1 \times 10^{-6} \text{ m}^2 \text{ s}^{-1}$ (corresponding to a permeability $> 6.4 \times 10^{-13} \text{ m}^2$), broadly consistent with other reported fault zone permeabilities in subduction zones (Saffer, 2015).

The responses to earthquakes, in almost all cases, are manifested as increases in pore pressure and decreases in loading efficiency. Detectable changes of both quantities follow a systematic trend that larger earthquakes, or those with closer epicenters, produce larger changes of both pressure and loading efficiency. The magnitude-distance threshold for the perturbations we report is similar to the threshold for changes in water levels in global compilations from primarily terrestrial observations (10^{-3} J/m^3 ; Wang and Manga, 2010).

A comparison between expected static volumetric strain and PED reveals that dynamic strain is likely the primary driver of the observed changes. On the basis of our results, we suggest gas exsolution as a potential mechanism to explain the perturbations and subsequent recoveries. Gas exsolution drives a small pressure increase and an increased fluid phase compressibility.

Our study demonstrates the value of borehole monitoring as a highly sensitive and continuous measurement of formation physical properties, which provides new insights into the hydrological behavior of an active fault zone along a subduction plate boundary.

Table 9: Definitions and Values (where appropriate) of variables used in the text and supporting information.

Variable	Definition	Dimension
γ	Average 1-D Loading efficiency	0.74
β_f^a	Formation compressibility, Pa ⁻¹	7.0*10 ⁻⁰⁹
β'_f	1-D vertical formation compressibility, Pa ⁻¹	2.9*10 ⁻⁰⁹
β_w	Fluid compressibility, Pa ⁻¹	4.0*10 ⁻¹⁰
β_{steel}	Steel compressibility, Pa ⁻¹	5.0*10 ⁻¹²
β^*	Instrument compressibility, Pa ⁻¹	3.3*10 ⁻¹⁰
β_D	Formation-instrument compressibility ratio	28.9
n^b	Porosity	0.38
ν	Poisson' ratio	0.10
r_{to}	Tubing outer radius, m	0.044
r_{go}	GeniusPlug outer radius, m	0.100
r_{ci}	Casing inner radius, m	0.112
r_{co}	Casing outer radius, m	0.122
r_{so}	Screen outer radius, m	0.142
L_t	Tubing length, m	19.19
Z	GeniusPlug length, m	1.65
H	Observatory system Length, m	145.97
h	Screen part length, m	18.39
V_w	Volume of water , m ³	5.60
V_{steel}	Volume of steel part , m ³	1.25
V	Total volume , m ³	6.85
$P(r, t)$	Pressure, Pa	-
P_D	Dimensionless Pressure	-
r	Distance, m	-
r_D	Dimensionless distance	-
t	time, s	-
t_D	Dimensionless time	-
f	Frequency, rad	-
f_D	Dimensionless frequency	-
S_D	Dimensionless fluid source term	-
A	Amplitude, %	-
ζ	Phase lag, rad	-

^aFormation compressibility is defined on the basis of Constant Rate-of-Strain Consolidation test for core samples from equivalent lithologic units at Site C0004, located 3.5 km along-strike from Site C0010 (Figure 43) (Saffer et al., 2011).

^bThe value of porosity is determined from ring resistivity measured by logging while drilling data at Site C0010, as well as from measurements on core samples of the same formation, collected by drilling at nearby Site C0004 (Figure 43 B) (Hammerschmidt et al., 2013b; Saffer et al., 2010).

Table 10: Seismic events which induced changes in pressures and/or loading efficiency.

Date (UTC)	Lat. (°)	Long. (°)	Mw	Epicentral distance (km)	ΔP (kPa)	ΔP recovery time (day)	$\Delta \gamma$	$\Delta \gamma$ recovery time (day)	Static volum. strain	Theoretical ΔP (kPa)	PED (kPa*s)
11/30/10 3:24	28.36	139.59	6.7	606	-6.1E-02	0.75	-6.5E-03	9	4.8E-11	2.3E-04	3.0E+00
12/21/10 17:19	27.05	143.94	7.3	977	-	-	-7.1E-03	7	3.4E-10	-	1.4E+01
2/21/11 6:46	33.88	135.36	4.8	144	3.9E-02	0.24	-	-	1.8E-11	8.5E-05	9.2E-01
3/9/11 2:45	38.33	143.28	7.2	826	5.1E-02	>2.13	-5.1E-03	>2	3.8E-12	1.8E-05	6.3E+00
3/11/11 5:46	38.10	142.86	8.7	782	-	-	-2.9E-02	>27	-1.6E-08	-	9.2E+01
4/7/11 14:32	38.20	141.92	7.1	731	2.5E-02	0.30	-4.6E-03	6	-2.3E-10	-1.1E-03	5.3E+00
4/11/11 8:16	36.95	140.67	6.6	553	2.6E-02	0.10	-	-	-3.6E-10	-1.7E-03	7.8E+00
6/22/11 21:50	39.95	142.59	6.7	919	1.3E-02	0.15	-	-	-4.9E-12	-2.3E-05	1.5E+00
7/5/11 10:18	33.99	135.23	5.0	161	-3.1E-02	0.90	-6.1E-03	17	5.9E-11	2.8E-04	1.9E+00
7/24/11 18:51	37.71	141.63	6.3	673	1.4E-02	0.89	-	-	1.0E-12	4.7E-06	8.1E-01
8/1/11 14:58	34.71	138.55	5.8	241	3.6E-02	0.33	-	-	1.1E-10	5.0E-04	6.0E+00
8/9/11 23:13	34.05	135.52	4.6	144	2.5E-02	0.40	-	-	1.1E-11	5.0E-05	7.4E-01
8/19/11 5:36	37.65	141.80	6.3	679	3.8E-02	0.24	-	-	-2.8E-12	-1.3E-05	1.8E+00
10/25/11 19:34	32.18	138.38	5.1	196	-4.8E-02	28.93	-6.5E-03	10	2.5E-12	1.2E-05	2.7E+00
1/1/12 5:27	31.43	138.57	6.8	265	4.3E-02	4.08	-	-	1.1E-09	5.0E-03	7.3E+00
1/8/12 15:37	34.00	135.50	4.8	141	5.0E-02	0.22	-	-	2.6E-11	1.2E-04	1.9E+00
12/7/12 8:18	37.82	144.32	7.3	862	1.9E-01	80.11	-	-	-5.9E-12	-2.8E-05	1.8E+01
12/31/12 5:15	32.96	136.74	4.0	27	6.3E-02	0.21	-	-	1.7E-11	7.9E-05	2.9E+00
4/17/13 8:57	34.05	139.35	5.8	265	4.4E-02	0.19	-	-	-2.0E-10	-9.5E-04	3.3E+00
8/3/13 0:56	34.64	137.53	4.8	179	4.5E-02	0.35	-	-	9.0E-12	4.3E-05	1.1E+00
8/17/13 23:00	33.32	139.32	4.5	246	2.4E-02	0.43	-	-	-1.3E-12	-6.2E-06	6.8E-01
8/30/13 8:32	33.65	135.97	4.3	83	4.2E-02	0.36	-	-	2.8E-11	1.3E-04	1.3E+01
9/4/13 0:18	29.94	139.42	6.5	446	1.1E-01	4.55	-3.3E-03	1	3.7E-11	1.7E-04	3.5E+00
10/25/13 17:10	37.20	144.57	7.1	845	1.7E-01	6.71	-6.1E-03	3	-2.5E-10	-1.2E-03	7.5E+00
3/13/14 17:06	33.69	131.89	6.3	449	1.5E-01	18.30	-1.2E-02	>52	6.5E-12	3.1E-05	1.3E+01
5/4/14 20:18	34.94	139.50	6.0	324	9.2E-02	5.07	-7.6E-03	5	7.2E-11	3.4E-04	2.0E+00
11/22/14 13:08	36.69	137.89	6.3	404	2.3E-01	107.58	-9.3E-03	>7	-3.8E-11	-1.8E-04	5.0E+00
11/29/14 23:00	32.88	137.00	4.2	46	-	-	3.6E-03	8	6.3E-11	-	5.8E+00
5/12/15 21:12	38.86	142.15	6.8	800	3.1E-02	2.03	-	-	-1.2E-11	-5.4E-05	1.8E+00
5/17/15 16:33	31.88	138.36	4.7	215	5.3E-02	0.16	-	-	1.5E-12	7.0E-06	2.3E+00
5/30/15 11:23	27.86	140.68	7.9	707	1.8E-01	96.13	-9.7E-03	128	1.1E-09	5.1E-03	5.1E+01

Acknowledgments

We acknowledge funding by the German Science Foundation (DFG grant KO2108/8-1) and the Geological Survey of Canada for the GeniusPlug work and NSF grants OCE-0623633 and OCE-1334436 to Demian Saffer supporting the pressure instrumentation and the efforts of Integrated Ocean Drilling Program (IODP) members. This research used the data recovered during IODP Expedition 365 in 2016, which is available upon request from the authors. We also thank the CDEX operations group and scientists who supported the related drilling, installation, and recovery operations. We used the F-net and focal mechanism Catalog operated by the National Research Institute for Earth Science and Disaster Prevention and obtained seismic data of DONET from the Hi-net website. For preparation of figures, we used the Generic Mapping Tools (GMT) software (Wessel and Smith, 1991).

Author Contributions

C. Kinoshita wrote the manuscript about formation scale elastic properties inferred from borehole pressure data. I participated in the IODP expedition 365 where the GeniusPlug borehole observatory was recovered. As onboard observatory specialist, I was responsible for the pressure and temperature data acquisition. Besides the technical assistance, I did the preliminary pressure data processing on board. C. Kinoshita and I discussed her processing procedures and interpretation via email and during meetings in Japan. I reviewed and commented on the drafts before submissions.

Supplementary materials

Introduction

This supporting information describes: (1) the detailed recovery times of pressure and loading efficiency, (2) solutions to the radial flow problem described in section “Hydraulic Diffusivity” and shown in Figure 48, following Gibson (1958), Sawyer et al. (2008), and Hammerschmidt et al. (2013b); and (3) the derivation of Equation (28) and computation of sensing volume compressibility, β^* .

Figure 55 is an enlarged section of Figure 46 which shows the detailed recoveries of pressure and loading efficiency in 2014. Even though pressure shows a stable value after the earthquakes, loading efficiency continues to recovery, with a relatively constant rate. This suggests that the recovery of loading efficiency is distinct from that of pressure.

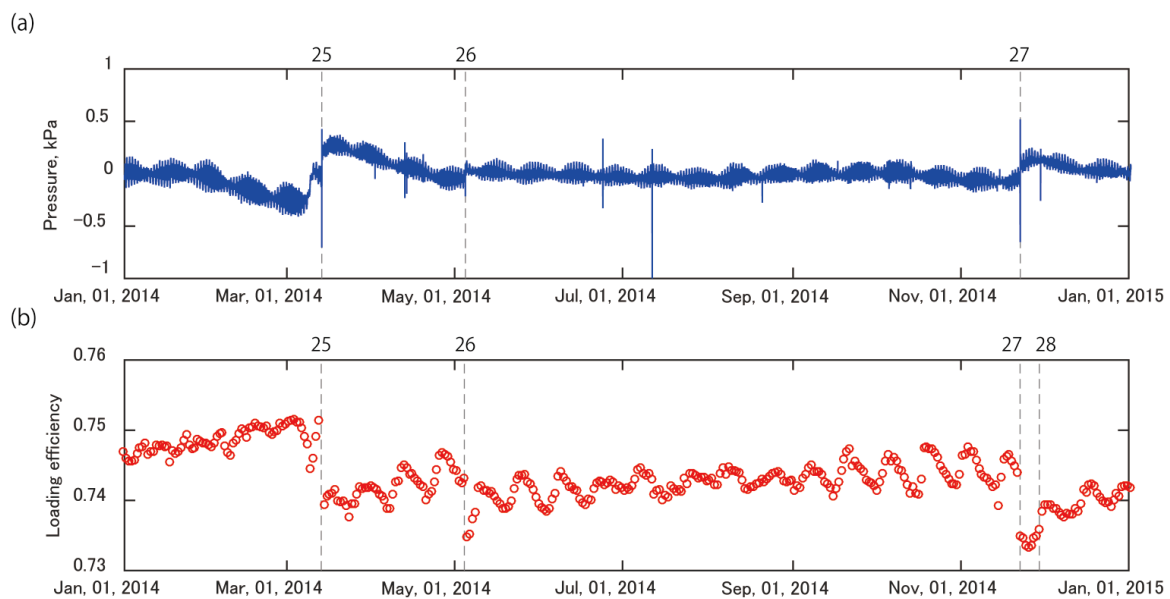


Figure 55: Time series of **A)** pressure and **B)** loading efficiency in 2014. De-tided and de-trended formation pressure, corrected as described in the text. The dashed lines indicate the timing of earthquake that produced detectable changes in pressure and/or loading efficiency.

Response of borehole sensing volume to pressure variations in the formation

Radial flow into or out of the borehole is described in terms of a series of dimensionless parameters (Gibson, 1958; Hsieh et al., 1987; Sawyer et al., 2008);

$$\frac{\partial^2 P_D}{\partial r_D^2} + \frac{1}{r_D} \frac{\partial P_D}{\partial r_D} + S_D(t_D) = \frac{\partial P_D}{\partial t_D} \quad (29)$$

where the dimensionless pressure (P_D), radius (r_D), time (t_D), fluid source term if present (S_D), and frequency (f_D) in radians are given by:

$$P_D = \frac{P(r, t)}{P(\infty, t)} \quad (30)$$

where P is the formation pressure and $P(\infty, t)$ represents the formation pressure in the far field, away from the influence of the well (all variables and their definitions are listed in Table 9).

$$r_D = \frac{r}{r_{so}} \quad (31)$$

$$t_D = \frac{c * t}{r_{so}^2} \quad (32)$$

$$S_D(t_D) = f_D \cos(f_D t_D) \quad (33)$$

$$f_D = \frac{r_{so}^2 f}{c} \quad (34)$$

where r is the horizontal distance from the center of borehole (pressure sensor is installed at the center of borehole; m), r_{so} is the screen outer radius (m; Figure 55), t is time (s), c is hydraulic diffusivity (m^2/s), and f is frequency (s^{-1}).

Sawyer et al. (2008) modified Hsieh et al. (1987)'s model for the case of a sealed borehole, and derived the following relationship between amplitude (A) and phase shift (ζ) in formation pressure relative to the ocean tidal loading (reference pressure), which depends on the dimensionless frequency (f_D) and the formation: instrument compressibility ratio (β_D) as shown in Figure 48 (see Equation (28)).

$$A = (E^2 + F^2)^{-\frac{1}{2}} \quad (35)$$

$$\zeta = -\tan^{-1}\left(\frac{F}{E}\right) \quad (36)$$

where the imaginary parameters E and F are;

$$E = 1 - \frac{f_D}{\beta_D} [\Psi Ker(\sqrt{f_D}) + \Phi Kei(\sqrt{f_D})] \quad (37)$$

$$F = \frac{f_D}{\beta_D} [\Phi Ker(\sqrt{f_D}) + \Psi Kei(\sqrt{f_D})] \quad (38)$$

$Ker(x)$ and $Kei(x)$ are the real and imaginary parts of Kelvin functions of order zero, and Φ and Ψ are given by:

$$\Phi = -\frac{[Ker_1(\sqrt{f_D}) + Kei_1(\sqrt{f_D})]}{\sqrt{2f_D}[Ker_1^2(\sqrt{f_D}) + Kei_1^2(\sqrt{f_D})]} \quad (39)$$

$$\Psi = -\frac{[Ker_1(\sqrt{f_D}) - Kei_1(\sqrt{f_D})]}{\sqrt{2f_D}[Ker_1^2(\sqrt{f_D}) + Kei_1^2(\sqrt{f_D})]} \quad (40)$$

Determination of instrument compressibility (β^*)

As is evident above (see also Figure 48) the magnitude of amplitude and phase response to periodic pressure fluctuations in the formation depends on the hydraulic diffusivity of the formation, the frequency of the pressure fluctuations, and the ratio of formation and sensing volume compressibilities (Hsieh et al., 1987; Sawyer et al., 2008). In our case, formation compressibility is constrained by laboratory experiments on core samples (Table 9). Here we derive the instrument compressibility (β^*), which represents the aggregate of the fluid and steel compressibilities in the sensing volume. This parameter includes the fluid in the borehole casing below the retrievable packer and above the cement plug at the base of the casing, as well as the steel tubing of the instrument package (Figure 56). The formation-instrument compressibility ratio (β_D) is then given by Equation (28). The volumes of water (V_w) and steel (V_{steel}) in the sensing volume of the observatory are defined as:

$$V_w = \pi\{r_{ci}^2 H - (r_{to}^2 L_t + r_{go}^2 Z)\} \quad (41)$$

$$V_{steel} = \pi H(r_{co}^2 - r_{ci}^2) + \pi(r_{to}^2 L_t + r_{go}^2 Z) \quad (42)$$

where L_t is the length of steel pipe (3" tubing) above the instrument package (m) (Figure 56), Z is the length of the instrument package (m), H is the length of the open casing volume below the packer and above the cement (m), and r_{to} is the tubing outer radius (m), r_{go} is the GeniusPlug outer radius (m), r_{ci} is the casing inner radius (m), r_{co} is the casing outer radius (m). The total volume (V) is simply the sum of V_w and V_{steel} (m^3), and the instrument

compressibility (β^*) is given by the aggregate of the two, weighted by the volumetric proportions of each:

$$V = V_w + V_{steel} \quad (43)$$

$$\beta^* = \beta_w \frac{V_w}{V} + \beta_{steel} \frac{V_{steel}}{V} \quad (44)$$

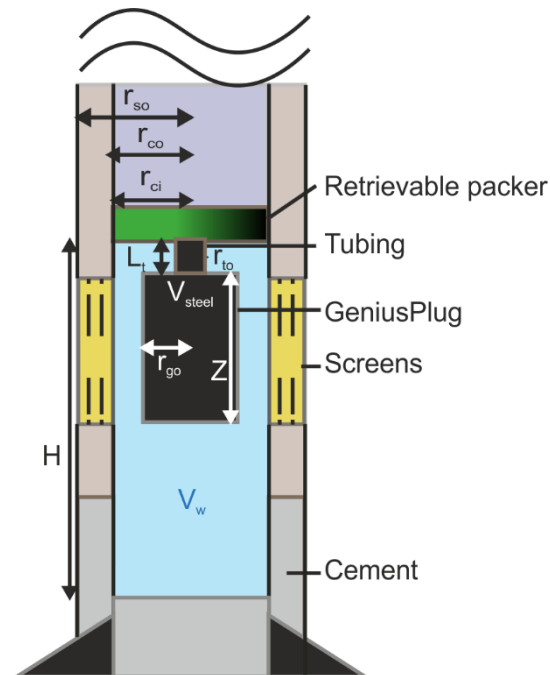


Figure 56: Engineering specifications of Hole C0010A and GeniusPlug (modified after Kinoshita et al., 2018a).

Table 11: Seismic events used for the comparison between pressure energy density (PED) and PGV in Figure 51.

No.	Date (UTC)	Latitude (°)	Longitude (°)	Mw	Epicentral distance (km)	PED (kPa · s)	PGV (cm/s)
1	11/12/14 1:13	34.24	135.70	4.2	148	6.3E-01	9.5E-02
2	11/22/14 13:08	36.69	137.89	6.3	404	5.0E+00	1.9E-01
3	11/29/14 23:00	32.88	137.00	4.2	46	5.8E+00	1.6E-01
4	12/5/14 16:01	35.50	135.69	5.1	272	3.5E-01	3.1E-02
5	2/6/15 1:25	33.73	134.37	4.8	223	7.6E-01	3.6E-02
6	2/16/15 23:06	39.87	143.19	6.7	944	2.4E+00	6.7E-02
7	2/20/15 4:25	39.91	143.73	6.1	978	1.2E+00	2.0E-02
8	2/25/15 7:00	31.09	142.14	6.1	565	1.1E+00	1.6E-02
9	3/3/15 15:04	35.34	136.80	4.7	239	3.3E-01	1.6E-02
10	5/10/15 21:25	31.23	142.15	6.1	559	2.4E+00	3.0E-02
11	5/12/15 21:12	38.86	142.15	6.8	800	1.8E+00	6.9E-02
12	5/17/15 16:33	31.88	138.36	4.7	215	2.3E+00	2.7E-02
13	5/30/15 11:23	27.86	140.68	7.9	707	5.1E+01	2.7E-01
14	6/23/15 12:18	27.70	140.18	6.5	697	6.8E-01	3.8E-02
15	9/1/15 15:25	31.47	142.14	6.0	549	1.2E+00	1.7E-02
16	9/2/15 7:07	33.21	134.64	4.4	190	5.1E-01	1.3E-02
17	11/13/15 20:51	30.94	128.59	6.8	804	1.0E+01	1.1E-01
18	1/11/16 17:08	44.43	141.21	6.3	1312	6.3E-01	7.0E-03
19	1/14/16 3:25	41.97	142.80	6.7	1116	1.5E+00	2.8E-02

4 Conclusions and Outlook

This cumulative doctoral thesis was designed to better understand fault zone deformation processes and earthquake slip in the framework of the NanTroSEIZE project in the Nankai Trough subduction zone. The thesis is mainly based on two different methods: First laboratory friction experiments on natural fault gouge to investigate the potential for coseismic slip and earthquake nucleation at shallow depths and second long-term borehole and seafloor pressure monitoring in order to investigate fault zone slip and elastic properties of the accretionary prism sediment on a kilometer wide scale. The main conclusions of the published and unpublished manuscripts are highlighted in the following paragraphs and are discussed with respect to future earthquake sciences.

Laboratory friction experiments on cores from IODP Sites C0004, C0010, C0006 and C0007 provide the most comprehensive physical properties data set of Nankai Trough fault gouge analyzed under simulated shallow depth conditions. The frontal thrust and the megasplay fault zone are frictionally weak. Cohesive strength, most often disregarded in laboratory friction studies related to earthquake mechanics, may account for a significant portion of fault strength within Nankai Trough phyllosilicate-rich fault gouge. The comparisons of intact sediment (structured, lithified) with powdered sediment revealed that powdering and high effective normal stress result in the overestimation of the velocity dependence of friction. Thus, intact lithified samples tested under in-situ stress conditions revealed lower $a - b$ values. The majority of friction studies analyze powdered samples at higher stresses than in-situ conditions. Therefore, the velocity dependence of friction may be overestimated in many studies. Consequently, major fault zones in the Nankai Trough could be velocity-weakening from seismogenic depth up to the seafloor. Thus, in-situ intact deep fault gouge samples are necessary to determine the in-situ velocity dependence unbiased by powdering and overconsolidation. This should be considered in targets for upcoming scientific drilling expeditions, which aim to a better understanding of earthquake nucleation processes and coseismic rupture. Moreover, our observations should be confirmed by further fault zone samples from other subduction zones (e.g. Cascadia, Barbados, Hikurangi).

The weak fault zone samples and the tendency to velocity-weakening behavior at simulated shallow depth conditions favor potential coseismic slip up to the seafloor along the megasplay fault and the frontal thrust zone. In most instances, frictional studies analyze the velocity dependence of friction to evaluate the stability of fault zones. These studies do not consider

superimposed trends on the frictional data. For C0004 megasplay fault sediment, these trends only showed slip dependent weakening which gets more pronounced at simulated shallow depths. Velocity and slip dependent weakening cause the weakening in megasplay fault gouge but slip weakening is dominant. The slip weakening distance and magnitude is controlled by effective normal stress. Slip dependence has to be considered in future frictional studies to describe the full spectrum of frictional behavior. In addition to the before-mentioned reasons, increasing slip weakening with decreasing simulated depths raise the risk for coseismic slip and shallow seafloor deformation. Consequently, the megasplay fault has to be regarded as a tsunamigenic fault in the next megathrust earthquake. Additionally, strong slip weakening is expected at depths relevant for landslide occurrence. Thus, the observed slip dependence of friction might influence the run out distance of submarine landslides in the megasplay fault zone.

By means of offshore seismological, geodetic and borehole measurements, deformation processes and earthquake hypocenters can be more precisely determined. Land-based networks have a limited resolution due to the large distance between hypocenters and stations. As a consequence, land-based networks mislocated the 1 April 2016 off Mie-earthquake as an intra slab earthquake in the downgoing plate. In contrast, the offshore measurements in particular the strain measurements in sealed boreholes narrowed down the possible fault plane solutions and categorized the earthquake as a plate interface earthquake. However, most subduction zones lack a dense permanent coverage of offshore instrumentation, therefore mislocation of offshore earthquake hypocenters are most likely abundant.

Even a dense offshore seismological network is not able to capture SSEs. Detection of SSEs is only possible by geodetic or borehole pressure measurements. Offshore the Kii peninsular the Nankai Trough hosts regular SSEs seaward of the rupture area of historical Mw 8 earthquakes. The several days to several weeks, long-lasting SSEs have a recurrence interval of 4 – 15 months, while being accompanied by very low frequency tremors. SSEs could be modelled with 1 – 4 cm of slip on the plate boundary fault approximately 30 km landward from the deformation front. These slip rates account for 30 – 55 % of yearly plate motion which is regularly released near the deformation front. This regular release of accumulated strain might reduce the hazard for shallow earthquake rupture close to the trench. Extrapolated long-term healing experiments reveal one to two order of magnitudes higher stress drops when compared to estimated in-situ SSEs stress drops. The discrepancy between in-situ and laboratory data can be explained by an interplay of three factors i) overestimation of vertical stress, ii) underestimation of in-situ seismic moment and iii) overestimation of laboratory healing rates. The long-term SHS experiments reveal that neither log-linear nor power-law

healing explain sufficiently laboratory healing experimental data. Frictional healing is a more complex time-dependent process.

Formation scale poroelastic rock properties are highly sensitive to hydraulic perturbations induced by near and far field earthquakes. Long-term pressure records reveal loading efficiency perturbations in pore water pressure after earthquakes due to gas exsolution from pore water by dynamic strains. Hydraulic perturbations follow a magnitude-distance relationship similar to observations in terrestrial water wells. A lower bound formation permeability of $6.4 \cdot 10^{-13} \text{ m}^2$ is inferred from the deduced hydraulic diffusivity. Borehole pressure measurements prove to be a very sensitive tool to investigate continuous changes in hydrological properties within an active accretionary prism.

A growing number of permanent and temporary offshore observatory networks e.g. DONET-I, DONET-II, the EMSO initiative and the Ocean network Canada initiative will improve our understanding of ocean and subduction zone processes in time and space extensively. Nowadays, the active networks consist of seafloor or shallow borehole observatories and lack resolution at seismogenic depth. Similarly until now, ocean drilling expeditions recovered wall rock and fault gouge from shallow depths but the most ambitious goals of the NanTroSEIZE project were the core recovery from and the installation of an observatory at the onset of seismogenic depth, which failed due to operational reasons in early 2019. In my opinion, upcoming IODP science plans should target again for this ambitious goal, since experiments conducted on seismogenic fault gouge are the only way to get ground truthing evidence for seismogenic processes at depth. In addition, long-term borehole measurements monitoring the seismic cycle are the most promising method to decipher potential earthquake precursory signals and to measure in-situ strain conditions during earthquake nucleation and propagation.

Appendices

Appendix A: Conference contributions

Appendix A lists in total 14 conference abstracts accepted for either poster or oral presentation. I acted four times as corresponding author and have presented a poster at the IODP-ICDP Kolloquium 2017, the JPGU-AGU Joint Meeting 2017, the AGU Fall Meeting 2018 and the EGU General Assembly 2019.

A.1 AGU Fall Meeting 2016 Abstracts

San Francisco, USA 12 – 16 December 2016

Changes in physical properties of the Nankai Trough megasplay fault induced by earthquakes, detected by continuous pressure monitoring

Chihiro Kinoshita¹, Demian M Saffer², Achim Kopf³, **Alexander Roesner**³, Laura Wallace⁴, Eiichiro Araki⁵, Toshinori Kimura⁵, Yuya Machida⁵, Reiji Kobayashi⁶, Earl Davis⁷, Sean Toczko⁵

¹Kyoto University

²Penn State University

³MARUM - University of Bremen

⁴University of Texas, Institute for Geophysics

⁵JAMSTEC Japan Agency for Marine-Earth Science and Technology

⁶Kagoshima University

⁷Geological Survey of Canada, Pacific Geoscience Centre

The Nankai Trough Seismogenic Zone Experiment (NanTroSEIZE) is a multi-expedition Integrated Ocean Drilling Program (IODP) project aimed at understanding seismogenic processes at subduction zones. The most recent NanTroSEIZE expedition was conducted in March – April 2016, with the main objectives of recovering a temporary observatory instrument and installing a permanent Long-Term Borehole Monitoring System at IODP Site C0010. The recovered instrument package, termed the “GeniusPlug” was installed in 2010 and produced a 5.3 year record of pressure and temperature within a screened interval spanning 387 – 409 mbsf, sampled at 30 sec intervals from November 2010 through March 2016.

In this study, we evaluate changes in the properties of the fault zone induced by several earthquakes, using the pressure time series. The GeniusPlug has two pressure sensors to measure the formation pressure and a hydrostatic reference. Here we focused on two phenomena: step changes in pressure induced by regional earthquakes, and associated

changes in formation properties. For the former, we filter the data to remove ocean tides and other oceanographic signals. For the latter, we use the amplitude of the response to ocean tide loading to probe changes in formation compressibility. To define step change in pressure, we compare a 10 minute average of pressure before and after each earthquake. We identify 30 events that exhibit a pressure response, and find that pressure changes strongly correlate with earthquake magnitude and hypocentral distance. To identify the details of the underlying cause of these step changes, we calculated the theoretical static volumetric strain for each event based on Okada (1992). Ongoing work will compare the observed pressure changes with peak ground acceleration (PGA) and peak ground velocity (PGV) determined using ocean bottom seismometers in the DONET (Dense Oceanfloor Network system for Earthquakes and Tsunamis) cabled offshore observatory. To evaluate changes in loading efficiency during the deployment time, we estimated the tidal loading efficiency at one-day intervals. We find that (1) there is a correlation between tidal loading efficiency and hypocentral distance, (2) when large pressure changes are detected, the tidal loading efficiency also deviates.

Repeating and triggered slow slip events in the near-trench region of the Nankai Trough detected by borehole observatories

Demian M Saffer¹, Eiichiro Araki², Achim Kopf³, Sean Toczko², Laura M Wallace⁴, Earl E Davis⁵, **Alexander Roesner**³

¹Penn State University

²JAMSTEC Japan Agency for Marine-Earth Science and Technology

³MARUM - University of Bremen

⁴University of Texas, Institute for Geophysics

⁵Geological Survey of Canada, Pacific Geoscience Center

Slow slip events (SSE), non-volcanic tremor, and very low-frequency earthquakes (VLFE) are well documented down-dip of the seismogenic zone of major faults, yet similar observations for the shallowest reaches of subduction megathrusts are rare. Here, we document a family of repeating strain transients in the outermost Nankai subduction zone, updip of the region that ruptures in great (M8-class) earthquakes. We report on data from two borehole observatories: IODP Site C0002, which penetrates the accretionary prism and monitors a zone 931 – 980 m below seafloor (mbsf) at a location 36 km landward of the trench; and Site C0010, 25 km landward, which monitors a zone spanning 389 – 407 mbsf. We focus on a time window from Dec. 2010 – Apr. 2016, for which we recovered records of formation pore pressure at both sites. After filtering oceanographic noise using a local hydrostatic reference at each site, the pressure records reveal seven transient signals that are synchronous at the two holes. Of

these, five arise spontaneously, and occur at ~ 1 yr intervals with durations of $\sim 7 - 21$ days. All are positive in sign at C0010, with magnitudes of $\sim 0.3 - 0.9$ kPa; at Site C0002 three are negative in sign and two are positive, with magnitudes of $\sim 0.3 - 0.7$ kPa. The remaining two events are larger ($1.7 - 2.7$ kPa), exhibit a negative sign at both sites, and immediately follow: (1) the Mar. 2011 M9 Tohoku earthquake; and (2) a sequence including an Apr. 1 M6 thrust event on the plate interface nearby and the Apr. 16 M7 Kumamoto event. In most cases, the pressure transients are accompanied by swarms of VLFE on the shallow plate interface. We interpret the pressure signals to reflect volumetric strain in response to SSEs. Simple dislocation models illustrate that the data at both sites are well fit by slip of $\sim 1 - 2$ cm on a patch at the plate interface that extends $20 - 40$ km in the down-dip direction, and is centered beneath Site C0002 (spontaneous events) or slightly updip (triggered events). This coincides with a region of the megathrust characterized in previous studies by anomalously low V_p , and elevated pore fluid pressure. The repeating nature of the events, taken together with apparent triggering by regional earthquakes, indicates that the outermost reaches of the subduction megathrust are highly sensitive to perturbation and are perched near a state of failure.

Near-field observations of an offshore Mw 6.0 subduction thrust earthquake from an integrated seafloor and sub-seafloor borehole monitoring network at the Nankai Trough

Laura M Wallace¹, Eiichiro Araki², Demian M Saffer³, Xiaoming Wang⁴, **Alexander Roesner**⁵, Achim Kopf⁵, Ayako Nakanishi², William L Power⁵, Reiji Kobayashi⁶, Chihiro Kinoshita⁷, Sean Toczko²

¹University of Texas at Austin

²JAMSTEC Japan Agency for Marine-Earth Science and Technology

³Penn State University

⁴GNS Science

⁵MARUM - University of Bremen

⁶GNS Science-Institute of Geological and Nuclear Sciences Ltd

⁷Kagoshima University

⁸Kyoto University

An Mw 6.0 earthquake struck ~ 50 km offshore the Kii Peninsula of southwest Honshu, Japan on April 1, 2016. This earthquake occurred directly beneath a cabled offshore monitoring network at the Nankai Trough subduction zone, and within $25 - 35$ km of two borehole observatories installed as part of the NanTroSEIZE IODP drilling project. The earthquake's location close to the seafloor and sub-seafloor network offers a unique opportunity to evaluate dense seafloor geodetic and seismological data in the near-field of a moderate-sized offshore

earthquake. We use the offshore seismic network to locate the mainshock and aftershocks, seafloor pressure sensors and borehole observatory data to determine the detailed distribution of seafloor and sub-seafloor deformation, and seafloor pressure observations to model the observed tsunami. Contractual strain estimated from formation pore pressure records in the borehole observatories (equivalent to 0.37 to 0.15 μ strain) provides a key to narrowing the possible range of fault plane solutions. Together, these data show that the rupture occurred on a landward dipping thrust fault at 9 – 10 km below the seafloor, most likely on the plate interface. Pore pressure changes recorded in one of the observatories also provides evidence for significant afterslip for at least a few days following the mainshock.

The earthquake and its aftershocks are located within the coseismic slip region of the 1944 Tonankai earthquake ($M_w \sim 8.0$), and immediately down-dip of swarms of very low frequency earthquakes in this region, highlighting the complex deformation processes occurring during the interseismic period at a mostly locked seismogenic zone. Access to offshore seismological and deformation data greatly enhances our ability to resolve the location and mechanisms of earthquakes relevant to the subduction earthquake cycle at the Nankai Trough.

Shallow observatory installations unravel earthquake processes in the Nankai accretionary complex (IODP Expedition 365)

Achim Kopf¹, Demian M Saffer², Sean Toczko³, **IODP Exp.365 Science Party**

¹University of Bremen

²Penn State University

³JAMSTEC Japan Agency for Marine-Earth Science and Technology

NanTroSEIZE is a multi-expedition IODP project to investigate fault mechanics and seismogenesis along the Nankai Trough subduction zone through direct sampling, in situ measurements, and long-term monitoring. Recent Expedition 365 had three primary objectives at a major splay thrust fault (termed the “megasplay”) in the forearc: (1) retrieval of a temporary observatory (termed a GeniusPlug) that has been monitoring temperature and pore pressure within the fault zone at 400 meters below seafloor since 2010; (2) deployment of a complex long-term borehole monitoring system (LTBMS) across the same fault; and (3) coring of key sections of the hanging wall, deformation zone and footwall of the shallow megasplay.

Expedition 365 achieved its primary monitoring objectives, including recovery of the GeniusPlug with a >5-year record of pressure and temperature conditions, geochemical samples, and its in situ microbial colonization experiment; and installation of the LTBMS. The

pressure records from the GeniusPlug include high-quality records of formation and seafloor responses to multiple fault slip events, including the 2011 M9 Tohoku and the 1 April Mie-ken Nanto-oki M6 earthquakes. The geochemical sampling coils yielded in situ pore fluids from the fault zone, and microbes were successfully cultivated from the colonization unit. The LTBMS incorporates multi-level pore pressure sensing, a volumetric strainmeter, tiltmeter, geophone, broadband seismometer, accelerometer, and thermistor string. This multi-level hole completion was meanwhile connected to the DONET seafloor cabled network for tsunami early warning and earthquake monitoring.

Coring the shallow megasplay site in the Nankai forearc recovered ca. 100 m of material across the fault zone, which contained indurated silty clay with occasional ash layers and sedimentary breccias in the hangingwall and siltstones in the footwall of the megasplay. The mudstones show different degrees of deformation spanning from occasional fractures to intensely fractured scaly claystones of up to >10 cm thickness. Sparse faulting with low displacement (usually <2 cm) is seen with both normal and reverse sense of slip. Post-cruise rock deformation experiments will relate physical properties to the earthquake response monitored by the observatory array.

A.2 IODP-ICDP Kolloquium 2017 Abstract

Braunschweig, Germany 14 – 16 March 2017

Formation fluid pressure and temperature transients along the Nankai Trough Kumano Transect - SE Japan

A. Rösner¹, A.J. Kopf¹, D.M. Saffer², S. Toczko³, Expedition 365 Scientists

¹MARUM - Center for Marine Environmental Sciences and Faculty of Geosciences, University of Bremen, Bremen, Germany

²Department of Geosciences, Pennsylvania State University, University Park, Pennsylvania 16802, USA

³Japan Agency for Marine Earth Science and Technology, Yokohama, Japan

The Nankai Trough Seismogenic Zone Experiment (NanTroSEIZE) is a multi-expedition Integrated Ocean Drilling Program (IODP) project along the Nankai Trough subduction zone with the purpose of better understanding subduction-zone earthquakes and seismogenic processes. Long-term pressure and temperature monitoring along the Kumano transect produced valuable data records which constrain potential fluid flow paths and help to identify regions of strain accumulation/release. Simultaneous pressure and temperature records are available for a mud volcano (MV4), IODP Site C0002 and IODP Site C0010.

Two recent expeditions, IODP Exp. 365 in April 2016 and Sonne Cruise 251 in October 2016, recovered an autonomous borehole observatory termed “GeniusPlug” and an earlier model observatory termed “SmartPlug”. The GeniusPlug was recovered from Site C0010, where it was installed within the mega splay fault zone at 407 mbsf. The SmartPlug observatory, initially also a borehole observatory, was recovered from a mud volcano in the Kumano Basin, where it was installed in the uppermost seafloor sediments. Both observatories were equipped with temperature loggers and two pressure sensors. One pressure sensor is used as hydrostatic reference, while the other measures formation pressure. The GeniusPlug record has a sampling period of 30 sec from November 2010 – April 2016, and the SmartPlug recorded data at 10 sec intervals from August 2012 – October 2015. Complementary formation pressure data at various depths are available via the C0002 long-term borehole monitoring system (LTBMS). These three observatories monitored temperature, formation and hydrostatic reference pressure over 45 km along dip from the megasplay fault zone into the deep Kumano Basin.

The data records are affected by sensor drifts, tidal loading and clock drifts. These artefacts were removed to analyze short-term and long-term pressure transients, which can be correlated with distant or regional earthquakes. Additionally, pressure transients were

observed which correlate with a period of slow slip in the Kumano forearc basin. Moreover, periods of high-frequency energy are present in the dataset, as well as signals from tsunami passing by the observatory sites. The pressure transients are used for formation physical properties characterization and as a proxy for strain accumulation or release along the Kumano transect. The GeniusPlug temperature data shows cold fluid injections into the borehole. One of these injections can be correlated with the M9 2011 Tohoku-Oki earthquake, whereas the rest is of unknown origin yet.

A.3 JPGU-AGU Joint Meeting 2017 Abstracts

Chiba, Japan 20 – 26 May 2017

Investigation of tidal-induced poroelastic responses at IODP Sites C0010 and C0002 along the Kumano Transect - SE Japan

A. Roesner¹, A.J. Kopf¹, E.E. Davis², D.M. Saffer³, C. Kinoshita³, S. Toczko⁴,
Expedition 365 Scientists

¹MARUM - Center for Marine Environmental Sciences and Faculty of Geosciences, University of Bremen, Bremen, Germany

²Pacific Geoscience Centre, Geological Survey of Canada, Canada

³Department of Geosciences, Pennsylvania State University, University Park, Pennsylvania 16802, USA

⁴Japan Agency for Marine Earth Science and Technology, Yokohama, Japan

The Nankai Trough Seismogenic Zone Experiment (NanTroSEIZE) is a multi-expedition Integrated Ocean Drilling Program (IODP) project along the Nankai Trough subduction zone with the purpose of better understanding subduction-zone earthquakes and seismogenic processes. Long-term pressure and temperature monitoring along the Kumano transect produced valuable data records, which constrain potential fluid flow paths and help to identify regions of strain accumulation/release. Simultaneous pressure and temperature records are available for IODP Site C0002 and IODP Site C0010.

The recent IODP Exp. 365 in April 2016 recovered an autonomous borehole observatory named “GeniusPlug”. The GeniusPlug was recovered from Site C0010, where it was installed within the megasplay fault zone at 407 mbsf. The GeniusPlug observatory was equipped with temperature loggers and two pressure sensors. One pressure sensor is used as hydrostatic reference, while the other measures formation pressure. The GeniusPlug recording has a sampling period of 30 sec from November 2010 – April 2016. Complementary formation pressure data at various depths (PPI 940 mbsf, PPII 920 mbsf, PPIII 770 mbsf) and a hydrostatic reference are available via the C0002 long-term borehole monitoring system (LTBMS) installed in November 2010. Hence, formation pressures can be compared via monitoring at the megasplay fault zone and the inner accretionary prism/deep Kumano Basin.

Amplitude and phase of formation pressure variation have been determined relative to tidal pressure variations at the hydrostatic reference. Mean formation pressure amplitudes are reduced to 62 – 74 % and not shifted in phase. Theory of porous media response to periodic loading allows the calculation of frame bulk modulus, specific storage, hydraulic diffusivity and

strain sensitivity. This approach allows investigation of formation-scale hydraulic and mechanical properties for the fractured mega splay fault sediments in C0010, and the inner accreted sediments of Unit IV at C0002 and the Kumano Basin sediments of Unit II at C0002.

Repeating and triggered slow slip events in the near-trench region of the Nankai Trough detected by borehole observatories

Demian M Saffer¹, Eiichiro Araki², Achim Kopf³, Laura Wallace⁴, Sean Toczko², Earl Davis⁵, **Alexander Roesner³**

¹The Pennsylvania State University

²JAMSTEC

³Univ. Bremen

⁴GNS Science

⁵Pacific Geoscience Centre

Slow slip events (SSE), non-volcanic tremor, and very low-frequency earthquakes (VLFE) are well documented down-dip of the seismogenic zone of major faults, yet similar observations for the shallowest reaches of subduction megathrusts are rare. Here, we document a family of repeating strain transients in the outermost Nankai subduction zone, updip of the region that ruptures in great (M8-class) earthquakes. We report on data from two borehole observatories: IODP Site C0002, which penetrates the accretionary prism and monitors a zone 931-980 m below seafloor (mbsf) at a location 36 km landward of the trench; and Site C0010, 25 km landward, which penetrates the prism and monitors a zone spanning 389 – -407mbsf. We focus on a time window from Dec. 2010 - Apr. 2016, for which we recovered records of formation pore pressure at both sites. After filtering oceanographic noise using a local hydrostatic reference at each site, the pressure records reveal seven transient signals that are synchronous at the two holes. Of these, five arise spontaneously, and occur at ~1 yr intervals with durations of ~7 – 21 days. All are positive in sign at C0010, with consistent magnitudes of ~0.3 – 0.9 kPa; at Site C0002 three are negative in sign and two are positive, with magnitudes of ~0.3 – 0.7 kPa. The remaining two events are larger (1.7 – 2.7 kPa), exhibit a negative sign at both sites, and occur immediately following: (1) the Mar. 2011 M9 Tohoku earthquake; and (2) a sequence including an Apr. 1 M6 thrust event on the plate interface nearby and the Apr. 16 M7 Kumamoto event. In most cases, the pressure transients are accompanied by swarms of VLFE on the shallow plate interface. We interpret the pressure signals to reflect volumetric strain in response to SSEs. Simple dislocation models illustrate that the data at both sites are well fit by slip of ~1 – 2 cm on a patch at the plate interface that extends 20 – 40 km in the down-dip direction, and is centered beneath Site C0002 (spontaneous events) or slightly updip

(triggered events). This coincides with a region of the megathrust characterized in previous studies by anomalously low V_p , and elevated pore fluid pressure. The repeating nature of the events, taken together with apparent triggering by regional earthquakes, indicates that the outer most reaches of the subduction megathrust are highly sensitive to perturbation and are perched near a state of failure.

Preliminary Results of the RV SONNE cruise SO251b in the Kumano Basin (Nankai Trough subduction zone, Japan)

Walter Menapace¹, **Alexander Rösner**¹, *Miho Asada^{2,3}, Christian Dos Santos Ferreira¹, Norbert Kaul⁴, Achim Kopf¹, SO251b onboard scientific party

¹MARUM - Center for Marine and Environmental Science

²Japan Society for the Promotion of Science

³Japan Agency for Marine-Earth Science and Technology

⁴Department of Geosciences, University of Bremen

Mud volcanoes are topographic highs on the ocean seafloor related to expulsion of sediments and fluids from depth. The characterization of the ejecta is helping to constrain the source origin of mud volcanoes and, at the same time, provides important mineralogical, geochemical and rheological information at depths not reachable through scientific drilling. Off the Kii peninsula, on the Kumano Basin seafloor, 13 mud volcanoes have been identified from previous scientific investigations in the area (Kuramoto et al., 2001; Morita et al., 2004; Pape et al., 2014). The mud volcanoes' ejecta have been suggested to originate both in the inner accretionary prism and below it, on the plate interface between the Philippine and Eurasian plates (Pape et al., 2014; Toki et al., 2014; Nishio et al., 2015). The Kumano region is known to be subject to large earthquakes, with last occurrences in 1944 (Tonankai, Mw=8.2) and 1946 (Nankai, Mw=8.3) (Ando et al., 1975; Cummins et al., 2002; Linde and Sacks, 2002; Kodaira et al., 2004). Multiple evidences from other regions affected by mud volcanism suggest that mud volcanoes activity is linked with earthquake (Mellors et al., 2007; Kopf et al., 2010; Rudolph and Manga., 2012). Tsunogai et al. (2012) hypothesized such link could also exist for the Kumano Basin mud volcanoes. However, full understanding of this relationship needs to be supported by detailed studies on mud volcanoes to understand their evolution both in time and space, as well as to link them with the seismogenic zone at depth. Two scientific cruises with the RV SONNE were held on the Kumano Basin in 2012 (SO222) and 2016 (SO251b). The main purposes of the SO251b cruise were (1) to recover the long-term monitoring devices installed in 2012 on 3 mud volcanoes (MV#2, MV#3, MV#4) and (2) to monitor heat flow, pore water geochemistry, bathymetric and subbottom variations on the Kumano Basin seafloor in order to compare the newly acquired data to the SO222 ones. Four long-term observatories,

measuring pressure and temperature in MeBo boreholes, were recovered during multiple dives with the ROV PHOCA from Geomar and are currently under analysis. The long-term data series, together with records from the DONET network, will allow to define the link between mud volcanoes and earthquakes. At the same time, the multibeam echosounder survey (Kongsberg EM122, 12 kHz) was expanded from 2012 to cover most of the Kumano Basin, from 136°10' to 137°30' East. The recently acquired data unraveled a new mud volcano (MV#14, which was also ground truthed with the recovery of mud breccia) and interesting bathymetric changes in correspondence of some of the most active mud volcanoes (MV#2, MV#13). The differential bathymetry provides constraints on mud flows occurrence between 2012 and 2016. Several loci of possible gas emission (>40) were discovered on the basin seafloor, often situated on top of mud volcanoes or near suspected ones, characterized by strong acoustic signals within the water column. Geochemistry results from sediment cores scattered through the research area showed, according to preliminary analyses conducted onboard, slight freshening with increasing depth, pointing towards a possible deep-seated fluid source. Heat flow measurements with a violin-bow probe through the basin and the active mud volcanoes (identified in 2012) revealed marked differences from the SO222 measurements, supporting ongoing fluid/mud emissions especially on MV#2 and MV#13.

Changes in physical properties of the Nankai Trough megasplay fault induced by earthquakes, detected by continuous pressure monitoring

Chihiro Kinoshita¹, Demian M Saffer², Achim Kopf³, **Alexander Rösner**³, Laura Wallace⁴, Eiichiro Araki⁵, Toshinori Kimura⁵, Yuya Machida⁵, Reiji Kobayashi⁶, Earl Davis⁷, Sean Toczko⁵, Stephanie Carr⁸

¹Graduate School of science, Kyoto University, Japan

²Department of Geology, Pennsylvania State University, USA

³MARUM, University of Bremen, Germany

⁴GNS Science, NZ

⁵JAMSTEC, Yokohama, Japan

⁶Kagoshima University, Kagoshima, Japan

⁷Pacific Geoscience Centre, Geological Survey of Canada, Canada

⁸Colorado School of Mines, USA

One primary objective of Integrated Ocean Drilling Program (IODP) Expedition 365, conducted as part of the NanTroSEIZE project, was to recover a temporary observatory, termed the “GeniusPlug“ emplaced to monitor formation, pore fluid pressure and temperature within a major splay fault that branches from the main plate interface, at a depth of ~400 m below sea

floor (mbsf). The instruments were installed in Dec. 2010 and recovered in April 2016, yielding 5.3 years record of formation pressure and temperature within fault zone. Here, we use the pressure time series, and in particular the response to ocean tidal loading, to evaluate changes in physical properties of fault zone induced by several regional earthquakes. To accomplish this, we quantify: (1) the amplitude of the formation's response to tidal loading, defined in terms of a tidal loading efficiency, governed primarily by the formation and fluid elastic properties; (2) the phase lag between the ocean tidal signal and the measured response in the observatory, which is governed by a combination of formation hydraulic diffusivity and the relative compressibilities of the formation and sensing volume; and (3) pressure steps associated with earthquakes, identified in formation pressure after removal of the tidal signal. We observe essentially no phase lag, but for many events we detect both pressure steps and transient decreases in loading efficiency. To reveal the cause of these changes, we investigate the effects of static and dynamic crustal strains. Changes in theoretical static volumetric strain and the associated expected pressure step for each event are calculated based on Okada (1992), and using a conversion from volumetric strain to pore pressure based on formation properties defined by laboratory experiments. We find that, there is no clear correlation between observed pressure steps and predicted static volumetric strain; furthermore, the predicted pressure steps are ten to hundreds of times smaller than observed. As a proxy for dynamic strains, we calculate the integrated "pressure energy density" over a 30 minute window for each event, and show a positive correlation with both step changes in pressure and changes in loading efficiency. Most of the detected changes represent pressure increases and loading efficiency decreases. We speculate that disruption of grain contacts and subsequent pore collapse induced by dynamic strain produces changes of hydraulic properties in the fault zone. Alternatively, these changes could reflect exsolution of gas from pore fluids that drives pore pressures up while simultaneously reducing loading efficiency by increasing the compressibility of pore-filling fluids. Finally, the observed amplitude response and negligible phase lag of the formation pressure response to ocean tidal loading, taken together, allow an estimate of the minimum hydraulic diffusivity of splay fault of $8.9 \times 10^5 \text{ m}^2/\text{s}$.

A.4 AGU Fall Meeting 2017 Abstract

New Orleans, USA 11 – 15 December 2017

Frictional properties of the Nankai frontal thrust explain recurring shallow slow slip events

Demian M Saffer¹, Matt Ikari², Achim Kopf², **Alexander Roesner²**

¹Penn State University

²MARUM - University of Bremen

Recent observations provide evidence for shallow slip reaching to the trench on subduction megathrusts, both in earthquakes and slow slip events (SSE). This is at odds with existing friction studies, which report primarily velocity-strengthening behavior (friction increases with slip velocity) for subduction fault material and synthetic analogs, which leads only to stable sliding. We report on direct shearing experiments on fault rocks from IODP Site C0007, which sampled the frontal thrust of the Nankai accretionary prism. This fault has been implicated in both coseismic slip and recurring SSE. We focus on material from 437.2 meters below seafloor, immediately above a localized shear zone near the base of the fault. In our experiments, a 25 mm diameter cylindrical specimen is loaded in an assembly of two steel plates. After application of normal stress (3, 10, or 17 MPa) and subsequent equilibration, the lower plate is driven at a constant velocity while the upper plate remains stationary; this configuration forces shear to localize between the two plates. After reaching a steady state residual friction coefficient (μ_{ss}), we conducted velocity-stepping tests to measure the friction rate parameter ($a-b$), defined as the change in friction for a change in velocity: $(a-b) = \Delta\mu_{ss} / \ln(V/V_0)$, over a range of velocities from 0.1 – 100 $\mu\text{m s}^{-1}$. We find that μ_{ss} ranges from 0.26 to 0.32 and exhibits a slight decrease with normal stress. We observe velocity-weakening behavior at low normal stresses (3 – 10 MPa) and for low sliding velocities ($< \sim 3 - 10 \mu\text{m s}^{-1}$). Values of $(a-b)$ increase systematically from -0.007 to -0.005 at velocities of 0.3 – 1 $\mu\text{m s}^{-1}$, to $\sim -0.001 - 0.045$ at velocities $> 30 \mu\text{m s}^{-1}$. At higher normal stress (17 MPa), we observe dominantly velocity-strengthening, consistent with previously reported measurements for 25 MPa normal stress. Our observation of rate weakening at slip rates matching those of SSE in the outer Nankai forearc provide a potential explanation for periodic strain accumulation and subsequent release during SSE near the trench. The observation of rate weakening behavior only at low normal stresses also suggests that nucleation of these SSE should be restricted to shallow depths ($< \sim 2 - 5 \text{ km}$) or zones of elevated pore fluid pressure.

A.5 AGU Fall Meeting 2018 Abstract

Washington D.C., USA 10 – 14 December 2018

Frictional properties of the Nankai frontal thrust and megasplay fault – Potential for shallow unstable slip

A. Roesner¹, M.J. Ikari¹, D.M. Saffer², K. Stanislawski¹, A.J. Kopf¹

¹MARUM - Center for Marine Environmental Sciences and Faculty of Geosciences, University of Bremen, Bremen, Germany

²Department of Geosciences, Pennsylvania State University, University Park, Pennsylvania 16802, USA

The Nankai Trough subduction zone hosts a wide spectrum of slip behavior from slow slip events to megathrust earthquakes. Shallow low frequency earthquakes and slow slip have been documented along the plate boundary and possibly within the accretionary prism, and slip in these events may have reached the seafloor. A systematic study of frictional properties and strength, including testing under in-situ stresses, is one key toward understanding the processes that control slip behavior along these shallow faults.

In our experiments, we conducted velocity step tests in a direct shear apparatus to investigate the velocity-dependence of friction for several fault zones along the Kumano transect. Natural fault material from burial depths between 250 – 440 mbsf from IODP Sites C0004, C0010, C0006 and C0007 were tested in both intact and remolded states under effective normal stresses ranging from the in-situ condition of ~3 MPa up to 17 MPa, simulating burial depths from ~300 mbsf to ~1700 mbsf. A velocity stepping sequence over a range from 0.1 – 30 $\mu\text{m/s}$ was chosen to determine friction rate parameters.

These materials exhibit a wide range in frictional strength ($\mu = 0.25 - 0.55$). The weakest samples ($\mu = 0.25$) are from the frontal thrust at Site C0007 and the hanging wall of the megasplay at Site C0010. At both the frontal thrust and megasplay fault regions, higher frictional strengths up to 0.55 are observed at neighboring sites within 4 km (C0004, C0010). Under in-situ effective stress conditions (2 – 4 MPa) remolded and intact samples from all sites show mainly velocity-weakening behavior whereas at 10 and 17 MPa the samples exhibit velocity-neutral behavior. This is consistent with previously published studies documenting velocity strengthening at 25 MPa. The frontal thrust samples show a higher potential for unstable slip (mostly velocity weakening) than the megasplay fault samples (mainly velocity neutral). Our data also show that the frictional strength and velocity-dependence of friction can

vary significantly over short distances, for example the 700 m between C0007 and C0006. Due to these facts, understanding earthquake slip propagation is even more challenging.

A.6 AOGS 2018 Abstract

Honolulu, USA 03 – 08 June 2018

Expectations for the Deep Megasplay Fault Zone at the Nankai Trough Based on Mechanical Properties of Shallow Nantroseize Samples

Matt Ikari¹, **Alexander Roesner**¹, Demian Saffer², Andre Huepers¹, Achim Kopf¹

¹University of Bremen

²Pennsylvania State University

With the goal of understanding the seismogenic and tsunamigenic potential of subduction megathrust systems, the Nankai Trough Seismogenic Zone Experiment (NanTroSEIZE) has provided data and borehole samples over the past 10 years. Key laboratory observations from the shallow megasplay fault zone (Site C0004) and the frontal thrust (C0007) at 25 MPa effective normal stress include intermediate frictional strength (friction coefficient $\leq 0.33 - 0.40$), and consistently velocity-strengthening friction at slip rates of 10^{-7} to 10^{-4} m/s. Shearing decreases permeability relative to unsheared samples, to values of $k \leq 7.00 \times 10^{-19}$ m². These behaviors are generally well-explained by the clay-rich composition of these hemipelagic mud samples. Recent data show that samples from the megasplay and frontal thrust/prism toe region exhibit velocity-neutral to weakening friction favorable for slow slip phenomena at lower effective stresses (≤ 17 MPa) and slip rates ($< 10^{-5}$ m/s).

Planned drilling at Site C0002 is expected to penetrate the deep megasplay at ~ 5 km below seafloor, in a region where slow slip and VLFE are observed by borehole and seafloor observatories. Because our data suggest that slow instabilities are favored at low effective stresses, high pore pressures may be expected. However, a study of the incoming stratigraphy at Sites C0011 and C0012 revealed extremely low friction (< 0.2) in a siliciclastic turbidite-bearing unit and pelagic red clay. The basaltic basement at these sites is relatively strong (friction coefficient > 0.5) but shows signs of alteration and contains clay veins, and therefore could also be involved in duplexing at depth. This suggests that the main plate boundary fault(s) may down step and shear may localize in lithologies other than hemipelagic mudstones at greater depths and distances from the trench. Expectations of pore overpressuring and unstable frictional behavior therefore depend on the lithology encountered in the deep megasplay.

A.7 JPGU 2018 Abstract

Chiba, Japan 20 – 24 May 2018

Real-time monitoring of seismic and geodetic activities by long term borehole monitoring system in the Nankai Trough subduction zone

Toshinori Kimura¹, Eiichiro Araki¹, Yuya Machida¹, Kier Becker², Masataka Kinoshita³, Sean Toczko⁴, **Alexander Roesner**⁵, Tianhaozhe Sun⁶, Joshua Edgington⁷, Burhan Senyener⁵, Earl Davis⁸, Takashi Yokobiki¹, Shuheji Nishida¹, Shuichi Kodaira¹, Katsuyoshi Kawaguchi¹, Narumi Takahashi⁹, Masanori Kyo⁴, Keita Akiyama⁴, Tomokazu Saruhashi⁴, Takahiro Yokoyama⁴, Noriaki Sakurai⁴

¹JAMSTEC

²RSMAS, University of Miami

³Earthquake Research Institute, the University of Tokyo

⁴CDEX, JAMSTEC

⁵MARUM, the University of Bremen

⁶The Pennsylvania State University

⁷Texas A&M University

⁸Pacific geoscience centre, Geological survey of Canada

⁹NIED

The Nankai Trough, Japan, is a major subduction zone formed by the subducting Philippine Sea plate beneath the Eurasian plate with a rate of approximately 4 – 6.5 cm/year, and over M 8.0 huge mega-thrust earthquake occurred along plate interface repeatedly with intervals of 100 to 150 years. These earthquakes generate not only strong ground motion but also huge tsunamis, which cause serious and widespread damage in coastal urban area in the southcentral part of Japan. It is very important to understand earthquake preparation and generation process by in-situ seismic and geodetic monitoring to assess the risk of mega-thrust earthquakes including huge tsunamis. In the Nankai Trough, submarine cable network observation system named DONET (Dense Oceanfloor Network system for Earthquake and Tsunamis) is now monitoring real-time seismic and tsunami activities, which cannot be captured by conventional land-based observations. Moreover, to measure very weak geodetic and seismic events, which cannot be measured by DONET seafloor observatories, borehole observatories have been constructed as a part of the IODP NanTroSEIZE project. From January 12 to February 7, 2018, the IODP expedition 380 was conducted to install long-term borehole monitoring system (LTBMS) to the C0006G hole. The C0006G observatory has a suite of borehole sensors comprising a volumetric strainmeter, tiltmeter, broadband seismometer, thermometer array, and pressure gauges. The IODP C0002G and C0010A LTBMS observatories, which were respectively installed during IODP expeditions 332 and 365,

have the same observation system as the C0006G, and are now real-time observatories connected to the DONET submarine cable. The C0006G will be also connected to DONET submarine cable in March, 2018 by ROV Hyper-dolphin and Shinsei-maru, and become the third real-time LTBMS observatory located in the toe region of the accretionary prism. In this presentation, we will report the initial data observed by the C0006G LTBMS sensors after the DONET connection. Also, we will show the recent results obtained from long-term LTBMS data observed by the C0002G and C0010A LTBMS including slow slip events, which occurred repeatedly every 8 to 15 months and would accommodate 30 to 55 % of the plate motion as reported by Araki et al. (2017). We will also discuss the possibility of future C0006G observed data providing new information to discuss spatial distribution of SSEs and other seismic and geodetic events along the Nankai Trough subduction zone.

A.8 EGU General Assembly 2019 Abstract

Vienna, Austria 07 – 12 April 2019

Frictional healing of the Nankai frontal thrust and megasplay fault - Bridging the gap between laboratory and in-situ data

A. Roesner¹, M.J. Ikari¹, K. Stanislawski¹, A.J. Kopf¹

¹MARUM - Center for Marine Environmental Sciences and Faculty of Geosciences,
University of Bremen, Bremen, Germany

The Nankai Trough subduction zone hosts a wide spectrum of slip behavior, from slow slip events to megathrust earthquakes. Recent studies documented shallow recurring slow slip events at the Nankai Trough subduction megathrust fault; these events occur every 8 to 15 months, releasing accumulated elastic strain energy.

This study used slide-hold-slide (SHS) experiments in a ring shear device to investigate fault restrengthening (or "healing") for the megasplay and the frontal thrust faults (IODP Sites C0004 and C0007) along the Kumano transect. For both fault zones, saturated samples were tested under 4 MPa effective normal stress at room temperature and humidity. We employed hold times from 10 – 106 seconds and two different shearing velocities (10 and 0.01 $\mu\text{m/s}$). These loading velocities are chosen to represent the slip velocities of previously documented very low-frequency earthquakes and slow slip events in the subduction zone. To study the time-dependent restrengthening of faults in a laboratory setup, the SHS experiments are commonly employed as an analogue for the seismic cycle. Our study is designed to bridge the gap between laboratory and in-situ derived healing rates between repeated slow slip events.

Our data show that the megasplay fault heals faster than the frontal thrust fault. When a log-linear fit is applied to our data, we see that the healing rates in the megasplay fault are ~2.5 times larger than in the frontal thrust fault at the higher velocity, and 5 times larger at the lower velocity. We observe that higher shearing velocity correlates with increased frictional healing and creep. The megasplay fault exhibits log-linear healing rates 25 times higher at 10 $\mu\text{m/s}$ than at 0.01 $\mu\text{m/s}$. In contrast, the frontal thrust fault shows a log-linear healing rate 2 times greater at the higher shearing velocity. In addition to the standard log-linear law we also applied an alternative power-law fit to our data that accounts for accelerated healing. Both healing laws produce good fits with R^2 of 0.9 – 0.97. The 10 $\mu\text{m/s}$ SHS experiments are well-described by both laws, whereas the 0.01 $\mu\text{m/s}$ experiments are significantly better described by the power-law fit. Therefore, at the slower velocity advanced fault healing is expected at

larger hold times. Moreover, we speculate that slow slip events on the megasplay fault would recur more frequently than on the frontal thrust fault due to higher healing rates.

Ongoing work includes derivation of in-situ healing rates in between consecutive slow slip events from geodetic and long-term borehole measurements, which we will compare with our experimental data set.

Appendix B: Cruises

This chapter summarizes my contributions to international scientific expeditions. During my Ph.D. studies, I have been on three expeditions, located offshore Japan. My Ph.D. thesis is mainly based on the data and cores acquired during this cruises. Two expeditions were IODP expeditions on the drilling vessel D/V Chikyu, the third expedition took place on the German research vessel R/V Sonne. As a shipboard scientist, I have been contributing to the IODP proceedings chapters and the cruise report. In the following, the proceeding abstracts and the cruise report summary are shown exemplarily for these comprehensive documents. In addition, a manuscript abstract is shown which is based on the R/V Sonne Research Cruise SO251.

B.1 Proceedings of the IODP Volume 365 Abstract

NanTroSEIZE Stage 3: Shallow Megasplay Long-Term Borehole Monitoring System

A.J. Kopf¹, D.M. Saffer², S. Toczko³, E. Araki³, S. Carr⁴, T. Kimura³, C. Kinoshita², R. Kobayashi⁵, Y. Machida³, **A. Roesner**¹, L. Wallace⁶

contributing authors:

S. Chiyonobu⁷, K. Kanagawa⁸, T. Kanamatsu³, G. Kimura⁹, M.B. Underwood¹⁰

¹MARUM - Center for Marine Environmental Sciences and Faculty of Geosciences, University of Bremen, Bremen, Germany

²Department of Geosciences, Pennsylvania State University, University Park, Pennsylvania 16802, USA

³Japan Agency for Marine Earth Science and Technology, Yokohama, Japan

⁴Bigelow Laboratory for Ocean Sciences, Boothbay, USA

⁵Departments of Earth and Environmental Sciences, Kagoshima University, Kagoshima, Japan

⁶Institute for Geophysics, University of Texas at Austin, Austin, USA

⁷Faculty of International Resource Sciences, Akita, Japan

⁸Department of Earth Science, Chiba University, Chiba-city, Japan

⁹Tokyo University of Marine Science and Technology, Tokyo, Japan

¹⁰Department of Earth and Environmental Science, New Mexico Institute of Mining and Technology, Socorro, USA

The Nankai Trough Seismogenic Zone Experiment (NanTroSEIZE) is a coordinated, multiexpedition International Ocean Discovery Program (IODP) drilling project designed to investigate fault mechanics and seismogenesis along subduction megathrusts through direct

sampling, in situ measurements, and long-term monitoring in conjunction with allied laboratory and numerical modeling studies. The fundamental scientific objectives of the NanTroSEIZE drilling project include characterizing the nature of fault slip and strain accumulation, fault and wall rock composition, fault architecture, and state variables throughout the active plate boundary system. IODP Expedition 365 is part of NanTroSEIZE Stage 3, with the following primary objectives:

1. Retrieval of a temporary observatory at Site C0010 that began monitoring temperature and pore pressure within the major splay thrust fault (termed the “megasplay”) at 400 mbsf in November 2010.
2. Deployment of a complex long-term borehole monitoring system (LTBMS) designed to be connected to the Dense Oceanfloor Network System for Earthquakes and Tsunamis (DONET) seafloor cabled observatory network postexpedition.

The LTBMS incorporates multilevel pore pressure sensing, a volumetric strainmeter, tiltmeter, geophone, broadband seismometer, accelerometer, and thermistor string. Together with an existing observatory at Integrated Ocean Drilling Program Site C0002 and a planned future installation near the trench, the Site C0010 observatory allows monitoring within and above regions of contrasting behavior of the megasplay fault and the plate boundary as a whole. These include a site above the updip edge of the locked zone (Site C0002), a shallow site in the megasplay fault zone and its footwall (Site C0010), and a site at the tip of the accretionary prism (possible future installation at Integrated Ocean Drilling Program Site C0006). Together, this suite of observatories has the potential to capture deformation spanning a wide range of timescales (e.g., seismic and microseismic activity, slow slip, and interseismic strain accumulation) across a transect from near-trench to the seismogenic zone. Site C0010 is located 3.5 km along strike to the southwest of Integrated Ocean Drilling Program Site C0004. The site was drilled and cased during Integrated Ocean Drilling Program Expedition 319, with casing screens spanning a ~20 m interval that includes the megasplay fault, and suspended with a temporary instrument package (a “SmartPlug”), which included pressure and temperature sensors. During Integrated Ocean Drilling Program Expedition 332 in late 2010, the instrument package was replaced with an upgraded sensor package (the “GeniusPlug”), which included a set of geochemical and biological experiments in addition to pressure and temperature sensors.

Expedition 365 achieved its primary scientific and operational objectives, including recovery of the GeniusPlug with a >5 y record of pressure and temperature conditions within the shallow megasplay fault zone, geochemical samples, and its in situ microbial colonization experiment; and installation of the LTBMS. The pressure records from the GeniusPlug include high-quality

records of formation and seafloor responses to multiple fault slip events, including the 11 March 2011 Tohoku M9 and 1 April 2016 Mie-ken Nanto-oki M6 earthquakes. The geochemical sampling coils yielded in situ pore fluids from the splay fault zone, and microorganisms were successfully cultivated from the colonization unit. The complex sensor array, in combination with the multilevel hole completion, is one of the most ambitious and sophisticated observatory installations in scientific ocean drilling (similar to that in Hole C0002G, deployed in 2010). Overall, the installation went smoothly, efficiently, and ahead of schedule. The extra time afforded by the efficient observatory deployment was used for coring in Holes C0010B–C0010E. Despite challenging hole conditions, the depth interval corresponding to the screened casing across the megasplay fault was successfully sampled in Hole C0010C, and the footwall of the megasplay was sampled in Hole C0010E, with >50 % recovery for both zones.

In the hanging wall of the megasplay fault (Holes C0010C and C0010D), we recovered indurated silty clay with occasional ash layers and sedimentary breccias. Mudstones show different degrees of deformation spanning from occasional fractures to intervals of densely fractured scaly claystones of up to >10 cm thickness. Sparse faulting with low displacement (usually <2 cm) is seen in core and exhibits primarily normal and, rarely, reversed sense of slip. When present, ash was entrained along fractures and faults. In Hole C0010E, the footwall to the megasplay fault was recovered. Sediments are horizontally to gently dipping and mainly comprise silt of olive-gray color. The hanging wall sediments recovered in Holes C0010C–C0010D range in age from 3.79 to 5.59 Ma and have been thrust over the younger footwall sediments in Hole C0010E, ranging in age from 1.56 to 1.67 Ma. The deposits of the underthrust sediment prism are less indurated than the hanging wall mudstones and show lamination on a centimeter scale. The material is less intensely deformed than the mudstones, and apart from occasional fracturation (some of it being drilling disturbance), evidence of structural features is absent.

B.2 Proceedings of the IODP Volume 380 Abstract

NanTroSEIZE Stage 3: Frontal Thrust Long-Term Borehole Monitoring System (LTBMS)

M. Kinoshita¹, K. Becker², S. Toczko³, J. Edgington⁴, T. Kimura³, Y. Machida³,
A. Roesner⁵, B. Senyener⁵, Tianhaozhe Sun⁶

¹Earthquake Research Institute, University of Tokyo, Tokyo, Japan

²Department of Marine Geosciences, University of Miami, USA

³Japan Agency for Marine Earth Science and Technology, Yokohama, Japan

⁴Texas A&M University, College Station, USA

⁵MARUM - Center for Marine Environmental Sciences and Faculty of Geosciences, University of Bremen, Bremen, Germany

⁶Department of Geosciences, Pennsylvania State University, University Park, Pennsylvania 16802, USA

The multiexpedition Integrated Ocean Drilling Program/International Ocean Discovery Program (IODP) Nankai Trough Seismogenic Zone Experiment (NanTroSEIZE) project was designed to investigate fault mechanics and seismogenesis along subduction megathrusts through direct sampling, in situ measurements, and long-term monitoring in conjunction with allied laboratory and numerical modeling studies. Overall NanTroSEIZE scientific objectives include characterizing the nature of fault slip and strain accumulation, fault and wall rock composition, fault architecture, and state variables throughout the active plate boundary system. Expedition 380 was the twelfth NanTroSEIZE expedition since 2007. Refer to Kopf et al. (2017) for a comprehensive summary of objectives, operations, and results during the first 11 expeditions. Expedition 380 focused on one primary objective: riserless deployment of a long-term borehole monitoring system (LTBMS) in Hole C0006G in the overriding plate at the toe of the Nankai accretionary prism.

The LTBMS installed in Hole C0006G incorporates multilevel pore-pressure sensing and a volumetric strainmeter, tiltmeter, geophone, broadband seismometer, accelerometer, and thermistor string. Similar previous LTBMS installations were completed farther upslope at IODP Sites C0002 and C0010. The ~35 km trench-normal transect of three LTBMS installations will provide monitoring within and above regions of contrasting behavior in the megasplay fault and the plate boundary as a whole, including a site above the updip edge of the locked zone (Site C0002), a shallow site in the megasplay fault zone and its footwall (Site C0010), and a site at the tip of the accretionary prism (the Expedition 380 installation at Site C0006). In combination, this suite of observatories has the potential to capture stress and deformation spanning a wide range of timescales (e.g., seismic and microseismic activity, slow

slip, and interseismic strain accumulation) across the transect from near-trench to the seismogenic zone.

Expedition 380 achieved its primary scientific and operational goal with successful installation of the LTBMS to a total depth of 457 m below seafloor in Hole C0006G. The installation was conducted in considerably less time than budgeted, partly because the Kuroshio Current had shifted away from the NanTroSEIZE area after 10 y of seriously affecting D/V Chikyu NanTroSEIZE operations. After Expedition 380, the LTBMS was successfully connected to the Dense Oceanfloor Network System for Earthquakes and Tsunamis (DONET) in March 2018 using the remotely operated vehicle Hyper-Dolphin from the Japan Agency for Marine-Earth Science and Technology (JAMSTEC) R/V Shinsei Maru.

B.3 Report and preliminary results of R/V Sonne cruise SO251 Summary

Extreme events Archived in the Geological Record of Japan's Subduction margins (EAGER-Japan)

M. Strasser¹, A.J. Kopf², F.W. Abegg³, M. Asada⁴, A.K. Bachmann², P. Cuno³, C. Dos Santos Ferreira², T. Fleischmann², T. Fujiware⁴, E. Hatakeyama⁴, B.R. Heesemann², J.I.T. Hillman³, M. Hoehne², H. Huusmann³, M. Ikari², K. Ikehara^{5,6}, F.D. Jaeger¹, T. Kanamatsu⁴, M.-H. Kang⁷, N.E. Kaul², A. Kioka¹, M. Koelling², K. Lange², N. Luebben², T. Matthiessen³, C.M. Mchugh⁸, A. Meier³, W. Menapace², K. Mochizuki⁹, J. Moernaut¹, A.W. Molenaar¹, G.F. Moore¹⁰, L.-J. Mu⁷, Y. Nakano⁴, M. Pieper³, M.L.P.A. Rex², **A. Roesner**², T. Schwesternmann¹, T. Sun¹¹, W. Szczucinski¹², P. Toechterle¹, S. Truetner², K. Usami^{5,6}, G. Wiemer², Y. Yamaguchi¹³

¹University of Innsbruck, Austria

²MARUM Center for Environmental Sciences, University of Bremen, Germany

³Geomar, Kiel, Germany

⁴JAMSTEC Japan Agency for Marine-Earth Science and Technology, Japan

⁵National Institute of Advanced Industrial Science and Technology, Japan

⁶GSJ Geological Survey Japan

⁷Taiwan Ocean Research institute, Kaohsiung, Taiwan

⁸Lamont-Doherty Earth Observatory, Columbia University, USA

⁹University of Yamaguchi, Japan

¹⁰University of Hawaii, USA

¹¹Pacific Geoscience Centre, Sidney, B.C., Canada

¹²University of Poznan, Poland

¹³Atmosphere and Ocean Research Institute, University of Tokyo, Japan

At the southeastern edge of the Eurasian Plate, Japan hosts two of the most interesting subduction systems, both prone to devastating megathrust earthquakes: The Japan Trench (JT) east of Honshu with subduction erosion/subsidence in the north, and the Nankai Trough (NT) with a huge accretionary prism in the southwest. In 2011 the JT area was struck by a Magnitude 9 earthquake that caused unusually large slip all the way to the trench, and a series of landslides, which are believed to be partly responsible for amplification of the catastrophic tsunami following the event. At Nankai, frequent M8+ earthquakes are also documented, and landslides and other sediment remobilization processes related to seismicity are attested. Despite the fact that either area has recently been the target of both IODP drilling (Exp. 343 vs 332/333/338/348) and MARUM cruises (SO219A vs. SO222), remaining gaps in knowledge remain. R/V Sonne Research Cruise SO251 was dedicated to collect data and samples to address the EAGER-Japan research project objectives such as (i) characterization and precise dating of extreme event layers, (ii) recovery of long-term instruments monitoring physical triggers to such events, and (iii) study geochemistry and fluid flow and link them to mass wasting in order to determine recurrence time and assess risk in two key scenarios: The mega-

earthquake super-cycle in the subsiding, highly segmented Japan Trench, and records of megasplay slip in the Nankai region.

The achievements from SO251-1 to the Japan Trench include:

- Acquisition of a complete high-resolution bathymetric map of the Japan trench axis and nearly 2000 km of subbottom Parasound profiles, covering the entire along-strike extent of the Japan Trench from 36° to 40.3° N.
- Recovery of 5 nearly 10 m long piston cores retrieved from the very deep waters (7 to 8 km below sea level).
- Recovery of three double cores on the continental slope, one of which was analyzed onboard while the other is sent to MARUM Bremen for geotechnical tests that simulate deformation behavior when dynamic loads are applied to the sediment, as is the case during large EQs.

Initial results from SO251-1 are:

- Several smaller submarine landslides (up to several 100's m of lateral extent) are imaged in the new bathymetric data that were either not yet present, or not resolved in the lower-resolution bathymetric dataset acquired before 2011.
- Parasound data image striking, up to several meter thick, acoustically transparent bodies interbedded in the otherwise parallel reflection pattern of the trench fill basins, providing a temporal and spatial inventory of major sediment remobilization events along the Japan Trench with potential quantitative constraints on volumes and mass fluxes of material mobilized during each event.
- Core from the southern and northern part of the Japan Trench confirm previous findings from the central part near the Tohoku-oki epicenter, that the small deepsea trench-fill basins, that are associated with very high sedimentation rates, comprise repeated thick turbidite sequences to be further tested for correlation to historic earthquakes.

The main results from SO251-2 at the Nankai Trough encompass:

- Acquisition of a complemented high-resolution, fill coverage bathymetric map of the entire Kumano Basin and adjacent slopes, including the associated subbottom Parasound profiles.

- Discovery of more than a dozen flares in the study area, which indicate fluid seepage activity along mud volcano summits, the seafloor trace of the megasplay fault, and other areas yet to be studied in more detail.
- Recovery of gravity cores and piston cores that documented mud breccia at some dome-shaped features, collected slope deposits seaward of the Kumano Basin for geotechnical analysis, and recovered basin deposits to describe background deposition and onlapping sequences throughout the Kumano basin.
- With ROV PHOCA, we successfully retrieved two MeBoPLUG observatories, one MeBoCORK-A observatory, and a GeniusPlug piezometer, where time series data of P and T reveal frequent EQ activity and also excursions owing to meteorological events.
- Cores from selected mud volcanoes reveal seepage of methane-rich fluids given the cemented carbonate conduits embedded in muddy matrix. Shore based chemical analysis will try to unravel changes in fluid chemistry over time and their link to tectonic processes.
- On MV#2 in the Kumano basin, we discovered a recent (past 4.5 y) mudflow episode towards the NW. Both the moat around the MV and the adjacent seafloor NW of the dome were covered with mud breccia, as evidenced from both HF data and a gravity core. The change is supported when using differential bathymetry methods based on the 2012 (SO222) and 2016 (SO251) data sets.

Abstract: Extremely elevated shear strength caused by diatoms on active margin slope sediments offshore north-eastern Japan [co-authorship]

Gauvain Wiemer¹, Ting-Wei Wu¹, Jasper Moernaut², Witold Szczuciński³, **Alexander Roesner**¹, Tobias Schwestermann², Ken Ikehara⁴, Andre Hüpers¹, Negar Haghypour⁵, Michael Strasser², Achim Kopf¹

¹MARUM-Center for Marine Environmental Sciences, University of Bremen, Germany

²University of Innsbruck, Austria

³Adam Mickiewicz University in Poznań, Poland

⁴National Institute of Advanced Industrial Science and Technology, Japan

⁵Geological Institute, ETH Zurich, Switzerland

The north-eastern Japan continental margin is frequently subjected to strong earthquake shaking and therefore its slope sedimentary sequences may be affected by the phenomenon called seismic-strengthening, potentially leading to elevated shear strength and enhanced slope stability. We present on-board shear strength measurements acquired on new sediment cores from the continental slope adjacent to the Japan Trench. These data reveal extremely higher than expected sediment strength, even beyond other active margins worldwide where seismic strengthening is suspected. Moreover, one-dimensional consolidation tests reveal very high apparent over-consolidation, which contradicts the continuity of the age-depth models, excluding significant sediment removal in the past. We interpret that seismic strengthening is remarkably effective in the Japan Trench slope areas due to the existence of diatomaceous mud. This is supported by previous lab experiments on generic samples, showing increased shear strength and apparent over-consolidation due to high particle interlocking and surface roughness related to the shape of diatom frustules. This interpretation for the Japan Trench slope is supported by comparison with the Kumano Basin slope (Nankai Trough) where the sediment is composed of silty-clay in which diatoms are rare, and where shear strength data follow the expected trend for active margins. We conclude that seismically active margins with diatom-rich sediments have a higher chance to demonstrate increased shear strength, thus reducing the susceptibility to submarine landslide hazards.

Author Contributions

During the R/V Sonne Research Cruise SO251 I was responsible for the piston-coring system and set up the laboratory environment for the vane shear measurements. Furthermore, I assisted in the physical properties measurements such as vane shear and fall cone testing and sediment sampling. Back at the research center MARUM, I contributed to many discussions at early stages of the data analysis and the writing process. I created figures and

took responsibility to critical review and update all figures before submission. I reviewed and commented on the drafts before submission with a special focus on the geotechnical properties analysis.

Acknowledgments

Five years ago, Achim recruited me as a student assistant during his lecture on active convergent margins in the Marine Geoscience program at the University of Bremen. One week after we had a discussion in class about the sources for tsunamis he offered me a job on his offshore scientific cruise, NORGeotech in Norway. This was my first scientific expedition offshore and many followed. It was exciting and I fell in love with ocean science, in particular with offshore data acquisition. Through Achim's guidance and network, I had the opportunity to sail several times on various research vessels. Based on my participation on scientific cruises in the Mediterranean and the Pacific Ocean we developed my master thesis and dissertation projects. I would like to thank Achim for the opportunity to work offshore, to meet brilliant scientist from around the world, and for helping me discover my passion for ocean science and geohazards.

Throughout my Ph.D. project, Matt was patient and helpful but he also challenged me to become a better scientist at the right moments. He always reminded me of the big picture. I am sure that without his help and many discussions about friction and earthquake mechanics this thesis would have never been written. Together with Gauvain, the supervisor of my master thesis, I was able to publish my first scientific article in the high quality journal *Landslides*. He stimulated me in thinking outside the box, a skill I would still like to improve on. Over the years we became friends, shared a passion for bouldering, and we climbed Mt. Fuji together, the highest summit in Japan. Furthermore, I would like to thank my colleagues and friends of the Meerestechnik/Sensorik, Marine Geotechnics, and the Experimental Geochmechanics working groups for their help whenever it was needed. I also feel the need to specially thank Katja and Aagje for the great teamwork in the lab, the hours of discussion about friction experiments, rate and state friction theory, and laboratory results. During scientific expeditions, I had the opportunity to work with colleagues from all over the world who shared extensively their knowledge and experience, which broaden my general scientific understanding. Discussions with Demian, Keir, Laura, Tian and Chi substantially improved my understanding of subduction zone processes. Michael Stipp is to thank for being my external reviewer. Additionally, I would like to thank all of the people who proof read this thesis: Rebecca, Laura, Walter, Keir, Hanaya, Gauvain, Aagje, Axel, Sophie and any others I might have forgotten. Finally, I want to thank my parents Burkhard and Ulrike and my sister Christine, without whom I would not have made it throughout this ridiculously long path of education. They always supported me together with my girlfriend Rebecca in finding my own way of life and keeping me sane and focused.

References

- Aharonov, E., Scholz, C.H., 2018. A Physics-Based Rock Friction Constitutive Law: Steady State Friction. *J. Geophys. Res.* 123, 1591–1614. 10.1002/2016JB013829.
- Alwi, L., 1995. X Window Graphical Analysis Program for Rock Friction Data. Advanced Undergraduate Project.
- Ando, M., 1975a. Possibility of a major earthquake in the tokai district, Japan and its pre-estimated seismotectonic effects. *Tectonophysics* 25, 69–85. 10.1016/0040-1951(75)90011-6.
- Ando, M., 1975b. Source mechanisms and tectonic significance of historical earthquakes along the nankai trough, Japan. *Tectonophysics* 27, 119–140. 10.1016/0040-1951(75)90102-X.
- Ando, M., 1982. A fault model of the 1946 Nankaido earthquake derived from tsunami data. *Physics of the Earth and Planetary Interiors* 28, 320–336. 10.1016/0031-9201(82)90089-9.
- Annoura, S., Hashimoto, T., Kamaya, N., Katsumata, A., 2017. Shallow episodic tremor near the Nankai Trough axis off southeast Mie prefecture, Japan. *Geophys. Res. Lett.* 44, 3564–3571. 10.1002/2017GL073006.
- Aoki, Y., Tamano, T., Kato, S., 1983. Detail structure of the Nankai Trough from migrated seismic sections, in: Watkins, J.S., Drake, C.L. (Eds.), *Studies in continental margin geology*. American Association of Petroleum Geologists, Tulsa, Okla.
- Araki, E., Saffer, D.M., Kopf, A.J., Wallace, L.M., Kimura, T., Machida, Y., Ide, S., Davis, E., IODP Expedition 365 shipboard scientist, 2017. Recurring and triggered slow-slip events near the trench at the Nankai Trough subduction megathrust. *Science (New York, N.Y.)* 356, 1157–1160. 10.1126/science.aan3120.
- Becker, K., Davis, E.E., 2004. In situ determinations of the permeability of the igneous oceanic crust. *Hydrogeology of the Oceanic Lithosphere*, 189–224.
- Becker, K., Davis, E.E., 2005. A review of CORK designs and operations during the Ocean Drilling Program, in: Fisher, A.T., Urabe, T., Klaus, A. (Eds.), *Proceedings of the IODP*, 301, vol. 301. Integrated Ocean Drilling Program.
- Becker, K., Davis, E.E., Spiess, F.N., deMoustier, C.P., 2004. Temperature and video logs from the upper oceanic crust, Holes 504B and 896A, Costa Rica Rift flank: Implications for the permeability of upper oceanic crust. *Earth and Planetary Science Letters* 222, 881–896. 10.1016/j.epsl.2004.03.033.
- Becker, K., Fisher, A.T., Davis, E.E., 1997. The CORK experiment in Hole 949C: Long-term observations of pressure and temperature in the Barbados accretionary prism, in: Shipley, T.H., Ogawa, Y., Blum, P., Bahr, J.M. (Eds.), *Proceedings of the Ocean Drilling Program*, 156 Scientific Results, vol. 156. Ocean Drilling Program.
- Becker, K., Kinoshita, M., Toczko, S., Edgington, J., Kimura, T., Machida, Y., Roesner, A., Senyener, B., Sun, T., 2018. Expedition 380 summary, in: Becker, K., Kinoshita, M., Toczko, S. (Eds.). *International Ocean Discovery Program*.
- Beeler, N.M., 2007. Laboratory-observed faulting in intrinsically and apparently weak materials: Strength, seismic coupling, dilatancy, and pore fluid pressure, in: Moore, J.C., Dixon, T.H. (Eds.), *The seismogenic zone of subduction thrust faults*. Columbia University Press, New York, pp. 370–449.
- Bekins, B.A., McCaffrey, A.M., Dreiss, S.J., 1995. Episodic and constant flow models for the origin of low-chloride waters in a modern accretionary complex. *Water Resour. Res.* 31, 3205–3215. 10.1029/95WR02569.

- Berger, G., Schott, J., Loubet, M., 1987. Fundamental processes controlling the first stage of alteration of a basalt glass by seawater: An experimental study between 200° and 320°C. *Earth and Planetary Science Letters* 84, 431–445. 10.1016/0012-821X(87)90008-2.
- Beroza, G.C., Ide, S., 2011. Slow Earthquakes and Nonvolcanic Tremor. *Annu. Rev. Earth Planet. Sci.* 39, 271–296. 10.1146/annurev-earth-040809-152531.
- Bilek, S.L., Lay, T., 2002. Tsunami earthquakes possibly widespread manifestations of frictional conditional stability. *Geophys. Res. Lett.* 29, 18-1-18-4. 10.1029/2002GL015215.
- Blanpied, M.L., Marone, C.J., Lockner, D.A., Byerlee, J.D., King, D.P., 1998. Quantitative measure of the variation in fault rheology due to fluid-rock interactions. *J. Geophys. Res.* 103, 9691–9712. 10.1029/98JB00162.
- Boutt, D.F., Saffer, D., Doan, M.-L., Lin, W., Ito, T., Kano, Y., Flemings, P., McNeill, L.C., Byrne, T., Hayman, N.W., Moe, K.T., 2012. Scale dependence of in-situ permeability measurements in the Nankai accretionary prism: The role of fractures. *Geophys. Res. Lett.* 39. 10.1029/2012GL051216.
- Bowden, F.P., Tabor, D., 1964. *The friction and lubrication of solids*. Oxford University Press, Oxford, 374 pp.
- Brace, W.F., Byerlee, J.D., 1966. Stick-slip as a mechanism for earthquakes. *Science (New York, N.Y.)* 153, 990–992. 10.1126/science.153.3739.990.
- Brace, W.F., Byerlee, J.D., 1970. California earthquakes: Why only shallow focus? *Science (New York, N.Y.)* 168, 1573–1575. 10.1126/science.168.3939.1573.
- Brodsky, E.E., Roeloffs, E., Woodcock, D., Gall, I., Manga, M., 2003. A mechanism for sustained groundwater pressure changes induced by distant earthquakes. *J. Geophys. Res.* 108, 331. 10.1029/2002JB002321.
- Brown, K.M., Kopf, A., Underwood, M.B., Weinberger, J.L., 2003. Compositional and fluid pressure controls on the state of stress on the Nankai subduction thrust: A weak plate boundary. *Earth and Planetary Science Letters* 214, 589–603. 10.1016/S0012-821X(03)00388-1.
- Buijze, L., Niemeijer, A.R., Han, R., Shimamoto, T., Spiers, C.J., 2017. Friction properties and deformation mechanisms of halite(-mica) gouges from low to high sliding velocities. *Earth and Planetary Science Letters* 458, 107–119. 10.1016/j.epsl.2016.09.059.
- Byerlee, J., 1978. Friction of rocks. *pure and applied geophysics* 116, 615–626. 10.1007/BF00876528.
- Byerlee, J.D., Brace, W.F., 1968. Stick slip, stable sliding, and earthquakes-Effect of rock type, pressure, strain rate, and stiffness. *J. Geophys. Res.* 73, 6031–6037. 10.1029/JB073i018p06031.
- Byrne, D.E., Davis, D.M., Sykes, L.R., 1988. Loci and maximum size of thrust earthquakes and the mechanics of the shallow region of subduction zones. *Tectonics* 7, 833–857. 10.1029/TC007i004p00833.
- Candela, T., Brodsky, E.E., Marone, C., Elsworth, D., 2014. Laboratory evidence for particle mobilization as a mechanism for permeability enhancement via dynamic stressing. *Earth and Planetary Science Letters* 392, 279–291. 10.1016/j.epsl.2014.02.025.
- Carpenter, B.M., Ikari, M.J., Marone, C., 2016. Laboratory observations of time-dependent frictional strengthening and stress relaxation in natural and synthetic fault gouges. *J. Geophys. Res.* 121, 1183–1201. 10.1002/2015JB012136.
- Carpenter, B.M., Mollo, S., Viti, C., Collettini, C., 2015a. Influence of calcite decarbonation on the frictional behavior of carbonate-bearing gouge: Implications for the instability of volcanic flanks and fault slip. *Tectonophysics* 658, 128–136. 10.1016/j.tecto.2015.07.015.
- Carpenter, B.M., Saffer, D.M., Marone, C., 2012. Frictional properties and sliding stability of the San Andreas fault from deep drill core. *Geology* 40, 759–762. 10.1130/G33007.1.

- Carpenter, B.M., Saffer, D.M., Marone, C., 2015b. Frictional properties of the active San Andreas Fault at SAFOD: Implications for fault strength and slip behavior. *J. Geophys. Res. Solid Earth* 120, 5273–5289. 10.1002/2015JB011963.
- Chadwick, W.W., Nooner, S.L., Zumberge, M.A., Embley, R.W., Fox, C.G., 2006. Vertical deformation monitoring at Axial Seamount since its 1998 eruption using deep-sea pressure sensors. *Journal of Volcanology and Geothermal Research* 150, 313–327. 10.1016/j.jvolgeores.2005.07.006.
- Chadwick Jr, W.W., Nooner, S.L., Butterfield, D.A., Lilley, M.D., 2012. Seafloor deformation and forecasts of the April 2011 eruption at Axial Seamount. *Nature Geosci* 5, 474 EP -. 10.1038/ngeo1464.
- Chamot-Rooke, N., Renard, V., Le Pichon, X., 1987. Magnetic anomalies in the Shikoku Basin: A new interpretation. *Earth and Planetary Science Letters* 83, 214–228. 10.1016/0012-821X(87)90067-7.
- Chester, F.M., More, J., Eguchi, N., Toczko, S., and the Expedition 343 Scientists, 2013. Japan Trench Fast Drilling Project (JFAST). Integrated Ocean Drilling Program.
- Cho, Y.S., 1995. Numerical simulations of tsunami propagation and run-up. PhD Thesis, School of Civil and Environmental Engineering, Cornell University.
- Davis, E., Becker, K., Wang, K., Kinoshita, M., 2009. Co-seismic and post-seismic pore-fluid pressure changes in the Philippine Sea plate and Nankai decollement in response to a seismogenic strain event off Kii Peninsula, Japan. *Earth, Planets and Space* 61, 649–657. 10.1186/BF03353174.
- Davis, E., Becker, K., Wang, K., OBARA, K., ITO, Y., Kinoshita, M., 2006. A discrete episode of seismic and aseismic deformation of the Nankai trough subduction zone accretionary prism and incoming Philippine Sea plate. *Earth and Planetary Science Letters* 242, 73–84. 10.1016/j.epsl.2005.11.054.
- Davis, E., Kinoshita, M., Becker, K., Wang, K., Asano, Y., Ito, Y., 2013. Episodic deformation and inferred slow slip at the Nankai subduction zone during the first decade of CORK borehole pressure and VLFE monitoring. *Earth and Planetary Science Letters* 368, 110–118. 10.1016/j.epsl.2013.03.009.
- Davis, E.E., Becker, K., 1994. Formation Temperatures and Pressures in a Sedimented Rift Hydrothermal System: 10 Months of CORK Observations, Holes 857D and 858G, in: Mottl, M.J., Davis, E.E., Fisher, A.T., Slack, J.F. (Eds.), *Proceedings of the Ocean Drilling Program, 139 Scientific Results*, vol. 139. Ocean Drilling Program.
- Davis, E.E., Becker, K., 2001. Using ODP Boreholes for Studying Sub-seafloor Hydrogeology: Results from the First Decade of CORK Observations. *GS 28*.
- Davis, E.E., Becker, K., Pettigrew, T., Carson, B., Macdonald, R., 1992. CORK: A Hydrologic Seal and Downhole Observatory for Deep-Ocean Boreholes, in: Davis, E.E., Mottl, M.J., Fisher, A.T. (Eds.), *Proceedings of the Ocean Drilling Program, 139 Initial Reports*, vol. 139. Ocean Drilling Program.
- Davis, E.E., Villinger, H., Sun, T., 2015. Slow and delayed deformation and uplift of the outermost subduction prism following ETS and seismogenic slip events beneath Nicoya Peninsula, Costa Rica. *Earth and Planetary Science Letters* 410, 117–127. 10.1016/j.epsl.2014.11.015.
- Davis, E.E., Wang, K., Becker, K., Thomson, R.E., 2000. Formation-scale hydraulic and mechanical properties of oceanic crust inferred from pore pressure response to periodic seafloor loading. *J. Geophys. Res.* 105, 13423–13435. 10.1029/2000JB900084.
- DeMets, C., Gordon, R.G., Argus, D.F., 2010. Geologically current plate motions. *Geophysical Journal International* 181, 1–80. 10.1111/j.1365-246X.2009.04491.x.
- Dieterich, J.H., 1972. Time-dependent friction in rocks. *J. Geophys. Res.* 77, 3690–3697. 10.1029/JB077i020p03690.

- Dieterich, J.H., 1978. Time-dependent friction and the mechanics of stick-slip. *PAGEOPH* 116, 790–806. 10.1007/BF00876539.
- Dieterich, J.H., 1979. Modeling of rock friction: 1. Experimental results and constitutive equations. *J. Geophys. Res.* 84, 2161. 10.1029/JB084iB05p02161.
- Dieterich, J.H., 1981. Constitutive Properties of Faults With Simulated Gouge, in: *Mechanical Behavior of Crustal Rocks: The Handin Volume*. American Geophysical Union, pp. 103–120.
- Dieterich, J.H., 1986. A model for the nucleation of earthquake slip. *Earthquake source mechanics* 37, 37–47.
- Dieterich, J.H., 1992. Earthquake nucleation on faults with rate-and state-dependent strength. *Tectonophysics* 211, 115–134. 10.1016/0040-1951(92)90055-B.
- Dieterich, J.H., Kilgore, B.D., 1994. Direct observation of frictional contacts: New insights for state-dependent properties. *PAGEOPH* 143, 283–302. 10.1007/BF00874332.
- Dieterich, J.H., Kilgore, B.D., 1996a. Imaging surface contacts: Power law contact distributions and contact stresses in quartz, calcite, glass and acrylic plastic. *Tectonophysics* 256, 219–239. 10.1016/0040-1951(95)00165-4.
- Dieterich, J.H., Kilgore, B.D., 1996b. Implications of fault constitutive properties for earthquake prediction. *Proceedings of the National Academy of Sciences of the United States of America* 93, 3787–3794.
- D'Ignazio, M., Lämsivaara, T., 2015. Shear bands in soft clays: Strain-softening behavior in finite element method. *Rakenteiden mekaniikka* 48, 83–98.
- Dixon, T.H., Jiang, Y., Malservisi, R., McCaffrey, R., Voss, N., Protti, M., Gonzalez, V., 2014. Earthquake and tsunami forecasts: Relation of slow slip events to subsequent earthquake rupture. *Proceedings of the National Academy of Sciences of the United States of America* 111, 17039–17044. 10.1073/pnas.1412299111.
- Dixon, T.H., Moore, J.C., 2007. 1. The Seismogenic Zone of Subduction Thrust Faults Introduction, in: Moore, J.C., Dixon, T.H. (Eds.), *The seismogenic zone of subduction thrust faults*. Columbia University Press, New York.
- Dragert, G., Wang, K., James, T.S., 2001. A silent slip event on the deeper Cascadia subduction interface. *Science (New York, N.Y.)* 292, 1525–1528. 10.1126/science.1060152.
- Dugan, B., Daigle, H., 2011. Data report: Permeability, compressibility, stress state, and grain size of shallow sediments from Sites C0004, C0006, C0007, and C0008 of the Nankai accretionary complex. *Proceedings of the Integrated Ocean Drilling Program, Volume 314/315/316*. 10.2204/iodp.proc.314315316.208.2011.
- Dziwonski, A.M., Chou, T.-A., Woodhouse, J.H., 1981. Determination of earthquake source parameters from waveform data for studies of global and regional seismicity. *J. Geophys. Res.* 86, 2825–2852. 10.1029/JB086iB04p02825.
- Ekström, G., Nettles, M., Dziewoński, A.M., 2012. The global CMT project 2004–2010: Centroid-moment tensors for 13,017 earthquakes. *Physics of the Earth and Planetary Interiors* 200-201, 1–9. 10.1016/j.pepi.2012.04.002.
- Elkhoury, J.E., Brodsky, E.E., Agnew, D.C., 2006. Seismic waves increase permeability. *Nature* 441, 1135–1138. 10.1038/nature04798.
- Elkhoury, J.E., Niemeijer, A., Brodsky, E.E., Marone, C., 2011. Laboratory observations of permeability enhancement by fluid pressure oscillation of in situ fractured rock. *J. Geophys. Res.* 116, B04204. 10.1029/2010JB007759.
- Expedition 316 Scientists, 2009a. Expedition 316 Site C0004, in: Kinoshita, M., Tobin, H., Ashi, J., Kimura, G., Lallemand, S., Screatton, E.J., Curewitz, D., Masago, H., Moe, K.T., and the Expedition 314/315/316 Scientists (Eds.), *NanTroSEIZE Stage 1: investigations of seismogenesis, Nankai Trough, Japan*. Integrated Ocean Drilling Program, Washington, D.C.

- Expedition 316 Scientists, 2009b. Expedition 316 Site C0006, in: Kinoshita, M., Tobin, H., Ashi, J., Kimura, G., Lallemand, S., Screatton, E.J., Curewitz, D., Masago, H., Moe, K.T., and the Expedition 314/315/316 Scientists (Eds.), *NanTroSEIZE Stage 1: investigations of seismogenesis, Nankai Trough, Japan*. Integrated Ocean Drilling Program, Washington, D.C.
- Expedition 316 Scientists, 2009c. Expedition 316 Site C0007, in: Kinoshita, M., Tobin, H., Ashi, J., Kimura, G., Lallemand, S., Screatton, E.J., Curewitz, D., Masago, H., Moe, K.T., and the Expedition 314/315/316 Scientists (Eds.), *NanTroSEIZE Stage 1: investigations of seismogenesis, Nankai Trough, Japan*. Integrated Ocean Drilling Program, Washington, D.C.
- Expedition 332 Scientists, 2011. Expedition 332 summary, in: Kopf, A., Araki, E., Toczko, S., Expedition 332 Scientists (Eds.), *Proc. IODP, 332: Integrated Ocean Drilling Program*.
- Faulkner, D.R., Mitchell, T.M., Behnsen, J., Hirose, T., Shimamoto, T., 2011. Stuck in the mud?: Earthquake nucleation and propagation through accretionary forearcs. *Geophys. Res. Lett.* 38, 1-5. 10.1029/2011GL048552.
- Fisher, A.T., Becker, K., Davis, E.E., 1997. The permeability of young oceanic crust east of Juan de Fuca Ridge Determined using borehole thermal measurements. *Geophys. Res. Lett.* 24, 1311–1314. 10.1029/97GL01286.
- Fisher, A.T., Zwart, G., 1997. Packer experiments along the décollement of the Barbados accretionary complex: Measurements of in situ permeability, in: Shipley, T.H., Ogawa, Y., Blum, P., Bahr, J.M. (Eds.), *Proceedings of the Ocean Drilling Program, 156 Scientific Results*, vol. 156. Ocean Drilling Program, pp. 199–218.
- Foucher, J.-P., Henry, P., Harmegnies, F., 1997. Long-term observations of pressure and temperature in Hole 948D, Barbados accretionary prism, in: Shipley, T.H., Ogawa, Y., Blum, P., Bahr, J.M. (Eds.), *Proceedings of the Ocean Drilling Program, 156 Scientific Results*, vol. 156. Ocean Drilling Program.
- Freed, A.M., 2005. Earthquake triggering by static, dynamic, and postseismic stress transfer. *Annu. Rev. Earth Planet. Sci.* 33, 335–367. 10.1146/annurev.earth.33.092203.122505.
- Frisch, W., Meschede, M., Blakey, R.C., 2011. Plate tectonics: Continental drift and mountain building, VIII, 212 S.
- Fujiwara, T., Kodaira, S., No, T., Kaiho, Y., Takahashi, N., Kaneda, Y., 2011. The 2011 Tohoku-Oki earthquake: displacement reaching the trench axis. *Science (New York, N.Y.)* 334, 1240. 10.1126/science.1211554.
- Fukuyama, E., 1998. Automated seismic moment tensor determination by using on-line broadband seismic wave-forms. *Zisin 2* 51, 149–156.
- Fulton, P.M., Brodsky, E.E., 2016. In situ observations of earthquake-driven fluid pulses within the Japan Trench plate boundary fault zone. *Geol* 44, 851–854. 10.1130/G38034.1.
- Gao, H., Schmidt, D.A., Weldon, R.J., 2012. Scaling Relationships of Source Parameters for Slow Slip Events. *Bulletin of the Seismological Society of America* 102, 352–360. 10.1785/0120110096.
- Gibson, R.E., 1958. The Progress of Consolidation in a Clay Layer Increasing in Thickness with Time. *Géotechnique* 8, 171–182. 10.1680/geot.1958.8.4.171.
- Gomberg, J., Davis, S., 1996. Stress/strain changes and triggered seismicity at The Geysers, California. *J. Geophys. Res.* 101, 733–749. 10.1029/95JB03250.
- Greene, H.G., Gardner-Taggart, J., Ledbetter, M.T., Barminski, R., Chase, T.E., Hicks, K.R., Baxter, C., 1991. Offshore and onshore liquefaction at Moss Landing spit, central California—Result of the October 17, 1989, Loma Prieta earthquake. *Geol* 19, 945. 10.1130/0091-7613(1991)019<0945:OAOOLAM>2.3.CO;2.

- Gu, J.-C., Rice, J.R., Ruina, A.L., Tse, S.T., 1984. Slip motion and stability of a single degree of freedom elastic system with rate and state dependent friction. *Journal of the Mechanics and Physics of Solids* 32, 167–196. 10.1016/0022-5096(84)90007-3.
- Guo, J., Likos, W.J., Underwood, M.B., Skarbak, R.M., Adamson, N., Saffer, D., 2011. Data report: Consolidation characteristics of sediments from Sites C0002, C0006, and C0007, IODP Expeditions 315 and 316, NanTroSEIZE Stage 1. *Proceedings of the Integrated Ocean Drilling Program, Volume 314/315/316*. 10.2204/iodp.proc.314315316.213.2011.
- Haines, S.H., Kaproth, B., Marone, C., Saffer, D., van der Pluijm, B., 2013. Shear zones in clay-rich fault gouge: A laboratory study of fabric development and evolution. *Journal of Structural Geology* 51, 206–225. 10.1016/j.jsg.2013.01.002.
- Haines, S.H., van der Pluijm, B.A., Ikari, M.J., Saffer, D.M., Marone, C., 2009. Clay fabric intensity in natural and artificial fault gouges: Implications for brittle fault zone processes and sedimentary basin clay fabric evolution. *J. Geophys. Res.* 114, 500. 10.1029/2008JB005866.
- Hall, R., 2012. Late Jurassic–Cenozoic reconstructions of the Indonesian region and the Indian Ocean. *Tectonophysics* 570–571, 1–41. 10.1016/j.tecto.2012.04.021.
- Hammerschmidt, S., Davis, E.E., Kopf, A., 2013a. Fluid pressure and temperature transients detected at the Nankai Trough Megasplay Fault: Results from the SmartPlug borehole observatory. *Tectonophysics* 600, 116–133. 10.1016/j.tecto.2013.02.010.
- Hammerschmidt, S.B., Davis, E.E., Hüpers, A., Kopf, A., 2013b. Limitation of fluid flow at the Nankai Trough megasplay fault zone. *Geo-Mar Lett* 33, 405–418. 10.1007/s00367-013-0337-z.
- Handin, J., 1969. On the Coulomb-Mohr failure criterion. *J. Geophys. Res.* 74, 5343–5348. 10.1029/JB074i022p05343.
- Higuchi, Y., Yanagimoto, Y., Hoshi, K., Unou, S., Akiba, F., Tonoike, K., Koda, K., 2007. Cenozoic stratigraphy and sedimentation history of the northern Philippine Sea based on multichannel seismic reflection data. *Island Arc* 16, 374–393. 10.1111/j.1440-1738.2007.00588.x.
- Hirata, N., Matsu'ura, M., 1987. Maximum-likelihood estimation of hypocenter with origin time eliminated using nonlinear inversion technique. *Physics of the Earth and Planetary Interiors* 47, 50–61. 10.1016/0031-9201(87)90066-5.
- Hirose, F., Maeda, K., 2013. Simulation of recurring earthquakes along the Nankai trough and their relationship to the Tokai long-term slow slip events taking into account the effect of locally elevated pore pressure and subducting ridges. *J. Geophys. Res.* 118, 4127–4144. 10.1002/jgrb.50287.
- Hirose, T., Hiramatsu, Y., Obara, K., 2010. Characteristics of short-term slow slip events estimated from deep low-frequency tremors in Shikoku, Japan. *J. Geophys. Res.* 115, B00A05. 10.1029/2010JB007608.
- Hodder, A.P.W., Naish, T.R., Nelson, C.S., 1993. A two-stage model for the formation of smectite from detrital volcanic glass under shallow-marine conditions. *Marine Geology* 109, 279–285. 10.1016/0025-3227(93)90066-5.
- Hsieh, P.A., Bredehoeft, J.D., Farr, J.M., 1987. Determination of aquifer transmissivity from Earth tide analysis. *Water Resour. Res.* 23, 1824–1832. 10.1029/WR023i010p01824.
- Hüpers, A., Ikari, M.J., Dugan, B., Underwood, M.B., Kopf, A.J., 2015. Origin of a zone of anomalously high porosity in the subduction inputs to Nankai Trough. *Marine Geology* 361, 147–162. 10.1016/j.margeo.2015.01.004.
- Ichinose, G.A., Thio, H.K., Somerville, P.G., Sato, T., Ishii, T., 2003. Rupture process of the 1944 Tonankai earthquake (Ms 8.1) from the inversion of teleseismic and regional seismograms. *J. Geophys. Res.* 108, 119. 10.1029/2003JB002393.
- Ide, S., 2012. Variety and spatial heterogeneity of tectonic tremor worldwide. *J. Geophys. Res.* 117, 3. 10.1029/2011JB008840.

- Ide, S., Beroza, G.C., Shelly, D.R., Uchide, T., 2007. A scaling law for slow earthquakes. *Nature* 447, 76–79. 10.1038/nature05780.
- Ide, S., Yabe, S., 2014. Universality of slow earthquakes in the very low frequency band. *Geophys. Res. Lett.* 41, 2786–2793. 10.1002/2014GL059712.
- Iinuma, T., Hino, R., Kido, M., Inazu, D., Osada, Y., ITO, Y., Ohzono, M., Tsushima, H., Suzuki, S., Fujimoto, H., Miura, S., 2012. Coseismic slip distribution of the 2011 off the Pacific Coast of Tohoku Earthquake (M9.0) refined by means of seafloor geodetic data. *J. Geophys. Res.* 117. 10.1029/2012JB009186.
- Ikari, M.J., 2019. Laboratory slow slip events in natural geological materials. *Geophysical Journal International* 218, 354–387. 10.1093/gji/ggz143.
- Ikari, M.J., Carpenter, B.M., Marone, C., 2016a. A microphysical interpretation of rate- and state-dependent friction for fault gouge. *Geochem. Geophys. Geosyst.* 17, 1660–1677. 10.1002/2016GC006286.
- Ikari, M.J., Carpenter, B.M., Vogt, C., Kopf, A.J., 2016b. Elevated time-dependent strengthening rates observed in San Andreas Fault drilling samples. *Earth and Planetary Science Letters* 450, 164–172. 10.1016/j.epsl.2016.06.036.
- Ikari, M.J., Hüpers, A., Kopf, A.J., 2013a. Shear strength of sediments approaching subduction in the Nankai Trough, Japan as constraints on forearc mechanics. *Geochem. Geophys. Geosyst.* 14, 2716–2730. 10.1002/ggge.20156.
- Ikari, M.J., Kameda, J., Saffer, D.M., Kopf, A.J., 2015. Strength characteristics of Japan Trench borehole samples in the high-slip region of the 2011 Tohoku-Oki earthquake. *Earth and Planetary Science Letters* 412, 35–41. 10.1016/j.epsl.2014.12.014.
- Ikari, M.J., Knuth, M.W., Marone, C., Saffer, D.M., 2012. Data report: Frictional healing and compressibility of sheared sediment from fault zones, in Sites C0004 and C0007. *Proceedings of the Integrated Ocean Drilling Program, Volume 314/315/316*, 1–23.
- Ikari, M.J., Kopf, A.J., 2011. Cohesive strength of clay-rich sediment. *Geophys. Res. Lett.* 38. 10.1029/2011GL047918.
- Ikari, M.J., Kopf, A.J., 2015. The role of cohesion and overconsolidation in submarine slope failure. *Marine Geology* 369, 153–161. 10.1016/j.margeo.2015.08.012.
- Ikari, M.J., Kopf, A.J., 2017. Seismic potential of weak, near-surface faults revealed at plate tectonic slip rates. *Science advances* 3, e1701269. 10.1126/sciadv.1701269.
- Ikari, M.J., Marone, C., Saffer, D.M., Kopf, A.J., 2013b. Slip weakening as a mechanism for slow earthquakes. *Nature Geosci* 6, 468–472. 10.1038/ngeo1818.
- Ikari, M.J., Niemeijer, A.R., Marone, C., 2011a. The role of fault zone fabric and lithification state on frictional strength, constitutive behavior, and deformation microstructure. *J. Geophys. Res.* 116, 423. 10.1029/2011JB008264.
- Ikari, M.J., Saffer, D.M., 2011. Comparison of frictional strength and velocity dependence between fault zones in the Nankai accretionary complex. *Geochem. Geophys. Geosyst.* 12, 1-16. 10.1029/2010GC003442.
- Ikari, M.J., Saffer, D.M., Marone, C., 2007. Effect of hydration state on the frictional properties of montmorillonite-based fault gouge. *J. Geophys. Res.* 112, 8697. 10.1029/2006JB004748.
- Ikari, M.J., Saffer, D.M., Marone, C., 2009. Frictional and hydrologic properties of a major splay fault system, Nankai subduction zone. *Geophys. Res. Lett.* 36, B03207. 10.1029/2009GL040009.
- Ikari, M.J., Strasser, M., Saffer, D.M., Kopf, A.J., 2011b. Submarine landslide potential near the megasplay fault at the Nankai subduction zone. *Earth and Planetary Science Letters* 312, 453–462. 10.1016/j.epsl.2011.10.024.
- Ike, T., Moore, G.F., Kuramoto, S.'i., Park, J.-O., Kaneda, Y., Taira, A., 2008. Variations in sediment thickness and type along the northern Philippine Sea Plate at the Nankai Trough. *Island Arc* 17, 342–357. 10.1111/j.1440-1738.2008.00624.x.

- Ishii, T., Sato, H., Machida, S., Haraguchi, S., Usui, A., Ishizuka, O., Taniguchi, H., Yagi, K., 2000. Geological and petrological studies of the Kinan and Izu-Ogasawara-back arc-echelon Seamount Chains. *Bull. Geol. Surv. Jpn.* 51.
- Itaba, S., Ando, R., 2011. A slow slip event triggered by teleseismic surface waves. *Geophys. Res. Lett.* 38. 10.1029/2011GL049593.
- Ito, Y., Hino, R., Kido, M., Fujimoto, H., Osada, Y., Inazu, D., Ohta, Y., Iinuma, T., Ohzono, M., Miura, S., Mishina, M., Suzuki, K., Tsuji, T., Ashi, J., 2013. Episodic slow slip events in the Japan subduction zone before the 2011 Tohoku-Oki earthquake. *Tectonophysics* 600, 14–26. 10.1016/j.tecto.2012.08.022.
- Ito, Y., Ikari, M.J., 2015. Velocity- and slip-dependent weakening in simulated fault gouge: Implications for multimode fault slip. *Geophys. Res. Lett.* 42, 9247–9254. 10.1002/2015GL065829.
- Ito, Y., Ikari, M.J., Ujiie, K., Kopf, A., 2017. Coseismic slip propagation on the Tohoku plate boundary fault facilitated by slip-dependent weakening during slow fault slip. *Geophys. Res. Lett.* 44, 8749–8756. 10.1002/2017GL074307.
- Ito, Y., Obara, K., 2006a. Dynamic deformation of the accretionary prism excites very low frequency earthquakes. *Geophys. Res. Lett.* 33. 10.1029/2005GL025270.
- Ito, Y., Obara, K., 2006b. Very low frequency earthquakes within accretionary prisms are very low stress-drop earthquakes. *Geophys. Res. Lett.* 33, 1131. 10.1029/2006GL025883.
- Ito, Y., Obara, K., Shiomi, K., Sekine, S., Hirose, H., 2007. Slow earthquakes coincident with episodic tremors and slow slip events. *Science (New York, N.Y.)* 315, 503–506. 10.1126/science.1134454.
- Jannasch, H.W., Davis, E.E., Kastner, M., Morris, J.D., Pettigrew, T.L., Plant, J.N., Solomon, E.A., Villinger, H.W., Wheat, G.C., 2003. CORK-II: Long-Term Monitoring of Fluid Chemistry, Fluxes, and Hydrology in Instrumented Boreholes at the Costa Rica Subduction Zone, in: Morris, J.D., Villinger, H.W., Klaus, A. (Eds.), *Proceedings of the Ocean Drilling Program, 205 Initial Reports*, vol. 205. Ocean Drilling Program.
- Jeppson, T.N., Tobin, H.J., Hashimoto, Y., 2018. Laboratory measurements quantifying elastic properties of accretionary wedge sediments: Implications for slip to the trench during the 2011 Mw 9.0 Tohoku-Oki earthquake. *Geosphere* 14, 1411–1424. 10.1130/GES01630.1.
- Kame, N., Rice, J.R., Dmowska, R., 2003. Effects of prestress state and rupture velocity on dynamic fault branching. *J. Geophys. Res.* 108, 5679. 10.1029/2002JB002189.
- Kamei, R., Pratt, R.G., Tsuji, T., 2012. Waveform tomography imaging of a megasplay fault system in the seismogenic Nankai subduction zone. *Earth and Planetary Science Letters* 317–318, 343–353. 10.1016/j.epsl.2011.10.042.
- Kanamatsu, T., Kawamura, K., Strasser, M., Novak, B., Kitamura, Y., 2014. Flow dynamics of Nankai Trough submarine landslide inferred from internal deformation using magnetic fabric. *Geochem. Geophys. Geosyst.* 15, 4079–4092. 10.1002/2014GC005409.
- Kanamori, H., Anderson, D.L., 1975. Theoretical basis of some empirical relations in seismology. *Bulletin of the Seismological Society of America* 65, 1073–1095.
- Kanamori, H., Brodsky, E.E., 2001. *The Physics of Earthquakes*. *Physics Today* 54, 34–40. 10.1063/1.1387590.
- Kanamori, H., Brodsky, E.E., 2004. The physics of earthquakes. *Reports on Progress in Physics* 67, 1429–1496. 10.1088/0034-4885/67/8/r03.
- Kanamori, H., Rivera, L., 2006. Energy Partitioning During an Earthquake, in: Abercrombie, R., McGarr, A., Di Toro, G., Kanamori, H. (Eds.), *Earthquakes. Radiated energy and the physics of faulting*, vol. 170. American Geophysical Union, Washington, D.C, pp. 3–13.
- Kaneda, Y., 2014. DONET: A Real-Time Monitoring System for Megathrust Earthquakes and Tsunamis Around Southwestern Japan. *oceanog* 27, 103. 10.5670/oceanog.2014.45.

- Kaneda, Y., Kawaguchi, K., Araki, E., Matsumoto, H., Nakamura, T., Kamiya, S., Ariyoshi, K., Hori, T., Baba, T., Takahashi, N., 2015. Development and application of an advanced ocean floor network system for megathrust earthquakes and tsunamis, in: Favali, P., DeSantis, A., Beranzoli, L. (Eds.), *Seafloor observatories: A New Vision of the Earth from the Abyss*. Springer, Heidelberg, pp. 643–662.
- Kaneko, L., Ide, S., Nakano, M., 2018. Slow Earthquakes in the Microseism Frequency Band (0.1-1.0 Hz) off Kii Peninsula, Japan. *Geophys. Res. Lett.* 45, 2618–2624. 10.1002/2017GL076773.
- Kato, A., Obara, K., Igarashi, T., Tsuruoka, H., Nakagawa, S., Hirata, N., 2012. Propagation of slow slip leading up to the 2011 M(w) 9.0 Tohoku-Oki earthquake. *Science (New York, N.Y.)* 335, 705–708. 10.1126/science.1215141.
- Kawaguchi, K., Kaneko, S., Nishida, T., Komine, T., 2015. Construction of the DONET real-time seafloor observatory for earthquakes and tsunami monitoring, in: Favali, P., DeSantis, A., Beranzoli, L. (Eds.), *Seafloor observatories: A New Vision of the Earth from the Abyss*. Springer, Heidelberg, pp. 211–228.
- Kikuchi, M., Nakamura, M., Yoshikawa, K., 2003. Source rupture processes of the 1944 Tonankai earthquake and the 1945 Mikawa earthquake derived from low-gain seismograms. *Earth Planet Sp* 55, 159–172. 10.1186/BF03351745.
- Kilb, D., Gombert, J., Bodin, P., 2000. Triggering of earthquake aftershocks by dynamic stresses. *Nature* 408, 570–574. 10.1038/35046046.
- Kimura, G., Hashimoto, Y., Kitamura, Y., Yamaguchi, A., Koge, H., 2014. Middle Miocene swift migration of the TTT triple junction and rapid crustal growth in southwest Japan: A review. *Tectonics* 33, 1219–1238. 10.1002/2014TC003531.
- Kimura, G., Kitamura, Y., Hashimoto, Y., Yamaguchi, A., Shibata, T., Ujiie, K., Okamoto, S., 2007. Transition of accretionary wedge structures around the up-dip limit of the seismogenic subduction zone. *Earth and Planetary Science Letters* 255, 471–484. 10.1016/j.epsl.2007.01.005.
- Kimura, G., Moore, G.F., Strasser, M., Sreaton, E., Curewitz, D., Streiff, C., Tobin, H., 2011. Spatial and temporal evolution of the megasplay fault in the Nankai Trough. *Geochem. Geophys. Geosyst.* 12. 10.1029/2010GC003335.
- Kimura, G., Yamaguchi, A., Hojo, M., Kitamura, Y., Kameda, J., Ujiie, K., Hamada, Y., Hamahashi, M., Hina, S., 2012. Tectonic mélangé as fault rock of subduction plate boundary. *Tectonophysics* 568-569, 25–38. 10.1016/j.tecto.2011.08.025.
- Kinoshita, C., Kano, Y., Ito, H., 2015. Shallow crustal permeability enhancement in central Japan due to the 2011 Tohoku earthquake. *Geophys. Res. Lett.* 42, 773–780. 10.1002/2014GL062792.
- Kinoshita, C., Saffer, D., Kopf, A., Roesner, A., Wallace, L.M., Araki, E., Kimura, T., Machida, Y., Kobayashi, R., Davis, E., Toczko, S., Carr, S., 2018a. Changes in Physical Properties of the Nankai Trough Megasplay Fault Induced by Earthquakes, Detected by Continuous Pressure Monitoring. *J. Geophys. Res.* 27, 119. 10.1002/2017JB014924.
- Kinoshita, M., Becker, K., Toczko, S., Edgington, J., Kimura, T., Machida, Y., Roesner, A., Senyener, B., Sun, T., 2018b. Expedition 380 methods, in: Becker, K., Kinoshita, M., Toczko, S. (Eds.). *International Ocean Discovery Program*.
- Kinoshita, M., Tobin, H., Ashi, J., Kimura, G., Lallemand, S., Sreaton, E.J., Curewitz, D., Masago, H., Moe, K.T., and the Expedition 314/315/316 Scientists (Eds.), 2009. *NanTroSEIZE Stage 1: investigations of seismogenesis, Nankai Trough, Japan. Integrated Ocean Drilling Program, Washington, D.C.*
- Kitada, K., Araki, E., Kimura, T., Kinoshita, M., Kopf, A., Saffer, D., 2013. Long-term monitoring at C0002 seafloor borehole in Nankai Trough seismogenic zone, in: 2013 IEEE International Underwater Technology Symposium (UT). 2013 IEEE International

- Underwater Technology Symposium (UT 2013), Tokyo. 5/3/2013 - 8/3/2013. IEEE, pp. 1–3.
- Kitagawa, Y., Kano, Y., 2016. Changes in permeability of the Nojima fault damage zone inferred from repeated water injection experiments. *Earth Planet Sp* 68, 206. 10.1186/s40623-016-0566-2.
- Kitagawa, Y., Koizumi, N., Takahashi, M., Matsumoto, N., Sato, T., 2006. Changes in groundwater levels or pressures associated with the 2004 earthquake off the west coast of northern Sumatra (M9.0). *Earth Planet Sp* 58, 173–179. 10.1186/BF03353375.
- Kitajima, H., Saffer, D.M., 2012. Elevated pore pressure and anomalously low stress in regions of low frequency earthquakes along the Nankai Trough subduction megathrust. *Geophys. Res. Lett.* 39. 10.1029/2012GL053793.
- Kodaira, S., Hori, T., Ito, A., Miura, S., Fujie, G., Park, J.-O., Baba, T., Sakaguchi, H., Kaneda, Y., 2006. A cause of rupture segmentation and synchronization in the Nankai trough revealed by seismic imaging and numerical simulation. *J. Geophys. Res.* 111, 119. 10.1029/2005JB004030.
- Kopf, A., 2013. Effective strength of incoming sediments and its implications for plate boundary propagation: Nankai and Costa Rica as type examples of accreting vs. erosive convergent margins. *Tectonophysics* 608, 958–969. 10.1016/j.tecto.2013.07.023.
- Kopf, A., Araki, E., Toczko, S., Expedition 332 Scientists (Eds.), 2011a. Proc. IODP, 332: Integrated Ocean Drilling Program.
- Kopf, A., Brown, K.M., 2003. Friction experiments on saturated sediments and their implications for the stress state of the Nankai and Barbados subduction thrusts. *Marine Geology* 202, 193–210. 10.1016/S0025-3227(03)00286-X.
- Kopf, A., Saffer, D., Toczko, S., 2016. Expedition 365 Preliminary Report: NanTroSEIZE Stage 3: Shallow Megasplay Long-Term Borehole Monitoring System (LTBMS). International Ocean Discovery Program.
- Kopf, A., Saffer, D., Toczko, S., Araki, E., Carr, S., Kimura, T., Kinoshita, C., Kobayashi, R., Machida, Y., Rösner, A., Wallace, L.M., Chiyonobu, S., Kanagawa, K., Kanamatsu, T., Kimura, G., Underwood, M.B., 2017. Expedition 365 summary, in: Saffer, D., Kopf, A., Toczko, S., and the Expedition 365 Scientists (Eds.), NanTroSEIZE Stage 3: Shallow Megasplay Long-Term Borehole Monitoring System. International Ocean Discovery Program, College Station.
- Kopf, A., Saffer, D.M., Davis, E.E., Hammerschmidt, S., LaBonte, A., Meldrum, R., Toczko, S., Lauer, R., Heesemann, M., Macdonald, R., Wheat, C.G., Jannasch, H.W., Edwards, K., Orcutt, B., Haddad, A., Villinger, H., Araki, E., Kitada, K., Kimura, T., Kido, Y., 2011b. The SmartPlug and GeniusPlug: Simple retrievable observatory systems for NanTroSEIZE borehole monitoring, in: Kopf, A., Araki, E., Toczko, S., Expedition 332 Scientists (Eds.), Proc. IODP, 332: Integrated Ocean Drilling Program.
- Kramer, S.L., 1996. Geotechnical earthquake engineering. Prentice Hall, Upper Saddle River, N.J., xviii, 653.
- Kyo, M., Namba, Y., Saruhashi, T., Araki, E., Kitada, K., Kimura, T., Fuluton, P., 2014. Development on long term borehole monitoring system for earthquake and geodetic research, in: Oceans 2014 - Taipei. [conference] ; 7 - 10 April 2014, Taipei. OCEANS 2014 - TAIPEI, Taipei, Taiwan. 7/4/2014 - 10/4/2014. IEEE, Piscataway, NJ, pp. 1–6.
- Lay, T., Kanamori, H., 2011. Insights from the great 2011 Japan earthquake. *Physics Today* 64, 33–39. 10.1063/PT.3.1361.
- Lay, T., Kanamori, H., Ammon, C.J., Nettles, M., Ward, S.N., Aster, R.C., Beck, S.L., Bilek, S.L., Brudzinski, M.R., Butler, R., DeShon, H.R., Ekstrom, G., Satake, K., Sipkin, S., 2005. The great Sumatra-Andaman earthquake of 26 December 2004. *Science (New York, N.Y.)* 308, 1127–1133. 10.1126/science.1112250.

- Leeman, J.R., Saffer, D.M., Scuderi, M.M., Marone, C., 2016. Laboratory observations of slow earthquakes and the spectrum of tectonic fault slip modes. *Nature communications* 7, 11104. 10.1038/ncomms11104.
- Leroueil, S., Vaughan, P.R., 1990. The general and congruent effects of structure in natural soils and weak rocks. *Géotechnique* 40, 467–488. 10.1680/geot.1990.40.3.467.
- Li, Y.-G., Vidale, J., Day, S., Oglesby, D., Cochran, E., 2003. Postseismic Fault Healing on the Rupture Zone of the 1999 M 7.1 Hector Mine, California, Earthquake. *Bulletin of the Seismological Society of America* 93, 854–869. 10.1785/0120020131.
- Liu, Y., Rice, J.R., 2007. Spontaneous and triggered aseismic deformation transients in a subduction fault model. *J. Geophys. Res.* 112. 10.1029/2007JB004930.
- Liu, Y., Rice, J.R., 2009. Slow slip predictions based on granite and gabbro friction data compared to GPS measurements in northern Cascadia. *J. Geophys. Res.* 114, 1987. 10.1029/2008JB006142.
- Logan, J.M., Rauenzahn, K.A., 1987. Frictional dependence of gouge mixtures of quartz and montmorillonite on velocity, composition and fabric. *Tectonophysics* 144, 87–108. 10.1016/0040-1951(87)90010-2.
- Lupini, J.F., Skinner, A.E., Vaughan, P.R., 1981. The drained residual strength of cohesive soils. *Géotechnique* 31, 181–213. 10.1680/geot.1981.31.2.181.
- Manga, M., Wang, C.-y., Shirzaei, M., 2016. Increased stream discharge after the 3 September 2016 M w 5.8 Pawnee, Oklahoma earthquake. *Geophys. Res. Lett.* 43, 11,588–11,594. 10.1002/2016GL071268.
- Manga, M., Wang, C.-Y., 2007. 4.10 - Earthquake Hydrology, in: Schubert, G. (Ed.), *Treatise on Geophysics*. Elsevier, Amsterdam, pp. 293–320.
- March, A., 1932. Mathematische Theorie der Regelung nach der Korngestalt bei affiner Deformation. *Zeitschrift für Kristallographie - Crystalline Materials* 81. 10.1524/zkri.1932.81.1.285.
- Marone, C., 1998a. Laboratory-derived friction laws and their application to seismic faulting. *Annu. Rev. Earth Planet. Sci.* 26, 643–696. 10.1146/annurev.earth.26.1.643.
- Marone, C., 1998b. The effect of loading rate on static friction and the rate of fault healing during the earthquake cycle. *Nature* 391, 69–72. 10.1038/34157.
- Marone, C., 2019. The spectrum of fault slip modes from elastodynamic rupture to slow earthquakes, in: Bizzarri, A., Das, S., Petri, A. (Eds.), *Mechanics of earthquake faulting. Meccanica delle faglie sismogenetiche*. IOS Press, Amsterdam.
- Marone, C., Raleigh, C.B., Scholz, C.H., 1990. Frictional behavior and constitutive modeling of simulated fault gouge. *J. Geophys. Res.* 95, 7007. 10.1029/JB095iB05p07007.
- Marone, C., Saffer, D.M., 2015. The Mechanics of Frictional Healing and Slip Instability During the Seismic Cycle, in: Schubert, G. (Ed.), *Treatise on geophysics*. Elsevier, Amsterdam, pp. 111–138.
- Marone, C., Scholz, C.H., 1988. The depth of seismic faulting and the upper transition from stable to unstable slip regimes. *Geophys. Res. Lett.* 15, 621–624. 10.1029/GL015i006p00621.
- Marone, C., Vidale, J.E., Ellsworth, W.L., 1995. Fault healing inferred from time dependent variations in source properties of repeating earthquakes. *Geophys. Res. Lett.* 22, 3095–3098. 10.1029/95GL03076.
- Matsumoto, N., Kitagawa, G., Roeloffs, E.A., 2003. Hydrological response to earthquakes in the Haibara well, central Japan - I. Groundwater level changes revealed using state space decomposition of atmospheric pressure, rainfall and tidal responses. *Geophysical Journal International* 155, 885–898. 10.1111/j.1365-246X.2003.02103.x.
- Mazzotti, S., Le Pichon, X., Henry, P., Miyazaki, S.-I., 2000. Full interseismic locking of the Nankai and Japan-west Kurile subduction zones: An analysis of uniform elastic strain

- accumulation in Japan constrained by permanent GPS. *J. Geophys. Res.* 105, 13159–13177. 10.1029/2000JB900060.
- McCaffrey, R., 2009. Time-dependent inversion of three-component continuous GPS for steady and transient sources in northern Cascadia. *Geophys. Res. Lett.* 36. 10.1029/2008GL036784.
- McNeill, L., Saffer, D., Byrne, T., Araki, E., Toczko, S., Eguchi, N., Takahashi, K., 2010. IODP Expedition 319, NanTroSEIZE Stage 2: First IODP Riser Drilling Operations and Observatory Installation Towards Understanding Subduction Zone Seismogenesis. *Scientific Drilling*. 10.2204/iodp.sd.10.01.2010.
- Melbourne, T.I., Webb, F.H., Stock, J.M., Reigber, C., 2002. Rapid postseismic transients in subduction zones from continuous GPS. *J. Geophys. Res.* 107, ETG 10-1-ETG 10-10. 10.1029/2001JB000555.
- Menapace, W., Völker, D., Kaul, N., Tryon, M.D., Kopf, A.J., 2017. The role of mud volcanism and deep-seated dewatering processes in the Nankai Trough accretionary prism and Kumano Basin, Japan. *Geochem. Geophys. Geosyst.* 18, 2486–2509. 10.1002/2016GC006763.
- Mikada, H., Becker, K., Moore, J.C., Klaus, A. (Eds.), 2002. *Proceedings of the Ocean Drilling Program, 196 Initial Reports*. Ocean Drilling Program.
- Mitchell, J.K., Soga, K., 2005. *Fundamentals of soil behavior*, 3rd ed. John Wiley & Sons, Hoboken, N.J., xiii, 577.
- Miyazaki, S.i., Heki, K., 2001. Crustal velocity field of southwest Japan: Subduction and arc-arc collision. *J. Geophys. Res.* 106, 4305–4326. 10.1029/2000JB900312.
- Montgomery, D.R., Manga, M., 2003. Streamflow and water well responses to earthquakes. *Science (New York, N.Y.)* 300, 2047–2049. 10.1126/science.1082980.
- Moore, D.E., Summers, R., Byerlee, J.D., 1986. The effects of sliding velocity on the frictional and physical properties of heated fault gouge. *pure and applied geophysics* 124, 31–52. 10.1007/BF00875718.
- Moore, G.F., Bangs, N.L., Taira, A., Kuramoto, S., Pangborn, E., Tobin, H.J., 2007. Three-dimensional splay fault geometry and implications for tsunami generation. *Science (New York, N.Y.)* 318, 1128–1131. 10.1126/science.1147195.
- Moore, G.F., Boston, B.B., Strasser, M., Underwood, M.B., Ratliff, R.A., 2015. Evolution of tectono-sedimentary systems in the Kumano Basin, Nankai Trough forearc. *Marine and Petroleum Geology* 67, 604–616. 10.1016/j.marpetgeo.2015.05.032.
- Moore, G.F., Kanagawa, K., Strasser, M., Dugan, B., Maeda, L., Toczko, S., 2014. IODP Expedition 338: NanTroSEIZE Stage 3: NanTroSEIZE plate boundary deep riser 2. *Scientific Drilling* 17, 1–12. 10.5194/sd-17-1-2014.
- Moore, G.F., Park, J.-O., Bangs, N.L., Gulick, S.P., Tobin, H.J., Nakamura, Y., Saito, S., Tsuji, T., Yoro, T., Tanaka, H., Uraki, S., Kido, Y., Sanada, Y., Kuramoto, S., Taira, A., 2009. Structural and seismic stratigraphic framework of the NanTroSEIZE Stage 1 transect, in: Kinoshita, M., Tobin, H., Ashi, J., Kimura, G., Lallemand, S., Scretton, E.J., Curewitz, D., Masago, H., Moe, K.T., and the Expedition 314/315/316 Scientists (Eds.), *NanTroSEIZE Stage 1: investigations of seismogenesis, Nankai Trough, Japan*. Integrated Ocean Drilling Program, Washington, D.C.
- Mulargia, F., Bizzarri, A., 2014. Anthropogenic Triggering of Large Earthquakes. *Scientific Reports* 4. 10.1038/srep06100.
- Nakano, M., Hori, T., Araki, E., Kodaira, S., Ide, S., 2018. Shallow very-low-frequency earthquakes accompany slow slip events in the Nankai subduction zone. *Nature communications* 9, 984. 10.1038/s41467-018-03431-5.
- Nakata, N., Snieder, R., 2011. Near-surface weakening in Japan after the 2011 Tohoku-Oki earthquake. *Geophys. Res. Lett.* 38. 10.1029/2011GL048800.

- Noda, H., Lapusta, N., Kanamori, H., 2013. Comparison of average stress drop measures for ruptures with heterogeneous stress change and implications for earthquake physics. *Geophysical Journal International* 193, 1691–1712. 10.1093/gji/ggt074.
- Obana, K., Kodaira, S., 2009. Low-frequency tremors associated with reverse faults in a shallow accretionary prism. *Earth and Planetary Science Letters* 287, 168–174. 10.1016/j.epsl.2009.08.005.
- Obana, K., Kodaira, S., Kaneda, Y., 2004. Microseismicity around rupture area of the 1944 Tonankai earthquake from ocean bottom seismograph observations. *Earth and Planetary Science Letters* 222, 561–572. 10.1016/j.epsl.2004.02.032.
- Obara, K., 2002. Nonvolcanic deep tremor associated with subduction in southwest Japan. *Science (New York, N.Y.)* 296, 1679–1681. 10.1126/science.1070378.
- Obara, K., Ito, Y., 2005. Very low frequency earthquakes excited by the 2004 off the Kii peninsula earthquakes: A dynamic deformation process in the large accretionary prism. *Earth Planet Sp* 57, 321–326. 10.1186/BF03352570.
- Obara, K., Kato, A., 2016. Connecting slow earthquakes to huge earthquakes. *Science (New York, N.Y.)* 353, 253–257. 10.1126/science.aaf1512.
- Okada, Y., 1985. Surface deformation due to shear and tensile faults in a half-space. *Bulletin of the Seismological Society of America* 75, 1135–1154.
- Okada, Y., 1992. Internal deformation due to shear and tensile faults in a half-space. *Bulletin of the Seismological Society of America* 82, 1018–1040.
- Okino, K., Ohara, Y., Kasuga, S., Kato, Y., 1999. The Philippine Sea: New survey results reveal the structure and the history of the marginal basins. *Geophys. Res. Lett.* 26, 2287–2290. 10.1029/1999GL900537.
- Ozawa, S., Suito, H., Tobita, M., 2007. Occurrence of quasi-periodic slow-slip off the east coast of the Boso peninsula, Central Japan. *Earth Planet Sp* 59, 1241–1245. 10.1186/BF03352072.
- Pacheco, J.F., Sykes, L.R., 1992. Seismic moment catalog of large shallow earthquakes, 1900 to 1989. *Bulletin of the Seismological Society of America* 82, 1306–1349.
- Park, J.-O., Tsuru, T., Kodaira, S., Cummins, P.R., Kaneda, Y., 2002. Splay fault branching along the Nankai subduction zone. *Science (New York, N.Y.)* 297, 1157–1160. 10.1126/science.1074111.
- Park, J.-O., Tsuru, T., Kodaira, S., Nakanishi, A., Miura, S., Kaneda, Y., Kono, Y., Takahashi, N., 2000. Out-of-sequence thrust faults developed in the coseismic slip zone of the 1946 Nankai Earthquake (Mw=8.2) off Shikoku, southwest Japan. *Geophys. Res. Lett.* 27, 1033–1036. 10.1029/1999GL008443.
- Pickering, K.T., Underwood, M.B., Saito, S., Naruse, H., Kutterolf, S., Scudder, R., Park, J.-O., Moore, G.F., Slagle, A., 2013. Depositional architecture, provenance, and tectonic/eustatic modulation of Miocene submarine fans in the Shikoku Basin: Results from Nankai Trough Seismogenic Zone Experiment. *Geochem. Geophys. Geosyst.* 14, 1722–1739. 10.1002/ggge.20107.
- Polet, J., Kanamori, H., 2000. Shallow subduction zone earthquakes and their tsunamigenic potential. *Geophysical Journal International* 142, 684–702. 10.1046/j.1365-246x.2000.00205.x.
- Polster, A., Fabian, M., Villinger, H., 2009. Effective resolution and drift of Paroscientific pressure sensors derived from long-term seafloor measurements. *Geochem. Geophys. Geosyst.* 10. 10.1029/2009GC002532.
- Rabinowicz, E., 1951. The Nature of the Static and Kinetic Coefficients of Friction. *Journal of Applied Physics* 22, 1373–1379. 10.1063/1.1699869.
- Reinen, L.A., Weeks, J.D., 1993. Determination of rock friction constitutive parameters using an iterative least squares inversion method. *J. Geophys. Res.* 98, 15937. 10.1029/93JB00780.

- Rice, J., 1980. The mechanics of earthquake rupture.
- Richardson, E., Marone, C., 1999. Effects of normal stress vibrations on frictional healing. *J. Geophys. Res.* 104, 28859–28878. 10.1029/1999JB900320.
- Rikitake, T., 1999. Probability of a great earthquake to recur in the Tokai district, Japan: Reevaluation based on newly-developed paleoseismology, plate tectonics, tsunami study, micro-seismicity and geodetic measurements. *Earth, Planets and Space* 51, 147–157. 10.1186/BF03352219.
- Roeloffs, E., 1996. Poroelastic Techniques in the Study of Earthquake-Related Hydrologic Phenomena, in: Dmowska, R., Saltzman, B. (Eds.), *Advances in Geophysics*, vol. 37, 1st ed. Elsevier textbooks, s.l., pp. 135–195.
- Rogers, G., Dragert, H., 2003. Episodic tremor and slip on the Cascadia subduction zone: The chatter of silent slip. *Science (New York, N.Y.)* 300, 1942–1943. 10.1126/science.1084783.
- Rouet-Leduc, B., Hulbert, C., Lubbers, N., Barros, K., Humphreys, C.J., Johnson, P.A., 2017. Machine Learning Predicts Laboratory Earthquakes. *Geophys. Res. Lett.* 44, 9276–9282. 10.1002/2017GL074677.
- Rudolph, M.L., Manga, M., 2010. Mud volcano response to the 4 April 2010 El Mayor-Cucapah earthquake. *J. Geophys. Res.* 115, 35. 10.1029/2010JB007737.
- Ruina, A., 1983. Slip instability and state variable friction laws. *J. Geophys. Res.* 88, 10359–10370. 10.1029/JB088iB12p10359.
- Sacks, I.S., Linde, A.T., Suyehiro, S., Snoke, J.A., 1978. Slow earthquakes and stress redistribution. *Nature* 275, 599–602. 10.1038/275599a0.
- Saffer, D., Guo, J., Underwood, M.B., Likos, W., Skarbak, R.M., Song, I., Gildow, M., 2011. Data report: Consolidation, permeability, and fabric of sediments from the Nankai continental slope, IODP Sites C0001, C0008, and C0004. *Proceedings of the Integrated Ocean Drilling Program, Volume 314/315/316*, 1–61. 10.2204/iodp.proc.314315316.218.2011.
- Saffer, D., Kopf, A., Toczko, S., and the Expedition 365 Scientists (Eds.), 2017a. NanTroSEIZE Stage 3: Shallow Megasplay Long-Term Borehole Monitoring System. International Ocean Discovery Program, College Station.
- Saffer, D., Kopf, A., Toczko, S., Araki, E., Carr, S., Kimura, T., Kinoshita, C., Kobayashi, R., Machida, Y., Rösner, A., Wallace, L.M., Chiyonobu, S., Kanagawa, K., Kanamatsu, T., Kimura, G., Underwood, M.B., 2017b. Expedition 365 methods, in: Saffer, D., Kopf, A., Toczko, S., and the Expedition 365 Scientists (Eds.), *NanTroSEIZE Stage 3: Shallow Megasplay Long-Term Borehole Monitoring System*. International Ocean Discovery Program, College Station.
- Saffer, D., Kopf, A., Toczko, S., Araki, E., Carr, S., Kimura, T., Kinoshita, C., Kobayashi, R., Machida, Y., Rösner, A., Wallace, L.M., Chiyonobu, S., Kanagawa, K., Kanamatsu, T., Kimura, G., Underwood, M.B., 2017c. Site C0010, in: Saffer, D., Kopf, A., Toczko, S., and the Expedition 365 Scientists (Eds.), *NanTroSEIZE Stage 3: Shallow Megasplay Long-Term Borehole Monitoring System*. International Ocean Discovery Program, College Station.
- Saffer, D., McNeill, L., Byrne, T., Araki, E., Toczko, S., Eguchi, N., Takahashi, K., and the Expedition 319 Scientists (Eds.), 2010. *NanTroSEIZE Stage 2: NanTroSEIZE Riser/Riserless Observatory*. Integrated Ocean Drilling Program.
- Saffer, D.M., 2015. The permeability of active subduction plate boundary faults. *Geofluids* 15, 193–215. 10.1111/gfl.12103.
- Saffer, D.M., Frye, K.M., Marone, C., Mair, K., 2001. Laboratory results indicating complex and potentially unstable frictional behavior of smectite clay. *Geophys. Res. Lett.* 28, 2297–2300. 10.1029/2001GL012869.

- Saffer, D.M., Lockner, D.A., McKiernan, A., 2012a. Effects of smectite to illite transformation on the frictional strength and sliding stability of intact marine mudstones. *Geophys. Res. Lett.* 39. 10.1029/2012GL051761.
- Saffer, D.M., Lockner, D.A., McKiernan, A., 2012b. Effects of smectite to illite transformation on the frictional strength and sliding stability of intact marine mudstones. *Geophys. Res. Lett.* 39. 10.1029/2012GL051761.
- Saffer, D.M., Marone, C., 2003. Comparison of smectite- and illite-rich gouge frictional properties: Application to the updip limit of the seismogenic zone along subduction megathrusts. *Earth and Planetary Science Letters* 215, 219–235. 10.1016/S0012-821X(03)00424-2.
- Saffer, D.M., Wallace, L.M., 2015. The frictional, hydrologic, metamorphic and thermal habitat of shallow slow earthquakes. *Nature Geosci* 8, 594–600. 10.1038/ngeo2490.
- Sakaguchi, A., Chester, F., Curewitz, D., Fabbri, O., Goldsby, D., Kimura, G., Li, C.-F., Masaki, Y., Screaton, E.J., Tsutsumi, A., Ujiie, K., Yamaguchi, A., 2011. Seismic slip propagation to the updip end of plate boundary subduction interface faults: Vitrinite reflectance geothermometry on Integrated Ocean Drilling Program NanTro SEIZE cores. *Geology* 39, 395–398. 10.1130/G31642.1.
- Sawyer, A.H., Flemings, P., Elsworth, D., Kinoshita, M., 2008. Response of submarine hydrologic monitoring instruments to formation pressure changes: Theory and application to Nankai advanced CORKs. *J. Geophys. Res.* 113, 247. 10.1029/2007JB005132.
- Schaff, D.P., Beroza, G.C., 2004. Coseismic and postseismic velocity changes measured by repeating earthquakes. *J. Geophys. Res.* 109, 101. 10.1029/2004JB003011.
- Scholz, C.H., 1998. Earthquakes and friction laws. *Nature* 391, 37–42. 10.1038/34097.
- Scholz, C.H., 2018. *The Mechanics of Earthquakes and Faulting*. Cambridge University Press, Cambridge, 1 p.
- Scholz, C.H., Engelder, J.T., 1976. The role of asperity indentation and ploughing in rock friction I: Asperity creep and stick-slip. *International Journal of Rock Mechanics and Mining Sciences & Geomechanics Abstracts* 13, 149–154. 10.1016/0148-9062(76)90819-6.
- Schwartz, S.Y., Rokosky, J.M., 2007. Slow slip events and seismic tremor at circum-Pacific subduction zones. *Rev. Geophys.* 45. 10.1029/2006RG000208.
- Screaton, E., Carson, B., Davis, E., Becker, K., 2000. Permeability of a decollement zone: Results from a two-well experiment in the Barbados accretionary complex. *J. Geophys. Res.* 105, 21403–21410. 10.1029/2000JB900220.
- Screaton, E., Kimura, G., Curewitz, D., Moore, G., Chester, F., Fabbri, O., Fergusson, C., Girault, F., Goldsby, D., Harris, R., Inagaki, F., Jiang, T., Kitamura, Y., Knuth, M., Li, C.-F., Liljedahl, L.C., Louis, L., Milliken, K., Nicholson, U., Riedinger, N., Sakaguchi, A., Solomon, E., Strasser, M., Su, X., Tsutsumi, A., Yamaguchi, A., Ujiie, K., Zhao, X., 2009. Interactions between deformation and fluids in the frontal thrust region of the NanTroSEIZE transect offshore the Kii Peninsula, Japan: Results from IODP Expedition 316 Sites C0006 and C0007. *Geochem. Geophys. Geosyst.* 10. 10.1029/2009GC002713.
- Screaton, E.J., Carson, B., Lennon, G.P., 1995. Hydrogeologic properties of a thrust fault within the Oregon Accretionary Prism. *J. Geophys. Res.* 100, 20025–20035. 10.1029/95JB02152.
- Screaton, E.J., Fisher, A.T., Carson, B., Becker, K., 1997. Barbados Ridge hydrogeologic tests: Implications for fluid migration along an active decollement. *Geology* 25, 239. 10.1130/0091-7613(1997)025<0239:BRHTIF>2.3.CO;2.
- Seno, T., 2002. Tsunami earthquakes as transient phenomena. *Geophys. Res. Lett.* 29, 58-1-58-4. 10.1029/2002GL014868.

- Seno, T., Stein, S., Gripp, A.E., 1993. A model for the motion of the Philippine Sea Plate consistent with NUVEL-1 and geological data. *J. Geophys. Res.* 98, 17941–17948. 10.1029/93JB00782.
- Shelly, D.R., Beroza, G.C., Ide, S., 2007. Non-volcanic tremor and low-frequency earthquake swarms. *Nature* 446. 10.1038/nature05666.
- Shelly, D.R., Beroza, G.C., Ide, S., Nakamura, S., 2006. Low-frequency earthquakes in Shikoku, Japan, and their relationship to episodic tremor and slip. *Nature* 442, 188–191. 10.1038/nature04931.
- Shibazaki, B., Iio, Y., 2003. On the physical mechanism of silent slip events along the deeper part of the seismogenic zone. *Geophys. Res. Lett.* 30, 1525. 10.1029/2003GL017047.
- Shipboard Scientific Party, 2002. Explanatory Notes, in: Mikada, H., Becker, K., Moore, J.C., Klaus, A. (Eds.), *Proceedings of the Ocean Drilling Program, 196 Initial Reports*, vol. 196. Ocean Drilling Program.
- Sintubin, M., Wenk, H.-R., Phillips, D.S., 1995. Texture development in platy materials: Comparison of Bi2223 aggregates with phyllosilicate fabrics. *Materials Science and Engineering: A* 202, 157–171. 10.1016/0921-5093(95)09811-9.
- Skarbek, R.M., Saffer, D.M., 2009. Pore pressure development beneath the décollement at the Nankai subduction zone: Implications for plate boundary fault strength and sediment dewatering. *J. Geophys. Res.* 114, 1. 10.1029/2008JB006205.
- Spinelli, G.A., Saffer, D.M., Underwood, M.B., 2006. Hydrogeologic responses to three-dimensional temperature variability, Costa Rica subduction margin. *J. Geophys. Res.* 111, 19207. 10.1029/2004JB003436.
- Stern, R.J., 2002. Subduction zones. *Rev. Geophys.* 40, 293. 10.1029/2001RG000108.
- Stern, R.J., Scholl, D.W., Fryer, G., 2016. An Introduction to Convergent Margins and Their Natural Hazards, in: Duarte, J.C., Schellart, W.P. (Eds.), *Plate boundaries and natural hazards*. John Wiley, Hoboken, New Jersey.
- Stipp, M., Rolfs, M., Kitamura, Y., Behrmann, J.H., Schumann, K., Schulte-Kortnack, D., Feeser, V., 2013. Strong sediments at the deformation front, and weak sediments at the rear of the Nankai accretionary prism, revealed by triaxial deformation experiments. *Geochem. Geophys. Geosyst.* 14, 4791–4810. 10.1002/ggge.20290.
- Strasser, M., Kölling, M., Ferreira, C.d.S., Fink, H.G., Fujiwara, T., Henkel, S., Ikehara, K., Kanamatsu, T., Kawamura, K., Kodaira, S., Römer, M., Wefer, G., 2013. A slump in the trench: Tracking the impact of the 2011 Tohoku-Oki earthquake. *Geol* 41, 935–938. 10.1130/G34477.1.
- Strasser, M., Moore, G.F., Kimura, G., Kitamura, Y., Kopf, A.J., Lallemand, S., Park, J.-O., Screatton, E.J., Su, X., Underwood, M.B., Zhao, X., 2009. Origin and evolution of a splay fault in the Nankai accretionary wedge. *Nature Geosci* 2, 648–652. 10.1038/ngeo609.
- Strasser, M., Moore, G.F., Kimura, G., Kopf, A.J., Underwood, M.B., Guo, J., Screatton, E.J., 2011. Slumping and mass transport deposition in the Nankai fore arc: Evidence from IODP drilling and 3-D reflection seismic data. *Geochem. Geophys. Geosyst.* 12. 10.1029/2010GC003431.
- Sugioka, H., Okamoto, T., Nakamura, T., Ishihara, Y., Ito, A., Obana, K., Kinoshita, M., Nakahigashi, K., Shinohara, M., Fukao, Y., 2012. Tsunamigenic potential of the shallow subduction plate boundary inferred from slow seismic slip. *Nature Geosci* 5, 414–418. 10.1038/ngeo1466.
- Suzuki, K., Nakano, M., Takahashi, N., Hori, T., Kamiya, S., Araki, E., Nakata, R., Kaneda, Y., 2016. Synchronous changes in the seismicity rate and ocean-bottom hydrostatic pressures along the Nankai trough: A possible slow slip event detected by the Dense Oceanfloor Network system for Earthquakes and Tsunamis (DONET). *Tectonophysics* 680, 90–98. 10.1016/j.tecto.2016.05.012.

- Takahashi, M., Azuma, S., Ito, H., Kanagawa, K., Inoue, A., 2014. Frictional properties of the shallow Nankai Trough accretionary sediments dependent on the content of clay minerals. *Earth Planet Space* 66. 10.1186/1880-5981-66-75.
- Takahashi, M., Azuma, S., Uehara, S.-i., Kanagawa, K., Inoue, A., 2013. Contrasting hydrological and mechanical properties of clayey and silty muds cored from the shallow Nankai Trough accretionary prism. *Tectonophysics* 600, 63–74. 10.1016/j.tecto.2013.01.008.
- Tamura, Y., Sato, T., Ooe, M., Ishiguro, M., 1991. A procedure for tidal analysis with a Bayesian information criterion. *Geophysical Journal International* 104, 507–516. 10.1111/j.1365-246X.1991.tb05697.x.
- Tanioka, Y., Satake, K., 2001. Detailed coseismic slip distribution of the 1944 Tonankai Earthquake estimated from tsunami waveforms. *Geophys. Res. Lett.* 28, 1075–1078. 10.1029/2000GL012284.
- Taylor, B., 1992. Rifting and the Volcanic-Tectonic Evolution of the Izu-Bonin-Mariana Arc, in: Taylor, B., Fujioka, K. (Eds.), *Proceedings of the Ocean Drilling Program*, 126 Scientific Results, vol. 126. Ocean Drilling Program.
- Tembe, S., Lockner, D.A., Wong, T.-F., 2010. Effect of clay content and mineralogy on frictional sliding behavior of simulated gouges: Binary and ternary mixtures of quartz, illite, and montmorillonite. *J. Geophys. Res.* 115, 827. 10.1029/2009JB006383.
- Terzaghi, K., Peck, R.B., Mesri, G., 1996. *Soil mechanics in engineering practice*, 3rd ed. John Wiley & Sons, xviii, 566.
- Tesei, T., Collettini, C., Barchi, M.R., Carpenter, B.M., Di Stefano, G., 2014. Heterogeneous strength and fault zone complexity of carbonate-bearing thrusts with possible implications for seismicity. *Earth and Planetary Science Letters* 408, 307–318. 10.1016/j.epsl.2014.10.021.
- Tesei, T., Collettini, C., Carpenter, B.M., Viti, C., Marone, C., 2012. Frictional strength and healing behavior of phyllosilicate-rich faults. *J. Geophys. Res.* 117, 1987. 10.1029/2012JB009204.
- To, A., Obana, K., Sugioka, H., Araki, E., Takahashi, N., Fukao, Y., 2015. Small size very low frequency earthquakes in the Nankai accretionary prism, following the 2011 Tohoku-Oki earthquake. *Physics of the Earth and Planetary Interiors* 245, 40–51. 10.1016/j.pepi.2015.04.007.
- Tobin, H., Kinoshita, M., 2007. The IODP Nankai Trough Seismogenic Zone Experiment. *Scientific Drilling*. 10.2204/iodp.sd.s01.30.2007.
- Tobin, H.J., Kinoshita, M., 2006a. Investigations of seismogenesis at the Nankai Trough, Japan. *Integrated Ocean Drilling Program*.
- Tobin, H.J., Kinoshita, M., 2006b. NanTroSEIZE: The IODP Nankai Trough Seismogenic Zone Experiment. *Scientific Drilling*. 10.2204/iodp.sd.2.06.2006.
- Toki, T., Higa, R., Ijiri, A., Tsunogai, U., Ashi, J., 2014. Origin and transport of pore fluids in the Nankai accretionary prism inferred from chemical and isotopic compositions of pore water at cold seep sites off Kumano. *Earth Planet Space* 66, 137. 10.1186/s40623-014-0137-3.
- Trütner, S., Hüpers, A., Ikari, M.J., Yamaguchi, A., Kopf, A.J., 2015. Lithification facilitates frictional instability in argillaceous subduction zone sediments. *Tectonophysics* 665, 177–185. 10.1016/j.tecto.2015.10.004.
- Tse, S.T., Rice, J.R., 1986. Crustal earthquake instability in relation to the depth variation of frictional slip properties. *J. Geophys. Res.* 91, 9452. 10.1029/JB091iB09p09452.
- Tsumura, K., 1967. Determination of earthquake magnitude from total duration of oscillation. *Bull. Earthquake Res. Inst. Univ. Tokyo* 45, 7–18.

- Tsutsumi, A., Fabbri, O., Karpoff, A.M., Ujiie, K., Tsujimoto, A., 2011. Friction velocity dependence of clay-rich fault material along a megasplay fault in the Nankai subduction zone at intermediate to high velocities. *Geophys. Res. Lett.* 38. 10.1029/2011GL049314.
- Tullis, T.E., 1976. Experiments on the origin of slaty cleavage and schistosity. *Geological Society of America Bulletin* 87, 745. 10.1130/0016-7606(1976)87<745:EOTOOS>2.0.CO;2.
- Ujiie, K., Tsutsumi, A., 2010. High-velocity frictional properties of clay-rich fault gouge in a megasplay fault zone, Nankai subduction zone. *Geophys. Res. Lett.* 37. 10.1029/2010GL046002.
- Underwood, M.B., 2007. 3. Sediment Inputs to Subduction Zones Why Lithostratigraphy and Clay Mineralogy Matter, in: Moore, J.C., Dixon, T.H. (Eds.), *The seismogenic zone of subduction thrust faults*. Columbia University Press, New York.
- Underwood, M.B., 2018. The origin of strata within the inner accretionary prism of Nankai Trough: Evidence from clay mineral assemblages along the NanTroSEIZE transect. *Island Arc* 27, e12252. 10.1111/iar.12252.
- Underwood, M.B., Moore, G.F., 2012. Evolution of Sedimentary Environments in the Subduction Zone v of Southwest Japan: Recent Results from the NanTroSEIZE Kumano Transect, in: Busby, C.J., Antonio, A. (Eds.), *Tectonics of sedimentary basins. Recent advances*, 1st ed.
- Vidale, J.E., Ellsworth, W.L., Cole, A., Marone, C., 1994. Variations in rupture process with recurrence interval in a repeated small earthquake. *Nature* 368, 624-626. 10.1038/368624a0.
- Vidale, J.E., Li, Y.-G., 2003. Damage to the shallow Landers fault from the nearby Hector Mine earthquake. *Nature* 421, 524–526. 10.1038/nature01354.
- Vigny, C., Simons, W.J.F., Abu, S., Bamphenyu, R., Satirapod, C., Choosakul, N., Subarya, C., Socquet, A., Omar, K., Abidin, H.Z., Ambrosius, B.A.C., 2005. Insight into the 2004 Sumatra–Andaman earthquake from GPS measurements in southeast Asia. *Nature* 436, 201–206. 10.1038/nature03937.
- Vogt, C., Fischer, R.X., Lauterjung, J., 2002. Investigation of the clay fraction (<2 µm) of the clay mineral society reference clays. *Clays and Clay Minerals* 50, 388–400.
- Wallace, L.M., Araki, E., Saffer, D., Wang, X., Roesner, A., Kopf, A., Nakanishi, A., Power, W., Kobayashi, R., Kinoshita, C., Toczko, S., Kimura, T., Machida, Y., Carr, S., 2016a. Near-field observations of an offshore Mw 6.0 earthquake from an integrated seafloor and subseafloor monitoring network at the Nankai Trough, southwest Japan. *J. Geophys. Res. Solid Earth* 121, 8338–8351. 10.1002/2016JB013417.
- Wallace, L.M., Webb, S.C., Ito, Y., Mochizuki, K., Hino, R., Henrys, S., Schwartz, S.Y., Sheehan, A.F., 2016b. Slow slip near the trench at the Hikurangi subduction zone, New Zealand. *Science (New York, N.Y.)* 352, 701–704. 10.1126/science.aaf2349.
- Wang, C.-y., Manga, M., 2010. Hydrologic responses to earthquakes and a general metric. *Geofluids* 17, 1. 10.1111/j.1468-8123.2009.00270.x.
- Wang, C.-Y., 2007. Liquefaction beyond the Near Field. *Seismological Research Letters* 78, 512–517. 10.1785/gssrl.78.5.512.
- Wang, C.-Y., Wong, A., Dreger, D.S., Manga, M., 2006. Liquefaction Limit during Earthquakes and Underground Explosions: Implications on Ground-Motion Attenuation. *Bulletin of the Seismological Society of America* 96, 355–363. 10.1785/0120050019.
- Wang, K., 2004. Applying fundamental principles and mathematical models to understand processes and estimate parameter. *Hydrogeology of the Oceanic Lithosphere*.
- Wang, K., Davis, E.E., 1996. Theory for the propagation of tidally induced pore pressure variations in layered subseafloor formations. *J. Geophys. Res.* 101, 11483–11495. 10.1029/96JB00641.

- Wang, K., Davis, E.E., van der Kamp, G., 1998. Theory for the effects of free gas in subsea formations on tidal pore pressure variations and seafloor displacements. *J. Geophys. Res.* 103, 12339–12353. 10.1029/98JB00952.
- Wang, X., 2008. Numerical modelling of surface and internal waves over shallow and intermediate water. PhD Thesis, School of Civil and Environmental Engineering, Cornell University.
- Wang, X., Power, W., 2011. COMCOT: a tsunami generation, propagation and run-up model. GNS Science report 43.
- Watanabe, H., 1971. Determination of earthquake magnitude at regional distance in and near Japan. *Zisin* 2 24, 189–200.
- Wessel, P., Smith, W.H.F., 1991. Free software helps map and display data. *Eos Trans. AGU* 72, 441. 10.1029/90EO00319.
- Williams, C.A., Wallace, L.M., 2015. Effects of material property variations on slip estimates for subduction interface slow-slip events. *Geophys. Res. Lett.* 42, 1113–1121. 10.1002/2014GL062505.
- Wu, J., Suppe, J., Lu, R., Kanda, R., 2016. Philippine Sea and East Asian plate tectonics since 52 Ma constrained by new subducted slab reconstruction methods. *J. Geophys. Res.* 121, 4670–4741. 10.1002/2016JB012923.
- Xue, L., Li, H.-B., Brodsky, E.E., Xu, Z.-Q., Kano, Y., Wang, H., Mori, J.J., Si, J.-L., Pei, J.-L., Zhang, W., Yang, G., Sun, Z.-M., Huang, Y., 2013. Continuous permeability measurements record healing inside the Wenchuan earthquake fault zone. *Science (New York, N.Y.)* 340, 1555–1559. 10.1126/science.1237237.
- Yamashita, Y., Yakiwara, H., Asano, Y., Shimizu, H., Uchida, K., Hirano, S., Umakoshi, K., Miyamachi, H., Nakamoto, M., Fukui, M., Kamizono, M., Kanehara, H., Yamada, T., Shinohara, M., OBARA, K., 2015. Geophysics. Migrating tremor off southern Kyushu as evidence for slow slip of a shallow subduction interface. *Science (New York, N.Y.)* 348, 676–679. 10.1126/science.aaa4242.
- Yao, L., Shimamoto, T., Ma, S., Han, R., Mizoguchi, K., 2013. Rapid postseismic strength recovery of Pingxi fault gouge from the Longmenshan fault system: Experiments and implications for the mechanisms of high-velocity weakening of faults. *J. Geophys. Res.* 118, 4547–4563. 10.1002/jgrb.50308.
- Yasuda, S., Towhata, I., Ishii, I., Sato, S., Uchimura, T., 2013. Liquefaction-induced damage to structures during the 2011 great east Japan earthquake. *Journal of JSCE* 1, 181–193. 10.2208/journalofjsce.1.1_181.
- Yokota, Y., Ishikawa, T., Watanabe, S.-i., Tashiro, T., Asada, A., 2016. Seafloor geodetic constraints on interplate coupling of the Nankai Trough megathrust zone. *Nature* 534, 374–377. 10.1038/nature17632.
- Zang, S.X., Chen, Q.Y., Ning, J.Y., Shen, Z.K., Liu, Y.G., 2002. Motion of the Philippine Sea plate consistent with the NUVEL-1A model. *Geophysical Journal International* 150, 809–819. 10.1046/j.1365-246X.2002.01744.x.
- Zelt, C.A., Barton, P.J., 1998. Three-dimensional seismic refraction tomography: A comparison of two methods applied to data from the Faeroe Basin. *J. Geophys. Res.* 103, 7187–7210. 10.1029/97JB03536.
- Zhang, J., Brink, U.S. ten, Toksöz, M.N., 1998. Nonlinear refraction and reflection travel time tomography. *J. Geophys. Res.* 103, 29743–29757. 10.1029/98JB01981.
- Zhang, J., Toksöz, M.N., 1998. Nonlinear refraction travelttime tomography. *Geophysics* 63, 1726–1737. 10.1190/1.1444468.

Declaration

Versicherung an Eides Statt / Affirmation in lieu of an oath

gem. § 5 Abs. 5 der Promotionsordnung vom 18.06.2018 /

according to § 5 (5) of the Doctoral Degree Rules and Regulations of 18 June, 2018

Ich / I Alexander, Rösner, Isarstrasse 100, 28199 Bremen, 2954892

versichere an Eides Statt durch meine Unterschrift, dass ich die vorliegende Dissertation selbständig und ohne fremde Hilfe angefertigt und alle Stellen, die ich wörtlich dem Sinne nach aus Veröffentlichungen entnommen habe, als solche kenntlich gemacht habe, mich auch keiner anderen als der angegebenen Literatur oder sonstiger Hilfsmittel bedient habe und die zu Prüfungszwecken beigelegte elektronische Version (PDF) der Dissertation mit der abgegebenen gedruckten Version identisch ist.

With my signature I affirm in lieu of an oath that I prepared the submitted dissertation independently and without illicit assistance from third parties, that I appropriately referenced any text or content from other sources, that I used only literature and resources listed in the dissertation, and that the electronic (PDF) and printed versions of the dissertation are identical.

Ich versichere an Eides Statt, dass ich die vorgenannten Angaben nach bestem Wissen und Gewissen gemacht habe und dass die Angaben der Wahrheit entsprechen und ich nichts verschwiegen habe.

I affirm in lieu of an oath that the information provided herein to the best of my knowledge is true and complete.

Die Strafbarkeit einer falschen eidesstattlichen Versicherung ist mir bekannt, namentlich die Strafandrohung gemäß § 156 StGB bis zu drei Jahren Freiheitsstrafe oder Geldstrafe bei vorsätzlicher Begehung der Tat bzw. gemäß § 161 Abs. 1 StGB bis zu einem Jahr Freiheitsstrafe oder Geldstrafe bei fahrlässiger Begehung.

I am aware that a false affidavit is a criminal offence which is punishable by law in accordance with § 156 of the German Criminal Code (StGB) with up to three years imprisonment or a fine in case of intention, or in accordance with § 161 (1) of the German Criminal Code with up to one year imprisonment or a fine in case of negligence.

Ort / Place, Datum / Date

Unterschrift / Signature